UCLouvain
Institute for Information
and Communication Technologies,
Electronics and Applied Mathematics

Stochastic Geometry-Based Models For Cellular Network Deployment

Simon Demey

Thesis submitted in partial fulfillment
of the requirements for the degree of
Docteur en sciences de l'ingénieur

Dissertation committee:

Prof. Claude Oestges (UCLouvain, advisor)
Prof. Philippe De Doncker (ULB, advisor)
Prof. Luc Vandendorpe (UCLouvain)
Prof. François Horlin (ULB)
Prof. Margot Deruyck (Gent University)
Prof. Laurent Clavier (IMT Nord Europe, France)
Prof. David Bol (UCLouvain, chair)

Version of May 26, 2023.

Stochastic Geometry-Based Models For Cellular Network Deployment
by Simon Demey

ICTEAM
Université catholique de Louvain
Place Sainte-Barbe, 2
1348 Louvain-la-Neuve
Belgium

Abstract

The growing use of mobile devices and data-hungry applications has created an unprecedented demand for network capacity. In response, engineers have been exploring advanced solutions to meet this demand. The most promising solution is network densification, particularly in urban areas, where small cells can complement the existing cellular network to improve the coverage in poorly served areas and provide faster data rates in high traffic areas.

To assist the deployment of this new technology, a network-level analysis is generally required. This analysis should provide network planners with valuable guidelines regarding network design parameters such as BS density. Controlling inter-tier interference and exposure, which are subject to legal thresholds, is particularly important and an efficient characterization of the power levels is thus needed. In that sense, the choice of the channel model plays a crucial role, and the discussion often revolves around the trade-offs between stochastic and deterministic channel models. While the decreased link distances and higher frequencies associated with small cells limit the propagation environment, making ray-tracing algorithms more suitable, conducting a network-level analysis based on this technique is still time-consuming.

In this study, we take an alternative approach using stochastic geometry theory, which enables us to derive analytical expressions for different network-level metrics averaged over numerous network realizations. However, this approach typically involves simpler assumptions regarding the network topology and the channel model. Specifically, we employ Poisson doubly stochastic point processes to model the deployment of small cells along streets and adopt simpler propagation-based channel models.

To validate these simpler assumptions and demonstrate their limitations, the deployment trends observed with our model are subsequently compared with specific Monte Carlo simulations. These simulations first use ray tracing as the channel model and then use existing street patterns for small cells deployment. It is demonstrated that a finely grained selection of the model parameters is critical for our simpler channel models to provide accurate results. In addition, it is shown that the use of Poisson doubly stochastic models can lead to an overestimation of the coverage probability, particularly because these models are unable to account for street repulsion. Nonetheless, these models consistently reveal that the utilization of beamforming techniques and a sparse but strategic deployment of small cells are crucial elements for enhancing network performance.

Finally, we quantify the losses that arise from using simpler channel models in an actual deployment optimization on a simple fixed scenario. As the network becomes denser, the use of a deterministic model is shown to become more relevant.

Acknowledgments

I would like to express my gratitude to all individuals who directly and indirectly contributed to the completion of this Ph.D. thesis.

First, I would like to thank my co-supervisors, Prof. Claude Oestges and Prof. Philippe De Doncker, for the generous amount of time you have devoted to me throughout our frequent meetings. I am immensely thankful for the invaluable feedback I have received from our discussions. I would like to highlight the significance of your honesty, which has enabled me to take a step back and embrace a more practical mindset towards my work. This has been instrumental in my scientific development and has allowed me to prioritize the essential aspects of my research.

I also greatly appreciate the time and effort devoted by the jury members to the reading of this thesis : Prof. Luc Vandendorpe, Prof. François Horlin, Prof. Margot Deruyck and Prof. Laurent Clavier. Their careful reviews and suggestions have substantially improved the quality of the manuscript.

I sincerely thank all my colleagues from the ICTEAM institute who have accompanied me throughout this journey.

> A special thanks to the current and past members of the COSY group for all the wonderful moments we shared: Thomas Pairon, Julian Villegas, François De Saint Moulin, Florian Quatresooz, Guillaume Thiran, Jérome Eertmans, Martin Willame, Gilles Monnoyer, Vasilii Semkin, Antoine Paris and many others. The lunchtime ping pong matches, the training schools in Barcelona and Lyon, the raclette gatherings at Claude's place or the birthday pies moments were fantastic.

Thanks also to everyone who played for the ELEN futsal team: Maxime Schramme, Simon Carbonelle, Damien Dasnoy, Ludovic Moreau and many others. Our matches brought life to many lunchtimes over the past years.

Thanks to Nicolas Roisin, Karim El Khoury, Romain Hanus, Quentin Courte, Mathieu Xhonneux, Denis Tihon and Anne-Sophie Collin, with whom I had the pleasure of supervising the practical sessions during these years. I had a great time during our numerous meetings (on site or via Teams), laboratories or boxes assemblies in P2.

Thanks to Jean Cavillot, Dani Manjah and Nicolas Leblanc for our corporate lunches.

Thanks to François Hubin and Brigitte Dupont for the computer assistance and to Isabelle Dargent, Jean Deschuyter, Christelle Derzelle and Marie-Hélène Dewael for the administrative support.

A special thanks to Charles Wiame, with whom I was lucky to share my office during this entire adventure. Thanks for making the room a better place. Thanks for your relentless support during periods of doubt. Thanks for your expertise and professionalism. But above all, thanks for being my friend.

Many thanks to my friends outside UCLouvain, you guys are amazing. I am certain that there are still many extraordinary experiences ahead of us.

Thank you Célina for supporting me for almost two years now, and especially during the tough last months of writing. You have made the past six months a lot more enjoyable and bearable, and I am sure that there are still countless moments awaiting us in the future. I will make every effort to be as supportive to you as you have been to me when the time comes for you to write your thesis. You are the best.

Finally, I want to express my deepest gratitude to my parents, my sister, my brother and my grandfather for being there since the beginning. You don't change a winning team even if it is that small. Thank you mom for consistently motivating me to confront any challenge and continuously surpass my boundaries since my early childhood. I would not be there without you. Thank you dad for your unwavering sense of family. You were there in any circumstances.

Contents

List of Figures . . . . **ix**

List of Tables . . . . **xiii**

Acronyms . . . . **xiv**

List of symbols . . . . **xvii**

1 Introduction **1**

1.1 Context of the thesis 1

1.2 Channel models 4

1.2.1 Analytical models 7

1.2.2 Physical models 7

1.3 Why is stochastic geometry a powerful tool? 10

1.4 Major contributions 12

1.5 Thesis outline 13

2 Introduction to stochastic geometry **17**

2.1 Introduction to point processes 18

2.1.1 Planar line processes 19

2.1.2 General properties 20

2.1.3 The Poisson point process 21

2.1.4 The Poisson Cox line process 24

2.1.5 The non homogeneous Poisson Cox line process 29

2.1.6 Finite length stick processes 32

2.2 Stochastic geometry based analytical techniques 34

2.2.1 Using the Laplace transform 35

2.2.2 Using the Gil-Pelaez inversion theorem 36

3 A general multi-tier urban network model . . . 37
3.1 Related works . . . 37
3.2 Network topology . . . 43
3.2.1 Street Tiers . . . 43
3.2.2 Roof Tiers . . . 44
3.3 Channel model . . . 45
3.3.1 Beamforming model . . . 45
3.3.2 Blockage model . . . 46
3.3.3 Tiers classification . . . 49
3.3.4 Fading model . . . 50
3.3.5 Computation of the received powers . . . 54
3.3.6 Association rules . . . 56
3.3.7 Generalization to non-uniform users . . . 58
3.3.8 Generalization to crossroad users . . . 59
3.3.9 Generalization to sparser environments . . . 60
3.4 Calibrating the model parameters . . . 63
3.4.1 Link budget parameters for the different types of cells . . . 63
3.4.2 Line-of-sight probabilities . . . 63
3.4.3 Path loss model parameters . . . 64

4 Derivation of network-level performance metrics . . . 69
4.1 Notations and Abbreviations . . . 70
4.2 Useful distance distributions . . . 70
4.2.1 Distance distributions in case of blockage . . . 70
4.2.2 Distance distributions for typical street base stations . . . 71
4.2.3 Distance distributions for roof base stations in urban environments 72
4.2.4 Distance distributions in non typical streets . . . 73
4.2.5 Distance distributions in surburban and rural environments . . 74
4.3 Useful preference thresholds . . . 75
4.4 Association probabilities . . . 77
4.5 Serving base station distance distributions . . . 78
4.6 Characteristic functions of the different contributions . . . 80
4.6.1 Useful signal power level . . . 80
4.6.2 Contributions coming from the typical street . . . 80
4.6.3 Contributions coming from roof BSs . . . 81
4.6.4 Contributions coming from non typical streets . . . 81
4.6.5 Generalization to crossroads and T-junctions users . . . 84
4.7 SINR-based statistics . . . 85
4.7.1 Coverage probability . . . 85

4.7.2 Rate-based statistics 87
4.8 Exposure-based statistics 90
4.8.1 Average exposure 90
4.8.2 Exposure CDF 92
4.9 Joint SINR-exposure distribution 92
4.10 Generalization to non-uniform user distributions 94

5 Full characterization of realistic topologies 99
5.1 Dense urban environments 100
5.1.1 Manhattan environments 100
5.1.2 Cox-like environments 106
5.2 Sparse urban environments and rural environments 117
5.3 A few words on the numerical complexity 119

6 Full validation of stochastic geometry-based models 121
6.1 Related works 122
6.2 Comparison to deterministic channel models 122
6.2.1 Ray tracing network topology 122
6.2.2 Ray tracing power computation 123
6.2.3 Methodology to fix the parameters 127
6.2.4 Numerical results and discussion 128
6.3 Comparison to real city deployments 131
6.3.1 Methodology to extract the parameters 134
6.3.2 Methodology to compare the approaches 136
6.3.3 Numerical results and discussion 139

7 Optimization of small cell deployment 143
7.1 Preparing the optimization process 144
7.1.1 Network data 145
7.1.2 Candidates 145
7.1.3 UE demand maps 145
7.1.4 Propagation maps 147
7.2 Optimization strategy 148
7.2.1 Optimization metric 148
7.2.2 Optimization process 150
7.3 Numerical results 150
7.3.1 Impact of the effective isotropic radiated power 153
7.3.2 Interchanging optimals 153
7.3.3 Impact of an uneven UE distribution 154

8 Conclusion **157**
8.1 Future research 161

Appendices **163**
A Proof of Lemma 4.4 163
B Proof of Lemma 4.6 164
C Proof of Lemma 4.12 164
D Proof of Lemma 4.16 166
E Proof of Lemma 4.22 166
F Proof of Lemma 4.26 167
G Proof of Lemma 4.34 170
H Proof of Lemma 4.37 171
I Proof of Lemma 4.42 172
J Proof of Lemma 4.48 174

List of publications **177**

Bibliography **179**

List of Figures

1.1 Forecast number of mobile devices worldwide from 2020 to 2025 2
1.2 Data rate and latency requirements of various applications . . . 3
1.3 Existing channel models classification 7
1.4 Result of the UCLouvain RT software on a simple scenario. . . 9

2.1 Illustration of the mapping between the line process and the point process in the representation space 19
2.2 Illustration of the translation and rotation properties of a process 20
2.3 Illustration of HPPPs 22
2.4 PCLP building process 25
2.5 Distances notations for a PCLP 27
2.6 Homogenization of a PCLP 29
2.7 Illustration of a street angular orientation distribution 31
2.8 Illustration of a non homogeneous street density 32
2.9 Illustration of stick processes 33

3.1 Snapshot of the studied network 44
3.2 Beamforming scheme with varying half-beam width 46
3.3 Notations for the roof tiers blockage model 47
3.4 Illustration of the roof tiers LOS probability 48
3.5 Illustration of the tiers classification 51
3.6 Probability density function of various fading distributions and equivalence 53
3.7 Berg recursive method notations 56
3.8 Illustration of a street hostpot BS in urban environments 59
3.9 Visualization of the different types of UEs 60

3.10 Illustration of the difference between urban environments and sparser environments 61
3.11 Comparison of path losses: Winner model vs. our model 66

4.1 Approximating the LTE spectral efficiency 88

5.1 Comparison of the diffracted contributions for a Manhattan-like environment and a Cox environment 101
5.2 Analysis of the impact of the LOS β-coefficient 103
5.3 Impact of the BS and street densities 104
5.4 Analysis of the joint distribution 105
5.5 Analysis of the differences between street UE and crossroad UE 106
5.6 Analysis of the UE capacity as function of the LOS β-coefficient and the BS power 107
5.7 Generating a city street pattern with increased organization . . 108
5.8 Impact of tier densities on the coverage probability for a uniform UE at various SINR thresholds 110
5.9 Impact of tier densities on the coverage probability for a non uniform UE at various SINR thresholds 111
5.10 Impact of the roof base station height on the coverage probability for a uniform UE at low street tiers densities 112
5.11 Performance analysis of both types of UEs 113
5.12 Network performance under different beamforming schemes . . 115
5.13 Impact of fading on the coverage probability 116
5.14 Coverage probability for a UE located at an increasing distance from the city center 116
5.15 Impact of tier densities on the coverage probability for a uniform UE at various SINR thresholds in sparser environments 118

6.1 Illustration of an environment generated for ray tracing analysis 123
6.2 Conventions used for reflection 124
6.3 Conventions used for diffraction 125
6.4 Selection of the PL parameters 128
6.5 Selection of the fading model 129
6.6 Comparison of SG and RT approaches 130
6.7 Sensitivity analysis of the estimated PL exponents based on the CDFs of the useful received power and of the aggregate interference 131
6.8 Topological statistics for the city of Brussels 132

6.9 Studied environments 133
6.10 Approach for approximating a neighbourhood by means of a NHPCLP 134
6.11 Approximating the street angular distribution of the studied environments 136
6.12 Assessing the LOS conditions of roof BSs in real cities 138
6.13 MATLAB reproduction of Brussels' city center 139
6.14 Example of a NHPLM reproduction of Brussels based on the extracted statistics 141
6.15 Comparison for the coverage probability obtained from our model vs. real topologies 142

7.1 Different steps involved in the optimization approach 144
7.2 Illustration of the environment subject to optimization 146
7.3 RF elements 3-17 DS sector antenna and its radiation pattern . 148
7.4 Illustration of the difference between power maps 149
7.5 Optimal weighted coverage probability as a function of the number of deployed BSs for different coverage thresholds 151
7.6 Losses caused by an interchange between optimals 154
7.7 Impact of neglecting uneven UE distribution on optimal deployments: probability losses analysis for a 3-17 DS antenna 155
7.8 Optimal deployments in case of uneven UE distribution 156

F.1 Street types used in the proof 169

List of Tables

1.1 KPIs targeted by the future 5G release 2

3.1 Typical values for the LOS probability parameters in sparse environments. 62
3.2 Typical values for the link budget parameters for the different types of cells. 64
3.3 LOS probability parameters for urban environments 64
3.4 Path loss parameters for urban environments 66
3.5 Path loss parameters for suburban environments 67
3.6 Path loss parameters for rural environments 67
3.7 Path loss parameters for indoor environments 67

4.1 Summary of Berg model values to be used in the framework of a NHPSP/NHPLM model 83
4.2 Lookup table for mapping the SINR threshold to its corresponding modulation scheme and spectral efficiency 89

5.1 Summary of the tiers parameters used in the simulations . . 109
5.2 Probabilities to offer the typical UE a given throughput . . . 114
5.3 Modification of the tiers parameters for suburban and rural environments 117
5.4 Association probabilities in the different environments for the same densities 119
5.5 Evolution of the number of function evaluations for the computation of $\int_0^{10} \exp(\cos(ax))dx$ using the global adaptive quadrature method 120

6.1 Parameters employed in the SG and RT frameworks 127
6.2 Statistical parameters for the studied environments 137
6.3 Typical streets considered for comparison with our model . 140

7.1 Average exposure statistics in V/m associated with the optimal deployments 152
7.2 Optimal weighted coverage probability under varying EIRPs 153

F.1 Summary of Berg model values depending on the street type 168

Acronyms

AWGN **A**dditive **W**hite **G**aussian **N**oise.

BS **B**ase **S**tation.

CCDF **C**omplementary **C**umulative **D**istribution **F**unction.

CDF **C**umulative **D**istribution **F**unction.

CF **C**haracteristic **F**unction.

CSI **C**hannel **S**tate **I**nformation.

FSPL **F**ree **S**pace **P**ath **L**oss.

HPPP **H**omogeneous **P**oisson **P**oint **P**rocess.

I2O **I**ndoor **T**o **O**utdoor.

LT **L**aplace **T**ransform.

MGF **M**oment **G**enerating **F**unction.

MPLP **M**anhattan **P**oisson **L**ine **P**rocess.

NHPCLP **N**on **H**omogeneous **P**oisson **C**ox **L**ine **P**rocess.

NHPLM **N**on **H**omogeneous **P**oisson **L**ilypond **M**odel.

NHPSP **N**on **H**omogeneous **P**oisson **S**tick **P**rocess.

O2I **O**utdoor **T**o **I**ndoor.

PCLP **P**oisson **C**ox **L**ine **P**rocess.

PDF **P**robability **D**ensity **F**unction.

PGFL **P**robability **G**enerating **F**unctiona**L**.

PL **P**ath **L**oss.

PLLP **PL**anar **L**ine **P**rocess.

PLM **P**oisson **L**ilypond **M**odel.

PPP **P**oisson **P**oint **P**rocess.

PSP **P**oisson **S**tick **P**rocess.

QoS **Q**uality **o**f **S**ervice.

RMa **R**ural **Mi**crocell.

RMi **R**ural **Ma**crocell.

RMSE **R**oot **M**ean **S**quare **E**rror.

RT **R**ay **T**racing.

SA **S**teepest **A**scent.

SG **S**tochastic **G**eometry.

SINR **S**ignal to **I**nterference plus **N**oise **R**atio.

SIR **S**ignal to **I**nterference **R**atio.

SuMa **Su**burban **Ma**crocell.

SuMi **Su**burban **Ma**crocell.

UE **U**ser **E**quipment.

UMa **U**rban **Ma**crocell.

UMi **U**rban **Mi**crocell.

UTD **U**niform **T**heory of **D**iffraction.

List of symbols

$\alpha_{\tilde{t},k}$ — Path loss coefficient for k-th street tier interacting through building penetration (p. 56)

$\alpha_{k,d}$ — Path loss coefficient for k-th street or roof tier interacting by corner diffraction (p. 55)

$\alpha_{k,n}$ — Path loss coefficient for k-th LOS/NLOS street or roof tier (p. 54)

β_B — Beta factor for the blockage model of roof BSs (p. 48)

β_S — Beta coefficient for the blockage model of street tiers (p. 47)

ΔH_b — Height difference between the rooftop and the UE (p. 45)

ΔH_k — Height difference between the k-th street tier and the UE (p. 44)

δ_x — Dirac delta function (p. 24)

η_c — Crossroad probability (p. 60)

η_t — T-junction probability (p. 60)

$\kappa_{\tilde{t}}$ — Path loss intercept for street BSs interacting through building penetration (p. 56)

κ_d — Path loss intercept for street and roof BSs interacting by corner diffraction (p. 55)

κ_n — Path loss intercept for LOS/NLOS street and roof BSs (p. 54)

$\Lambda(S)$ — PPP intensity measure on space S (p. 21)

$\lambda(x)$ — PPP density at poisition x (p. 21)

λ_k — Density of the k-th street tier (p. 44)

λ_s — Street density (p. 43)

$\lambda_{b,k}$ — Density of the k-th roof tier (p. 45)

λ_{eff} — Effective line density (p. 32)

$\mathbb{E}[X]$ — Expected value of the random variable X (p. 22)

$\mathcal{A}$ — Association probability (p. 78)

$\mathcal{B}_n(\mathbf{X}, r))$ — n-dimensional ball of radius r centered at $\mathbf{X}$ (p. 22)

$\mathcal{L}_X(t)$ — Laplace transform of the random variable X (p. 35)

$\mathcal{R}(S)$ — Random counting measure on space S (p. 18)

$\mathbb{1}(\cdot)$ — Indicator function (p. 18)

μ_C — Average capacity (p. 87)

μ_E — Average exposure (p. 90)

$\overline{F}_X(X)$ — Complementary cumulative distibution function of the random variable X (p. 24)

$\overline{X}$ — Upper bound of X (p. 94)

Φ — Point process (p. 18)

$\phi_X(t)$ — Characteristic function of the random variable X (p. 36)

Ψ — Planar line process (p. 19)

$\underline{X}$ — Lower bound of X (p. 94)

Ξ — Doubly stochastic point process (p. 25)

C — Capacity (p. 87)

f — Frequency (p. 5)

$F(\theta_c, \theta_e)$ — Joint SINR-exposure distribution (p. 93)

$F_X(X)$ — Cumulative distibution function of the random variable X (p. 24)

$f_X(X)$ — Probability density function of the random variable X (p. 24)

g — Channel power gain (p. 50)

G_1 — Beamforming gain on the main lobe (p. 45)

G_2 — Beamforming gain on the back lobe (p. 45)

H_k — Height of the k-th street tier (p. 44)

H_u — Height of the typical UE (p. 44)

$H_{b,k}$ — Height of the k-th roof tier w.r.t the roof (p. 45)

H_b — Height of the rooftop (p. 45)

K — Rician K-factor (p. 52)

K_B — Number of roof tiers (p. 45)

K_S — Number of street tiers (p. 43)

$l(S)$ — Lebesgues measure on space S (p. 21)

$L_{\tilde{t},k}(d_1, d_2, \theta)$ — Path loss model for street BSs interacting through building penetration (p. 56)

$L_{d,k}(d_1, d_2, \theta)$ — Path loss model for street and roof BSs interacting by corner diffraction (p. 55)

$L_{k,n}(r)$ — Path loss model for LOS/NLOS street and roof BSs (p. 54)

$P_c(\theta_c)$ — Coverage probability (p. 85)

$P_e(\theta_e)$ — Exposure cumulative distribution function (p. 92)

P_k — Emit power of the k-th street tier (p. 44)

$P_{b,k}$ — Emit power of the k-th roof tier (p. 45)

$P_{cap}(\theta_r)$ — Rate coverage probability (p. 88)

$p_{d,B}(r, \theta)$ — Probability for roof BSs to interact by diffraction (p. 49)

$p_{L,B}(r, \theta)$ — LOS probability for roof BSs (p. 48)

$p_L(r)$ — LOS probability in the typical street (p. 47)

$p_{N,B}(r, \theta)$ — NLOS probability for roof BSs (p. 48)

$p_{NT,1}$ Probability to be in the main lobe direction of a non typical street BS (p. 46)

$p_{NT,2}$ Probability to be in the back lobe direction of a non typical street BS (p. 46)

$p_N(r)$ NLOS probability in the typical street (p. 47)

$p_{T,1}$ Probability to be in the main lobe direction of a typical street BS (p. 46)

$p_{T,2}$ Probability to be in the back lobe direction of a typical street BS (p. 46)

r_c Critical value for the geometric LOS of roof BSs (p. 48)

$u(x)$ Heaviside function (p. 50)

w_S Street width (p. 47)

Log-$\mathcal{N}(\mu, \sigma^2)$ Lognormal distribution with parameters μ and σ (p. 6)

1 Introduction

1.1 Context of the thesis

Back in the nineties, the world was about to know a small technological revolution. In fact, the mobile phone appeared as a key turning point in shaping nowadays social interactions. Providing flexibility and speed, it was quickly adopted by billions of people becoming an integral part of the landscape. Over the years, the phone evolved to a much more powerful tool offering its user a wider panel of functionalities, some of which consume a lot more data than traditional voice calls. In addition, the wireless ecosystem was completed with the arrival of many other wireless appliances such as laptops or tablets. Despite being already widespread, the number of mobile devices is still expected to grow in the upcoming years as shown on Fig. 1.1 [1].

Due to this ever-growing number of mobile devices, the global data traffic is expected to skyrocket in future wireless networks [2]. A significant increase of the number of phone applications is only partly responsible. In fact, many other functionalities relying on a wireless access emerged in modern networks and will continue to emerge in a foreseeable future. For some of them, very high data rate and/or very low latency requirements are targeted as depicted in Fig. 1.2 [3]. Often, mobile devices will

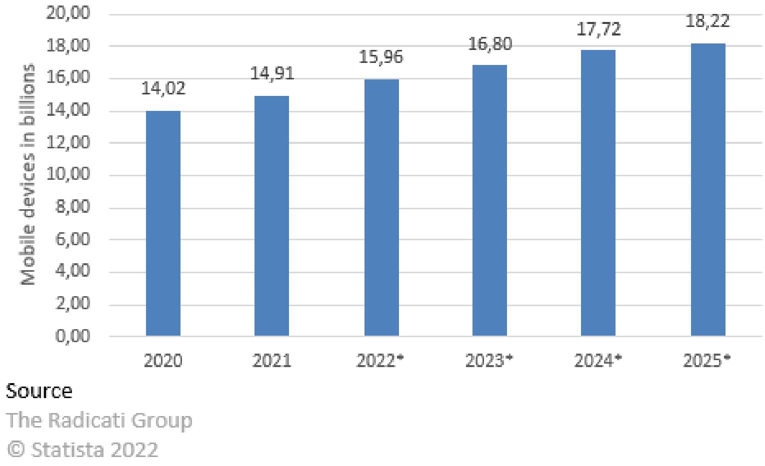

Fig. 1.1 Forecast number of mobile devices worldwide from 2020 to 2025 (in billions) [1].

even assist the user in its daily life activities and therefore need to be ultra reliable. For this reason, 5G networks are envisioned to play an important role in the pursuit of these requirements. According to Cisco annual internet report, the performance benefits of 5G are expected to reach the key performance indicators (KPI) summarized in Tab. 1.1 [4].

KPI	KPI objective w.r.t. 4G LTE	Explanation
Latency	10 × lower	Delivering latency as low as 1 ms
Connection density	10 × higher	Enabling more efficient signaling for IoT connectivity
Spectrum efficiency	3 × higher	Achieving even more bps with advanced antenna techniques
Throughput	10 × higher	Bringing more uniform, multi-Gbps peak rates
Traffic capacity	100 × higher	Driving network hyperdensification with more small cells
Network efficiency	100 × higher	Optimizing network energy consumption with more efficient processing

Table 1.1 KPIs targeted by the future 5G release [4].

In order to withstand the significant increase in capacity demand, three main solutions are identified [5]: (i) the network densification to reduce the cell size, (ii) the usage of higher bandwidths with the exploration of higher

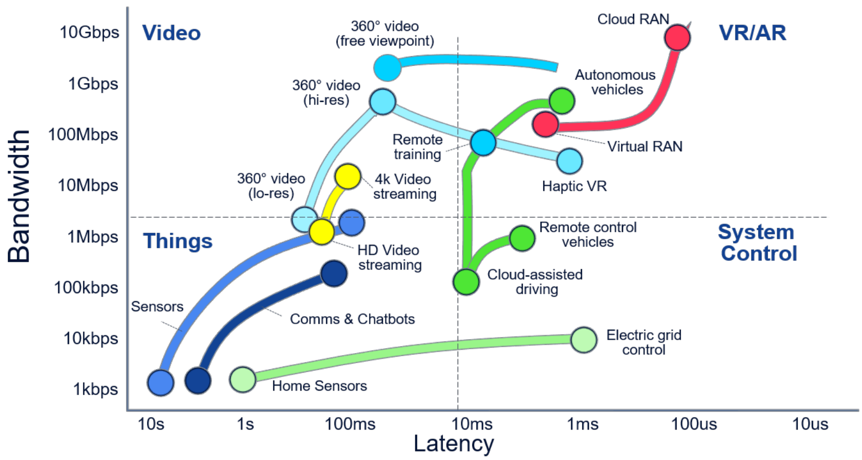

Fig. 1.2 Data rate and latency requirements of various applications [3].

carrier frequencies and (iii) the spectral efficiency improvement using enhanced signal processing techniques. Regarding the first paradigm, small cells and unmanned aerial vehicles (UAVs) are expected to extend the coverage provided by macro BSs in isolated or poorly covered areas. Such heterogeneous networks (Hetnets) also enable the offloading of macrocells to achieve a better spectral efficiency. This aggressive network densification however raises many concerns at different levels:

- **A technical level**. For instance, the coexistence of multiple tiers on the same frequency resources causes inter-tier interference. This additional interference can be responsible for coverage issues and thus needs to be addressed. Due to a time-varying capacity demand, power control techniques and smart algorithms are expected to mitigate this interference level by turning off small cells when not needed [2].

- **A financial level**. It may not be sustainable from a cost point of view especially as the BS misleadingly accounts for only 20% of the total deployment cost [6].

- **An ethical level**. In a world where the environment has become a priority, the potential increase in power consumption of ultra dense networks is firmly criticized.

- **A medical level**. Up to now, no evidence on the health effects directly linked to electric and magnetic fields (EMF) has been shown. Even though legal EMF exposure thresholds are imposed by the regulation organism and especially in Belgium where restrictive safety levels are in place, many users remain sceptical. This scepticism is reinforced by small cells being located closer to the ground level.

For all these reasons, flexible models for the characterization of the performance of the entire network need to be investigated. These models should cover many different scenarios and enable a fair view of the impact of the planning parameters.

On the one hand, if an indivual link is considered, an accurate description of the link parameters (antenna setting, channel conditions, etc...) and the environment is generally required [7]. The expected network densification and multi-service operations will moreover push towards site- and service-specific simulations making deterministic channel models even more suitable. On the other hand, if the wireless network has to be evaluated at a larger scale, some of the link-level details are generally abstracted due to limited time and computational resources. In addition, given the large randomness in future networks as well as the variable user density and network topology, it is not clear if a deterministic channel model is actually required. If not, simpler models could be alternatively used at a cheapest simulation cost.

Therefore, this thesis focuses on network-level models for the efficient deployment of urban cellular networks. By means of tools from the stochastic geometry (SG) theory, it gives insight about the trade-offs between deterministic channel models and very simple propagation models. Thanks to its interesting mathematical framework, SG enables an easy study of larger scale systems. This study is subsequently assessed on multiple levels.

1.2 Channel models

In telecommunications, the wireless channel refers to the propagation environment that lies between a transmit antenna and a receive antenna. Before reaching the receiver, the emitted electromagnetic waves will interact with their surrounding environment and the final signal strength will therefore strongly depend on that particular environment. Channel models are designed to predict that received power without the need to actually implement the link [8]. To that extent , different aspects impacting the received signal strength are generally considered in a propagation model:

- the **path loss** (PL), which models the attenuation of an electromagnetic wave as it propagates. In fact, the magnitude of the electrical field was shown to be inversely proportional to the distance from the source. The PL exponent α translates the magnitude of this attenuation which depends on the channel itself. It typically ranges from 2 in free space to 5 indoors. Simple PL models assume that the PL is equal for two sources being at the same distance, in the same environment and operating at the same frequency. Among them, we have:
  - the **Okumura-Hata** model [9]

    $$\begin{aligned} L[dB] = {} & 69.55 + 26.16 \log_{10}(f_{MHz}) - 13.82 \log_{10}(h_{BS}) - a_i(h_{MS}) \\ & + (44.9 - 6.55 \log_{10}(h_{BS})) \log_{10}(r) \end{aligned}$$

    where f_{MHz} is the signal frequency in MHz, h_{BS} and h_{MS} are the base station and mobile station heights, r is the link distance in kilometers and $a_i(h_{MS})$ is a correction factor that depends on the studied environment.
  - the **free space** path loss model

    $$L[dB] = 32.44 + 20 \log_{10}(f_{MHz}) + 20 \log_{10}(r).$$

  - the **single-slope** model

    $$L[dB] = L_0 + 10\alpha \log_{10}(r/r_0)$$

    where L_0 is the average path loss at a reference distance r_0.
  - the **dual-slope** model

    $$L[dB] = L_{BP} + 10\alpha(r) \log_{10}(r/r_{BP})$$

    where r_{BP} is the breakpoint distance and $\alpha(r) = \alpha_1$ if $r \leq r_{BP}$ and $\alpha(r) = \alpha_2$ otherwise. It is based on a two-ray propagation mechanism (the LOS ray and the reflection from the ground) as shown in [10].

- the **shadowing**, which models the impact of obstacles with a size of tens to hundreds of wavelengths like buildings, urban furniture or hills. This aspect is combined with path loss to take into account the fact that two sources located at the same distance will not provide the same contribution if one of them is obstructed. It is generally assumed to follow a log-normal distribution Log-$\mathcal{N}(0, \sigma^2)$ as reported by [11]. The depth σ of shadowing varies from around 6.5dB in rural environments to 8.5dB in dense urban environments.

- the **fading**, which models the multipath propagation of the wave. The channel has this particularity that it can dratiscally change over a short period of time. If the receiver moves even by very small distances, the instantaneous received signal power can vary up to 40 dB [12]. Each link is indeed characterized by its multiple paths with their own characteristics such as the delay or the attenuation. These paths are more or less constructively combined at the receiver therefore resulting in different power levels. Due to the numerous signal copies arriving at slightly different times, the enveloppe of the received signal can be statistically described by a fading distribution. Most widely adopted distributions are Rayleigh fading distribution, Rician fading distribution and Nakagami-m fading distribution that encompasses both previous distributions.

The perfect reproduction of a channel is however a useless task. In fact, due to the mobility of some obstacles and of the UE itself, a channel is never indefinitely fixed. For this reason, very simple channel models emerged in the literature. Their goal is to provide a sufficiently good approximation to the network planner for design purposes. A wide range of channel models characterizing different types of environments and taking into account various levels of details already exist. As it can be seen on Fig. 1.3, channel models are classified into two main categories: analytical models and physical models. Analytical models are very simple mathematical models that help us to easily assess the channel quality without taking into account the wave propagation mechanisms. On the contrary, physical models are able to fully deterministically characterize the wave propagation parameters like the complex amplitude, the direction of departure (DoD) or the direction of arrival (DoA) [13]. These models are briefly described below.

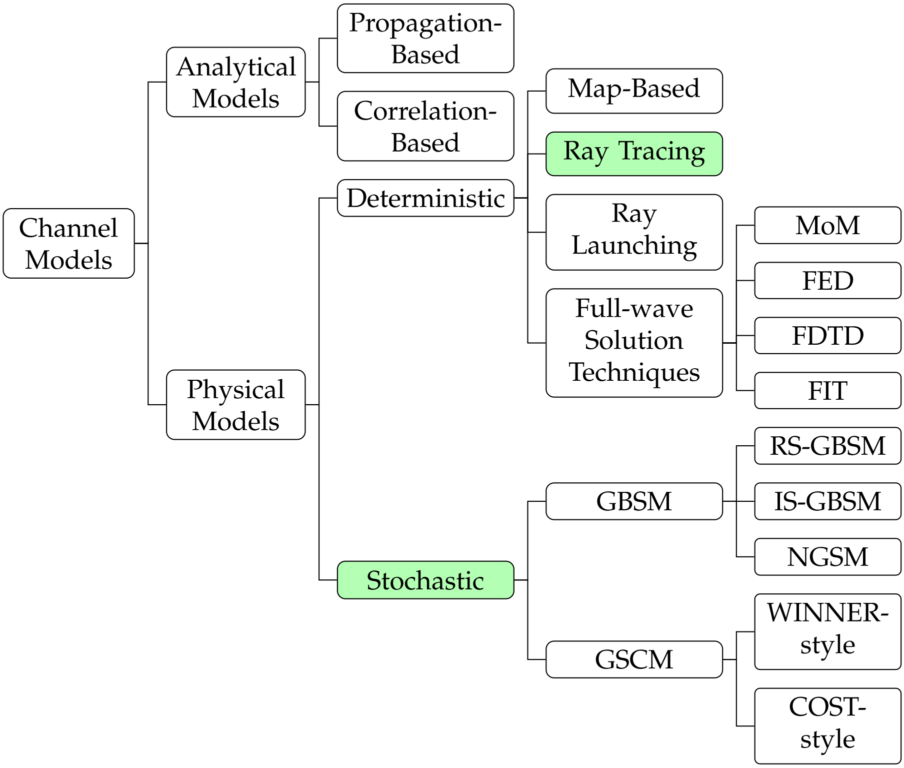

Fig. 1.3 Existing channel models classification. The models used in this document are highlighted in green [13, 14].

1.2.1 Analytical models

Analytical models are pure mathematical models that generally rely on system setups like the bandwidth or the antenna array configuration. Among them, we can cite the Kronecker model [15], the Weichselberger model [16] or the finite-scatterer model [17]. The major advantage is that they provide quick and easy to use analytical methods to evaluate the signal strength. They are typically used for information theory and signal processing.

1.2.2 Physical models

Physical models are separated into two subcategories: deterministic models and stochastic models [14]. On the one hand, stochastic models are generally considered as empirical models with stochastic principles integrated providing fair accuracy and sometimes environment dependency (modeling of scatterers) but giving a more restricted physical insight [18, 19]. On the other hand, deterministic models provide full understanding of the propagation mechanisms at the cost of an increased computational complexity as the studied environment has to be precisely reconstructed.

Deterministic models

Deterministic models either solve the Maxwell equations using full-wave solution techniques like the method of moments (MoM), the finite element method (FEM), the finite-difference time domain (FDTD) and the finite integration technique (FIT) or provide fairly accurate approximations using asymptotic techniques. These asymptotic methods regroup ray tracing (RT), ray launching (RL), map-based models and uniform theory of diffraction (UTD). These models are able to describe precisely the multipath effects of the channel. Therefore, they eliminate the need for costly measurement compaigns [20].

As full-wave solution techniques are based on the discretization of differential or integral equations, applying them is often time-consuming and generally requires a lot of memory [21]. As a consequence, techniques like RT are generally considered to output fairly accurate results within acceptable runtime. In addition, higher frequencies targeted by 5G networks are making the ray-optics approximation less drastic [22]. This is the case as small wavelength associated to higher frequencies are insignificant with respect to walls and object dimensions.

The main principle behind RT is to identify all the rays that link a transmitter (TX) and a receiver (RX) according to known propagation mechanisms like reflection, diffraction or diffuse scattering. These mechanisms will be more precisely described in Chapter 6. An example of the result of a RT algorithm is shown on Fig. 1.4 for a simple scenario where at maximum two reflections are considered. This principle has been applied to radio frequencies for field prediction in indoor and urban environments since the early 1990s [14]. Existing techniques are summarized in [23].

RT presents several advantages [14, 22]. First, it models the multidispersive characteristics of the channel. Second, it is less restricted by the bandwidth and the carrier frequency when compared to measurement

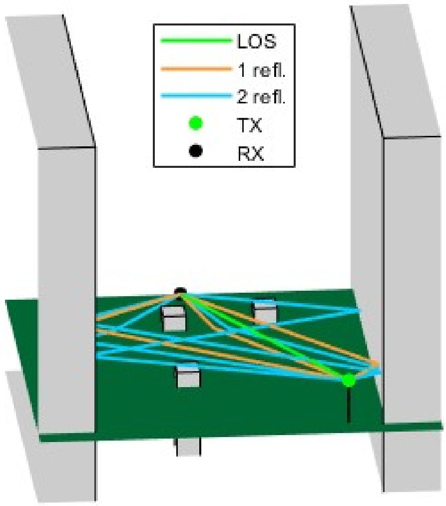

Fig. 1.4 Result of the UCLouvain RT software on a simple scenario.

based stochastic models. Third, it is able to describe the birth and death of rays, the coherence between different drops and the correlations of key parameters. In addition, several factors made this technique more and more suitable for 5G networks. Higher frequencies and shorter link distances limit the actual propagation environment therefore reducing the CPU time. However, this comes at the cost of a more precise description of the environment as even small objects can act as strong reflectors. Nowadays, this problem is partly solved by the availability of more accurate urban databases. The number of details that can be taken into account by a RT algorithm is however limited due a computational complexity that increases exponentially with the number of facets. Several improvements of the algorithm including many acceleration techniques have been however able to partly tackle this last problem.

Stochastic models

A model is considered stochastic once it incorporates a random variable as one of its parameters. Typically, the aim of these models is to replicate the statistical characteristics of the channel they represent [24]. They are generally subvided into (i) geometry-based stochastic MIMO channel models (GSCM) regrouping WINNER-style (e.g., 3GPP spatial channel model, extended SCM, WINNER, WINNER II, WINNER+, 3D MIMO channel models, and QuaDRiGa) and COST-style (e.g., COST2100) families and (ii) geometry-based stochastic models (GBSM) regrouping regular-shaped GBSMs (RS-GBSM), irregular shaped GBSMs (IS-GBSMs), and non-geometrical stochastic models (NGSMs). They provide an increased mathematical simplicity. The degree of simplicity depends on the phenomena being considered. These phenomena may include path loss, fading and shadowing as previously described.

The challenge in developing statistical channel models then lies in defining environments that exhibit consistent statistical properties. Common classifications include indoor, urban outdoor or suburban outdoor. Each environment type possesses unique characteristics, necessitating distinct statistical descriptions. The main drawback of stochastic models is their inherent limitation in adapting to environments that possess distinct characteristics compared to the ones for which they were originally developed. This lack of adaptability can result in poor fitting or inaccurate representations when applied to diverse environments. In addition, the classification of environments is generally quite subjective [21]. The same observation applies if the antenna system changes.

The trade-off between accuracy and computational complexity is generally at the center of the discussion. **Therefore, this thesis will consider two pretty opposite channel models, simple stochastic models and RT, and compare them at a network scale.** By incorporating stochastic models in a SG framework, the obtained results and tendencies will be benchmarked against RT results.

1.3 Why is stochastic geometry a powerful tool?

A wireless network can be viewed as a collection of nodes representing the different network elements. At a given time instant, many different links exist in the same frequency resources in different cells. The useful signal is thus affected by a certain level of interference that strongly depends on the network topology. In fact, it was shown to drastically impact the reference system-level metrics even when a simple single-slope path loss model is used to compute the received power [25]. A topological model that accurately reflects the environment under study is therefore required to quantify the ability of the network to offer to the UE a certain bit rate.

For years, grid-based models (e.g. hexagonal grid, square grid or triangular lattice) were widely accepted to model BSs in infrastructure-based networks (i.e. networks where two UEs can only communicate via a BS) [26]. In these models, base stations (BSs) are located on a regular grid with a fixed inter-BSs distance and a fixed cell region. The computation of network-level metrics like the interference is thus geometrically done.

However, in the real world, a grid-based deployment is far from feasible as the actual BSs sites are constrained by legal aspects or site accessibility. For this reason, BSs are placed more opportunistically. For a particular link, interfering BSs in the network can be very close. This particularity can not be taken into account by grid-based models as the minimum distance to an interfering BS is imposed by the grid. The grid hypothesis therefore leads to idealistic and very optimistic conclusions [27]. In addition, with the arrival of multi-tier networks, the presence of many different BS types (e.g. macro, micro, pico and femto) reinforces the uncertainty on the network topology.

In addition, network planning comes with a large amount of randomness as many varying or site-dependent parameters have to be considered (e.g. UEs and BS locations, channel gains, buildings geometry or street patterns). Some of these parameters are time-dependent [28] and can change frequently and unpredictably. For example, the UEs locations is not known in advance as well as the channel gain which can be affected by moving obstacles.

Stochastic geometry (SG) is a field of applied probability that eases the study of these random phenomena in large systems. It provides an interesting mathematical framework for modeling and studying the spatial distribution of many wireless network elements like base stations (BSs) and user equipments (UEs). The spatial distribution of network elements becomes probabilistic and the inherent randomness and uncertainty in their locations is thus captured. Network-level metrics can then be computed and averaged over a large amount of network realizations therefore avoiding any site- or time- specific influence on the large-scale analysis. This enables the network planner to more easily identify the key parameters that affect the network performance and to determine the optimal deployment strategies [29]. It is particularly useful to efficiently roll-out new technologies as parameters like the BS densities or the emit powers can be fixed according to the observed performance trends.

Finally, the SG approach usually prevents the need for computationally intensive and time consuming simulations or Monte Carlo analysis [7]. This analysis is generally left for model validation. In fact, the SG framework enables us to derive closed-form or semi closed-form analytical expressions for system-level metrics like the SINR. This last advantage of SG will be discussed in Chapter 5.

1.4 Major contributions

The guideline of this thesis is the development and validation of stochastic geometry-based models for urban cellular network deployment. The first areas where the BS densification is likely to be planned are city centers, which feature a particularly high user activity. Due to the important density of buildings in urban environments, small cells BSs will be more probably concentrated along streets. As a consequence, models taking into account this linear dependency must be developed. This document focuses on such models.

Nowadays, one of the biggest shortcomings of SG-based models is their validation. In fact, many works focus on the analysis of emerging networks using pure SG approaches. However, a very limited number of publications propose validations of these SG models using other methods (e.g. comparison to datasets, measurements, or softwares capturing additional electromagnetic phenomenons such as diffraction or scattering, etc). This document gives a more fair view on the validity and limits of the results obtained through a SG analysis.

The contributions of this thesis follow the thesis structure and can be summarized as follows:

1. New SG-based models for the efficient deployment of Hetnets in urban, suburban and rural areas are developed. The SINR-based cover-

age probability of modern networks in which the locations of nodes are modeled by a Poisson Cox line process or a Manhattan Poisson line process is characterized. In particular, the works presented in [30–32] are fully revisited to offer more flexibility in the design parameters choices. As the potential increase in exposure levels due to densification has raised many concerns, available metrics are extended to include exposure-based statistics and joint SINR-exposure statistics. Multi-dimensional analysis quantifying the impact of the network densification, the beamforming scheme and the street density on these metrics are proposed. The impact of the UE location with respect to street intersections and to the network infrastructure is also quantified.

2. We propose a validation of the performance trends observed with SG-based models using the RT tool developed at UCLouvain. Most SG publications validate their analytical results using equivalent Monte Carlo simulations. While such procedure enables to verify the correctness of the derived expressions, it does not provide indications on whether or not they are realistic compared to more physical propagation models.
3. We perform a validation of the above-mentioned models by comparing them to real city deployments for which the street patterns, buildings locations and buildings heights are extracted from open city 3D databases. As the street pattern of real cities does not always follow a grid plan but still presents some organization, we further propose a new point process covering all different topologies: the non homogeneous Poisson Cox line process.
4. We optimize the network deployment for a reference scenario and quantify the losses that arise if a simpler propagation-based model is used instead of the RT tool.

1.5 Thesis outline

The manuscript is structured as follows.

In Chapter 2, we recall the basic concepts of the stochastic geometry theory. The principles of point process and planar line process together with several examples are introduced. The associated mathematical background is fully covered to ease the understanding of the analytical developments of network-level metrics. A new point process named the non homogeneous Poisson Cox line process is proposed

In Chapter 3, we set up the general multi-tier urban network model analyzed throughout this document. The network topology specifities and the full channel model are detailed. Modeling differences between urban, suburban and rural environments are highlighted. The calibration of the parameters based on Winner 2 channel models is performed.

In Chapter 4, the studied network-level performance metrics are defined. Semi closed-form expressions for all metrics are derived. The way analytical expressions can be adapted to all studied point processes is specified. Some metrics are generalized to UEs located near hotspot BSs and to UEs located at street intersections.

In Chapter 5, a full parametric analysis is proposed. The impact of the association rule and of the location of UEs with respect to crossroads is quantified. The benefits of beamforming on the global throughput are highlighted. Insight on how the network design parameters can be tuned to satisfy both uniform UEs and hotspots UEs is given.

In Chapter 6, a complete validation of the observed trends is successively performed by comparison to RT and to real city deployments. In that sense, usual Monte Carlo simulations were performed twice: first, using the UCLouvain RT tool to compute the power levels, and second, employing real city topologies. These two simulations sets are then used for comparison against the results obtained through our SG-based models.That way, we are able to reveal the boundaries of the conclusions drawn from these models.

In Chapter 7, we perform an actual small cells deployment optimization for a neighbourhood in Barcelona. The potential candidates are installed on street lampposts. Using the steepest ascent algorithm, the optimal deployment among these candidates is identified based on the received powers maps. The process is repeated for maps that are calculated through a basic propagation-based model and through the UCLouvain RT tool. Since these optimal results often vary, the losses incurred by utilizing simpler models are emphasized.

General conclusions and perspectives for future works end this thesis in Chapter 8.

2

Introduction to stochastic geometry

STOCHASTIC geometry is a mathematical discipline in which one studies the relations between geometry and probabilities theory (i.e. random spatial patterns). It was originally used in fields like signal procesing, astronomy or even forestry before being used for modeling wireless networks. Interestingly, SG eases the study of random phenomena in large communication systems as it captures the randomness of the network spatial configuration in time. In fact, tools like point processes (PP) and planar line processes (PLP) are particularly interesting to model network elements locations and roads in many different environments. These two useful tools will be considered in turn in this chapter. Particular attention will be paid to the Poisson point process (PPP) and the Poisson Cox line process (PCLP). In addition, a newly developed point process named the non homogeneous Poisson Cox line process (NHPCLP) will be introduced. The essential mathematical properties associated with each of these processes will be detailed to enable a full understanding of the mathematical framework presented throughout this thesis.

2.1 Introduction to point processes

Point processes (PP) are considered as one of the most important tools in SG models. In wireless networks modeling, they are used to represent the different network elements locations (e.g. UEs or BSs). As each realization of a PP distributes the elements differently, network-level metrics can be averaged over many different network snapshots therefore accounting for the randomness of the network topology.

Definition 2.1 (point process)**.** Formally, a point process Φ is a probabilistic model for random collections of points $\{\mathbf{X_i}, i \in \mathbb{N}\}$ on a measurable space S often considered as a subset of $\mathbb{R}^d$ for a given integer d.

To each realization of a PP Φ, a random counting measure $\mathcal{R}(S)$ can be assigned. For example, $\mathcal{R}(S)$ can be defined as

$$\mathcal{R} : S \subset \mathbb{R}^d \rightarrow \mathbb{N} : \mathcal{R}(S) = \sum_{\mathbf{X_i} \in \Phi} \mathbb{1}\left(\mathbf{X_i} \in S\right)$$

where $\mathbb{1}\left(\cdot\right)$ is the indicator function. The distribution of $\mathcal{R}(S)$ strictly depends on the considered PP and its mean is often used to characterize a given PP. If the PP admits a density function $\lambda(x)$, where $x \in \mathbb{R}^d$ is the considered location, then the PPP intensity is given by $\Lambda(S) = \overline{\mathcal{R}}(S) = \int_S \lambda(x)dx$ where $\overline{\mathcal{R}}(S)$ is the average random couting measure.

There exist many different PPs that distribute UEs and BSs uniformly (e.g. the Poisson point process), with some repulsion (e.g. the Matérn hard-core point process) or with some clustering ability (e.g the Poisson cluster point process). This PP diversity strenghtens even more the ability this tool has to model many different network classes. Besides, many efforts have been put into action in order to fit real deployments to different existing point processes as the elements locations have a direct impact on the accuracy of network performance evaluation [33]. The interested reader can find a complete taxonomy of existing works on many PPs with their associated mathematical complexity in [34]. This document will however focus on the PPs that are actually used in the presented works.

2.1.1 Planar line processes

Line processes are used to model road patterns in the desired environment. In particular, the position and orientation of streets can be modeled using a planar line process (PLLP).

Definition 2.2 (planar line process)**.** A planar line process Ψ is a random collection of lines in $\mathbb{R}^2$ where each line i can be defined by

- r_i, its radial distance from the origin
- θ_i, the angle subtended by the line formed by the origin and its projection on the street line and the x-axis measured in a counter-clockwise direction.

This PLLP is the result of two following steps:

1. the process $\Psi = \{(r_i, \theta_i), i \in \mathbb{N}\}$ is generated on the cylindrical representation space $\mathcal{C} : \mathbb{R} \times (0, 2\pi)$ following a desired distribution (e.g. a Poisson distribution).
2. each obtained pair (r_i, θ_i) is mapped onto its corresponding point in $\mathbb{R}^2$. The line is then drawn from this point. This mapping is illustrated on Fig. 2.1.

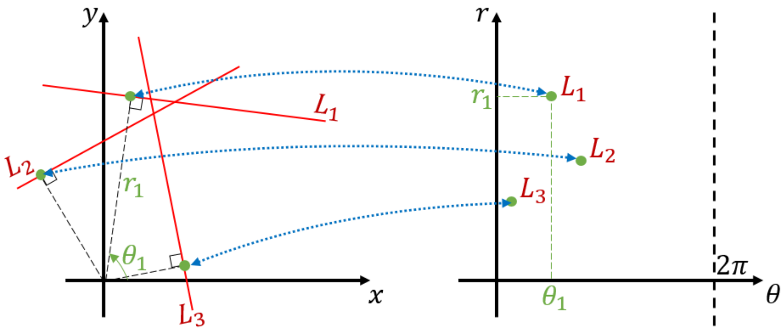

Fig. 2.1 Illustration of the mapping between the line process and the point process in the representation space $\mathcal{C}$ [35].

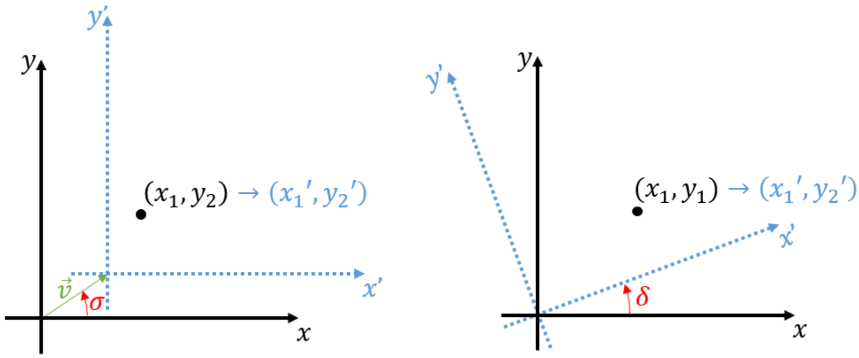

Fig. 2.2 Illustration of the translation (left) and rotation (right) of the axes.

2.1.2 General properties

Different properties can be associated to PPs and defined independentely from the PP itself. These properties can then be generalized to PLLPs.

Stationarity

A PP or a PLLP is said to be **stationary** if its law is invariant by translation. Let us consider a translation of the origin by a vector $\vec{v} = (|v|cos(\sigma), |v|sin(\sigma))$ for a given PP $\Phi = \{(x_i, y_i), i \in \mathbb{N}\}$ as shown on Fig. 2.2. Φ is said stationary if and only if the translated PP $\Phi' = \{(x_i', y_i') = (x_i + |v|cos(\sigma), y_i + |v|sin(\sigma)), i \in \mathbb{N}\}$ has the same distribution as Φ. Similarly, a PLLP $\Psi = \{(r_i, \theta_i), i \in \mathbb{N}\}$ is stationary if and only if the translated PLLP $\Psi' = \{(r_i', \theta_i') = (r_i - |v|cos(\theta_i - \sigma), \theta_i), i \in \mathbb{N}\}$ has the same distribution as Φ [35].

Isotropy and motion-invariance

A PP or a PLLP is said to be **isotropic** if its law is invariant by rotation. Let us consider a rotation of the axis by a angle δ for a given PP $\Phi = \{(x_i, y_i), i \in \mathbb{N}\}$ as shown on Fig. 2.2. Φ is said isotropic if and only if the rotated PP $\Phi' = \{(x_i', y_i') = (x_i cos(\delta) + y_i sin(\delta), -x_i sin(\delta) + y_i cos(\delta)), i \in \mathbb{N}\}$ has the same distribution as Φ. Similarly, a PLLP $\Psi = \{(r_i, \theta_i), i \in \mathbb{N}\}$ is stationary if and only if the rotated PLLP $\Psi' = \{(r_i', \theta_i') = (r_i, \theta_i - \delta), i \in \mathbb{N}\}$ has the same distribution as Φ [35]. A PP or a PLLP is said to be **motion-invariant** if it is both stationary and isotropic.

Motion-invariance and centric user analysis

Let us assume a UE is placed somewhere in a network defined on $\mathbb{R}^2$ and strictly reproduced by means of motion-invariant PPs and PLLPs. The motion-invariance property of all used processes makes the surrounding environment characteristics independent from the actual UE position. For this reason, the analysis of the network performance at a centric UE located in (0,0) is representative of the whole network. Such a UE is usually called a typical (centric) UE.

Thinning

Thinning or p-thinning is an operation performed on a given realization of a PP Φ. Each point of the realization is considered in turn and kept in the thinned PP Φ' with a probability p. The thinned PP Φ' can therefore be seen as a subset of Φ. The same operation can be applied to PLLPs.

2.1.3 The Poisson point process

The Poisson point process (PPP) is a PP where, for any realization, there is no correlation between the points. For a given realization of the PPP, the different points are therefore uniformly distributed in the considered space S. This particular PP was massively studied in the literature and is still often considered for its interesting mathematical properties.

Definition 2.3 (Poisson point process)**.** A Poisson point process defined on $S \subset \mathbb{R}^d$ is a motion-invariant PP with intensity measure $\Lambda(\cdot)$ where

- $\mathcal{R}(S)$ is Poisson distributed with mean $\Lambda(S)$.
- $\mathcal{R}(S_1)$,...,$\mathcal{R}(S_n)$ are independent random variables for any disjoint bounded sets S_1,...,S_n.

In some cases, the density function of a PPP $\lambda(x)$ is a constant $\lambda \in \mathbb{R}$ in space and is therefore independent from the position x. We will then rather talk of an homogeneous Poisson point process (HPPP) with density λ. An example of a one-dimensional (1D) HPPP and a two-dimensional (2D) HPPP is depicted in Fig. 2.3.

The intensity measure is then given by $\Lambda(S) = \lambda \int_S 1dx = \lambda l(S)$ where $l(S)$ is the Lebesgues measure. In particular, the Lebesgues measure of a

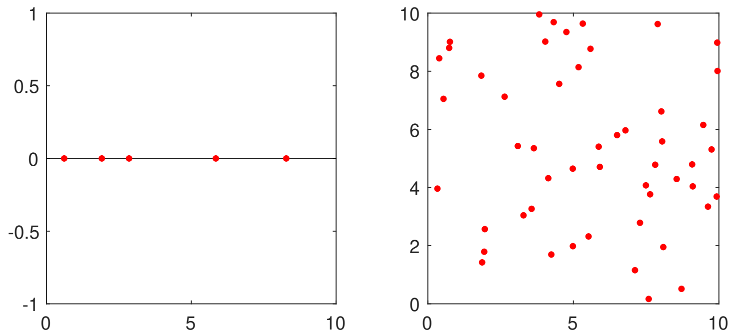

Fig. 2.3 Left: 1D HPPP of intensity 0.5/km on a 10km long segment Right: 2D HPPP of intensity 0.5/km² on a 10km² square area.

d-dimensional ball $\mathcal{B}_d(\mathbf{0}, r)$ of radius r centered at the origin is given by :

$$l(\mathcal{B}_d(\mathbf{0}, r)) = \frac{\pi^{d/2}}{\Gamma\left(\frac{d}{2}+1\right)} r^d. \tag{2.1}$$

Interestingly, one can note that:

- The superimposition of n independent PPPs with respective densities $\lambda_1(x), ..., \lambda_n(x)$ is a PPP with density $\lambda_1(x) + ... + \lambda_n(x)$.
- The p-thinning of a PPP with density $\lambda(x)$ is a PPP with density $p\lambda(x)$.

In addition, the PPP comes with its own mathematical properties. These are very useful to simplify the derivation of many interesting metrics like the coverage probability or the exposure cumulative distribution function (CDF). The next sections will be dedicated to the ones that are used in the presented works.

Probability generating functional

The probability generating functional (PGFL) of the PPP is a broadly used theorem in SG. It is particularly useful to characterize the Laplace transform (LT) of network-level metrics like the interference.

Theorem 2.4 (PGFL)**.** *Let $\{\mathbf{X_i}, i \in \mathbb{N}\}$ be a realization of a PPP Φ with intensity measure $\Lambda(\cdot)$ defined on $\mathbb{R}^d$. For any positive function $f : \mathbb{R}^d \to \mathbb{R}^+$, the PGFL* *of f can be expressed as follows [34]:*

$$\mathbb{E}\left[\prod_{\mathbf{X_i}\in\Phi} f\left(\mathbf{X_i}\right)\right] = \exp\left(-\int_{\mathbb{R}^d} \left(1 - f(x)\right)\Lambda(dx)\right).$$

Corollary 2.5. *Let us apply a simple transformation $f(x) \mapsto \exp(-f(x))$. Knowing the exponential function properties, Theorem 2.4 can be used to obtain:*

$$\mathbb{E}\left[\exp\left(-\sum_{\mathbf{X_i}\in\Phi} f(\mathbf{X_i})\right)\right] = \exp\left(-\int_{\mathbb{R}^d} \left(1 - \exp\left(-f(x)\right)\right)\Lambda(dx)\right).$$

Example 2.6. Let us consider a PPP Φ defined on $\mathbb{R}^2$ with density function $\lambda(r)$ where r is the radial distance. We then have:

$$\mathbb{E}\left[\exp\left(-\sum_{\mathbf{X_i}\in\Phi} f(\mathbf{X_i})\right)\right] = \exp\left(-2\pi\int_0^{\infty} \left(1 - \exp\left(-f(r)\right)\right)\lambda(r)rdr\right).$$

Campbell's theorem

Theorem 2.7 (Campbell's theorem)**.** *Let $\{\mathbf{X_i}, i \in \mathbb{N}\}$ be a realization of a PPP Φ with intensity measure $\Lambda(\cdot)$ defined on $\mathbb{R}^d$. For any measurable function $f : \mathbb{R}^d \to \mathbb{R}^+$, Campbell's theorem states that [36]:*

$$\mathbb{E}\left[\sum_{\mathbf{X_i}\in\Phi} f\left(\mathbf{X_i}\right)\right] = \int_{\mathbb{R}^d} f(x)\Lambda(dx).$$

Proof. Campbell's theorem is a direct consequence of Corollary 2.5. It is obtained by considering $tf(x) \mapsto f(x), t \geq 0$ and by differentiating with respect to t at $t = 0$ [34]. □

Palm distribution and Slyvniak theorem

Definition 2.8 (reduced Palm distribution)**.** Let us consider an initial PP Φ. Let us assume the location of a point $\mathbf{X} \in \Phi$ is known. The reduced Palm distribution of Φ is the distribution of $\Phi' = \Phi \setminus \mathbf{X}$ knowing $\mathbf{X} \in \Phi$.

Theorem 2.9 (Slyvniak-Mecke's theorem)**.** *The reduced Palm distribution of a PPP Φ remains a Poisson distribution with the same properties [37]. This enables us to add or remove a point without changing the distribution.*

Example 2.10. Let us assume a network in $\mathbb{R}^2$ where BSs are deployed following a PPP Φ. Let us compute the interference level at a typical UE served by a BS located at $\mathbf{X} \in \Phi$. The Slyvniak-Mecke's theorem ensures that the distribution of the PP $\Phi' = \Phi \setminus \mathbf{X}$ of the interfering BSs has the same distribution as the initial PP Φ. For this reason, all PPP-specific theorems can still be used to characterize the interference level.

Remark 2.11. This theorem only applies for PPPs. For example, adding an arbitrary point to a repulsive PP clearly changes its properties.

Distance distributions

Let us assume a network in $\mathbb{R}^d$ where BSs are deployed following an HPPP Φ_b of density λ_b. We assume a typical UE located at the origin and served by its closest BS. By definition, the distance between the UE and this BS is denoted by r. The CDF of r is easily obtained as follows :

$$F_{d,R}(r) = 1 - \mathbb{P}(R > r) = 1 - \mathbb{P}(\mathcal{R}(\mathcal{B}_d(0,r)) = 0) \overset{(a)}{=} 1 - e^{-\lambda_b l(\mathcal{B}_d(0,r))}.$$

where (a) results from the void probability of an HPPP [37] and $l(\mathcal{B}_d(0,r))$ is given by Eq. (2.1).

The PDF of r is then easily obtained by derivating the last expression with respect to r. If a one-dimensional HPPP is considered (i.e. d=1), the statistical distributions of r are then given by :

$$\underline{PDF:} \quad f_{P1,R}(r) = 2\lambda_b \exp\left(-2\lambda_b r\right) \tag{2.2}$$

$$\underline{CDF:} \quad F_{P1,R}(r) = 1 - \exp\left(-2\lambda_b r\right). \tag{2.3}$$

If a two-dimensional HPPP is considered (i.e. d=2), the statistical distributions of r become:

$$\underline{PDF:} \quad f_{P2,R}(r) = 2\pi\lambda_b r \exp\left(-\lambda_b \pi r^2\right) \tag{2.4}$$

$$\underline{CDF:} \quad F_{P2,R}(r) = 1 - \exp\left(-\lambda_b \pi r^2\right). \tag{2.5}$$

Remark 2.12. Throughout this document, the complementary cumulative distribution function of a random variable (RV) X will be denoted by $\overline{F}_X(x) = 1 - F_X(x)$.

2.1.4 The Poisson Cox line process

The Poisson Cox line process (PCLP) is a point process that makes it possible to distribute the network elements along lines representing roads in real deployments. It is particularly useful for modeling the distribution of wireless devices in urban environments, where devices are often concentrated along streets and in buildings. One of the main interests of the PCLP is that it can take into account the beam orientation of the wireless devices, which can be important for characterizing the propagation of radio signals in a given area. The nodes locations in a given street are thus conditoned by the fact that they lie on the same road. This road dependence is disregarded when a PPP is considered. Other PPs can always be independently superimposed over the PCLP. BSs located on the roofs or between buildings in sparser environments are thus easily modeled by means of these additional PPs.

Practically, the PCLP Ξ comes from the combination of a PLLP Ψ_l and of several 1D HPPPs Φ_i indenpendently generated on the i streets forming the PLLP. We therefore consider a PPP $\Phi_l = \{(r_i, \theta_i), i \in \mathbb{Z}\}$ on the cylinder set $C := \mathbb{R} \times [0, 2\pi]$ with intensity measure $\Lambda_\Phi(drd\theta) = \lambda_l dr G(d\theta)$ where $G(d\theta)$ is the lines angular distribution. If Φ_l is assumed homogeneous with constant density λ_l, then $G(d\theta) = \frac{d\theta}{\pi}$ and the resulting PCLP has a line density $\mu_l = \lambda_l \pi$. If $G(d\theta) = 0.5\delta_0 + 0.5\delta_{\pi/2}$ is used instead, all lines become vertical and horizontal. This particular case is called the Manhattan Poisson line process (MPLP). Each couple (r_i, θ_i) can be mapped to its corresponding line in $\mathbb{R}^2$ as shown on Fig. 2.1. Along each individual line, an independant 1D HPPP Φ_i of constant density λ_b is then generated. An example of a PCLP is depicted in Fig. 2.4.

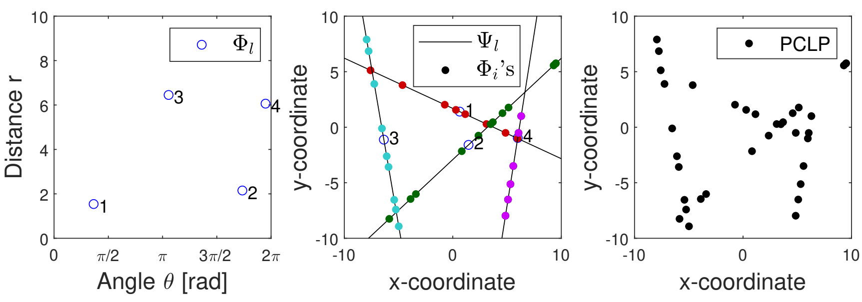

Fig. 2.4 PCLP building process: Left: drawing the initial 2D HPPP Φ_l of density λ_l=0.06/km². Middle: mapping to the corresponding PLLP Ψ_l of line density μ_l and generation of the 1D HPPPs Φ_i of density 0.3/km. Right: obtention of the resulting PCLP.

Remark 2.13. Note that the MPLP can be alternatively generated using two independent 1D HPPPS to generate horizontal and vertical lines as the street angle is imposed. Different densities λ_v and λ_h can then be used for horizontal and vertical streets. This will be the procedure used to generate MPLPs in this document.

Distance distributions

Let us assume a network in $\mathbb{R}^2$ where BSs are deployed following a PCLP generated as explained in the previous section. We assume a typical UE located at the origin and served by its closest BS. By definition, the distance between the UE and this BS is denoted by r. Using the same approach as for the HPPP, the statistical distributions of r are given by [38]:

$$\underline{PDF:} \quad f_{C,R}(r) = \left[2\pi\lambda_l \int_0^r \frac{2\lambda_b r}{\sqrt{r^2-\rho}} \exp(-2\lambda_b\sqrt{r^2-\rho})d\rho\right] \times \exp\left[-2\pi\lambda_l \int_0^r \left(1-\exp(-2\lambda_b\sqrt{r^2-\rho})\right)d\rho\right] \tag{2.6}$$

$$\underline{CDF:} \quad F_{C,R}(r) = 1-\exp\left[-2\pi\lambda_l \int_0^r \left(1-\exp(-2\lambda_b\sqrt{r^2-\rho})\right)d\rho\right]. \tag{2.7}$$

In addition, let us define L_n to be the n-th closest line to the typical centric UE in the initial PLLP Ψ. Due to space constraints, the reader can refer to [31] where the following distributions are defined:

1. $f_{Y_n}(y_n)$ and $F_{Y_n}(y_n)$, the PDF and CDF of the distance between the typical UE and line L_n denoted by Y_n ([31], Lemma 1).
2. $f_{S_n}(s_n|y_n)$ and $F_{S_n}(s_n|y_n)$, the PDF and CDF of the distance between the typical UE and the closest node on line L_n denoted by S_n and conditioned on the distance Y_n ([31], Lemma 3).
3. $f_{U_n}(u_n|y_n)$ and $F_{U_n}(u_n|y_n)$, the PDF and CDF of the distance between the typical UE and the closest node on lines $\{L_1, ..., L_{n-1}\}$ denoted by U_n and conditioned on the distance Y_n ([31], Lemma 4).
4. $f_{V_n}(v_n|y_n)$ and $F_{V_n}(v_n|y_n)$, the PDF and CDF of the distance between the typical UE and the closest node on lines $\{L_{n+1}, L_{n+2}, ...\}$ denoted by V_n and conditioned on the distance Y_n ([31], Lemma 5).

The probability $\mathbb{P}(\mathcal{E}_n|y_n)$ of the event $\mathcal{E}_n$ that the closest node in the PCLP is located on L_n conditioned on the distance Y_n is given by Lemma 6 in [31]. In case the typical street is disregarded, this expression is adapted as:

$$\begin{aligned}\mathbb{P}(\mathcal{E}_n|y_n) &= \mathbb{P}(s_n < u_n, s_n < v_n|y_n)\\ &= \int_0^\infty (1 - F_{U_n}(u_n|y_n))(1 - F_{V_n}(v_n|y_n)) f_{S_n}(s_n|y_n)ds_n.\end{aligned}$$

Example 2.14. These distances are illustrated on Fig. 2.5 for the line L_5. The closest node on L_5 is at a distance s_5 while the closest nodes on line sets $\{L_1, ..., L_4\}$ and $\{L_6, ...\}$ are respectively at a distance u_5 and v_5. As $u_5 < s_5 < v_5$, L_2 will be the serving street in this example and $r = u_5$.

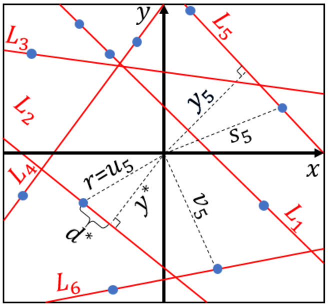

Fig. 2.5 Distances notations for a PCLP: an example.

Lemma 2.15. *Let us assume y^* to be the distance between the typical centric UE and the street on which the closest node lies as depicted in Fig. 2.5. Based on the aferomentioned expressions, the PDF and CDF of y^* are given by:*

$$\underline{PDF:}\quad f_{Y^*}(y^*) = \sum_{n=1}^{\infty} \mathbb{P}(\mathcal{E}_n|y^*) f_{Y_n}(y^*) \tag{2.8}$$

$$\underline{CDF:}\quad F_{Y^*}(y^*) = \sum_{n=1}^{\infty} \int_0^{y^*} \mathbb{P}(\mathcal{E}_n|y_n) f_{Y_n}(y_n)dy_n. \tag{2.9}$$

Proof. The mathematical expression of the CDF of y^* is computed as

$$F_{Y^*}(y^*) \overset{(1)}{=} \sum_{n=1}^{\infty} \mathbb{P}(\mathcal{E}_n)\, \mathbb{E}_{Y_n}\left[\mathbb{1}(Y_n \le y^*)\,|\mathcal{E}_n\right]$$

$$F_{Y^*}(y^*) \overset{(2)}{=} \sum_{n=1}^{\infty} \mathbb{P}\left(\mathcal{E}_n\right) \int_0^{y^*} f_{Y_n|\mathcal{E}_n}(y_n|\mathcal{E}_n) dy_n$$
$$\overset{(3)}{=} \sum_{n=1}^{\infty} \int_0^{y^*} \mathbb{P}\left(\mathcal{E}_n|y_n\right) f_{Y_n}(y_n) dy_n$$

where (1) follows from the total law of probability, (2) comes from the definition of the expectation and (3) is a consequence of Bayes' theorem [39]. The PDF of y^* is then easily obtained by derivating the CDF expression with respect to y^*. □

Lemma 2.16. *Let us assume d^* to be the distance between the centric UE projection on the serving line and the serving node as depicted in Fig. 2.5. Conditioned on the distance y^*, the PDF of d^* is given by:*

$$f_{D^*}(d^*|y^*) = \frac{\overline{F}_{C,R}(\sqrt{y^{*2} + d^{*2}}) f_{1,R}(d^*)}{\int_0^{\infty} \overline{F}_{C,R}(\sqrt{y^{*2} + x^2}) f_{1,R}(x) dx}. \tag{2.10}$$

Proof. This result is a direct consequence of Bayes' theorem. In fact, the first numerator term represents the probability for a line located at a distance y^* to be serving knowing the distance d^* to the closest node on this line. This is nothing else but the void probability in $\mathcal{B}_2(0, \sqrt{y^{*2} + d^{*2}})$. Following the same principle, the denominator is the total probability for a line located at a distance y^* to be serving. □

Corollary 2.17. *Conditioned on the distance y^*, the PDF of r is given by:*

$$f_{C,R}(r|y^*) = f_{D^*}\left(\sqrt{r^2 - y^{*2}}|y^*\right) \frac{r}{\sqrt{r^2 - y^{*2}}}. \tag{2.11}$$

Proof. The PDF is easily obtained considering the variable change $R = \sqrt{D^{*2} + Y^{*2}}$. □

Corollary 2.18. *Conditioned on the distance r, the PDF of y^* is given by:*

$$f_{C,R}(y^*|r) = \frac{f_{C,R}(r|y^*) f_{Y^*}(y^*)}{f_{C,R}(r)}. \tag{2.12}$$

Proof. This is the result of applying Bayes' theorem.. □

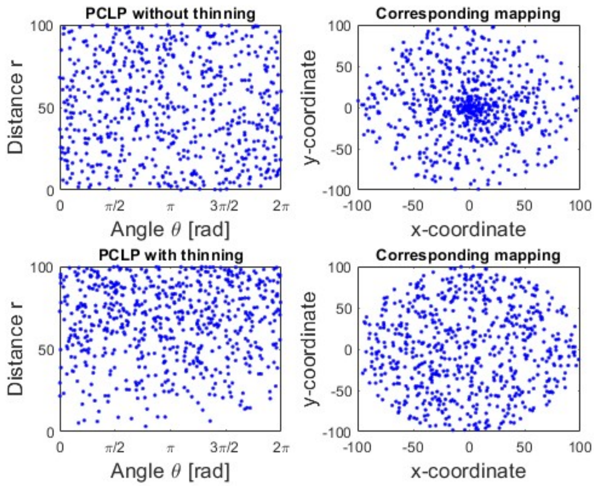

Fig. 2.6 Homogenization of a PCLP firstly generated on the representation space: comparison of a PCLP with the same effective line density with and without thinning.

Homogenization of a line process generated in the representation space

Homogeneously generating the line process in the representation space does not mean its corresponding mapping in the usual coordinates system is homogeneous as depicted in Fig. 2.6. To ensure an homogeneous line process in the latter coordinates system, an additional thinning function $p(r) = \frac{2r}{R_{max}^2}$ (where R_{max} is the radius of the studied area) needs to be applied in the representation space. To do so, the initial line density needs to be increased to obtain the same effective density as the thinning operation will downsample the number of lines. Fig. 2.6 shows the comparison of a PCLP with the same effective density obtained with and without the thinning step.

2.1.5 The non homogeneous Poisson Cox line process

In this section, a new PP called the non homogeneous Poisson Cox line process (NHPCLP) is introduced. The idea of this PP comes from two main observations on real cities street patterns. First, the angular distribution of streets in real cities is shown not to be totally uniform as some form of organization still exists (e.g. parallel neighbour streets) as shown in [40]. Second, the street density is not constant within cities hence the need for an inhomogeneous street distribution. For example, a UE located in the suburbs could experience different levels of exposure and coverage with respect to a UE located in the city center. Both observations are succesively illustrated in the next sections. Formally, the NHPCLP Ξ is thus generated in a two steps fashion:

1. a PCLP with wisely chosen parameters is generated.
2. the obtained PCLP is thinned with a distance- and angular-dependent probability $p(r, \theta)$ that reflects the angular orientation distribution $f_\Theta(\theta)$ of streets and the inhomogeneous distance dependence within the city.

Remark 2.19. Note that the thinning function can also be used to model environments where one side of the city is constrained by a physical limit (e.g. the sea). In that particular case, the occurence of the street orientation in the physical limit's direction will be lower than other directions. This can be captured by the thinning function.

Non-uniform street orientation

As already mentioned, the street angular orientation distribution is not exactly uniform. Instead, another distribution $f_\Theta(\theta)$ can be assumed.

Example 2.20. Suppose the following function :

$$g(\theta) = \sum_{\mu_i \in \mathbf{m}} \frac{1}{\sigma\sqrt{\pi}} \exp\left(-\left(\frac{\theta - \mu_i}{\sigma}\right)^2\right) \quad \text{for} \quad 0 \leq \theta \leq 2\pi$$

where $\mathbf{m} = \{0, \pi/2, \pi, 3\pi/2, 2\pi\}$ and $\sigma \in \mathbb{R}$. The angular distribution is obtained by normalizing this function as $f_\Theta(\theta) = g(\theta) / \int_0^{2\pi} g(\theta) d\theta$. An example of the obtained network for different values σ is shown on Fig. 2.7. The higher σ is, the closer we are to the uniform distribution. Conversely, the lower σ is, the closer we are to a Manhattan-like environment. In the latter case, the distribution can be simplified to five delta functions. To replicate such an angular distribution in our framework, the initial PCLP can be thinned with a thinning function $p_1(\theta) = f_\Theta(\theta) / \max(f_\Theta(\theta))$.

UE located in the suburbs

Let us assume the maximum street density λ_s is observed in the city center located at (x_c, y_c) with respect to the typical UE. If the typical UE is ex-

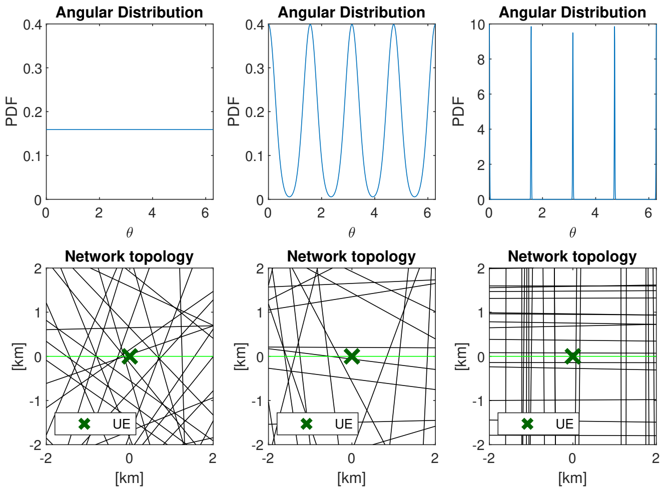

Fig. 2.7 Illustration of the street angular orientation distribution. Left: NHPCLP with $\sigma = 100$. Middle: NHPCLP with $\sigma = 0.25$. Right: NHPCLP with $\sigma = 0.01$.

actly at the city center, the street density $\lambda_s(r) = \lambda_s f(r)$ is a function that decreases with the radial distance r from the UE point of view. If the typical UE is not at the city center, the street density with respect to this UE becomes $\lambda_s(r, \theta) = \lambda_s f(\sqrt{r^2 + r_c^2 - 2x_c r cos(\theta) - 2y_c r sin(\theta)}) = \lambda_s p_2(r, \theta)$ where $r_c^2 = \sqrt{x_c^2 + y_c^2}$.

Example 2.21. Suppose the function $f(r) = 0.98 \exp(-r/b) + 0.02$ where $b \in \mathbb{R}$. An example of the obtained network for several parameters sets is depicted in Fig. 2.8. As expected, the street density is maximum near the city center in all cases. In addition, the higher b is, the faster the street density decreases with the distance (w.r.t. the city center).

Distance distributions

Based on the distance distributions for the PCLP, the statistical distributions of r are modified as:

$$\underline{PDF:} \quad f_{NC,R}(r) = \left[\lambda_l \int_0^{2\pi} \int_0^r \frac{2\lambda_b r}{\sqrt{r^2 - \rho}} \mathcal{Z}_1(r, \rho, \lambda_b) p(\rho, \theta) d\rho d\theta\right] \times \exp\left[-\lambda_l \int_0^{2\pi} \int_0^r \Big(1 - \mathcal{Z}_1(r, \rho, \lambda_b)\Big) p(\rho, \theta) d\rho d\theta\right] \quad (2.13)$$

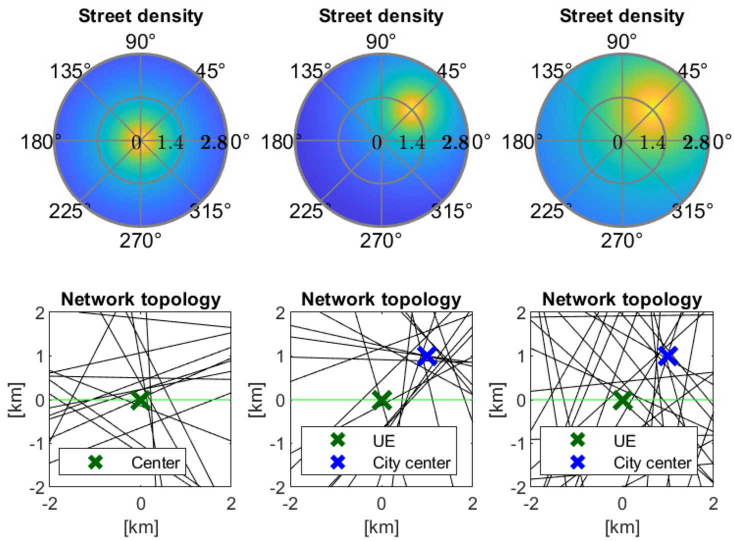

Fig. 2.8 Illustration of the non homogeneous street density. Left: NHPCLP with $b = 1200$ and $(x_c, y_c) = (0, 0)$. Middle: NHPCLP with $b = 1200$ and $(x_c, y_c) = (1, 1)$. Right: NHPCLP with $b = 3000$ and $(x_c, y_c) = (1, 1)$.

$$\underline{CCDF:} \quad F_{NC,R}(r) = 1 - \exp\left[-\lambda_l \int_0^{2\pi} \int_0^r \Big(1 - \mathcal{Z}_1(r, \rho, \lambda_b)\Big) p(\rho, \theta) d\rho d\theta \right]. \tag{2.14}$$

where $\mathcal{Z}_1(r, \rho, \lambda_b) = \exp(-2\lambda_b\sqrt{r^2 - \rho^2})$ and $p(r, \theta) = p_1(\theta)p_2(r, \theta)$.

Remark 2.22. Ideally, the thinning function should consider both the angular and distance dependency jointly. However, this generally leads to non analytical expressions and prevents us to incorporate it in our mathematical framework. For this reason, we will settle for that approximation.

Note that the thinning function modifies the interpretation of the line density λ_l as the number of lines is downsampled by the thinning operation. For this reason, the notion of effective line density λ_{eff} is introduced and refers to the actual observed street density (i.e. the line density after downsampling).

2.1.6 Finite length stick processes

Recently, other processes have been proposed in [41]: the Poisson stick process (PSP) and the Poisson lilypond model (PLM). The PSP is a generalization of the PCLP where streets have a finite length and are therefore drawn as segments instead of lines. In that case, each segment i is represented by a quadruple $(r_i, \phi_i, \theta_i, h_i)$ where (r_i, ϕ_i) are the polar coordinates of the middle of the segment, θ_i is the angular orientation of the segment and h_i is the segment half-length. Assuming a constant density λ_l, the initial PLLP $\Phi_l = \{(r_i, \phi_i), i \in \mathbb{Z}\}$ is generated using the same approach as for the PCLP. Then, θ_i is drawn from a uniform distribution $\mathcal{U}_{[0,\pi[}$ and h_i is drawn from known distribution $f_H(h)$. As for the PCLP, independent 1D HPPPs of density λ_b are then generated on each segment. An illustration of the PSP with its notations is depicted in Fig. 2.9a.

The PLM is a generalization of the PSP where segments are constrained by their surrounding segments. Each segment is said to grow at a constant rate on both ends until it hits another segment on one of the sides. This process is shown on Fig. 2.9b where the segments centers are represented by black crosses. The half-lengths in a PLM are Rayleigh distributed with $f_H(h) = 2bh \exp(-bh^2)$ where b is proportional to the street density and can be estimated from the empirical mean of half-lengths.

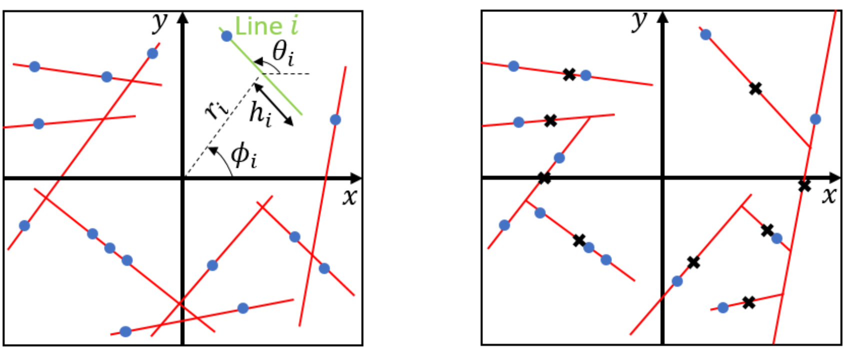

(a) Poisson stick process.

(b) Poisson lilypond model.

Fig. 2.9 Illustration of stick processes.

Distance distributions

Both processes can become inhomogeneous as for the PCLP. The generalization to inhomogeneous cases is similarly done. Using the same approach as for the NHPCLP, the statistical distributions of the distance r to the closest node of the NHPSP/NHPLM are given by:

$$\underline{PDF:} \quad f_{NS,R}(r) = \left[\lambda_l \int_0^{\infty}\int_0^{\pi}\int_0^{2\pi}\int_0^{r+h} \frac{\partial \mathcal{Z}_2(r,\rho,\phi,\theta,\lambda_b)}{\partial r} p(\rho,\phi) f_{\Theta}(\theta) f_H(h) dA\right]$$

$$exp\left[-\lambda_l \int_0^{\infty}\int_0^{\pi}\int_0^{2\pi}\int_0^{r+h} \Big(1-\mathcal{Z}_2(\rho,\phi,\theta,\lambda_b)\Big) p(\rho,\phi) f_{\Theta}(\theta) f_H(h) dA\right] \tag{2.15}$$

$$\underline{CDF:} \quad F_{NS,R}(r) = 1-$$

$$\exp\left[-\lambda_l \int_0^{\infty}\int_0^{\pi}\int_0^{2\pi}\int_0^{r+h} \Big(1-\mathcal{Z}_2(r,\rho,\phi,\theta,\lambda_b)\Big) p(\rho,\phi) dA\right]. \tag{2.16}$$

where $dA = d\rho d\phi d\theta dh$, $\mathcal{Z}_2(r,\rho,\phi,\theta,\lambda_b) = \exp(-\lambda_b l(r,\rho,\phi,\theta))$, $l(r,\rho,\phi,\theta) = l_1(r,\rho,\phi,\theta)\mathbb{1}_{\rho\leq r} + l_2(r,\rho,\phi,\theta)\mathbb{1}_{\rho>r}$ and $p(r,\phi) = p_1(\phi)p_2(r,\phi)$. $l_1(r,\rho,\phi,\theta)$, $l_2(r,\rho,\phi,\theta) = |\min(u_1,h) \pm \min(u_2,h)|$, where $u_1, u_2 = |-\rho\cos(\phi-\theta) \pm \sqrt{r^2-\rho^2\sin^2(\phi-\theta)}|$.

2.2 Stochastic geometry based analytical techniques

In the literature, several analytical techniques have been proposed for deriving network-level metrics of interest. These techniques make use of the mathematical framework developed using SG and are available for different PPs. However, due to an increased mathematical tractability with respect to other PPs, the PPP has been particularly popular. Up to date, eleven techniques with various degrees of tractability, accuracy and flexibility were investigated [34]. This document will focus on two of the most commonly used techniques for the derivation of the coverage probability.

To illustrate these techniques, we will use a common definition of the SINR measured at a typical UE u assuming the serving distance r to the serving BS k^* is known. BSs are here distributed following an HPPP Φ of density λ. Assuming a noise power W, the SINR is given as

$$\mathrm{SINR}_u = \frac{gL^{-1}(r)}{W + \sum_{\substack{k\in\Phi\\k\neq k^*}} g_k L^{-1}(r_k)} = \frac{gL^{-1}(r)}{W+I} = \frac{S}{W+I} \tag{2.17}$$

where g is the fading power gain on the link between the serving BS and the typical UE, g_k is the fading power gain on the link between the interfering BS k and the typical UE and $L(\cdot)$ is the path loss function.

2.2.1 Using the Laplace transform

The coverage probability defined as $\mathbb{P}(\mathrm{SINR}_u > \theta_c)$ is given by:

$$\begin{aligned}\mathbb{P}_c(\theta_c) = \mathbb{P}(\mathrm{SINR}_u > \theta_c) &= \mathbb{P}\left(\frac{gL^{-1}(r)}{W+I} > \theta_c\right) \\ &= \mathbb{E}_R\left[1 - \mathbb{P}\left(g < \theta_c L(r)(W+I)\right)\right].\end{aligned}$$

Depending on the fading distribution $f_G(g)$ observed on the useful link, the final expression is then given by

$$\begin{aligned}\underline{Rayleigh:}\quad & \mathbb{P}_c(\theta_c) = \mathbb{E}_R\left[\exp(-\theta_c W L(r))\mathcal{L}_I(\theta_c L(r))\right] \\ \underline{Rice:}\quad & \mathbb{P}_c(\theta_c) = \mathbb{E}_R\left[\sum_{k=0}^{\infty}\sum_{j=0}^{k}\gamma_{jk}\left(-\theta_c L'(r)\right)^{k-j}\frac{\partial^{k-j}\mathcal{L}_{W+I}(\theta_c L'(r))}{\partial^{k-j}s}\right] \\ \underline{Nakagami:}\quad & \mathbb{P}_c(\theta_c) = \mathbb{E}_R\left[\sum_{k=0}^{m-1}\frac{(-m\theta_c L(r))^k}{k!}\frac{\partial^k\mathcal{L}_{W+I}(m\theta_c L(r))}{\partial^k s}\right]\end{aligned}$$

where $\gamma_{jk} = \frac{K^k}{(k!)^2}e^{-K}j!\binom{k}{j}$, $L'(r) = (K+1)L(r)$, $\mathcal{L}(\cdot)$ is the Laplace transform and K and m are the Rice and Nakagami parameters as defined in Section 3.3.4 [34, 42].

The Laplace transform is then easily computed using the PGFL property of PPPs (see Theorem 2.4) as

$$\mathcal{L}_I(i) = \exp\Big(-2\pi\lambda\int_{f(r)}^{\infty}\frac{dr}{1+\frac{L(r)}{i}}\Big)$$

where the threshold $f(r)$ depends on the association rule (cfr. Section 3.3.6).

While the expression of the coverage probability under Rayleigh fading is very tractable, the presence of partial derivatives associated with other fading distributions renders a full parametric analysis more time-consuming. For this reason, the next technique can be considered as a good alternative.

2.2.2 Using the Gil-Pelaez inversion theorem

To incorporate generalized fading distributions, a good solution comes from the use of the Gil-Pelaez inversion theorem [43].

Theorem 2.23. *The Gil-Pelaez inversion theorem states that the CDF of a random variable X is given by:*

$$F_X(x) = \frac{1}{2} - \frac{1}{\pi}\int_0^{\infty} \frac{Im(e^{-j\omega x}\phi_X(\omega))}{\omega} d\omega \tag{2.18}$$

where $\phi_X(\omega)$ is the characteristic function (CF) of X.

Based on this theorem, the coverage probability can be computed as:

$$\begin{aligned}\mathbb{P}_c\left(\theta_c\right) &= \mathbb{P}\left(S - (W+I)\theta_c > 0\right) \\ &= \frac{1}{2} - \frac{1}{\pi}\mathbb{E}_R\left[\int_0^{\infty} \frac{\mathrm{Im}(e^{-jW\theta_c\omega}\phi_S(\omega)\phi_I(-\theta_c\omega)}{\omega})d\omega\right]\end{aligned}$$

where $\phi_S(\omega)$ can be computed using the CF of the considered fading distribution and

$$\phi_I(\omega) = \exp\Big(-2\pi\lambda\int_{f(r)}^{\infty}\left[1 - \mathbb{E}_g[\exp(j\omega g L^{-1}(r))\right] r dr\Big).$$

This method will be considered in this document.

3

A general multi-tier urban network model

WITH the increased complexity and heterogeneity of modern wireless networks, the development of flexible network models has become a priority. In that sense, SG has been identified as one of the potential model-driven tools as it enables us to cover many different scenarios [34] and as it offers easy scalability. In this chapter, a completely general multi-tier urban network model is proposed for a subsequent SG-based analysis. With no or low increased complexity, this model enables us to modify (i) the environment street pattern, (ii) the number of studied tiers (roof or street tiers), (iii) the propagation characteristics of each individual tier including the beamforming model, the path loss model, the fading model and the LOS probability (iv) the interaction properties between the UE and BSs (e.g. the association rule and the relative proximity) and (v) the UE's environment including its position with respect to street intersections.

3.1 Related works

Wireless networks perfomance is said to be mostly interference-limited [36]. As it enables an easy characterization of the interference level, stochastic geometry has been considered to model wireless networks as early as 1978 [44]. Since then, the field has drawn an increasing attention in the scientific community. Many different PPs have been investigated (e.g. the PPP, the Matern hard core PP or the binomial PP) and a wide panel of network-level metrics have been studied (e.g. the coverage probability, the area spectral efficiency or the throughput). As previously mentioned, the PPP was undoubtedly the most popular PP due to an increased mathematical tractability. Most notable works treating the PPP include [25, 36, 37, 45–48]. As the present work mainly focus on doubly stochastic models (i.e. models in which both the network elements and the street pattern are stochastically generated), a particular interest will be exclusively dedicated to these models in the forthcoming state of the art. However, the interested reader can find a complete taxonomy of the current advances in SG in this recently published study [34]. This work was reviewed by some of the biggest experts in the field and offers an extensive overview of SG-based models and analytical techniques.

In the near future, 5G networks are expected to be boosted by small cells located closer to the ground level. For example, the New York municipality recently accepted to deploy BSs integrated with the streetlights to provide high-speed connectivity to pedestrian users [49]. After different trials conducted in 2021, AT&T is planning to extend the use of such cells to multiple cities [50]. Motivated by the fact that small cells sites will be found along streets in dense urban areas, doubly stochastic models have drawn an increasing attention in the SG field. The study in [30] firstly introduced the MPLP to model roads in Manhattan-like environments. The coverage distribution is derived using a correlated blockage model accounting for building penetration. In [51], the same metric is analyzed for vehicle-to-infrastructure networks operating at mmWave frequencies. The MPLP is shown to accurately describe Manhattan networks by comparison with the fixed grid model and the actual street deployment in Chicago. MPLP models are also used for indoor scenarios [52–55], drones-to-ground networks [56] and relay assisted networks [57].

Other works also consider Cox line processes as generalization of the MPLP to model non-prependicular streets [31, 32, 58–63]. In particular, [38] and [32] have laid the foundations of the PCLP. Among the different technologies that have been studied, one can mention vehicle-to-everything communication [58], vehicular ad hoc networks [61] and multi-radio access technology [63]. In [58], trends on the network deployment design have been highlighted and the benefit of small cells to offload macro BSs has been proven.

According to future deployments, the superimposition of a tier of macro-BSs (MBs) modeled by a 2D HPPP and a second tier of road side units (RSUs) modeled by a PCLP is often considered [38, 60, 63–65]. In [60], it was shown that a denser deployment of RSUs deteriorates the SINR coverage probability but boosts the rate coverage by reducing the load on MBs. This enables an improved spatial reuse of frequency resources. In that case, the available bandwidth can be shared among a lower number of UEs. As increasing the number of RSUs is not always feasible due to practical constraints, they also proposed to enhance the performance by adjusting the selection bias between MBSs and RSUs. Discriminating MBs was shown to lead to significant improvements in terms of rate coverage if the bias is finely tuned. [63] further enabled the RSUs' tier to communicate in both sub-6GHz and millimeter wave (mm-wave) bands. The serving tier is first chosen based on the sub-6GHz received power. In case the RSUs' tier is chosen, the band selection is then perfomed either on the biased average or instantaneous received power knowing the mm-wave signals are automatically lost if they are obstructed by a car. The bias is here selected to satisfy the requirements of different 5G services (i.e. ultra-reliable lower-latency communications, machine-type communications and enhanced mobile broadband) in terms of reliability, coverage and data rates. System design insights are provided to sustain the differents applications. [62] proposes a generalization to vehicle-to-vehicle, vehicle-to-infrastructure, infrastructure-to-vehicle, and infrastructure-to- infrastructure communications. Finally, [41] takes into account the UE position with respect to street intersections. It distinguishes a UE located in a street, a UE located at a crossroad and a UE located at a T-junction.

In a PCLP framework, the mathematical expressions associated with contributions coming from non typical streets usually become complex. For this reason, [41, 66] have tried to circumvent this complexity by providing equivalences between the PLCP and other processes. The authors have shown that the street geometry plays an important role in the high-reliability regime. They proposed an alternative to the PLCP called the transdimensional Poisson point process (TPPP). This process consists in superimposing one or two 1D PPPs for the typical street BSs and a 2D

PPP for other streets BSs. It was shown on the SIR meta distribution that the TPPP can be a good approximation. Considering shadowing emphasizes even more the correspondance between both processes. As in the latter work, [38] also considered lognormal shadowing χ. By means of the displacement theorem, contributions coming from the typical street(s) are then computed considering a new 1D PPP with modified density. This PPP has a density of $\mathbb{E}[\chi^{-\frac{1}{\alpha}}\lambda]$ if a single-slope path loss is used. As the displacement is made in the direction of the typical UE, applying shadowing in non typical streets is more complicated. For this reason, [60] proposed an approach to accurately approximate the PLCP by means of the combination of a 1D PPP and a 2D PPP of wisely chosen densities. As the goal of this work is to physically model different propagation mechanisms (e.g. diffraction), it will stick to the PCLP model as it needs the street geometry information.

Recently, new doubly stochastic processes have been introduced in the literature. Processes accounting for finite street lengths have been proposed in [41]: the Poisson stick process (PSP) and the Poisson lilypond model (PLM). In addition, [67] proposed a first step into inhomogeneous processes by defining a new process named the binomial line Cox process. Based on a study on the street patterns of Paris and Lyon, the street density was shown to fluctuate within the city. This triggered the need for non homogeneous processes.

On the basis of the aforementioned works, the main findings of this study can be summarized as follows:

- The works originally presented in [30, 31, 41] are fully revisited. A number of features are added to capture additional propagation aspects. These new characteristics are detailed below:
  - The framework is adapted to encompass urban, suburban and rural environments for which the propagations models and parameters are different. The required model modifications for the three environments are highlighted.
  - The proposed analysis takes into account power contributions coming from BSs outside the user street and propagating via diffraction at crossroad corners. As explained in [51], contributions from such a corner diffraction can be significant com-

pared to building penetration, hence the need to address their modeling. To this purpose, Berg recursive method is employed for its simplicity and its accuracy regarding the path loss (PL) levels [68]. This model also has the advantage of featuring a general expression, depending on both Euclidean distances and corner angles. These dependencies open perspectives for a generalization to Cox processes, and differ from [51] where constant diffraction losses are considered.

- The power contributions of two very close BSs are more or less correlated. In particular, the direct paths for two BSs outside the user street are expected to cross a similar amount of buildings. In that sense, the authors of [30] proposed a correlated blockage model where the number of crossed walls depends on a street numbering system. For sake of mathematical tractability, this numbering system can not be applied in our framework. Therefore, we propose to use a Winner-style propagation model taking into account link distances to enable a correlation-based modeling and a viable mathematical framework.
- Any fading distribution for which the characteristic function is known can be incorporated in the model. Our work focusses on Rayleigh, Rice and Nakagami distribution.
- The presence of street obstacles (cars, trucks,...) is included using the blockage model of [69], and integrated in the SG framework via inhomogeneous thinning. This thinning is function of a line-of-sight (LOS) probability which is distance dependent and continuous everywhere, unlike the LOS ball model [70].
- BSs on the roofs are considered. As for diffracted contributions in the streets, Berg recursive method is generalized to roof BSs to enable the computation of both LOS and NLOS contributions coming from these BSs. A geometrical LOS probability is combined with the blockage model for street BSs to distinguish LOS roof BSs from non LOS roof BSs. The propagation model is calibrated differently for roof BSs and street BSs.
- In practical deployments, a non-negligible proportion of users can be located at street intersections (e.g. pedestrians waiting at traffic lights). In such cases, the simultaneous presence of BSs in the two crossing streets results in power levels differing from those measured at other users. In the original work of [30],

users were almost surely never located at street intersections. Conversely, our work includes a non-zero probability for this event to happen, in which case power signals coming from the two streets are considered.

- The heights of the UEs and BSs are here considered. Neglecting this feature might result in underestimations in the PLs, especially for BSs in the user vicinity. The power contributions associated to these BSs might hence be overestimated, which could bias the performance metrics especially for high SINR values. Since small cells will be pushed closer to the UE, this new feature makes it possible to distinguish these cells from usual macro cells generally located on roofs.
- Due to efforts made by the operators to deploy small cells where the UEs actually are, assuming the UE location is not related to the network BSs locations is a pretty strong hypothesis. For this reason, our model generalizes the framework to a non uniform typical UE whose location is coupled with a hotspot BS. The differences with a uniform UE are then highlighted.
- Due to the linear dependence between tiers in a PCLP, street tiers can not be considered independent as it is the case for K-tier HPPPs. In most K-tier models, a single street tier is generally assumed. This deletes the need to take into account the observed dependency. This model enables any number of street tiers to be generated on the same street pattern and provides the required associated mathematical tools.
- Our system model allows the use of three different association strategies.

- We study the EMF exposure in Poisson line processes. In order to characterize the statistics of exposure and its correlation to the spectral efficiency, the following metrics are derived: the first moments of the data rate and exposure, their marginal distributions, as well as their joint distribution.
- Like [67], we focus on inhomogeneous doubly stochastic models by proposing a new point process named the non homogeneous Poisson Cox line process (NHPCLP). We fully adapt the analytical expressions for most of the above-mentioned metrics to the NHPCLP.

3.2 Network topology

In this work, the network is generated by superimposition of several tiers that can be grouped into two main categories: street tiers and roof tiers. The modeling of each category will be respectively described in Sections 3.2.1 and 3.2.2. These tiers are assumed to be deployed on a circular area of radius $R \in \mathbb{R}$. As the model used for street tiers depends on the street pattern of the studied environment, the point process used for street tiers can be chosen between a (NH)PCLP, a (NH)PSP or a (NH)PLM. As this chapter intends to propose a completely general model, the following sections will first assume street tiers are deployed by means of an inhomogeneous process: the NHPCLP. The discussion is however easily adapted to all other cases.

3.2.1 Street Tiers

A K_S-tier NHPCLP Ξ is generated as explained in Sections 2.1.4 and 2.1.5. The initial PLLP Ψ_l is drawn assuming:

- a given street orientation angular distribution $f_\Theta(\theta)$
- a distance- and angular-dependent line density $\lambda_s p(r,\theta)$ where λ_s is the density observed at the city center located in (x_c, y_c) and $p(r,\theta)$ is the probability for a line represented by the couple (r,θ) to be generated in Ψ_l.

An additional line is then virtually superimposed to the horizontal axis of the coordinate system. This line will represent the street of the typical UE, located at $(0, 0, H_u)$. Without loss of generality (cfr. Theorem 2.9), all the performance metrics of this analysis will be derived for this UE. This additional street l_0 will be referred to as typical street. By definition, $\Psi_0 = \Psi_l \cup l_0$. Yet, the NHPCLP makes the evaluation of the network performance at the central UE not representative of the whole network as we lose the motion-invariance property of PPs. Indeed, the location of the UE in the city will impact its performance. The analysis is thus only valid for that specific UE but the impact of the UE non-centrality will be quantified. The use of a PCLP however restores the motion-invariance property.

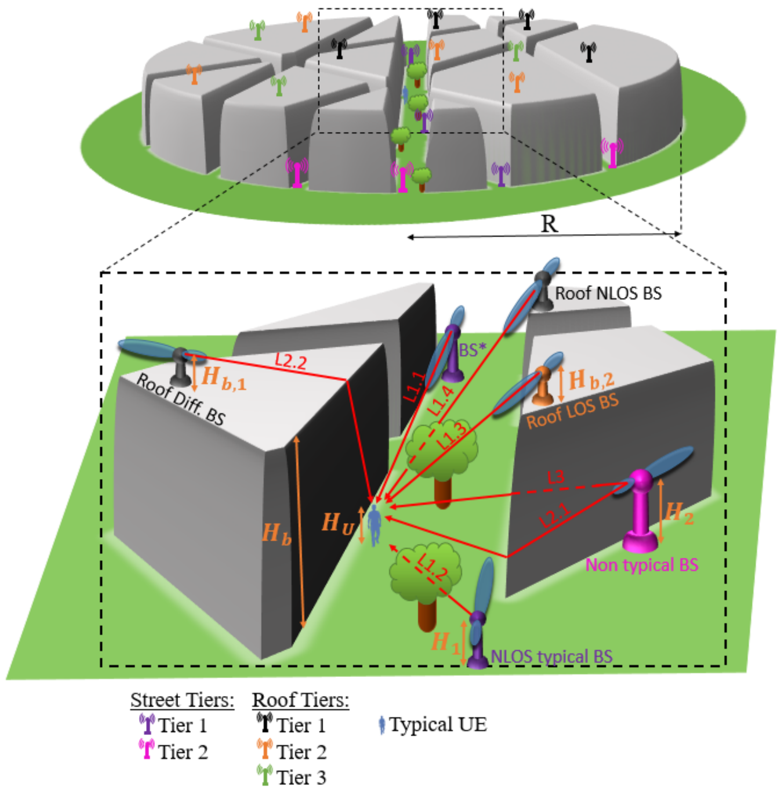

Fig. 3.1 Snapshot of the studied network: $K_S = 2$ and $K_B = 3$.

On each line of Ψ_0, K_S 1D HPPPs Φ_k are then systematically deployed. Note that the different tiers are thus linked and conditioned by the line realization. The transmit power, density and height of the base stations (BS) of tier Φ_k are denoted by (P_k, λ_k, H_k) for all lines. The BSs of all tiers are assumed to be equipped with one transmit antenna. One will denote $\Delta H_k = H_k - H_u$, the height difference between a BS of tier k and the typical UE.

3.2.2 Roof Tiers

Additional tiers on the buildings' roofs are then considered. Roof BSs are said to belong to any of the K_B roof tiers and are located at roof height H_b.

Each roof tier $\Phi_{B,k}$ is deployed following a 2D HPPP of density $\lambda_{b,k}$. BSs of this tier emit with a power $P_{b,k}$. The height of a roof BS of tier k with respect to the roof itself is denoted by $H_{b,k}$. The height difference between buildings and the typical UE is denoted by $\Delta H_b = H_b - H_u$. An example of the network under study is depicted in Fig. 3.1.

Remark 3.1. Note that an exclusion zone r_0 should be considered for tiers where $H_k < 1$ to avoid path loss singularities. Consequently, the constraint $\sqrt{r_0^2 + H_k^2} \geq 1$ has to be respected.

3.3 Channel model

The channel model for the different types of BSs in the network under study will be detailed in the following sections. In particular, the beamforming model, the blockage model for both street tiers and roof tiers, the fading model and the path loss model for each BS type will be successively defined.

3.3.1 Beamforming model

A binary beamforming scheme is here assumed for mathematical tractability. This scheme is formalized by means of the following beamforming function:

$$G(\theta) = \begin{cases} G_1 & \text{for} \quad -\gamma \leq \theta \leq \gamma \\ G_2 & \text{for} \quad \pi - \gamma \leq \theta \leq \pi + \gamma \\ 0 & \text{elsewhere} \end{cases} . \tag{3.1}$$

where G_1 is the main lobe beamforming gain, G_2 is the side lobe beamforming gain and γ is the half-beam width. As the BS power is distributed over the different directions, the condition $\frac{1}{2\pi}\int_0^{2\pi} G(\theta) d\theta = 1$ or equivalently $G_1 + G_2 = \frac{\pi}{\gamma}$ has to be respected. An example of the beamforming scheme is depicted in Fig. 3.2. It is shown that the narrower the beam is, the bigger the main lobe gain can be.

Assume a typical UE is randomly located in the network. Let us define $p_{T,1}$ and $p_{T,2}$ the probabilities that the power contribution at this UE from a given BS in the typical street is respectively affected by the main lobe gain

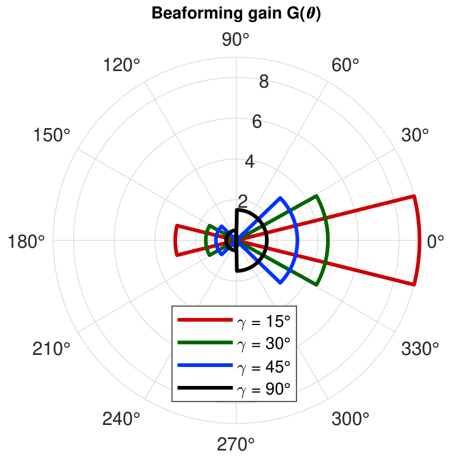

Fig. 3.2 Beamforming scheme for several values of the half-beam width γ: $G_1 = \frac{3}{4}\frac{\pi}{\gamma}$ and $G_2 = \frac{1}{4}\frac{\pi}{\gamma}$.

and by side lobe gain. Similarly, $p_{NT,1}$ and $p_{NT,2}$ are defined for BSs that are not in the typical street. Two different cases are considered:

1. All BSs can send in any direction. Based on the beamforming function, all probabilities are equal and given by $\frac{2\gamma}{2\pi}$.
2. Street BSs are only serving UEs in their own street. The main lobe of these BSs is therefore more or less aligned with the street itself unless the served UE is very close. This main lobe thus points at one of the two street sides. Assuming the beam width is large enough to cover the street width, another UE in the same street will therefore receive contributions on the main lobe from half of the BSs in the same street and on the side lobe from the other half of the BSs in the same street. As a consequence, the probabilities can be modified as $p_{T,1} = p_{T,2} = \frac{1}{2}$. The probabilities in non typical streets remain unchanged.

3.3.2 Blockage model

Street Tiers

Obstacles (vehicles, urban furniture, etc) are here considered in the typical street(s). These blockages cause the coexistence of non line-of-sight (NLOS)

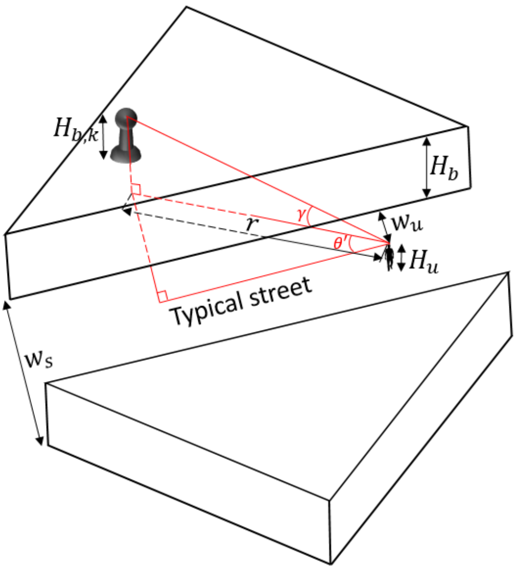

Fig. 3.3 Notations for the roof tiers blockage model.

and line-of-sight (LOS) links in these streets. As in [69], the probability for a BS to be in LOS is given by $p_L(r) = e^{-\beta_S r}$ ($\beta_S \in \mathbb{R}^+$) where r is the distance between this BS and the user. In a complementary way, the probability of NLOS is given by $p_N(r) = 1 - p_L(r)$.

Roof Tiers

Regarding the roof links LOS condition, the geometrical approach proposed in [71] is combined with the blockage model for street tiers. Let us assume the street width is w_s for all streets in the network. In addition, the typical UE is said to be at a distance w_u from the street side as represented on Fig. 3.3. As the UE position is not known at every time instant, w_u is here uniformly distributed in the range $[0, w_s]$. As it can be seen, a BS of roof tier k is here placed at 2D polar coordinates $(r, \pi - \theta')$.

In this configuration and in absence of any obstacles in the streets, the LOS is thus geometrically ensured with probability [71]:

$$p_{L,B,geom}(r,\theta') = \begin{cases} 1 - \frac{\Delta H_b}{w_s}\frac{\sin(\theta')}{\Delta H_b + H_{b,k}} r & \text{for} \quad r \le \frac{w_s}{\Delta H_b}\frac{\Delta H_b + H_{b,k}}{\sin(\theta')} \\ 0 & \text{otherwise} \end{cases} . \tag{3.2}$$

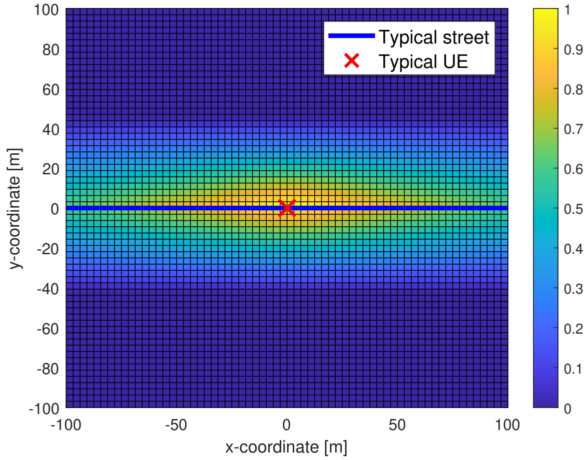

Fig. 3.4 Illustration of the roof tiers LOS probability for $w_s = 35m$, $H_{b,k} = 5m$, $\Delta H_b = 18.5m$ and $\beta_B = 0.005$.

depending on the UE location with respect to the street side. Taking into account street obstacles and generalizing to the usual polar coordinates system (r, θ), the LOS probability is finally given by

$$p_{L,B}(r,\theta) = \begin{cases} \left(1 - \frac{r}{r_c}\right) \exp\left(-\beta_B r\right) & \text{for} \quad r \leq r_c \\ 0 & \text{otherwise} \end{cases} . \tag{3.3}$$

where $r_c = \frac{w_s}{\Delta H_b} \frac{\Delta H_b + H_{b,k}}{|\sin(\theta)|}$ is the critical distance value.

An example of this probability is shown on Fig. 3.4. It is shown that BS locations with non-zero LOS probabilities are found along the typical street. In addition, the probability logically decreases with the distance along this typical street.

The NLOS probability is then given by :

$$p_{N,B}(r,\theta) = \begin{cases} \left(1 - \frac{r}{r_c}\right) \left(1 - \exp\left(-\beta_B r\right)\right) & \text{for} \quad r \leq r_c \\ 0 & \text{otherwise} \end{cases} . \tag{3.4}$$

The probability that a roof BS reaches the UE by corner diffraction is finally given by :

$$p_{d,B}(r,\theta) = \begin{cases} \frac{r}{r_c} & \text{for} \quad r \leq r_c \\ 1 & \text{otherwise} \end{cases} . \tag{3.5}$$

Remark 3.2. Note that β_B should be smaller than β_S as the elevation angles are expected to be bigger. Small street obstacles thus have a lower probability to obstruct the links. Ideally, the β-coefficient for both street tiers and roof tiers should be distance-dependent due to grazing link paths on long-range communications.

Remark 3.3. The geometrical LOS probability for two close BSs should normally be correlated as the UE position at a given time instant is fixed. Geometrically, two very close BSs should both be either in LOS or in NLOS at that time instant. However, due to the random draw of the LOS condition for both BSs in the SG framework, this condition is not always ensured. Unfortunately, this constraint has to be relaxed in our model for mathematical tractability.

3.3.3 Tiers classification

In this study, BSs are classified as a function of (1) their tier (index $k \in \{1, ..., K\}$), (2) their beamforming gain (index $m \in \{1, 2\}$) and (3) their propagation condition (index $n \in \{L, N\}$) respectively introduced in Sections 3.2, 3.3.1 and 3.3.2. A tier is thus characterized by its indexes $\{k, n, m\}$. Due to this three-fold classification, the following PPs are defined :

- $\Phi_{T,(k,n,m)}$, the 1D PPP of BSs located in the typical street and belonging to tier $\{k, n, m\}$. Its density can be expressed as $\lambda_{T,(k,n,m)}(r) = p_{T,m} p_n(r) \lambda_k$ (cfr. thinning property of PPPs).

- $\Phi_{T,(k,n)}$, the 1D PPP of BSs located in the typical street and belonging to tier $\{k, n\}$. Its density is then $\lambda_{T,(k,n)}(r) = p_n(r)\lambda_k$. This tier is defined for cases where the beamforming gain is not fixed yet (e.g. when performing the serving BS selection).

- $\Phi_{ld,(k,m)}$, the 1D HPPP of BSs located in street $l \in \Psi_l$, belonging to tier $\{k, m\}$ and contributing by corner diffraction. Its density is given by $\lambda_{ld,(k,m)} = p_{T,m}\lambda_k$.

- $\Phi_{lp,(k,m)}$, the 1D HPPP of BSs located in street $l \in \Psi_l$, belonging to tier $\{k, m\}$ and contributing by building penetration. Its density is given by $\lambda_{lp,(k,m)} = p_{NT,m}\lambda_k$.
- $\Xi_{NT,(k)}$, the NHPCLP of BSs located in non typical streets, belonging to tier $\{k\}$. $\Xi_{NT,(k)}$ for different values of k are linked by the street realization Ψ_l.
- $\Phi_{B,(k,n,m)}$, the 2D PPP of BSs located on the roofs and belonging to tier $\{k, n, m\}$. Its density is $\lambda_{B,(k,n,m)}(r, \theta) = p_{NT,m}p_{n,B}(r, \theta)\lambda_{b,k}$.
- $\Phi_{Bd,(k,m)}$, the 2D PPP of BSs located on the roofs, belonging to tier $\{k, m\}$ and contributing by corner diffraction. Its density is $\lambda_{Bd,(k,m)}(r, \theta) = p_{NT,m}p_{d,B}(r, \theta)\lambda_{b,k}$.
- $\Phi_{Bd,(k)}$, the 2D PPP of BSs located on the roofs, belonging to tier $\{k\}$ and contributing by corner diffraction. Its density is $\lambda_{Bd,(k)}(r, \theta) = p_{d,B}(r, \theta)\lambda_{b,k}$.
- $\Phi_{B,(k,n)}$, the 2D PPP of BSs located on the roofs and belonging to tier $\{k, n\}$. Its density is $\lambda_{B,(k,n)}(r, \theta) = p_{n,B}(r, \theta)\lambda_{b,k}$.
- The set of all BSs is denoted by Φ_{BS}.

To better understand this tier classification, an illustration for a single street tier network is shown on Fig. 3.5.

3.3.4 Fading model

Rayleigh fading

If there is no dominant path, the channel gain amplitude $|h_n|$ can be modelled by a Rayleigh distributed RV with a scale parameter $\sigma = \frac{\sqrt{2}}{2}$ for normalization. As a consequence, the channel power gain $g = |h_n|^2$ PDF is given by:

$$f_G(g) = \exp(-g)u(g) \tag{3.6}$$

where $u(g)$ is the Heaviside function.

This fading distribution will thus be preferred in the absence of a dominant path like a LOS path or a strong reflection. In particular, the fading distribution for BSs interacting with the typical UE by corner diffraction will be considered to be Rayleigh.

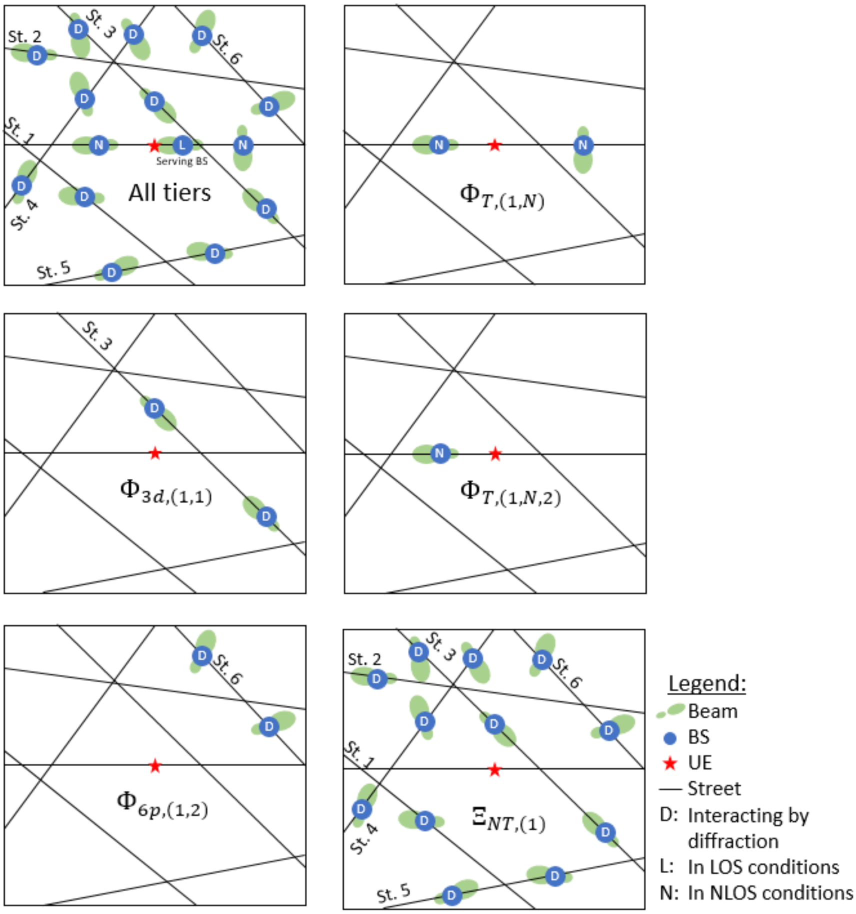

Fig. 3.5 Illustration of the tiers classification for a single street tier network. The top left figure represents all BSs in the network. All different types of subtiers are then isolated on their respective figures.

Rician fading

If there is a dominant path, the channel gain amplitude $|h_n|$ can follow a Rice distribution with non-centrality parameter $\nu = \sqrt{\frac{K}{K+1}}$ and scale parameter $\sigma = \sqrt{\frac{1}{2(K+1)}}$ where K is the Rician K-factor. This factor represents the ratio between the power of the dominant path and the other scattered paths. The channel power gain $g = |h_n|^2$ PDF is subsequently given by :

$$f_G(g) = (K+1)\exp(-K-(K+1)g)I_0\left(2\sqrt{K(K+1)g}\right)u(g) \tag{3.7}$$

where $I_0(\cdot)$ is the zeroth order modified Bessel function of the first kind.

The CF of the Rician fading model is given by Lemma 4.6 in [72]:

$$\phi_{Ri}(t;K) = \frac{K+1}{K+1-jt}\exp\left(\frac{Kjt}{K+1-jt}\right). \tag{3.8}$$

Similarly, the Rice fading distribution will be used for BSs that might have a dominant path. Interestingly, the Rician K-factor can be set separately for the different concerned tiers. For example, a higher K-factor is expected for LOS BSs in the typical street.

Remark 3.4. Rician fading with K-factor K=0 is strictly equivalent to Rayleigh fading. The CF of the Rayleigh fading model is then easily obtained as $\phi_{Ra}(t) = \phi_{Ri}(t;0)$.

Nakagami-m fading

Nakagami-m fading distribution is more general as it enables us to model both cases with a single distribution. If the channel gain amplitude $|h_n|$ follows a Nakagami-m distribution with shape parameter m and spread parameter $\Omega = 1$, the channel power gain $g = |h_n|^2$ PDF is given by:

$$f_G(g) = \frac{m^m}{\Gamma(m)}g^{m-1}\exp(-mg)u(g) \tag{3.9}$$

where $\Gamma(\cdot)$ is the gamma function.

Remark 3.5. Rician fading with K-factor K can be approximated by Nakagami-m fading with shape parameter $m = \frac{(K+1)^2}{2K+1}$ and spread parameter $\Omega = 1$.

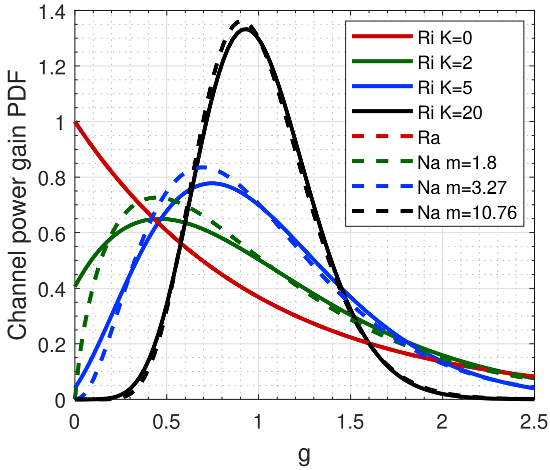

Fig. 3.6 Probability density function of the considered fading distributions and illustration of the matching between these distributions.

The CF of the Nakagami-m fading model is given by Lemma 4.5 in [72]:

$$\phi_{Na}(t;m) = \left(\frac{m}{m+jt}\right)^m. \tag{3.10}$$

The Nakagami-m fading distribution can alternatively be used for all BSs. In a SG framework, this fading distribution was often preferred to the Rice distribution as in [73] due to the presence of the Bessel functions in the Rice channel power gain PDF. As only the CF of the fading distributions is used in the proposed work, both distributions can be used equivalently without increasing the mathematical complexity. However, Rice fading distribution offers more physical insight. In fact, K quantifies how strong the dominant path is with respect to the other paths while m is just a parameter with no physical meaning.

A comparison of all presented fading distributions is depicted in Fig. 3.6. The approximation of the Rice fading distribution by the Nakagami-m fading distribution is shown to be better for higher values of the Rician K-factor.

3.3.5 Computation of the received powers

The received power signals are classified into three main link types for which the path loss (PL) model is different. These types are structured as follows:

- A first link type (L1) subdivided into three subcategories: LOS signals in the typical street (L1.1), NLOS signals in the typical street (L1.2), LOS roof BSs (L1.3) and NLOS roof BSs (L1.4).
- A second link type (L2) subdivided into two subcategories: diffracted signal coming from BSs in the non typical street (L2.1) and from roof BSs (L2.2).
- A third link type (L3) for signals received from BS in non typical streets through building penetration.

A path loss (PL) model is therefore defined for each of these link types. Every link type is illustrated on Fig. 3.1.

Contributions coming from the typical street and from (N)LOS roof BSs (L1)

The power received at the UE from a BS of tier $\Phi_{T,(k,n,m)}$ or $\Phi_{B,(k,n,m)}$ is respectively given by:

$$P_k G_m \left|h_n\right|^2 L_{k,n}^{-1}(r) \tag{3.11}$$

$$P_{b,k} G_m \left|h_n\right|^2 L_{k,n}^{-1}(r) \tag{3.12}$$

where

- $|h_n|^2$ accounts for the small scale Rayleigh or Rician fading;
- $L_{k,n}(r) = \kappa_n \left(r^2 + \Delta H^2\right)^{\alpha_{k,n}/2}$ is the PL model where;
  - κ_n is the intercept of the PL model;
  - r, the distance between the BS and the UE;
  - $\alpha_{k,n}$, the path loss exponent associated to the tier and the LOS/NLOS conditions.
  - ΔH, the height difference between the BS and the UE. This height difference respectively corresponds to ΔH_k and $\Delta H_b + H_{b,k}$ for typical street BSs and LOS roof BSs.

Contributions coming from other streets and from roof BSs by diffraction (L2)

The diffracted contributions are here modeled using Berg recursive method [68]. The power received from a BS of tier $\Phi_{ld,(k,m)}$ ($\forall\ l \in \Psi_L$) or $\Phi_{Bd,(k,m)}$ is in that case given by:

$$P_k G_m \left|h_d\right|^2 L_{d,k}^{-1}(d_1, d_2, \theta) \tag{3.13}$$

$$P_{b,k} G_m \left|h_d\right|^2 L_{d,k}^{-1}\left(\sqrt{r^2 + H_{b,k}^2}, \Delta H_b, \frac{\pi}{2}\right) \tag{3.14}$$

where

- $\left|h_d\right|^2$ accounts for the small scale Rayleigh fading;
- r, the 2D distance between the NLOS roof BS and the UE.
- $L_{d,k}(d_1, d_2, \theta) = \kappa_d \left(d_1 + d_2 + \sqrt{\frac{q_\lambda f}{c}\left(\frac{\theta_d}{\pi/2}\right)^\nu d_1 d_2}\right)^{\alpha_{k,d}}$ is the PL model where;
  - κ_d is the intercept of the PL model;
  - d_1, the distance between the UE and the diffraction corner;
  - d_2, the distance between the BS and the diffraction corner;
  - θ_d, the Berg angle between the initial ray direction $\vec{s_i}$ and the diffracted direction $\vec{s_d}$;
  - f and c, respectively the operating frequency and the speed of light;
  - q_λ and ν, constant empirical parameters defined in [74];
  - $\alpha_{k,d}$, the path loss exponent associated to BSs of tier k interfering via diffraction.

The distances d_1 and d_2 as well as the Berg angle θ_d are illustrated on Fig. 3.7 on a simple case. It is shown that $d_2 = \Delta H_b$ and $\theta_d = \frac{\pi}{2}$ for every roof BS interacting with the UE by corner diffraction. This explains the PL model for roof BSs.

Contributions coming from non typical streets through building penetration (L3)

This PL model for this type of link is strongly inspired by the WINNER 2 channel models presented in [75]. In particular, the indoor-to-outdoor scenario (scenario A2 p.44) PL model was slightly adapted for mathematical

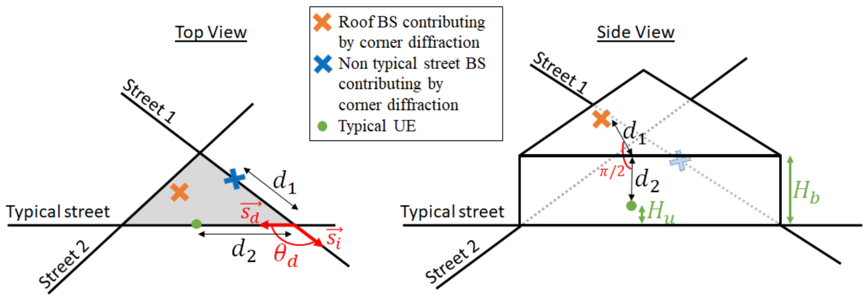

Fig. 3.7 Berg recursive method notations for a non typical street BS and a NLOS roof BS on a simple case.

tractability. The power received from a BS of tier $\Phi_{lp,(k,m)}$ ($\forall\ l \in \Psi_L$) is then given by:

$$P_k G_m \left|h_{\tilde{t}}\right|^2 L_{\tilde{t},k}^{-1}(r) \tag{3.15}$$

where

- $\left|h_{\tilde{t}}\right|^2$ accounts for the small scale Rayleigh fading;
- $L_{\tilde{t},k}(r) = \kappa_{\tilde{t}} K_{in}^{-\sqrt{r^2+\Delta H_k^2}} (r^2 + \Delta H_k^2)^{\alpha_{\tilde{t},k}/2}$ is the path loss (PL) model where;
  - $\kappa_{\tilde{t}}$ is the intercept of the PL model;
  - r, the 2D distance between the typical receiver and the BS;
  - $\alpha_{\tilde{t},k}$, the path loss exponent associated to BSs of tier k in non typical streets;
  - $K_{in} \leq 1$ is the attenuation caused by building walls and furniture.

Remark 3.6. Note that link type L1 corresponds to the case where $K_{in} = 1$. This happens when no building is penetrated like in sparser urban environments or rural environments. In these scenarios, link type L1 can be alternatively used for BSs in non typical streets.

3.3.6 Association rules

The association rule defines which BS in the network should serve the typical UE. In order to achieve the best performance, the serving BS should provide the best observed SINR among all selectable BSs. Unfortunately, considering this association rule generally leads to non tractable results hence the need to use simpler rules. Existing association rules in the SG framework are summarized in [34]. Some of them will be presented in the following sections.

In this work, the typical UE can associate itself to any of the following tiers: $\Phi_{T,(k,n)}$, $\Phi_{B,(k,n)}$, $\Phi_{Bd,(k)}$ and $\Xi_{NT,(k)}$. For BSs in $\Xi_{NT,(k)}$, only the signal received through building penetration (L3) or by direct path (L1) in sparser environments is considered. Including the diffracted contribution in the selection for these BSs is mathematically unfeasible. Considering BSs in $\Xi_{NT,(k)}$ as candidates is only possible if street BSs can serve UEs that are not in their streets.

In a multi-tier scenario, the serving tier will be denoted by the indexes $\{k^*, n^*\}$ or $\{k^*\}$ for tiers $\Phi_{Bd,(k)}$ and $\Xi_{NT,(k)}$. Note that the beamforming gain is here not taken into account in the BS selection as the selected BS will automatically serve the UE on the main lobe as depicted in Fig. 3.1.

Nearest neighbour cell association rule

In a single-tier scenario, the nearest neighbour cell association rule is often considered for its simplicity. This rule is based on the hypothesis that the closest BS more likely provides the best SINR. This rule is only suitable for cases where either a single roof tier or a single street tier is considered. In fact, the BS transmit power and antenna height will play an important role in the selection for multi-tier scenarios.

Example 3.7. If a single street tier is considered, then the serving BS is given by

$$\mathbf{X}^* = \arg_{\mathbf{X_i} \in \Phi_{T,(1,j)}} \min_{\forall j \in \{L,N\}} ||X_i||. \tag{3.16}$$

Remark 3.8. A NLOS BS can thus be preferred to a LOS BS if it's closer even if the attenuation is stronger for NLOS BSs. If the BS density is very high or if the LOS and NLOS PL coefficients are significantly different, the strongest average received power association rule is then more appropriate.

Strongest average received power association rule

This rule connects the user to the BS providing the highest long term power, combining path loss and transmit power. The instantaneous small scale fading is hence not taken into account in the serving BS selection. Let us assume there are N_s potential serving tiers denoted Φ_j, $\forall j \in 1, ..., N_s$. For example, $\Phi_1 = \Phi_{T,(1,L)}$ could be the first tier in this numbering system. The serving BS is given by:

$$\mathbf{X}^* = \arg_{\mathbf{X_i} \in \Phi_j} \max_{\forall j \in 1,...,N_s} P_j L_j(||X_i||) \tag{3.17}$$

where P_j is the emit power of tier Φ_j and $L_j(||X_i||)$ is the PL model corresponding to that particular tier (either L1, L2 or L3).

Biased strongest average received power association rule

The previous rule can be modified to encourage a better distribution of UEs on the different tiers as some cells might be overloaded. The UE could then select its serving BS as the one delivering the maximum average power weighted by a bias. According to the same numbering system as in the previous section, the serving BS is given by:

$$\mathbf{X}^* = \arg_{\mathbf{X_i} \in \Phi_j} \max_{\forall j \in 1,...,N_s} P_j B_j L_j(||X_i||) \tag{3.18}$$

where B_j is the bias value for tier Φ_j.

3.3.7 Generalization to non-uniform users

Many SG studies assume that there is no correlation between the position of the UE and the location of BSs. However, in real-world scenarios, this assumption does not always hold true, as operators tend to deploy BSs where there is a high concentration of UEs, such as city malls, train stations, or airports. While some UEs may be uniformly distributed, others will be clustered around network infrastructure. Therefore, this particularity needs to be taken into account. Since this modification alters the mathematical framework significantly, the resulting analytical results will need to be separated from the general framework.

A so-called *non-uniform* typical UE is here defined. By definition, this type of UE will be located in the close vicinity of a *hotspot* BS that belongs to any of the K_S street tiers. As depicted in Fig. 3.8, the distance from the typical UE to its hotspot BS is said to follow a half-normal distribution with associated PDF $f_H(r_h) = \frac{2}{\sigma_h \sqrt{2\pi}} \exp\left(-\frac{r_h^2}{2\sigma_h^2}\right)$.

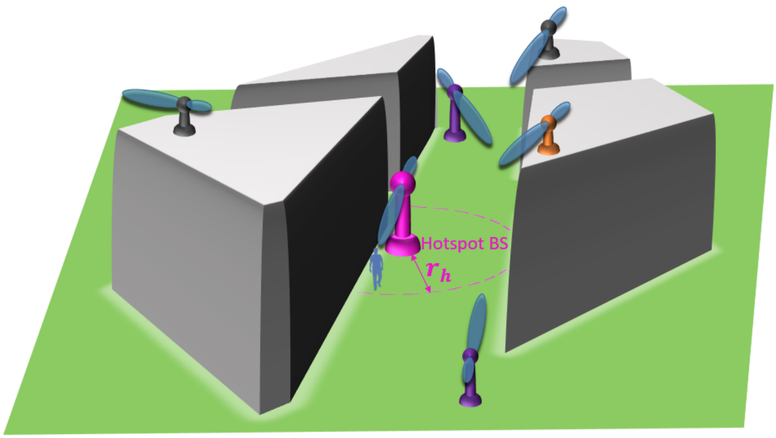

Fig. 3.8 Illustration of a street hostpot BS in urban environments.

As the hotspot BS can be either in LOS or in NLOS conditions, it can be in $2N_S$ different conditions. While the tier of this hotspot BS is randomly selected, the LOS/NLOS selection is performed in a distance-dependent way as it was done for other tiers. The condition in which the hotspot BS is will be denoted by $\gamma = (k_\gamma, n_\gamma)$ where $k_\gamma \in \{1, ..., K_S\}$ and $n_\gamma \in \{N, L\}$. Also, it will be assumed that the hotspot BS forms its own tier Φ_0 that we will refer to as *tier 0*. Although the hotspot UE is likely to connect to this particular BS, it always has the option to connect to a BS of a different tier.

3.3.8 Generalization to crossroad users

As previously mentioned, the location of the typical UE will strongly impact the received power levels: users located at crossroads are in average more exposed to LOS signal compared to users that are not located at street intersections. To take this feature into account, the analysis proposed in this study can also be performed in two steps:

1. Street, crossroad and T-junction UEs are first separately investigated. The performance metrics are independently derived for each of these three user types. In the case of the crossroad UE, two or more streets can be added to the considered line process to model the intersection. Similarly, an semi-infinite street and a perpendicular typical street is

considered for the T-junction UE. By contrast, a single typical street is generated for the street UE. These additional lines in which the typical user is located will be referred to as *typical streets* in the rest of this document. The different types of UEs are illustrated on Fig. 3.9.

2. General metrics can be deduced for an arbitrary UE possibly located at a crossroad with probability η_c, at a T-junction with probability η_t and in a street with probability $1 - \eta_c - \eta_t$. By the law of total probability, the expressions for these final metrics are derived using a weighted average depending on these parameters η_c and η_t.

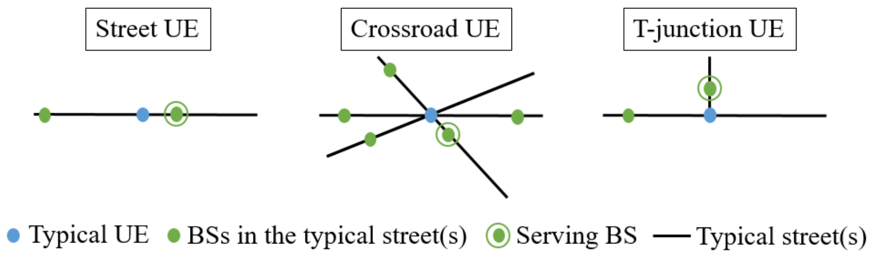

Fig. 3.9 Visualization of the different types of UEs.

3.3.9 Generalization to sparser environments

The study of a typical UE located in a sparser environment (suburban or rural) requires several modeling modifications. In fact, BSs located in non typical streets and roof BSs not located along the typical street can be in LOS conditions with non negligible probability as shown on Fig. 3.10. As the studied environment is now a lot more open, roof BSs and non typical street BSs will be assumed to be either in LOS or in NLOS conditions as for typical street BSs. Diffracted contributions and contributions received through building penetration will be disregarded for mathematical tractability. In addition, roof tiers will be extended to include tiers located on pylones as it is usually the case in rural environments. As a consequence, the blockage model and the computation of the received powers needs to be adapted. These modifications are detailed in the next sections.

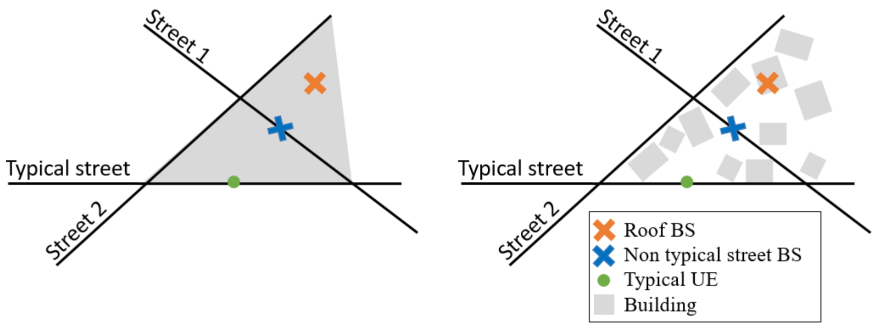

Fig. 3.10 Illustration of the difference between urban environments and sparser environments using the same street pattern. Left (urban): both BSs interact with the UE only by diffraction. Right (sparse): the same BSs now are in LOS conditions with the UE.

Modification of the blockage model

In this section, the blockage model for urban macrocells (UMa), suburban macrocells (SuMa) and rural macrocells (RMa) will be distinguished. As mentioned in [76], the LOS probability for roof tiers can be exactly computed as:

$$p_{L,B}(r) = \prod_{n=0}^{m} \left[1 - \exp\left(- \frac{\left(H_b + H_{b,k} - \frac{(n+\frac{1}{2})(\Delta H_b + H_{b,k})}{m+1}\right)^2}{2\gamma^2} \right) \right] \tag{3.19}$$

where $m = \text{floor}((r/1000)\sqrt{\alpha\beta} - 1)$, α is the built-up ratio, β is the buildings' density per km² and γ is the scale parameter assuming the building's heights are distributed following a Rayleigh distribution $f(H) = (H/\gamma^2)\exp(-H^2/2\gamma^2)$.

Assuming the UE's height is negligible with respect to the macro BSs' height, the LOS and NLOS probabilities can be approximated using a modified sigmoid function as:

$$p_{L,B}(r) = \frac{1}{1 + a\exp\left(- b\left(\text{atan}\left(\frac{H_b + H_{b,k}}{r}\right) - a\right)\right)} \tag{3.20}$$

and $p_{N,B}(r) = 1 - p_{L,B}(r)$ where a and b are the sigmoid parameters.

These parameters can be directly linked to the environments variables α, β and γ. Typical values for different environments are summarized in Tab. 3.1. The distance for which the LOS probability is equal to 0.1 is then highlighted. In comparison, these distances are repectively given by 233m, 658m and 2303m fo UMa, SuMa and RMa if the Winner 2 LOS probability is used [75]. Note that the Winner 2 LOS probabilities were only designed for a macro BS located at a 30m height while the considered model enables us to modify this BS height.

	Case	α	β	γ	a	b	h_{BS}	$d_{0.1}$
UMa	Normal	0.3	500	15	10.37	0.182	30m	153m
							70m	357m
	Dense	0.5	300	20	12.93	0.155	30m	110m
							70m	258m
	Highrise	0.5	300	50	26.18	0.124	30m	43m
							70m	104m
SuMa		0.1	750	8	4.64	0.327	30m	461m
							70m	1533m
RMa		0.05	200	8	1.76	1.66	30m	2213m
							70m	5162m

Table 3.1 Typical values for the LOS probability parameters in sparse environments.

As for typical street BSs, the probability for a BS in non typical streets to be in LOS conditions is given by $p_{L,NT}(r) = e^{-\beta_{\tilde{t}} r}$ ($\beta_{\tilde{t}} \in \mathbb{R}^+$) where r is the distance between this BS and the user. The NLOS probability is then given by $p_{N,NT}(r) = 1 - p_{L,NT}(r)$. To compute the $\beta_{\tilde{t}}$ factors for the different environments, we generate a virtual city with the corresponding (α, β, γ) parameters and evaluate the LOS condition for multiple links. Typical values are respectively given by 0.019, 0.012 and 0.004 for urban, suburban and rural environments.

Tiers modification and associated power computation

As already mentioned, roof BSs and non typical BS will now exclusively interact with the typical UE in LOS or NLOS conditions. Tiers $\Phi_{ld,(k,m)}$ ($l \in \Psi_l$), $\Phi_{lp,(k,m)}$ ($l \in \Psi_l$), $\Phi_{Bd,(k,m)}$ and $\Phi_{Bd,(k)}$ therefore disappear. Instead, the following tiers are considered:

- $\Phi_{l,(k,n,m)}$, the 1D HPPP of BSs located in street $l \in \Psi_l$, belonging to tier $\{k, n, m\}$. Its density is given by $\lambda_{l,(k,n,m)}(r) = p_{NT,m} p_{n,NT}(r) \lambda_k$.

- $\Xi_{NT,(k,n)}$, the NHPCLP of BSs located in non typical streets where each BS has a probability $p_{n,NT}(r)$ to be in (N)LOS conditions.
- $\Phi_{B,(k,n,m)}$, the 2D PPP of BSs located on the roofs and belonging to tier $\{k,n,m\}$. Its density is $\lambda_{B,(k,n,m)}(r) = p_{NT,m}p_{n,B}(r)\lambda_{b,k}$.
- $\Phi_{B,(k,n)}$, the 2D PPP of BSs located on the roofs and belonging to tier $\{k,n\}$. Its density is $\lambda_{B,(k,n)}(r) = p_{n,B}(r)\lambda_{b,k}$.

The power contributions received from tier $\Phi_{l,(k,n,m)}$ ($l \in \Psi_l$) are computed as the contributions received from typical street tiers.

3.4 Calibrating the model parameters

The section summarizes the global approach to calibrate the different parameters involved in this study. In particular, the propagation model parameters are adapted to the considered environment. Unless otherwise stated, similar values will be considered throughout the numerical analysis to provide the most realistic results.

3.4.1 Link budget parameters for the different types of cells

Tab. 3.2 gives typical values for the link budget parameters for macrocells, microcells and femtocells [77]. The beam half-width γ associated with the BS antenna gain is computed assuming a 13dB front-to-back ratio (i.e. main lobe/side lobe).

3.4.2 Line-of-sight probabilities

Tab. 3.3 gives typical values for the LOS β-factors introduced in Section 3.3.2. We will assume a typical macrocell BS height of 30m and a 2D distance d between the BS and the UE. These values are computed to minimize the RMSE observed with the considered model. The distance $d_{0.1}$ for which the LOS probability is equal to 0.1 is then highlighted.

These analytical models disregard the fact that a micro/macro BS is located in/along the UE's street. They were derived for a completely general BS for which only the 2D distance to the UE is known. In [78], they compared the Winner 2 formula to the LOS condition of BSs in a single street

	Macrocell	Microcell	Femtocell	Unit
Power P_k	31.5 to 43	33	21 to 23	dBm
BS antenna gain	16 to 18	4 to 6	2	dBi
EIRP	48.9 to 61	37 to 39	23 to 25	dBm
Corr. beam half-width γ	2.7 to 4.3	43.1 to 68.2	~ 90	deg
UE antenna gain	0 to 8	0 to 2	0 to 2	dBi
BS height H_k	30	6	3	m
UE height H_u	1.5	1.5	1.5	m
Receiver noise floor W (UE noise figure and thermal noise)	-96 to -99	-96 to -97	-97 to -99	dBm

Table 3.2 Typical values for the link budget parameters for the different types of cells.

	Model	$p_{LOS} =$	β	$d_{0.1}$
UMa	Winner	$\min(18/d, 1)(1 - \exp(-d/63)) + \exp(-d/63)$	0.009	237m
	[76]	$\frac{1}{10.37\exp\left(-0.182\left(\operatorname{atan}\left(\frac{h}{d}\right)-10.37\right)\right)}$	0.011	209m
UMi	Winner	$\min(18/d, 1)(1 - \exp(-d/36)) + \exp(-d/36)$	0.013	182m

Table 3.3 LOS probability parameters for urban environments

at 30GHz using ray tracing. Winner 2 channel models are shown to underestimate the real LOS probability inside the same street. Therefore, slightly lower values for the β-factors are considered as we know the considered BSs fall in the latter condition.

3.4.3 Path loss model parameters

The PL parameters selection is mainly based on the Winner 2 channel models [75] that were developed for the frequency range 2-6GHz. A general PL model is proposed as

$$\begin{aligned} PL &= A\log_{10}(d_{3D}[m]) + B + C\log_{10}(f[GHz]) \\ &= A\log_{10}(\sqrt{d_{2D}[m]^2 + \Delta H^2[m]}) + B + C\log_{10}(f[GHz]) \end{aligned} \quad (3.21)$$

where d_{2D} and d_{3D} are the 2D and 3D distances in meters between the transmitter and the receiver, $\Delta H = h_{BS} - h_{UE}$ is the height difference in meters between the transmitter and the receiver, f is the frequency in GHz and A, B, C are fitting parameters representing the PL exponent, the PL intercept and the PL frequency dependence. These are fixed based on measure campaigns conducted at the studied frequency range.

Note that Winner channel models consider a dual-slope model for LOS contributions. However, for mathematical tractability, our model has to be based on a single-slope model. In our calibration process, the PL model for small distances is taken into account. Unless the serving BS is located at distance bigger than the breakpoint distance, this leads to a slight deterioration of the SINR and a slight overestimation of the exposure level. In addition, in Winner channel models, a BS for which the LOS is temporarily blocked by traffic is considered as a LOS BS. Unlike in our model, a NLOS BS is a BS where the LOS is blocked by a building. Blockage due to urban furniture is considered in the shadowing term of Winner channel models.

Path Loss in urban environments

Tab. 3.4 summarizes PL parameters used in urban environments. Our model parameters are fixed to minimize the RMSE between our model and the Winner model on small distances. A graphical comparison of both models is proposed on Fig. 3.11.

Path loss in suburban environments

Tab. 3.5 summarizes PL parameters in suburban environments. As the measurements campaigns were only conducted for urban microcells, the PL parameters for surburban microcells are fixed based on the tendencies observed for urban macrocells. The PL parameters for rural microcells are similarly fixed.

Path loss in rural environments

Tab. 3.6 summarizes PL parameters in rural environments.

Path Loss in Indoor environments

Tab. 3.7 summarizes PL parameters for outdoor to indoor (O2I) and indoor to outdoor (IO2) scenarios. As the number of lines intersecting a segment of length d in a homogeneous Cox process is given by $2d\lambda_S$, the signal will penetrate on average $2d\lambda_S + 1$ pairs of external walls on a distance d. Assuming an average 20dB loss per penetrated wall, the loss due to external walls will be assumed to be equal to $40 + 80\lambda_{eff}d$ dB where λ_{eff} is the effective street density.

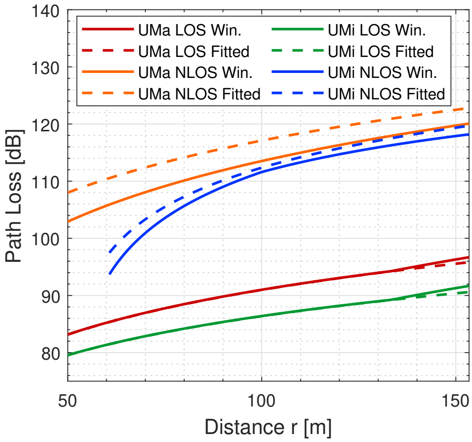

Fig. 3.11 Comparison of path losses: Winner model vs. our single-slope model fitted for $d < d'_{BP}$.

<table>
<tr><th>Scenario</th><th>Model</th><th>Path loss [dB]</th><th>Applicability range</th></tr>
<tr><td rowspan="2">UMa LOS</td><td rowspan="2">Winner</td><td>A=26, B=25, C=20</td><td>10m<d_{2D}<d'_{BP} [1)]</td></tr>
<tr><td>A=40, C=6,
B=9.28-14 $\log_{10}(h'_{UE}h'_{BS})$</td><td>$d'_{BP}$ <d_{2D}<5km</td></tr>
<tr><td colspan="4">In our model, this corresponds to (κ_L, α_L)=($10^{2.5} f^2$, 2.6)</td></tr>
<tr><td>UMa NLOS</td><td>Winner</td><td>A=44.9-6.55$\log_{10}(h_{BS})$, C=23,
B=18.38+5.83 $\log_{10}(h_{BS})$</td><td>50m<d_{2D}<5km</td></tr>
<tr><td colspan="4">In our model, this corresponds to (κ_D, α_D)=($f^{2.3}$, 3.1) for h_{BS}=30m
and to (κ_D, α_D)=($f^{2.3}$, 2.98) for h_{BS}=70m</td></tr>
<tr><td rowspan="2">UMi LOS</td><td rowspan="2">Winner</td><td>A=22.7, B=27, C=20</td><td>10m<d_{2D}<d'_{BP}</td></tr>
<tr><td>A=40, C=2.7,
B=7.56-17.3$\log_{10}(h'_{UE}h'_{BS})$</td><td>$d'_{BP}$<$d_{2D}$<5km</td></tr>
<tr><td colspan="4">In our model, this corresponds to (κ_L, α_L)=($10^{2.7} f^2$, 2.27)</td></tr>
<tr><td>UMi NLOS</td><td>Winner</td><td>$PL = \min(PL(d_1, d_2), PL(d_2, d_1))$
where $PL(d_k, d_l) =$
$\mathrm{PL}_{UMi,LOS}(d_k) + 20 - 12.5 n_j$
$+ 10 n_j \log_{10}(d_l) + 3 \log_{10}(f/5)$
and $n_j = \max(2.8 - 0.0024 d_k, 1.84)$</td><td>10m<$d_1$<5km [3)]
$w_S/2$<d_2<5km</td></tr>
<tr><td colspan="4">In our model, this corresponds to (κ_D, α_D)=($10^{3.07} f^{0.57}$, 2.37) for h_{UE}=1.5m</td></tr>
</table>

[1)] $d'_{BP} = 4h'_{BS}h'_{UE}f[Hz]/c$ where $h'_{BS} = h_{BS} - 1$m and $h'_{UE} = h_{UE} - 1$m.

[2)] $d'_{BP,3D} = \sqrt{d'^2_{BP} + \Delta H^2}$

[3)] d_1 , d_2 and w_S are resp. the Berg distances (cfr. L2 link type) and the street width.

Table 3.4 Path loss parameters for urban environments

Scenario	Model	Path loss [dB]	Applicability range
SuMa LOS	Winner	A=23.8, B=27.22, C=20	30m< $d_{2D} < d_{BP}$ 1)
		A=40, C=3.8, B=8.99-16.2 $\log_{10}(h'_{UE}h'_{BS})$	$d_{BP} < d_{2D}$ <5km
In **our model**, this corresponds to (κ_L, α_L)=($10^{2.72}f^2$,2.38)			
SuMa NLOS	Winner	A=44.9-6.55$\log_{10}(h_{BS})$, C=23, B=15.38+5.83 $\log_{10}(h_{BS})$	50m< d_{2D} <5km
In **our model**, this corresponds to (κ_N, α_N)=($10^{2.4}f^{2.3}$,3.52) for h_{BS}=30m			
SuMi LOS	**Ours**	Corr. to (κ_L, α_L)=($10^{2.92}f^2$,2.02)	/
SuMi NLOS	**Ours**	Corr. to (κ_N, α_N)=($10^{1.94}f^{2.13}$,3.53)	/

1) $d_{BP} = 4h_{BS}h_{UE}f[Hz]/c$.

Table 3.5 Path loss parameters for suburban environments

Scenario	Model	Path loss [dB]	Applicability range
RMa LOS	Winner	A=21.5, B=30.22, C=20	30m< $d_{2D} < d_{BP}$
		A=40, C=1.5, B=9.45-18.5 $\log_{10}(h'_{UE}h'_{BS})$	$d_{BP} < d_{2D}$ <5km
In **our model**, this corresponds to (κ_L, α_L)=($10^{3.02}f^2$,2.15)			
RMa NLOS	Winner	A=25.11 -0.13$\log_{10}(h_{BS}-25)$ B=40.51+0.26$\log_{10}(h_{BS}-25)$ -0.9(h_{UE}-1.5), C=21.3	50m< d_{2D} <5km
In **our model**, this corresponds to (κ_N, α_N)=($10^{4.07}f^{2.13}$,2.49) for h_{BS}=30m and h_{UE}=1.5m			
RMi LOS	**Ours**	Corr. to (κ_L, α_L)=($10^{3.22}f^2$,1.8)	/
RMi NLOS	**Ours**	Corr. to (κ_N, α_N)=($10^{3.61}f^{1.96}$,2.5)	/

Table 3.6 Path loss parameters for rural environments

Scenario	Model	Path loss [dB]	Applicability range
I2O/O2I	Winner	$\mathrm{PL}_{UMiLOS}(d_{out}+d_{in})+0.5d_{in}$ $+14+15(1-\cos(\theta))^2$	3m< $d_{in}+d_{out}$ <1km
In **our model**, this corresponds to $(\kappa_{\tilde{i}}, \alpha_{\tilde{i}}, K_{in})$=($10^{6.7}f^2$,2.27,$10^{-8\lambda_{eff}-0.05}$) for O2O and $(\kappa_{\tilde{i}}, \alpha_{\tilde{i}}, K_{in})$=($10^{4.7}f^2$,2.27,$10^{-8\lambda_{eff}-0.05}$) for I2O/O2I.			

Table 3.7 Path loss parameters for indoor environments

4

Derivation of network-level performance metrics

SINCE Shannon's work on the channel capacity [79], the received SINR has been the reference measure to assess the channel quality. Unsurprisingly, most commonly studied network-level performance metrics are generally closely related to it. For instance, one can mention the coverage probability (i.e. the probability to exceed a given SINR thershold) as one of the most popular metrics in stochastic geometry. In this chapter, some of these SINR-based metrics are introduced. Moreover, with raising concerns on the exposure level due to densification, the available panel of metrics is extended to include exposure-based metrics. The analytical expression of all defined metrics is derived. When necessary, the impact of the doubly-stochastic model on the considered mathematical expression is highlighted. In this way, the performance of the network model described in the previous chapter can be fully characterized no matter how the street pattern is generated.

4.1 Notations and Abbreviations

In the following developments, several mathematical expressions will involve multiple summations or products, performed over the different tiers $\{k, n, m\}$. For this reason, the following abbreviations are defined:

$$\sum_{\{j,k,n,m\}} \quad \text{as abbreviation for} \quad \sum_{j=\{S,B\}} \sum_{k=1}^{K} \sum_{n=\{N,L\}} \sum_{m=1}^{2}$$

$$\prod_{\{j,k,n,m\}} \quad \text{as abbreviation for} \quad \prod_{j=\{S,B\}} \prod_{k=1}^{K} \prod_{n=\{N,L\}} \prod_{m=1}^{2}$$

where $K = K_S$ for street tiers and $K = K_B$ for roof tiers. Indexes S and B are respectively used to characterize street tiers and roof tiers.

Remark 4.1. Removing one of the summation/product abbreviations indexes removes the corresponding summation/product. For instance, $\sum_{\{k,n\}}$ will be the abbreviation for $\sum_{k=1}^{K} \sum_{n=\{N,L\}}$.

4.2 Useful distance distributions

In this section, different useful distance distributions will be derived. These distributions are prequisited as they will be repeatedly used in the mathematical expressions of the studied metrics.

4.2.1 Distance distributions in case of blockage

This section will provide the CCDFs and PDFs expressions of the closest LOS and NLOS nodes for 1D and 2D HPPPs given the studied blockage models. The general proof for these distributions relies on the thinning property of PPPs. Let us assume (1) a 1D HPPP of density λ_1 thinned with a distance-dependent probability $p_1(r)$ and (2) a 2D HPPP of density λ_2 thinned with a distance- and angular-dependent probability $p_2(r, \theta)$.

By definition of the void probability [80], the CDF of the closest node in the considered HPPPs are then respectively given by:

$$F_{R,1}(r) = 1 - \exp\left(- \int_0^r 2\lambda_1(r')dr' \right) \tag{4.1}$$

$$F_{R,2}(r) = 1 - \exp\left(- \int_0^r \int_0^{2\pi} \lambda_2(r',\theta)r'd\theta dr' \right). \tag{4.2}$$

where $\lambda_1(r) = \lambda_1 p_1(r)$ and $\lambda_2(r,\theta) = \lambda_2 p_2(r,\theta)$.

The corresponding PDF is then obtained by taking the derivative of these expressions. For 2D HPPPs, it gives:

$$f_{R,2}(r) = \int_0^{2\pi} \lambda_2(r,\theta)rd\theta \times \exp\left(- \int_0^r \int_0^{2\pi} \lambda_2(r',\theta)r'd\theta dr' \right). \tag{4.3}$$

4.2.2 Distance distributions for typical street base stations

Let us define the distance $R_{T,k,n}$ to be the distance to the closest node of tier $\Phi_{T,k,n}$ in a given realization.

Lemma 4.2. *The PDF and CCDF of the distances $R_{T,k,N}$ between the UE and the closest BS of tiers $\Phi_{T,(k,N)}$ are respectively given by:*

$$\underline{PDF:} \quad f_{C,R_{T,k,N}}(r) = 2\lambda_k\left(1 - e^{-\beta_s r}\right) \exp\left(\frac{-2\lambda_k}{\beta_s}\left[e^{-\beta_s r} - 1\right] - 2\lambda_k r \right) \tag{4.4}$$

$$\underline{CCDF:} \quad \bar{F}_{C,R_{T,k,N}}(r) = \exp\left(\frac{-2\lambda_k}{\beta_s}\left[e^{-\beta_s r} - 1\right] - 2\lambda_k r \right). \tag{4.5}$$

The modified (M) PDF and CCDF of the distances $R_{T,k,L}$ between the UE and the closest BS of tiers $\Phi_{T,(k,L)}$ are respectively given by:

$$\underline{MPDF:} \quad f_{C,R_{T,k,L}}(r) = 2\lambda_k \exp\left(\frac{-2\lambda_k}{\beta_s}\left[1 - e^{-\beta_s r}\right] - \beta_s r \right) \tag{4.6}$$

$$\underline{MCCDF:} \quad \bar{F}_{C,R_{T,k,L}}(r) = \exp\left(\frac{-2\lambda_k}{\beta_s}\left[1 - e^{-\beta_s r}\right] \right) \tag{4.7}$$

Proof. This follows from Eq. (4.1) knowing $\lambda_{T,(k,L)}(r)$ and $\lambda_{T,(k,N)}(r)$ defined in Section 3.3.3. The MCDF does not mathematically converge to 1 and the integral of the MPDF on its domain is not equal to 1. Yet, their use enables us to compact some of the incoming mathematical expressions.

□

4.2.3 Distance distributions for roof base stations in urban environments

Lemma 4.3. *The PDFs and CCDFs of the distances $R_{B,k,n}$ and $R_{Bd,k}$ between the UE and the closest BS of tiers $\Phi_{B,(k,n)}$ and $\Phi_{Bd,(k)}$ are respectively given by:*

$$\underline{PDF:} \quad f_{C,R_{B,k,n}}(r) = \begin{cases} 2\lambda_{b,k} f_1(r) p_n(r) r \exp\left[-\int_0^r 2\lambda_{b,k} f_1(r') p_n(r') r' dr'\right] \\ \qquad\qquad\qquad\qquad \text{for} \quad r \leq r'_c \\ 4\lambda_{b,k} f_2(r) p_n(r) r \exp\left[-\int_0^{r'_c} 2\lambda_{b,k} f_1(r') p_n(r') r' dr' \right. \\ \qquad \left. - \int_{r'_c}^r 4\lambda_{b,k} f_2(r') p_n(r') r' dr'\right], \text{otherwise} \end{cases} \tag{4.8}$$

$$f_{C,R_{Bd,k}}(r) = \begin{cases} 4\lambda_{b,k} \frac{r^2}{r'_c} \exp\left[-\frac{4}{3}\lambda_{b,k} \frac{r^3}{r'_c}\right] \quad \text{for} \quad r \leq r'_c \\ 2\lambda_{b,k} f_3(r) r \exp\left[-\frac{4}{3}\lambda_{b,k} r'^2_c \right. \\ \qquad \left. - \int_{r'_c}^r 2\lambda_{b,k} f_3(r') r' dr'\right], \text{otherwise} \end{cases} \tag{4.9}$$

$$\underline{CCDF:} \quad \overline{F}_{C,R_{B,k,n}}(r) = \begin{cases} \exp\left[-\int_0^r 2\lambda_{b,k} f_1(r') p_n(r') r' dr')\right] \quad \text{for} \quad r \leq r'_c \\ \exp\left[-\int_0^{r'_c} 2\lambda_{b,k} f_1(r') p_n(r') r' dr' \right. \\ \qquad \left. - \int_{r'_c}^r 4\lambda_{b,k} f_2(r') p_n(r') r' dr'\right], \text{otherwise} \end{cases} \tag{4.10}$$

$$\overline{F}_{C,R_{Bd,k}}(r) = \begin{cases} \exp\left[-\frac{4}{3}\lambda_{b,k} \frac{r^3}{r'_c}\right] \quad \text{for} \quad r \leq r'_c \\ \exp\left[-\frac{4}{3}\lambda_{b,k} r'^2_c - \int_{r'_c}^r 2\lambda_{b,k} f_3(r') r' dr'\right], \text{otherwise} \end{cases} \tag{4.11}$$

where

$$f_1(r) = \pi - 2r r'^{-1}_c$$
$$f_2(r) = \sqrt{r^2 r'^{-2}_c - 1} - r r'^{-1}_c + \text{arccsc}\left(r r'^{-1}_c\right)$$
$$f_3(r) = \pi - 2\sqrt{r^2 r'^{-2}_c - 1} + 2r r'^{-1}_c - 2\arcsin\left(r'_c r^{-1}\right)$$

and $r'_c = \frac{w_s}{\Delta H_b}(\Delta H_b + H_{b,k})$, $p_L(r) = exp(-\beta_B r)$, $p_N(r) = 1 - p_L(r)$ *are respectively the modified critical distance value and the roof BS LOS and NLOS probabilities.*

Proof. This comes from Eq. (4.2) using $\lambda_{B,(k,n)}(r,\theta)$ and $\lambda_{Bd,(k)}(r,\theta)$ defined in Section 3.3.3. The PDFs are then obtained by means of Eq. (4.3). □

4.2.4 Distance distributions in non typical streets

Knowing the BS density is λ_k, the PDFs and CCDFs of the distances $R_{NT,k}$ between the UE and the closest BS of tier $\Xi_{NT,(k)}$ are given by Eq. (2.13) and (2.14) if a NHPCLP is used and by Eq.(2.15) and (2.16) if a NHPSP/NHPLM is used. The notations of these equations will be used in the following developments. As non typical street tiers are always linked by the street realization, deriving the joint distance distributions is required for the computation of the association probabilities.

Lemma 4.4. *For the NHPCLP, the joint CCDF of the distances $R_{NT,k}, \forall k \in$ {1-K_S} is given by:*

$$\begin{aligned}
&\overline{F}_{J,NT}(\theta_1, ..., \theta_{K_S}) \\
&\triangleq \mathbb{P}\Big(R_{NT,1} \geq \theta_1, ..., R_{NT,K_S} \geq \theta_{K_S}\Big) \\
&= \exp\left(- \lambda_s \int_0^{\infty} \int_0^{2\pi} \Big[1 - \prod_{\{k\}} \tilde{\mathcal{Z}}_1(\theta_k, \rho, \lambda_k)\Big] p(\rho,\theta) d\theta d\rho \right). \qquad (4.12)
\end{aligned}$$

Proof. The proof is available in Appendix A. Note that $\tilde{\mathcal{Z}}_1(\theta_k, \rho, \lambda_k)$ is a mofidied version of $\mathcal{Z}_1(\theta_k, \rho, \lambda_k)$ where the result is replaced by 1 if it is imaginary. □

Lemma 4.5. *For the NHPSP/NHPLM, the joint CCDF of the distances $R_{NT,k}, \forall k \in$ {1-K_S} is given by:*

$$\begin{aligned}
&\overline{F}_{J,NT}(\theta_1, ..., \theta_{K_S}) \\
&= \exp\left(\lambda_s \int_0^{\infty} \int_0^{\pi} \int_0^{2\pi} \int_0^{r+h} \Big[1 - \prod_{\{k\}} \tilde{\mathcal{Z}}_2(\theta_k, \rho, \phi, \theta, \lambda_k)\Big] p(\rho,\phi) f_\Theta(\theta) f_H(h) dA \right). \qquad (4.13)
\end{aligned}$$

Proof. The proof is similar to the proof of the previous lemma. Note that $\tilde{\mathcal{Z}}_2(\theta_k, \rho, \phi, \theta, \lambda_k)$ is equivalently defined. □

Let us now introduce the notation $\{k,n\}^*$ as the collection of all combinations $\{k,n\}$ unless the serving one $\{k^*,n^*\}$. When no LOS condition is considered (i.e. for tiers $\Phi_{Bd,k}$ and $\Xi_{NT,k}$), it becomes $\{k\}^*$.

Lemma 4.6. *For the NHPCLP, conditioned on the distance r to the closest node of serving tier $\Xi_{NT,(k^*)}$, the joint modified CCDF of the distances $R_{NT,k}$, $\forall k \in$ {1-$k^* - 1$,k^*+1-K_S} is given by:*

$$\overline{F}_{m,J,NT}(\theta_1, ..., \theta_K, r) = \int_0^\infty \Big[\prod_{\{k\}^*} \tilde{\mathcal{Z}}_1(\theta_k, y^*, \lambda_k)\Big] f_{C,R}(y^*|r) dy^*$$
$$\exp\left(- \int_0^\infty \int_0^{2\pi} \Big[1 - \prod_{\{k\}^*} \tilde{\mathcal{Z}}_1(\theta_k, \rho, \lambda_k)\Big] \lambda_s(\rho) p(\rho, \theta) d\theta d\rho \right). \tag{4.14}$$

where $f_{C,R}(y^*|r)$ is given by Eq. (2.12) and $\lambda_s(\rho) = \lambda_s \tilde{\mathcal{Z}}_1(r, \rho, \lambda_{k^*})$ if $\rho < r$ and λ_s elsewhere.

Proof. The proof is available in Appendix B. □

Lemma 4.7. *For the NHPSP/NHPLM, conditioned on the distance r to the closest node of serving tier $\Xi_{NT,(k^*)}$, the joint modified CCDF of the distances $R_{NT,k}$, $\forall k$ $\in$ {1-$k^* - 1$,k^*+1-K_S} is given by:*

$$\overline{F}_{m,J,NT}(\theta_1, ..., \theta_K, r) = \int_0^\infty \Big[\prod_{\{k\}^*} \tilde{\mathcal{Z}}_2(\theta_k, y^*, \phi\theta, \lambda_k)\Big] f_{2,C,R}(y^*|r) dy^*$$
$$\exp\left(\int_0^\infty \int_0^\pi \int_0^{2\pi} \int_0^{r+h} \Big[1 - \prod_{\{k\}^*} \tilde{\mathcal{Z}}_2(\theta_k, \rho, \phi, \theta, \lambda_k)\Big] \lambda_{s,2}(\rho) p(\rho, \phi) f_\Theta(\theta) f_H(h) dA \right). \tag{4.15}$$

where $f_{2,C,R}(y^*|r)$ is based on Eq. (2.12) and is adapted to the NHPSP/NHPLM using the corresponding distributions. As in the previous lemma, $\lambda_{s,2}(\rho) = \lambda_s \tilde{\mathcal{Z}}_2(r, \rho, \phi, \theta, \lambda_{k^*})$

Proof. The proof is similar to the proof of the previous lemma. □

4.2.5 Distance distributions in surburban and rural environments

In sparser environments, the PDFs and CCDFs of the distances $R_{B,k,n}$ between the UE and the closest BS of tiers $\Phi_{B,(k,n)}$ are adapted using Eq. (3.20) , (4.2) and (4.3). Furthermore, Eqs. (2.13), (2.14), (2.15) and (2.16) can be slightly adapted to compute the PDFs and CCDFs of the distances $R_{NT,k,n}$ between the UE and the closest BS of tier $\Xi_{NT,(k,n)}$. In that case, $\mathcal{Z}_1(r, \rho, \lambda_b)$

and $\mathcal{Z}_2(r,\rho,\phi,\theta,\lambda_b)$ are modified as:

$$\mathcal{Z}_{1,n}(r,\rho,\lambda_b) = \exp\Big(-2\lambda_b \int_0^{\sqrt{r^2-\rho^2}} p_{n,NT}\Big(\sqrt{\rho^2+t^2}\Big)dt\Big) \tag{4.16}$$

$$\mathcal{Z}_{2,n}(r,\rho,\phi,\theta,\lambda_b) = \exp\Big(-\lambda_b \int_0^{l(r,\phi,\rho,\theta)} p_{n,NT}\Big(\sqrt{\rho^2+t^2}\Big)dt\Big) \tag{4.17}$$

where $p_{n,NT}(r)$ are the LOS probabilities for non typical streets defined in Section 3.3.9. Note that this modification is equivalently done for the joint distributions.

4.3 Useful preference thresholds

This section will introduce the reader to several distance thresholds from which a particular tier is preferred to another one. This will enhance the conciseness of the mathematical expressions in this document. These thresholds will be derived for the case where the biased strongest average received power association rule is used.

Knowing the serving distance r, we will denote $z_{T,(k,n)}^{T,(k^*,n^*)}(r)$, the distance threshold from which the serving tier $\Phi_{T,(k^*,n^*)}$ is preferred to the tier $\Phi_{T,(k,n)}$. According to the association rule, the value is computed to satisfy the condition $P_{k^*}B_{T,k^*,n^*}L_{k^*,n^*}^{-1}(r) > P_k B_{T,k,n} L_{k,n}^{-1}(R_{k,n})$ where $B_{T,k,n}$ is the bias factor for street tier $\{k,n\}$. Let us introduce the biased power as $\mathcal{P}_{T,k,n} = P_k B_{T,k,n}$. This metric can be similarly computed for other tiers. Using the PL model for L1 link type, the distance threshold is given by:

$$z_{T,(k,n)}^{T,(k^*,n^*)}(r) = \sqrt{\left[\frac{\mathcal{P}_{T,k,n}L_{k^*,n^*}(r)}{\kappa_n \mathcal{P}_{T,k^*,n^*}}\right]^{\frac{2}{\alpha_{k,n}}} - \Delta H_k^2}. \tag{4.18}$$

Remark 4.8. Note that the above expression can become imaginary if the argument of the square root is negative. In that case, it is automatically reduced to 0 as the preference threshold only takes real values. This stands for any of the following thresholds.

Using the PL model for L2 and L3 link types, the distance thresholds for typical street tiers with respect to roof tiers interacting by diffraction (Bd) and to non typical street tiers (NT) can be similarly computed. The following values are thus introduced:

- the distance threshold from which tier $\Phi_{T,(k^*,n^*)}$ is preferred to roof tier $\Phi_{Bd,(k)}$ given by

$$z_{Bd,(k)}^{T,(k^*,n^*)}(r) = \sqrt{\left[\frac{1}{1+q_{\frac{\pi}{2}}\Delta H_b}\left(\left[\frac{\mathcal{P}_{Bd,k}L_{k^*,n^*}(r)}{\kappa_d \mathcal{P}_{T,k^*,n^*}}\right]^{\frac{1}{\alpha_{k,d}}} - \Delta H_b\right)\right]^2 - H_{b,k}^2}. \tag{4.19}$$

- the distance threshold from which tier $\Phi_{T,(k^*,n^*)}$ is preferred to tier $\Xi_{NT,(k)}$ given by

$$z_{NT,(k)}^{T,(k^*,n^*)}(r) = \sqrt{\left(\mathcal{Q}^{-1}\mathcal{W}\left[\mathcal{Q}\left(\frac{\mathcal{P}_{T,k^*,n^*}L_{k^*,n^*}^{-1}(r)}{\mathcal{P}_{NT,k}\kappa_{\tilde{t}}^{-1}}\right)^{-\frac{1}{\alpha_{\tilde{t},k}}}\right]\right)^2 - \Delta H_k^2} \tag{4.20}$$

where $\mathcal{Q} = -\frac{\ln(K_{in})}{\alpha_{\tilde{t},k}}$ and $\mathcal{W}(\cdot)$ is the Lambert W function.

- the distance thresholds $z_{T,(k,n)}^{Bd,(k^*)}(r)$, $z_{T,(k,n)}^{B,(k^*,n^*)}(r)$ and $z_{T,(k,n)}^{NT,(k^*)}(r)$ from which tiers $\Phi_{Bd,(k^*)}$, $\Phi_{B,(k^*,n^*)}$ and $\Xi_{NT,(k^*)}$ are preferred to tier $\Phi_{T,(k,n)}$ are retrieved from Eq. (4.18) using the following respective transformations
  - $L_{k^*,n^*}(r) \mapsto L_{k^*,d}(r)$ and $\mathcal{P}_{T,k^*,n^*} \mapsto \mathcal{P}_{Bd,k^*}$
  - $\mathcal{P}_{T,k^*,n^*} \mapsto \mathcal{P}_{B,k^*,n^*}$ and an adaptation of the PL model $L_{k^*,n^*}(r)$ to roof BSs as mentioned in Section 3.3.5
  - $L_{k^*,n^*}(r) \mapsto L_{k^*,\tilde{t}}(r)$ and $\mathcal{P}_{T,k^*,n^*} \mapsto \mathcal{P}_{NT,k^*}$.

- the distance thresholds $z_{Bd,(k)}^{Bd,(k^*)}(r)$, $z_{Bd,(k)}^{B,(k^*,n^*)}(r)$ and $z_{Bd,(k)}^{NT,(k^*)}(r)$ from which tiers $\Phi_{Bd,(k^*)}$, $\Phi_{B,(k^*,n^*)}$ and $\Xi_{NT,(k^*)}$ are preferred to tier $\Phi_{Bd,(k)}$ are computed by means of Eq. (4.19) using the same respective transformations.

- the distance thresholds $z_{NT,(k)}^{Bd,(k^*)}(r)$, $z_{NT,(k)}^{B,(k^*,n^*)}(r)$ and $z_{NT,(k)}^{NT,(k^*)}(r)$ from which tiers $\Phi_{Bd,(k^*)}$, $\Phi_{B,(k^*,n^*)}$ and $\Xi_{NT,(k^*)}$ are preferred to tier $\Xi_{NT,(k)}$ are computed by means of Eq. (4.20) using the same respective transformations.

- the distance thresholds $z_{B,(k,n)}^{T,(k^*,n^*)}(r)$, $z_{B,(k,n)}^{Bd,(k^*)}(r)$, $z_{B,(k,n)}^{B,(k^*,n^*)}(r)$ and $z_{B,(k,n)}^{NT,(k^*)}(r)$ from which tiers $\Phi_{T,(k^*,n^*)}$, $\Phi_{Bd,(k^*)}$, $\Phi_{B,(k^*,n^*)}$ and $\Xi_{NT,(k^*)}$ are preferred to tier $\Xi_{B,(k,n)}$ are computed by means of Eq. (4.18) using the same respective transformations for the three latter tiers and by applying the additional transformations $\mathcal{P}_{T,k,n} \mapsto \mathcal{P}_{B,k,n}$ and $\Delta H_k \mapsto \Delta H_b + H_{b,k}$.

Remark 4.9. In sparser environment, tiers $\Xi_{NT,(k,n)}$ are treated as tiers $\Phi_{T,(k,n)}$. Only the PL coefficients need to be adapted in case they take different values.

Remark 4.10. If the strongest average received power association rule is used instead, all biased powers in the threshold expressions become the simple tiers powers.

Remark 4.11. If the nearest neighbour cell association rule is used instead, all thresholds can be fixed to r. Remember this rule is only used in a single-tier scenario hence the fact that the antenna height is not taken into account.

4.4 Association probabilities

In this section, the probabilities that the typical UE associates itself to a particular tier are derived. Remember from Section 3.3.6 that the UE can associate itself to any of the following tiers: $\Phi_{T,(k,n)}$, $\Phi_{B,(k,n)}$, $\Phi_{Bd,(k)}$ and $\Xi_{NT,(k)}$ ($\Xi_{NT,(k,n)}$ in sparser environments). The association probabilities for each of these tiers are derived hereafter. In the following computations, it is assumed that $k \in$\{1-N_S\}, $k' \in$\{1-N_B\} and $n \in \{L, N\}$.

Lemma 4.12. *The association probability for tier $\Phi_{T,(k^*,n^*)}$:*

$$\begin{aligned}
\mathcal{A}_{T,k^*,n^*} = &\int_0^\infty \prod_{\{k,n\}^*} F_{C,R_{T,k,n}}\left(z_{T,(k,n)}^{T,(k^*,n^*)}(r)\right) \prod_{\{k'\}} F_{C,R_{Bd,k'}}\left(z_{Bd,(k')}^{T,(k^*,n^*)}(r)\right) \\
&\prod_{\{k',n\}} F_{C,R_{B,k',n}}\left(z_{B,(k',n)}^{T,(k^*,n^*)}(r)\right) \\
&F_{J,NT}\left(z_{NT,(1)}^{T,(k^*,n^*)}(r),\ldots,z_{NT,(N_S)}^{T,(k^*,n^*)}(r)\right) f_{C,R_{T,k^*,n^*}}(r)dr \\
= &\int_0^\infty \Omega_{T,k^*,n^*}(r) f_{C,R_{T,k^*,n^*}}(r)dr
\end{aligned}$$

Proof. The proof is available in Appendix C. □

The association probabilities for the other considered tiers are then similarly computed.

Lemma 4.13. *The association probability for tier* $\Phi_{B,(k^*,n^*)}$*:*

$$\begin{aligned}\mathcal{A}_{B,k^*,n^*} = \int_0^\infty & \prod_{\{k,n\}} F_{C,R_{T,k,n}}\left(z^{B,(k^*,n^*)}_{T,(k,n)}(r)\right) \prod_{\{k'\}} F_{C,R_{Bd,k'}}\left(z^{B,(k^*,n^*)}_{Bd,(k')}(r)\right) \\ & \prod_{\{k',n\}^*} F_{C,R_{B,k',n}}\left(z^{B,(k^*,n^*)}_{B,(k',n)}(r)\right) \\ & F_{J,NT}\left(z^{B,(k^*,n^*)}_{NT,(1)}(r), \ldots, z^{B,(k^*,n^*)}_{NT,(N_S)}(r)\right) f_{C,R_{B,k^*,n^*}}(r)dr \\ = \int_0^\infty & \Omega_{B,k^*,n^*}(r) f_{C,R_{B,k^*,n^*}}(r)dr\end{aligned}$$

Lemma 4.14. *The association probability for tier* $\Phi_{Bd,(k^*)}$*:*

$$\begin{aligned}\mathcal{A}_{Bd,k^*} = \int_0^\infty & \prod_{\{k,n\}} F_{C,R_{T,k,n}}\left(z^{Bd,(k^*)}_{T,(k,n)}(r)\right) \prod_{\{k'\}^*} F_{C,R_{Bd,k'}}\left(z^{Bd,(k^*)}_{Bd,(k')}(r)\right) \\ & \prod_{\{k',n\}} F_{C,R_{B,k',n}}\left(z^{Bd,(k^*)}_{B,(k',n)}(r)\right) \\ & F_{J,NT}\left(z^{Bd,(k^*)}_{NT,(1)}(r), \ldots, z^{Bd,(k^*)}_{NT,(N_S)}(r)\right) f_{C,R_{Bd,k^*}}(r)dr \\ = \int_0^\infty & \Omega_{Bd,k^*}(r) f_{C,R_{Bd,k^*}}(r)dr\end{aligned}$$

Lemma 4.15. *The association probability for tier* $\Xi_{NT,(k^*)}$*:*

$$\begin{aligned}\mathcal{A}_{NT,k^*} = \int_0^\infty & \prod_{\{k,n\}} F_{C,R_{T,k,n}}\left(z^{NT,(k^*)}_{T,(k,n)}(r)\right) \prod_{\{k'\}} F_{C,R_{Bd,k'}}\left(z^{NT,(k^*)}_{Bd,(k')}(r)\right) \\ & \prod_{\{k',n\}} F_{C,R_{B,k',n}}\left(z^{NT,(k^*)}_{B,(k',n)}(r)\right) \\ & F_{m,J,NT}\left(z^{NT,(k^*)}_{NT,(1)}(r), \ldots, z^{NT,(k^*)}_{NT,(N_S)}(r), r\right) f_{C,R_{NT,k^*}}(r)dr \\ = \int_0^\infty & \Omega_{NT,k^*}(r) f_{C,R_{NT,k^*}}(r)dr\end{aligned}$$

4.5 Serving base station distance distributions

Compared to the distance distributions of the closest BS of each tier, the PDF derived in this section now takes into account the fact that the considered BS has been selected according to the association rule. This section is thus particularly useful if the (biased) strongest average received power association rule is used.

Lemma 4.16. *If the serving BS belongs to tier $\Phi_{T,(k^*,n^*)}$, then the serving distance PDF is given by:*

$$f_{S,R_{T,k^*,n^*}}(r) = \frac{1}{\mathcal{A}_{T,k^*,n^*}} \Omega_{T,k^*,n^*}(r) f_{C,R_{T,k^*,n^*}}(r). \tag{4.21}$$

Proof. The proof is available in Appendix D. □

Similarly, we compute the other PDFs as:

Lemma 4.17. *If the serving BS belongs to tier $\Phi_{B,(k^*,n^*)}$, then the serving distance PDF is given by:*

$$f_{S,R_{T,k^*,n^*}}(r) = \frac{1}{\mathcal{A}_{B,k^*,n^*}} \Omega_{B,k^*,n^*}(r) f_{C,R_{B,k^*,n^*}}(r). \tag{4.22}$$

Lemma 4.18. *If the serving BS belongs to tier $\Phi_{Bd,(k^*)}$, then the serving distance PDF is given by:*

$$f_{S,R_{Bd,k^*}}(r) = \frac{1}{\mathcal{A}_{Bd,k^*}} \Omega_{Bd,k^*}(r) f_{C,R_{Bd,k^*}}(r). \tag{4.23}$$

Lemma 4.19. *If the serving BS belongs to tier $\Xi_{NT,(k^*)}$, then the serving distance PDF is given by:*

$$f_{S,R_{NT,k^*}}(r) = \frac{1}{\mathcal{A}_{NT,k^*}} \Omega_{NT,k^*}(r) f_{C,R_{NT,k^*}}(r). \tag{4.24}$$

Remark 4.20. If one of the selectable tiers is not serving anymore, the factor associated to that tier in the association probabilities mathematical expressions and in the serving distance PDF mathematical expressions disappears. As an example, if a UE can only be served by a typical street tier then the association probability and the serving distance PDF become:

$$\mathcal{A}_{T,k^*,n^*} = \int_0^\infty \prod_{\{k,n\}^*} F_{C,R_{T,k,n}}\left(z_{T,(k,n)}^{T,(k^*,n^*)}(r)\right) f_{C,R_{T,k^*,n^*}}(r) dr$$

$$f_{S,R_{T,k^*,n^*}}(r) = \frac{1}{\mathcal{A}_{T,k^*,n^*}} \prod_{\{k,n\}^*} F_{C,R_{T,k,n}}\left(z_{T,(k,n)}^{T,(k^*,n^*)}(r)\right) f_{C,R_{T,k^*,n^*}}(r).$$

4.6 Characteristic functions of the different contributions

In this section, we will provide the CFs for the contributions coming from all different tiers. By definition, $\phi_F(t;\iota)$ is introduced as the general fading distribution CF where ι is the distribution parameter. Depending on the desired fading distibution, it is given by one of the fading CFs available in Section 3.3.4. This CF is thus respectively given by $\phi_{Ri}(t;0)$, $\phi_{Ri}(t;K)$ or $\phi_{Na}(t;m)$ if Rayleigh, Rician or Nakagami-m fading is assumed.

4.6.1 Useful signal power level

Lemma 4.21. *The CF of the useful signal power level S knowing the serving tier is tier $\Phi_{T,(k^*,n^*)}$ is computed as:*

$$\phi_S^{T,(k^*,n^*)}(t|r) = \phi_F\left(P_k G_1 L_{k^*,n^*}^{-1}(r)t;\iota\right). \tag{4.25}$$

Proof. This comes from averaging the useful signal power over the fading channel power by means of the fading distribution CF. □

The CF of the useful signal power level can then be generalized to the cases where tiers $\Phi_{B,(k^*,n^*)}$, $\Phi_{Bd,(k^*)}$ or $\Xi_{NT,(k^*)}$ are serving. One only needs to use the appropriate PL model and emit power.

4.6.2 Contributions coming from the typical street

Lemma 4.22. *The CF of the interference $I_{T,k,n,m}$ coming from tier $\Phi_{T,(k,n,m)}$ knowing the serving tier is tier $\Phi_{T,(k^*,n^*)}$ is computed as*

$$\phi_{T,(k,n,m)}^{T,(k^*,n^*)}(t|r) = \exp\left[2\int_{z_{T,(k,n)}^{T,(k^*,n^*)}(r)}^{\infty}\left[\phi_F\left(P_k G_m L_{k,n}^{-1}(r')t;\iota\right) - 1\right]\lambda_{T,(k,n,m)}(r')dr'\right]. \tag{4.26}$$

Proof. The proof is available in Appendix E. □

Remark 4.23. The CF of the interference is here given assuming another typical street tier is serving. If another type of tier is serving, only the preference threshold needs to be adapted. All other preference tresholds are available in Section 4.3. This remark applies to all CFs in this document.

4.6.3 Contributions coming from roof BSs

Using a similar approach, the CF for contributions coming from roof BSs can be easily derived.

Lemma 4.24. *The CF of the interference $I_{B,k,n,m}$ coming from tier $\Phi_{B,(k,n,m)}$ knowing the serving tier is tier $\Phi_{T,(k^*,n^*)}$ is computed as*

$$\phi_{B,(k,n,m)}^{T,(k^*,n^*)}(t|r) = \exp\left[\int_{z_{T,(k,n)}^{B,(k^*,n^*)}(r)}^{\infty}\int_{0}^{2\pi}\left[\phi_F\left(P_k G_m L_{k,n}^{-1}(r')t;\iota\right)-1\right]\lambda_{B,(k,n,m)}(r',\theta)r'd\theta dr'\right]. \tag{4.27}$$

Corollary 4.25. *With no angular dependency on the density, it becomes:*

$$\phi_{B,(k,n,m)}^{T,(k^*,n^*)}(t|r) = \exp\left[2\pi\int_{z_{T,(k,n)}^{B,(k^*,n^*)}(r)}^{\infty}\left[\phi_F\left(P_{b,k} G_m L_{k,n}^{-1}(r')t;\iota\right)-1\right]\lambda_{B,(k,n,m)}(r')r'dr'\right]. \tag{4.28}$$

Note that the CF of the interference $I_{Bd,d,k,m}$ coming from tier $\Phi_{Bd,(k,m)}$ is similarly obtained by adapting the density function to $\lambda_{Bd,(k,m)}(r',\theta)$.

4.6.4 Contributions coming from non typical streets

Due to the linear dependency of the tiers located on non typical streets, all tiers need to be jointly considered.

Lemma 4.26. *If the street pattern is drawn by a NHPLCP, the CF of the interference $I_{NT,d} = \sum_{\{k,m\}} I_{NT,d,k,m}$ coming from tiers $\Phi_{ld,k,m}, \forall l$ by corner diffraction is given by*

$$\phi_D(t) = \exp\left[-\lambda_s\int_0^{\infty}\int_0^{2\pi} 1-\prod_{\{k,m\}}\exp\left[-p_{T,m}\lambda_k\int_{-\infty}^{\infty}1-\phi_F\left(P_k G_m h_{d,k}(r,\theta,r')t;0\right)dr'\right]p(r,\theta)d\theta dr\right] \tag{4.29}$$

where $h_{d,k}(r,\theta,r')$ abbreviated as $h_{d,k}$ is given by

$$h_{d,k} = \begin{cases} L^{-1}_{d,k}\left(\frac{r}{\sin(\frac{\pi}{2}-\theta)}, -\frac{y}{\sin(\frac{\pi}{2}-\theta)}, \frac{\pi}{2}-\theta\right) & \theta \in Q_1; r' \geq \frac{r}{tan(\frac{\pi}{2}-\theta)} \\ L^{-1}_{d,k}\left(\frac{r}{\sin(\frac{\pi}{2}-\theta)}, \frac{y}{\sin(\frac{\pi}{2}-\theta)}, \frac{\pi}{2}+\theta\right) & \theta \in Q_1; r' < \frac{r}{tan(\frac{\pi}{2}-\theta)} \\ L^{-1}_{d,k}\left(\frac{r}{\sin(\theta-\frac{\pi}{2})}, \frac{y}{\sin(\theta-\frac{\pi}{2})}, \frac{3\pi}{2}-\theta\right) & \theta \in Q_2; r' \geq \frac{-r}{tan(\theta-\frac{\pi}{2})} \\ L^{-1}_{d,k}\left(\frac{r}{\sin(\theta-\frac{\pi}{2})}, -\frac{y}{\sin(\theta-\frac{\pi}{2})}, \theta-\frac{\pi}{2}\right) & \theta \in Q_2; r' < \frac{-r}{tan(\theta-\frac{\pi}{2})} \\ L^{-1}_{d,k}\left(\frac{r}{\sin(\frac{3\pi}{2}-\theta)}, \frac{y}{\sin(\frac{3\pi}{2}-\theta)}, \frac{3\pi}{2}-\theta\right) & \theta \in Q_3; r' \geq \frac{r}{tan(\frac{3\pi}{2}-\theta)} \\ L^{-1}_{d,k}\left(\frac{r}{\sin(\frac{3\pi}{2}-\theta)}, -\frac{y}{\sin(\frac{3\pi}{2}-\theta)}, \theta-\frac{\pi}{2}\right) & \theta \in Q_3; r' < \frac{r}{tan(\frac{3\pi}{2}-\theta)} \\ L^{-1}_{d,k}\left(\frac{r}{\sin(\theta-\frac{3\pi}{2})}, -\frac{y}{\sin(\theta-\frac{3\pi}{2})}, \frac{5\pi}{2}-\theta\right) & \theta \in Q_4; r' \geq \frac{-r}{tan(\theta-\frac{3\pi}{2})} \\ L^{-1}_{d,k}\left(\frac{r}{\sin(\theta-\frac{3\pi}{2})}, \frac{y}{\sin(\theta-\frac{3\pi}{2})}, \theta-\frac{3\pi}{2}\right) & \theta \in Q_4; r' < \frac{-r}{tan(\theta-\frac{3\pi}{2})} \end{cases}$$

and $y = rsin(\theta) - r'cos(\theta)$ assuming Q_i represents the i-th quadrant.

Proof. The proof is available in Appendix F. □

Lemma 4.27. *If the street pattern is drawn by a NHPSP/NHPLM, the CF of the interference $I_{NT,d}$ is given by*

$$\phi_D(t) = \exp\left[-\lambda_s \int_0^{\infty}\int_0^{\pi}\int_0^{2\pi}\int_0^{\infty} 1 - \prod_{\{k,m\}} \exp\left[-p_{T,m}\lambda_k \int_{-h}^{h} 1 - \phi_F\left(P_k G_m h_{2,d,k}(r,\theta,r')t; 0\right) dr'\right] p(r,\theta) f_\Theta(\theta) f_H(h) dA\right] \tag{4.30}$$

where $h_{2,d,k}(r,\theta,r') = L^{-1}_{d,k}\left(d_1, d_2, \theta^{(B)}\right)$ if $\frac{y_{max}}{\sin(\theta')} < h$ and 0 otherwise. $y_{max} = \max(|y_1|,|y_2|)$, with $y_1, y_2 = r\sin(\phi) \pm h\sin(\theta)$. $\theta' = \theta$ if $\theta \in Q_1$ and $\pi - \theta$ if $\theta \in Q_2$. Berg distances are given by $d_1 = \frac{ay}{sin(\theta')}$ and $d_2 = |r\cos(\phi) - r\sin(\phi)\cot(\theta)| = |x_{int}|$. The a coefficient and the Berg angle can be deduced from Tab. 4.1. If the following condition $((\phi \in Q_1) \wedge (\theta \in Q_1) \wedge (x_{int} > 0)) \vee ((\phi \in Q_2) \wedge (\theta \in Q_2) \wedge (x_{int} < 0)) \vee ((\phi \in Q_3) \wedge (\theta \in Q_1) \wedge (x_{int} < 0)) \vee ((\phi \in Q_4) \wedge (\theta \in Q_2) \wedge (x_{int} > 0))$ is satisfied, then the alternate form $\theta^{(B)*}$ of the Berg angle must be used. Finally, we have $y = rsin(\phi) + r'sin(\theta)$.

Proof. If $\frac{y_{max}}{\sin(\theta')} > h$ then the stick has no intersection with the typical street

Case	Condition	a	$\theta^{(B)}$	$\theta^{(B)*}$
$\phi \in Q_1, Q_2$	$t \geq \frac{-r\sin(\phi)}{\sin(\theta')}$	1	$\pi - \theta'$	θ'
	$t < \frac{-r\sin(\phi)}{\sin(\theta')}$	-1	θ'	$\pi - \theta'$
$\phi \in Q_3, Q_4$	$t \geq \frac{r\sin(\phi)}{\sin(\theta')}$	1	θ'	$\pi - \theta'$
	$t < \frac{r\sin(\phi)}{\sin(\theta')}$	-1	$\pi - \theta'$	θ'

Table 4.1 Summary of Berg model values to be used in the framerwork of a NHPSP/NHPLM model.

and the UE receives no diffracted contributions coming from this stick. The approach used for Lemma 4.26 is then adapted to the NHPSP. □

Corollary 4.28. *Using symetry, if the street pattern is drawn by a PLCP, the CF of the interference $I_{NT,d}$ is given by*

$$\phi_D(t) = \exp\Bigg[-4\lambda_s \int_0^{\infty} \int_0^{\frac{\pi}{2}} 1 - \prod_{\{k,m\}} \exp\Bigg[-p_{T,m}\lambda_k \int_{-\infty}^{\infty} 1 - \phi_F\Big(P_{b,k}G_m h_{d,k}(r,\theta,r')t;0\Big) dr' \Bigg] d\theta dr \Bigg] \tag{4.31}$$

where

$$h_{d,k}(r,\theta,r') = \begin{cases} L_{d,k}^{-1}\left(\frac{r}{\sin(\frac{\pi}{2}-\theta)}, -\frac{y}{\sin(\frac{\pi}{2}-\theta)}, \frac{\pi}{2}-\theta\right) & \theta \in Q_1; r' \geq \frac{r}{tan(\frac{\pi}{2}-\theta)} \\ L_{d,k}^{-1}\left(\frac{r}{\sin(\frac{\pi}{2}-\theta)}, \frac{y}{\sin(\frac{\pi}{2}-\theta)}, \frac{\pi}{2}+\theta\right) & \theta \in Q_1; r' < \frac{r}{tan(\frac{\pi}{2}-\theta)} \end{cases}$$

Symetry can be similarly used to generalize Lemma 4.27 to the PSP and the PLM. Due to place constraints, this generalization is left to the reader.

Corollary 4.29. *If the street pattern is drawn by a MPLP, the CF of the interference $I_{NT,d}$ is given by*

$$\phi_D(t) = \exp\Bigg[-2\lambda_s \int_0^{\infty} 1 - \prod_{\{k,m\}} \exp\Bigg[-2p_{T,m}\lambda_k \int_0^{\infty} 1 - \phi_F\Big(P_{b,k}G_m L_{d,k}^{-1}\left(r', r, \frac{\pi}{2}\right) t;0\Big) dr' \Bigg] dr \Bigg]. \tag{4.32}$$

where $\lambda_s = \lambda_v$ is here the density of vertical lines as no first-order diffraction is received from horizontal lines.

Lemma 4.30. *If a NHPCLP is used, the CF of the interference $I_{NT,p} = \sum_{\{k,m\}} I_{NT,p,k,m}$ coming from tier $\Phi_{lp,k,m}, \forall l$ through building penetration if the serving tier is $\Phi_{T,(k^*,n^*)}$ is given by*

$$\phi_{NT}^{T,(k^*,n^*)}(t|r) = \exp\left[-\lambda_s \int_0^\infty \int_0^{2\pi} 1 - \prod_{\{k,m\}} \exp\left[-2p_{NT,m}\lambda_k \int_0^\infty 1 - \phi_F\left(P_k G_m \tilde{f}_k(v, z_{NT,(k)}^{T,(k^*,n^*)}(v))t; 0\right) dr'\right] p(r,\theta) d\theta dr\right] \tag{4.33}$$

where $\tilde{f}_k(x,a) = L_{\tilde{t},k}^{-1}(x)$ if $x \geq a$ (0 elsewhere) and $v = \sqrt{r^2 + r'^2}$.

Proof. The proof is similar to the proof of Lemma 4.26. □

Generalizations to the other processes made for $I_{B,k,n,m}$ and $I_{NT,p}$ should be sufficient to understand how the same generalizations can be applied to $I_{NT,p}$. Also, Eq. (4.33) can be generalized to sparser environments by adapting the PL model in the definition of $\tilde{f}_k(x,a)$.

4.6.5 Generalization to crossroads and T-junctions users

In this section, a typical UE located at the intersection of N_s streets in considered. It is shown that, on average, crossroad UEs experience higher power levels because :

- they experience more LOS/NLOS contributions coming from more than one typical street.
- they are N_s times closer to their closest BS which further increases the probability for this BS to be in LOS conditions.

The CFs expressions derived for the street UE can be easily generalized to the crossroad UE knowing the number of interferers is multiplied by N_s. Using the CFs properties, we therefore have:

$$\phi_{T,Cr,(k,n,m)}^{T,(k^*,n^*)}(t|r) = \left(\phi_{T,(k,n,m)}^{T,(k^*,n^*)}(t|r)\right)^{N_s} \tag{4.34}$$

$$\phi_{D,Cr}(t) = \left(\phi_D(t)\right)^{N_s}. \tag{4.35}$$

In addition, as the crossroad UE is at the intersection of N_s streets, the densities λ_k used in expressions (4.6)-(4.5) need to be multiplied by N_s. All other expressions remain unchanged. The approach can be generalized to T-junction UEs assuming $N_s = 3/2$ in all these modifications.

Remark 4.31. Note that the diffracted contributions coming from the different typical streets are correlated due to the fixed street pattern. While Eq. (4.35) is perfectly accurate for MPLPs, it can only be considered as an approximation for other processes.

4.7 SINR-based statistics

In this work, the general signal to interference ratio (SINR) is defined as

$$\mathrm{SINR}_u = \frac{S}{\sum_{\{j,k,n,m\}} I_{j,k,n,m} + \sum_{\{j,k,m\}} I_{j,d,k,m} + \sum_{\{k,m\}} I_{p,k,m} + W}. \tag{4.36}$$

In the above expressions, W represents the constant noise power considering additive white gaussian noise (AWGN). Let us assume the serving distance r and the serving tier are known. The useful signal power level is then given by $S = PG_1|h|^2L(r)$ where P, $|h|^2$ and $L(r)$ are respectively the emitted power, the fading model and the PL model associated with the serving tier (see section 3.3.5). The terms $I_{j,k,n,m}$, $I_{j,d,k,m}$ and $I_{p,k,m}$ are defined as the interference power levels coming from LOS/NLOS contributions (L1), from corner diffraction (L2) and from building penetration (L3). These quantities can be computed as mentioned in Section 3.3.5 using the corresponding indexes.

4.7.1 Coverage probability

The coverage probability $P_c(\theta_c)$ is the probability that the typical UE can reach a target SINR θ_c [81]. It is expressed as

$$P_c(\theta_c) = \mathbb{P}\left[\mathrm{SINR}_u > \theta_c\right] \tag{4.37}$$

which can be also interpreted as the success probability of the typical transmission averaged over all spatial links [34]. A link budget is usually performed to ensure that all UEs in the network can be granted a minimum quality of service. In particular, UEs located at the cell edge are generally studied as they may suffer from severe propagation losses. It generally tests if such UEs can benefit from a desired SINR considering all losses between the BS and UE. This metric sort of mimics the link budget analysis and quantifies the probability of a typical UE (including those at the cell edge) reaching the target SINR.

Due to limited space, only one tier's probability (i.e. the coverage probability conditioned on a given serving tier) is detailed here, as it will be the case for all upcoming metrics. Other probabilities can be derived using the same approach. The considered notations should enable the reader to establish a clear connection between these probabilities and their respective tiers. All conditional metrics can then combined using the the total law of probability and the association probabilities derived in Section 4.4.

Lemma 4.32. *Using the Gil-Pelaez analytical technique proposed in Section 2.2.2, the coverage probability if the serving tier is $\Phi_{T,(k^*,n^*)}$ is given by*

$$P_c^{T,(k^*,n^*)}(\theta_c) = \int_0^\infty \Big\{\frac{1}{2}+\frac{1}{\pi}\int_0^\infty Im\big[\phi_S^{T,(k^*,n^*)}(t|r)\phi_I(-\theta_c t|r)\big]\frac{dt}{t}\Big\} f_{S,R_{T,k^*,n^*}}(r)dr \tag{4.38}$$

where

$$\phi_I(q|r) = \phi_D(q)\prod_{\{k,n,m\}}\phi_{T,(k,n,m)}^{T,(k^*,n^*)}(q|r)\prod_{\{k,n,m\}}\phi_{B,(k,n,m)}^{T,(k^*,n^*)}(q|r)$$
$$e^{jqW}\phi_{NT}^{T,(k^*,n^*)}(q|r)\prod_{\{k,m\}}\phi_{Bd,(k,m)}^{T,(k^*,n^*)}(q|r).$$

Theorem 4.33. *By the total law of probability, the global coverage probability is then finally given by:*

$$P_c(\theta_c) = \sum_{\{k^*,n^*\}}\mathcal{A}_{T,k^*,n^*}P_c^{T,(k^*,n^*)}(\theta_c) + \sum_{\{k^*,n^*\}}\mathcal{A}_{B,k^*,n^*}P_c^{B,(k^*,n^*)}(\theta_c)$$
$$+\sum_{\{k^*\}}\mathcal{A}_{Bd,k^*}P_c^{Bd,(k^*)}(\theta_c) + \sum_{\{k^*\}}\mathcal{A}_{NT,k^*}P_c^{NT,(k^*)}(\theta_c) \tag{4.39}$$

4.7.2 Rate-based statistics

The channel capacity C is said to be the strict maximum rate at which the desired information can be reliably transmitted given the channel characteristics and given the bandwith B. If AWGN is considered, the Shannon-Hartley theorem states C is given by the following relation [79]:

$$C = B \log_2 \left(1 + \mathrm{SINR}_u\right). \tag{4.40}$$

Average rate

Shannon also defined the average ergodic rate [81]. It is defined as

$$\mu_C = \mathbb{E}\Big[C\Big]. \tag{4.41}$$

It is particularly useful when the channel state information (CSI) is unknown. Since the CSI is unavailable, the transmission may be performed on very good to very poor channels. The average ergodic rate then gives a general intuition about the maximum achievable rate on average.

Lemma 4.34. *The average rate if the serving tier is $\Phi_{T,(k^*,n^*)}$ is given by*

$$\mu_C^{T,(k^*,n^*)} = \frac{B}{\ln(2)} \int_0^\infty \frac{1}{z} \phi_D\left(\frac{-z}{j}\right) \int_0^\infty \left(1 - \phi_S^{T,(k^*,n^*)}\left(\frac{-z}{j}\middle| r\right)\right) \phi_I\left(\frac{-z}{j}\middle| r\right) f_{S,R_{T,k^*,n^*}}(r) dr dz \tag{4.42}$$

Proof. The proof is available in Appendix G. □

Theorem 4.35. *By the total law of probability, the global average rate is then finally given by:*

$$\mu_C = \sum_{\{k^*,n^*\}} \mathcal{A}_{T,k^*,n^*} \mu_C^{T,(k^*,n^*)} + \sum_{\{k^*,n^*\}} \mathcal{A}_{B,k^*,n^*} \mu_C^{B,(k^*,n^*)} + \sum_{\{k^*\}} \mathcal{A}_{Bd,k^*} \mu_C^{Bd,(k^*)} + \sum_{\{k^*\}} \mathcal{A}_{NT,k^*} \mu_C^{NT,(k^*)} \tag{4.43}$$

Rate coverage

The rate coverage is an alternative way to define the coverage. In this case, a constant capacity θ_r is used for the transmission regardless of the CSI. In case of deep fades, an outage occurs and the data is thus lost. The rate coverage probability quantifies how often this happens. It is defined as the probability that the typical UE can reach a target rate θ_r. It is given by:

$$P_{cap}(\theta_r) = \mathbb{P}\left[C > \theta_r\right]. \tag{4.44}$$

In the 3GPP TS 38.214 technical specification [82], different modulation schemes and coding rates are introduced. Tab. 4.2 summarizes the different schemes with their approximated spectral efficiencies and trigger thresholds. In [83], Vienna 5G link and system level simulators were used to characterize the spectral efficencies of these schemes for a block error rate of 0.1 with LTE-A and 5G technologies. These are depicted in Fig. 4.1 and graphically compared to the Shannon bound. The actual rate associated to a given SINR is shown to be upperbounded by the Shannon bound. This comes from implementation losses.

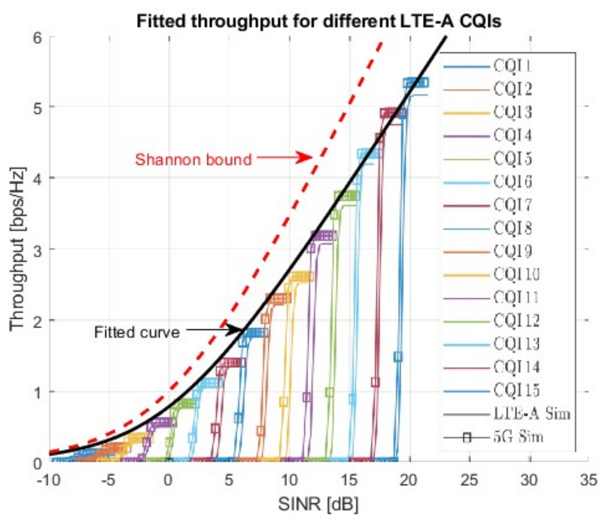

Fig. 4.1 Approximating the LTE spectral efficiency [83].

According to the approach proposed in 3GPP TR 38803 technical report [84], the actual rate can be approximated by

$$C^* = \begin{cases} 0, & \text{if SINR} \leq \text{SINR}_{min} \\ aC, & \text{if SINR}_{min} \leq \text{SINR} \leq \text{SINR}_{max} \\ aC_{max}, & \text{if SINR} \geq \text{SINR}_{max}. \end{cases} \tag{4.45}$$

CQI Index	Modulation	Coding Rate	Spectral efficiency [bps/Hz]	SINR estimate [dB]
0	out of range			
1	QPSK	0.0762	0.1523	-6.7
2	QPSK	0.1172	0.2344	-4.7
3	QPSK	0.1885	0.3770	-2.3
4	QPSK	0.3008	0.6016	0.2
5	QPSK	0.4385	0.8770	2.4
6	QPSK	0.5879	1.1758	4.3
7	16QAM	0.3691	1.4766	5.9
8	16QAM	0.4785	1.9141	8.1
9	16QAM	0.6016	2.4063	10.3
10	64QAM	0.4551	2.7305	11.7
11	64QAM	0.5537	3.3223	14.1
12	64QAM	0.6504	3.9023	16.3
13	64QAM	0.7539	4.5234	18.7
14	64QAM	0.8525	5.1152	21.0
15	64QAM	0.9258	5.5547	22.7

Table 4.2 Lookup table for mapping the SINR threshold to its corresponding modulation scheme and spectral efficiency [82].

where a is the attenuation factor associated with the implementation losses and SINR_{min} and SINR_{max} are the minimum and maximum SINRs of the code set. From Fig. 4.1, we approximate $a = 0.78$. The actual rate coverage can thus be computed by $\mathbb{P}[C* > \theta_r] = \mathbb{P}[C > \theta_r/0.78]$. In addition, a maximum achievable rate is here imposed by the code set. The rate coverage is thus reduced to zero for higher values.

Theorem 4.36. *The global rate coverage probability is then finally given by:*

$$\begin{aligned} P_{cap}(\theta_r) = &\sum_{\{k^*,n^*\}} \mathcal{A}_{T,k^*,n^*} P_c^{T,(k^*,n^*)}(2^{\frac{\theta_r}{B}} - 1) + \sum_{\{k^*\}} \mathcal{A}_{Bd,k^*} P_c^{Bd,(k^*)}(2^{\frac{\theta_r}{B}} - 1) \\ &+ \sum_{\{k^*,n^*\}} \mathcal{A}_{B,k^*,n^*} P_c^{B,(k^*,n^*)}(2^{\frac{\theta_r}{B}} - 1) + \sum_{\{k^*\}} \mathcal{A}_{NT,k^*} P_c^{NT,(k^*)}(2^{\frac{\theta_r}{B}} - 1). \end{aligned} \tag{4.46}$$

Proof. The rate coverage can be obtained via the change of variable $P_{cap}(\theta_r) = P_c(2^{\frac{\theta_r}{B}} - 1)$ in Theorem (4.33). □

4.8 Exposure-based statistics

As no evidence has been found about the health risks potentially caused by the growing amount of wireless links, except thermal effects, legal exposure thresholds have been preventively defined. Belgium has adopted a rather defensive strategy to handle that risk. The exposure threshold has been set at 0,05 W/m² for frequencies going from 2 GHz to 300 GHz in Brussels. This is significantly lower than other European countries and way lower than the World Health Organization recommendations. Exposure was however barely studied in a SG framework [85, 86] and still needs to be more deeply investigated. The exposure level is usually defined as

$$\mathrm{Exp}_u = S + \sum_{\{j,k,n,m\}} I_{j,k,n,m} + \sum_{\{j,k,m\}} I_{j,d,k,m} + \sum_{\{k,m\}} I_{p,k,m}. \tag{4.47}$$

Note that an active user is here studied. This can be considered as the worst case scenario since the main lobe of the serving BS is known to be directed towards this UE. However, the study could be easily generalized to a general UE.

Depending on the desired units for the exposure levels, the following conversion can be used

$$\mathrm{Exp}_u[\mathrm{W/m^2}] = \frac{\mathrm{Exp}_u}{A_e} \tag{4.48}$$

$$\mathrm{Exp}_u[\mathrm{V/m}] = \sqrt{\frac{Z_0 \mathrm{Exp}_u}{A_e}} \tag{4.49}$$

where $A_e = \frac{(c/f)^2}{4\pi}$ is the antenna effective area of the typical UE and $Z_0 = 120\pi$ is the impedance of free space.

4.8.1 Average exposure

The average exposure is defined as

$$\mu_E = \mathbb{E}\left[\mathrm{Exp}_u\right] = \sum_{\{j,k,n,m\}} \mu_{j,k,n,m} + \sum_{\{j,k,m\}} \mu_{j,d,k,m} + \sum_{\{k,m\}} \mu_{p,k,m}. \tag{4.50}$$

where $\mu_{j,k,n,m}$, $\mu_{j,d,k,m}$ and $\mu_{p,k,m}$ are respectively the mean total powers coming from LOS/NLOS contributions (L1), from corner diffraction (L2) and from building penetration (L3). With a slight abuse of notation, S is here included in one of those three terms depending on the serving tier.

Lemma 4.37. *The average exposure if the serving tier is $\Phi_{T,(k^*,n^*)}$ is given by*

$$\begin{aligned}\mu_O^{T,(k^*,n^*)} &= \int_0^\infty \Big\{ P_{k^*} G_1 L_{k^*,n^*}(r) \\ &+ \sum_{\{k,n,m\}} P_k G_m \int_{z_{T,(k,n,m)}^{T,(k^*,n^*)}(r)}^\infty L_{k,n}^{-1}(r')\lambda_{T,(k,n,m)}(r')dr' \\ &+ \sum_{\{k,n,m\}} P_{b,k} G_m \int_{z_{(B,k,n,m)}^{T,(k^*,n^*)}(r)}^\infty \int_0^{2\pi} L_{k,n}^{-1}(r')\lambda_{B,(k,n,m)}(r',\theta)d\theta dr' \\ &+ \sum_{\{k,m\}} P_{b,k} G_m \int_{z_{Bd,(k,m)}^{T,(k^*,n^*)}(r)}^\infty \int_0^{2\pi} L_{d,k}^{-1}(r')\lambda_{Bd,(k,m)}(r',\theta)d\theta dr' \\ &+ \sum_{\{k,m\}} P_k G_m \lambda_s \int_0^\infty \int_0^{2\pi} \int_0^\infty \tilde{f}_k(v, z_{NT,(k)}^{T,(k^*,n^*)}(v))\lambda_{NT,(k,m)}(r')dr' \\ &\qquad p(r,\theta)d\theta dr \Big\} f_{S,R_{T,k^*,n^*}}(r)dr. \end{aligned} \tag{4.51}$$

where $\tilde{f}_k(x,a) = L_{\bar{t},k}^{-1}(x)$ if $x \geq a$ (0 elsewhere) and $v = \sqrt{r^2 + r'^2}$.

Proof. The proof is available in Appendix H. □

Theorem 4.38. *By the total law of probability, the average exposure is given by:*

$$\begin{aligned}\mu_E = &\sum_{\{k^*,n^*\}} \mathcal{A}_{T,k^*,n^*}\mu_O^{T,(k^*,n^*)} + \sum_{\{k^*,n^*\}} \mathcal{A}_{B,k^*,n^*}\mu_O^{B,(k^*,n^*)} \\ &+ \sum_{\{k^*\}} \mathcal{A}_{Bd,k^*}\mu_O^{Bd,(k^*)} + \sum_{\{k^*\}} \mathcal{A}_{NT,k^*}\mu_O^{NT,(k^*)} \\ &+ \sum_{\{k,m\}} P_k G_m p_{T,m}\lambda_k\lambda_s \int_0^\infty \int_0^{2\pi} \int_0^\infty h_{d,k}(r,\theta,r')dr' p(r,\theta)d\theta dr \end{aligned} \tag{4.52}$$

where the last term is the average exposure associated to corner diffraction for signals coming from non typical streets. This term is not conditioned by the serving tier and can therefore be separately computed.

Remark 4.39. The exposure variance could be computed to understand how the average exposure value has to be interpreted. In fact, the average exposure is only representative if the variance is sufficiently low. To evaluate this, the exposure CDF presented in the next section will be used instead.

4.8.2 Exposure CDF

While it gives some intuition on the actual exposure levels that can be observed, the average exposure is not sufficient to ensure that the legal threshold is respected everywhere. In fact, high exposure values can be mitigated by low exposure values leading to an average exposure below the threshold. Still, locations where the high exposure values are detected do not conform to the norm. For this reason, the average exposure metric needs to be complemented by the exposure CDF defined as

$$P_e(\theta_e) = \mathbb{P}\left[\mathrm{Exp}_u < \theta_e\right] \tag{4.53}$$

which quantifies how likely the exposure level is kept below the legal threshold.

Lemma 4.40. *Using the Gil-Pelaez analytical technique proposed in Section 2.2.2, the exposure CDF if the serving tier is $\Phi_{T,(k^*,n^*)}$ is given by*

$$P_e^{T,(k^*,n^*)}(\theta_e) = \int_0^\infty \left\{\frac{1}{2} - \frac{1}{\pi}\int_0^\infty Im\left[\phi_S^{T,(k^*,n^*)}(t|r)\tilde{\phi}_I(t|r)\right]\frac{dt}{t}\right\} f_{S,R_{T,k^*,n^*}}(r)dr. \tag{4.54}$$

where $\tilde{\phi}_I(t|r) = e^{-j\theta_c t}\phi_I(t|r)/e^{jtW}$

Theorem 4.41. *By the total law of probability, the global exposure CDF is then finally given by:*

$$\begin{aligned} P_e(\theta_e) = &\sum_{\{k^*,n^*\}} \mathcal{A}_{T,k^*,n^*} P_e^{T,(k^*,n^*)}(\theta_e) + \sum_{\{k^*,n^*\}} \mathcal{A}_{B,k^*,n^*} P_e^{B,(k^*,n^*)}(\theta_e) \\ &+ \sum_{\{k^*\}} \mathcal{A}_{Bd,k^*} P_e^{Bd,(k^*)}(\theta_e) + \sum_{\{k^*\}} \mathcal{A}_{NT,k^*} P_e^{NT,(k^*)}(\theta_e) \end{aligned} \tag{4.55}$$

4.9 Joint SINR-exposure distribution

The joint SINR-exposure distribution is defined as

$$F(\theta_c, \theta_e) = \mathbb{P}\left[\mathrm{SINR}_u > \theta_c, \mathrm{Exp}_u < \theta_e\right]. \tag{4.56}$$

This distribution represents the probability for a mobile user to satisfy coverage requirements (SINR greater than θ_c) while experiencing an exposure below a safety threshold θ_e. It will help us identify the potential trade-offs if a restrictive exposure threshold has to be respected.

Lemma 4.42. *Under Rayleigh fading and assuming there is no noise, the joint distribution if the serving tier is $\Phi_{T,(k^*,n^*)}$ is given by*

$$\begin{aligned}
&J^{T,(k^*,n^*)}(\theta_c,\theta_e) \\
&= \frac{1}{2}\int_0^\infty F_G\left(\frac{\theta_e}{P_{k^*}G_m L^{-1}_{k^*,n^*}(r)}\right) f_{S,R_{T,k^*,n^*}}(r)dr - \frac{1}{\pi}\int_0^\infty \\
&\int_0^\infty Im\left[\phi_I(q|r)T_1 + \frac{e^{-jq\theta_e}(T_2-T_3)}{-1+jqP_{k^*}G_m L^{-1}_{k^*,n^*}(r)}\right] q^{-1}dqf_{S,R_{T,k^*,n^*}}(r)dr.
\end{aligned} \tag{4.57}$$

where

$$\begin{aligned}
T_1 &= 1-\exp\left(\theta_1(r)(1+j\frac{qP_{k^*}G_m L^{-1}_{k^*,n^*}(r)}{\theta_c})\right)\left(1+j\frac{qP_{k^*}G_m L^{-1}_{k^*,n^*}(r)}{\theta_c}\right)^{-1} \\
T_2 &= \exp\left(\frac{\theta_e}{P_{k^*}G_m L^{-1}_{k^*,n^*}(r)}\left(-1+jqP_{k^*}G_m L^{-1}_{k^*,n^*}(r)\right)\right) \\
T_3 &= \exp\left(\frac{\theta_c\theta_e}{(1+\theta_c)P_{k^*}G_m L^{-1}_{k^*,n^*}(r)}\left(-1+jqP_{k^*}G_m L^{-1}_{k^*,n^*}(r)\right)\right).
\end{aligned}$$

Proof. The proof is available in Appendix I. Note that $F_G(g) = -e^{-x}$ □

Theorem 4.43. *By the total law of probability, the joint distribution under Rayleigh fading is given by:*

$$\begin{aligned}
J(\theta_c,\theta_e) = &\sum_{\{k^*,n^*\}} \mathcal{A}_{T,k^*,n^*} J^{T,(k^*,n^*)}(\theta_c,\theta_e) + \sum_{\{k^*,n^*\}} \mathcal{A}_{B,k^*,n^*} J^{B,(k^*,n^*)}(\theta_c,\theta_e) \\
&+ \sum_{\{k^*\}} \mathcal{A}_{Bd,k^*} J^{Bd,(k^*)}(\theta_c,\theta_e) + \sum_{\{k^*\}} \mathcal{A}_{NT,k^*} J^{NT,(k^*)}(\theta_c,\theta_e).
\end{aligned} \tag{4.58}$$

Remark 4.44. Unlike all other metrics, the mathematical expression for the joint distribution only exists for the case where the Rayleigh fading model is used on all links in the network.

The joint distribution for all fading distributions can be lowerbounded and upperbounded using Fréchet inequalities [87]. These bounds, whose tightness varies depending on the thresholds being considered, are:

$$\underline{J}(\theta_c, \theta_e) = \max\left(0, P_c(\theta_c) + P_e(\theta_e) - 1\right) \tag{4.59}$$

$$\overline{J}(\theta_c, \theta_e) = \min\left(P_c(\theta_c), P_e(\theta_e)\right) \tag{4.60}$$

and will be used as approximations in some of the numerical results.

4.10 Generalization to non-uniform user distributions

The global coverage probability and the exposure CDF will be adapted to a non uniform UE distribution as presented in Section 3.3.7. Remember that the typical UE location is now coupled with the location of a given hotspot BS that belongs to the street tier (k_γ, n_γ). Under the considered hotspot BS distance distribution $f_H(r)$, the probabilities that this hotspot BS is in LOS or NLOS condition are respectively given by:

$$p_{0,L} = \int_0^\infty \exp\left(-\beta_S r\right) f_H(r) dr \tag{4.61}$$

$$p_{0,N} = \int_0^\infty \left(1 - \exp\left(-\beta_S r\right)\right) f_H(r) dr. \tag{4.62}$$

Lemma 4.45. *Using Bayes' theorem, the PDF and CCDF of the distance from the UE to the hotspot BS knowing its condition $\gamma = (k_\gamma, n_\gamma)$ is given by:*

$$\underline{PDF:} \quad f_{C,R_{0,\gamma}}(r) = \begin{cases} \frac{p_L(r) f_H(r)}{p_{0,L}} = \frac{\frac{2}{\sigma\sqrt{2\pi}} e^{-\beta_S r - \frac{r^2}{2\sigma^2}}}{p_{0,L}} & \text{if } n_\gamma{=}L \\ \frac{p_N(r) f_H(r)}{p_{0,N}} = \frac{\frac{2}{\sigma\sqrt{2\pi}} (1-e^{-\beta_S r}) e^{-\frac{r^2}{2\sigma^2}}}{p_{0,L}} & \text{if } n_\gamma{=}N \end{cases} \tag{4.63}$$

$$\underline{CCDF:} \quad \overline{F}_{C,R_{0,\gamma}}(r) = \begin{cases} 1 - \frac{1}{p_{0,L}} e^{\frac{\beta_S^2 \sigma^2}{2}} \Upsilon(r) & \text{if } n_\gamma{=}L \\ 1 - \frac{1}{p_{0,N}} \left(1 + \text{erf}\left(\frac{r}{\sqrt{2}\sigma}\right) - e^{\frac{\beta_S^2 \sigma^2}{2}} \Upsilon(r)\right) & \text{if } n_\gamma{=}N. \end{cases} \tag{4.64}$$

with $\Upsilon(r) = 1 + \text{erf}\left(\frac{\beta\sigma^2 + r}{\sqrt{2}\sigma}\right) - \text{erf}\left(\frac{\beta_S \sigma^2}{\sqrt{2}\sigma}\right)$.

Lemma 4.46. *Following the same approach as for the uniform UE and knowing the condition $\gamma = (k_\gamma, n_\gamma)$ of the hotspot BS, the following association probabilities are defined:*

- *the probability for the user to be associated to a BS of tier $\Phi_{T,(k^*,n^*)}$ is modified as:*

$$\mathcal{A}_{T,k^*,n^*,\gamma} = \int_0^\infty \Omega_{C,k^*,n^*}(r)\overline{F}_{C,R_{0,\gamma}}\left[z_{0,(k_\gamma,n_\gamma)}^{T,(k^*,n^*)}(r)\right] f_{C,R_{T,k^*,n^*}}(r)dr. \quad (4.65)$$

where $z_{0,(k_\gamma,n_\gamma)}^{T,(k^*,n^*)}(r) = z_{T,(k_\gamma,n_\gamma)}^{T,(k^*,n^*)}(r)$.

- *the probability for the user to be associated to tier Φ_0 is given by*

$$\mathcal{A}_{0,\gamma} = \int_0^\infty \Omega_0(r) f_{C,R_{0,\gamma}}(r)dr. \quad (4.66)$$

where $\Omega_0(r)$ is the completed product function that can computed as

$$\Omega_0(r) = \Omega_{T,k_\gamma,n_\gamma}(r) F_{C,R_{T,k_\gamma,n_\gamma}}\left(z_{T,(k_\gamma,n_\gamma)}^{T,(k_\gamma,n_\gamma)}(r)\right).$$

- *the joint probability that the UE is associated to tier $\Phi_0/\Phi_{T,(k^*,n^*)}$ and that the hotspot BS condition γ are then respectively given by:*

$$\mathcal{B}_{0,\gamma} = \begin{cases} \frac{p_{0,L}}{N}\mathcal{A}_{0,\gamma} & \text{if } n_\gamma = L \\ \frac{p_{0,N}}{N}\mathcal{A}_{0,\gamma} & \text{if } n_\gamma = N \end{cases} \quad (4.67)$$

$$\mathcal{B}_{T,k^*,n^*,\gamma} = \begin{cases} \frac{p_{0,L}}{N}\mathcal{A}_{T,k^*,n^*,\gamma} & \text{if } n_\gamma = L \\ \frac{p_{0,N}}{N}\mathcal{A}_{T,k^*,n^*,\gamma} & \text{if } n_\gamma = N. \end{cases} \quad (4.68)$$

- *the other association probabilities $\mathcal{A}_{B,k^*,n^*,\gamma}$, $\mathcal{A}_{Bd,k^*,\gamma}$ and $\mathcal{A}_{NT,k^*,\gamma}$ and joint probabilities $\mathcal{B}_{B,k^*,n^*,\gamma}$, $\mathcal{B}_{Bd,k^*,\gamma}$ and $\mathcal{B}_{NT,k^*,\gamma}$ are similarly computed.*

Lemma 4.47. *With the defined association rule,*

- *if the UE is connected to a BS of tier $\Phi_{T,(k^*,n^*)}$, the PDF of the distance from the UE to this BS is given by:*

$$f_{S,R_{T,k^*,n^*,\gamma}}(r) = \frac{1}{\mathcal{A}_{T,k^*,n^*,\gamma}} \Omega_{k^*,n^*}(r)\overline{F}_{C,R_{0,\gamma}}\left[z_{0,(k_H,n_H)}^{T,tk^*,n^*)}(r)\right] f_{C,R_{T,k^*,n^*}}(r)dr.$$

- *if the UE is connected to tier Φ_0, the PDF of the distance from the UE to this BS is*

$$f_{S,R_{0,\gamma}}(r) = \frac{1}{\mathcal{A}_{0,\gamma}} \Omega_0(r) f_{C,R_{0,\gamma}}(r). \tag{4.69}$$

- *the distance PDFs for the other serving tiers $f_{S,R_{B,k^*,n^*,\gamma}}(r)$, $f_{S,R_{Bd,k^*,\gamma}}(r)$ and $f_{S,R_{NT,k^*,\gamma}}(r)$ are similarly computed.*

Lemma 4.48. *In case tier 0 acts as an interferer (i.e. when the UE is served by another tier), the corresponding CF has to be computed as it will considerably affect the performance metrics. Given the condition $\gamma = (k_\gamma, n_\gamma)$ of the hotspot BS and knowing $\Phi_{T,(k^*,n^*)}$ is the serving tier, the CF is given by*

$$\phi^{T,(k^*,n^*)}_{0,(k_\gamma,n_\gamma,m)}(t) = \int_0^\infty \phi_F\left(P_{k_\gamma} G_m L^{-1}_{k_\gamma,n_\gamma}(r)t; \iota\right) f^{T,(k^*,n^*)}_{R_{0,\gamma}}(r')dr' \tag{4.70}$$

where the PDF of the distance between the UE and the hotspot BS knowing the serving tier is given by :

$$f^{T,(k^*,n^*)}_{R_{0,\gamma}}(r) = \frac{1}{\mathcal{A}_{T,k^*,n^*,\gamma}} f_{C,R_{0,\gamma}}(r) \int_0^\infty \mathbb{1}\left(r > z^{T,(k^*,n^*)}_{0,(k_H,n_H)}(x)\right) \Omega_{T,k^*,n^*}(x) f_{S,R_{T,k^*,n^*,\gamma}}(x)dx.$$

Proof. The proof is available in Appendix J. □

Lemma 4.49. *By means of the previous results, we are able to compute*

- *the coverage probability when the serving tier is $\Phi_{T,(k^*,n^*)}$*

$$P_c^{T,(k^*,n^*,\gamma)}(\theta) = \int_0^\infty \left\{ \frac{1}{2} + \frac{1}{2\pi} \int_0^\infty Im\left[\phi_S^{T,(k^*,n^*)}(t|r)\phi_I(-\theta_c t) \times \left(\sum_{\{m\}} \phi^{T,(k^*,n^*)}_{0,(k_\gamma,n_\gamma,m)}(-\theta t) \right)\right] \frac{dt}{t} \right\} f_{S,R_{T,k^*,n^*,\gamma}}(r)dr.$$

knowing the beamforming condition of the hotspot BS has to be taken into account.

- *the coverage probability for the other serving tiers $P_c^{B,(k^*,n^*,\gamma)}$, $P_c^{Bd,(k^*,\gamma)}$ and $P_c^{NT,(k^*,\gamma)}$ that are similarly computed.*

- *the coverage probability when the serving tier is* Φ_0

$$P_c^{0,(k_\gamma,n_\gamma)}(\theta_c) = \int_0^\infty \left\{ \frac{1}{2} + \frac{1}{\pi} \int_0^\infty Im\left[\phi_S^{0,(k_\gamma,n_\gamma)}(t|r)\phi_I(-\theta_c t) \right] \frac{dt}{t} \right\} f_{S,R_{0,\gamma}}(r)dr.$$

where the CFs associated with tier Φ_0 *are computed as the CFs for street tiers and* $\phi_I(-\theta_c t)$ *is evaluated assuming* $(k^*, n^*) = (k_\gamma, n_\gamma)$.

Theorem 4.50. *By the total law of probability, the global coverage probability is then finally given by:*

$$\begin{aligned} P_c(\theta_c) = &\sum_{\{k^*,n^*,\gamma\}} \mathcal{B}_{T,k^*,n^*,\gamma} P_c^{T,(k^*,n^*,\gamma)}(\theta_c) + \sum_{\{k^*,n^*,\gamma\}} \mathcal{B}_{B,k^*,n^*,\gamma} P_c^{B,(k^*,n^*,\gamma)}(\theta_c) \\ &+ \sum_{\{k^*,\gamma\}} \mathcal{B}_{Bd,k^*,\gamma} P_c^{Bd,(k^*,\gamma)}(\theta_c) + \sum_{\{k^*,\gamma\}} \mathcal{B}_{NT,k^*,\gamma} P_c^{NT,(k^*,\gamma)}(\theta_c) \\ &+ \sum_{\{\gamma\}} \mathcal{B}_{0,\gamma} P_c^{0,(k_\gamma,n_\gamma)}(\theta_c) \end{aligned} \tag{4.71}$$

The same approach can be used to generalize the exposure CDF presented in theorem 4.41 to the non uniform UE.

5 Full characterization of realistic topologies

BASED on the mathematical framework outlined in the previous chapter, we will now present numerical results for three types of environments that can reflect the street patterns and urban organization of many cities worldwide. These three main environments are as follows:

- Manhattan-like urban environments using the MPLP. This model is suitable for cities that follow a grid street plan in urban planning, such as New York, Barcelona, Lima, Beijing, and many others.
- Irregular urban environments using other doubly stochastic processes. Although many cities follow a grid plan, many more have an irregular street pattern, which necessitates a more general model. The Cox model is a good candidate since it offers more randomness in the street pattern while maintaining a manageable mathematical framework. However, most cities fall somewhere between the perfect regularity provided by the MPLP and the total randomness provided by the PCLP. We will therefore relax some of the constraints of the Cox model using the NHPCLP to more accurately mimic actual city deployments.
- Sparser irregular environments. In suburban or rural areas, the built-up ratio is usually lower. This enables BSs in non typical streets to

more easily serve the UE or to more strongly interfere with the actual serving BS. In that case, an adaptation of the LOS probabilities and the PL models is needed in order to more accurately reflect the actual performance of such environments.

5.1 Dense urban environments

In dense urban environments, BSs located far below the rooftop height and outside the UE's street will most probably interact with this UE through corner diffraction. In fact, due to a high built-up ratio, most of these BSs will generally be in NLOS conditions. Since the building penetration losses are very high, the received signal power is more importantly impacted by the diffracted contributions. In addition, based on Berg recursive method, the street orientations are shown to have a drastic impact on these contributions. To illustrate this, we generate streets that intersect the typical street with a linear density λ_S and either randomly choose the angle for Cox environments or fix it to $\pi/2$ for Manhattan environments. BSs are then generated in each of these streets with linear density λ_B and their total contributions are computed using the Berg method. The obtained results for 5000 streets generations are depicted in Fig. 5.1. It is shown that whatever the BS density, the diffracted contributions in Cox environments are generally higher. This explains why these environments are separately studied. The contributions received through building penetration will be equally characterized to demonstrate that they can be safely disregarded.

5.1.1 Manhattan environments

In order to generate the results of this section, a network of infinite size is considered: the network size R is hence set to $+\infty$ in the analytical expressions, and to $128km$ in the MC simulations (value sufficiently large to reproduce an infinite environment from the point of view of the centric user). In our analysis of Manhattan environments, a very basic scenario is considered. This scenario is established as follows: (1) a single street tier with parameters (P_B, λ_B, H_B), (2) with no beamforming, (3) under a nearest neighbour cell association rule , (4) generated on a MPLP where horizontal and vertical streets have the same density $\lambda_h = \lambda_v = \lambda_s$, (5) assuming respective PL exponents and PL intercepts (α_L,κ_L), (α_N,κ_N) and (α_D,κ_D)

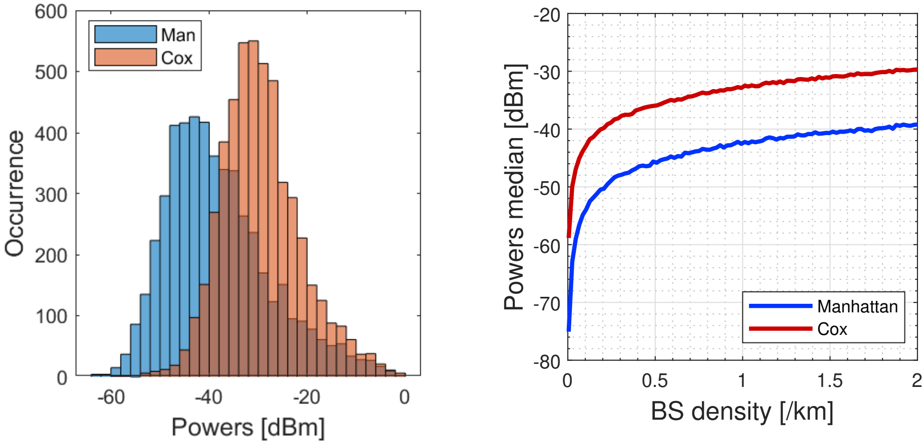

(a) Histogram of the total diffracted contributions for $\lambda_B = 1.8km^{-1}$.

(b) Impact of λ_s on powers median.

Fig. 5.1 Comparison of the diffracted contributions for a Manhattan-like environment and a Cox environment. The selected parameters are $\kappa_D = (10^3.07) f_{GHz}^{0.57}$, $\alpha_D = 2.37$, $\lambda_S = 5km^{-1}$, $P_B = 1W$, $f = 3.6GHz$, $\nu = 3.5$ and no fading.

for LOS, NLOS and diffracted contributions, (6) with a LOS probability β-factor for street tiers here denoted by $\beta_s = \beta$ and (7) considering Rician fading with parameter K on LOS and NLOS contributions. In addition, the typical UE is possibly located at a crossroad with probability η_c[1] and in a street with probability $1 - \eta_c$. Its height is finally given by H_u. Note that the index $q = \{1, 2\}$ for the coverage probability $P_{c,q}$ is used to denote expressions related to a street UE and to a crossroad UE respectively.

Remark 5.1. The upcoming exposure results are here presented for the usual definition introduced in Eq. 4.47. While this definition expresses the exposure in [W], the observed levels can always be converted to other units using Eqs. (4.48) and (4.49). The same remark applies to the UE capacity defined in Eq. (4.40) and refined in Eq. (4.45).

The following numerical results have been presented in [88].

[1]This probability η_c can for instance be defined as the ratio between the streets and building widths.

Impact of the propagation mechanisms

In this section, the roles of blockages and of diffraction are successively investigated. In order to study the impact of blockages, Fig. 5.2 displays the coverage and the exposure evaluated for different LOS probabilities. For the studied cases, different values of the parameter β are considered. The analytical results are validated using MC simulations and compared to the case without blockages ($\beta = 0$). The evolution of the exposure (Fig. 5.2b) is trivially explained by the presence of NLOS links, which increases with β and reduces the received power. Regarding the coverage (Fig. 5.2a), two opposite scenarios can arise when introducing obstacles:

- Scenario 1: the serving BS is in LOS and some of the interferers are in NLOS; this enhances the coverage probability when comparing to a case with no obstacle in the network.
- Scenario 2: the serving BS is NLOS while some interferers are still in LOS; this deteriorates the coverage probability.

These scenarios explain the impact of obstacles on the coverage. When progressively increasing the blockage probability up to $\beta = 0.012$, improvements in the coverage can be observed. These improvements therefore correspond to realizations associated to above scenario 1. By contrast, further increasing β to 0.04 reduces the coverage. This decrease is in turn explained by a higher number of realizations corresponding to scenario 2 (due to the high value of β), which is detrimental to the coverage. The second scenario is tied to the nearest neighbour cell association rule as a nearby NLOS BS can serve the UE, while a wiser association rule would most likely select another LOS BS. Also, isotropic antennas limit useful received power and amplify interference, reducing data rate potential. Later, we will thus show the benefits of both association rules and beamforming.

The graphs of Fig. 5.3 quantify the influence of diffraction on the performance. For each of these graphs, coverage probabilities are shown for coverage thresholds of 0, 5, 10 and 15 dB. The continuous and dashed lines respectively represent the values obtained with and without diffracted signals taken into account. Fig. 5.3a illustrates the evolution of these probabilities as function of the street density. Furthermore, it is also possible to show that the relative impact of diffraction can be more significant in street realizations characterized by a locally low BS density. For such cases, incident powers coming from BSs located outside the user street itself can proportionally have larger impacts on the coverage. Fig. 5.3*b* illustrates

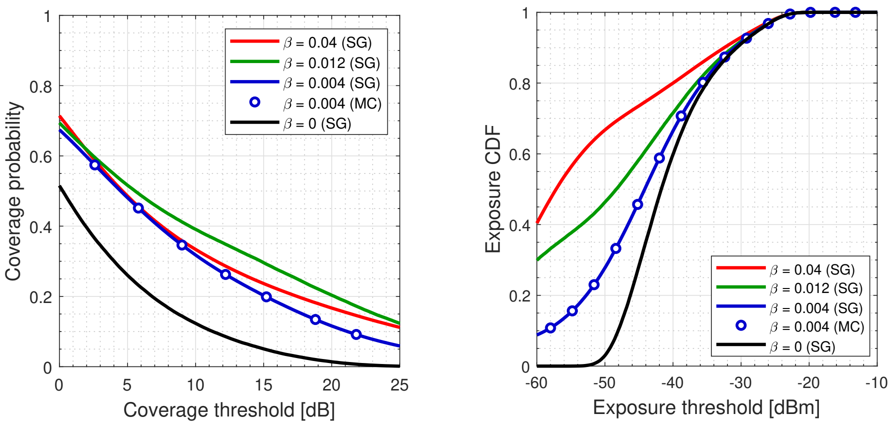

(a) Coverage probability $P_c(\theta_c)$ for an arbitrary UE.

(b) Exposure CDF $P_e(\theta_e)$ for an arbitrary UE.

Fig. 5.2 Analysis of the impact of β. The parameters selected are $h_U = 1.5m$, $h_B = 6m$, $\lambda_S = 5/km$, $\lambda_B = 5/km$, $P_B = 1W$, $f = 3.6GHz$, $\alpha_L = 1.7$, $\alpha_N = 2.5$, $\alpha_D = 3.5$, $\eta_c = 0.1$ and $K = 6$.

this statement by fixing the BS density λ_B^t in the user street and by progressively increasing the BS density in the other streets, denoted by λ_B^d in the legend. For a $5dB$ threshold, the inclusion of diffracted signals results in a decrease in coverage of around 0.06 if the BS density is identical in all streets ($\lambda_B^d/\lambda_B^t = 1$). When increasing the BS density in adjacent streets, this gap increases to 0.14 for $\lambda_B^d/\lambda_B^t = 4$.

Joint coverage and exposure distribution

Fig. 5.4 illustrates the joint coverage and exposure distribution. The SG lower bound of (4.59) is represented as function of the two thresholds θ_c and θ_e in Fig. 5.4(a). This bound is then compared to the MC simulations in Fig. 5.4(b) for fixed values of θ_c. One can observe on this graph that the probability of obtaining a low exposure decreases as the coverage threshold increases. This observation is due to the useful received power S, present in both SINR and exposure definitions. This power will statistically be high for users in good coverage, which increases for these users the probability to experience a high exposure. Some trade-offs are there-

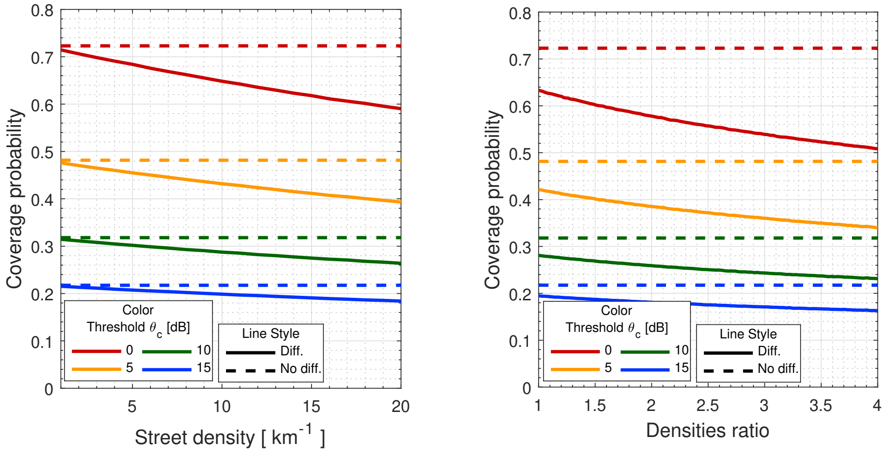

(a) Impact of λ_S on $P_{c,1}$.

(b) Impact of λ_B^d/λ_B^t on $P_{c,1}$.

Fig. 5.3 Impact of the BS and street densities. Unless stated otherwise, the selected parameters are $h_U = 1.5m$, $h_B = 6m$, $\lambda_S = 12.5km^{-1}$, $\lambda_B = 3km^{-1}$, $P_B = 1W$, $f = 2GHz$, $\alpha_L = 1.7$, $\alpha_N = 2.5$, $\alpha_D = 2.5$, $\kappa_L = \kappa_N = \kappa_D = (4\pi f/c)^2$, $\beta = 0.04$ and $K = 6$.

fore necessary in the coverage and exposure requirements.

User type comparison

Fig. 5.5 compares the performance achievable for a street (st.) UE and for a crossroad (cr.) UE. Fig. 5.5a shows the average user capacity as a function of the BS density. Independently of the UE type, one can note the existence of an optimal value for this quantity, as already shown in previous works [89]. For a low BS density, the SINR takes low values, to the detriment of the capacity. As the BS density progressively increases, the serving BS statistically becomes closer to the UE, which increases the useful received power. The densification hence enables to increase the average capacity, up to some optimum $\lambda_B = \lambda_B^{opt}$. Beyond this maximum, the improvements in useful power no longer compensate the increase of interference, resulting in a decreasing capacity. One will note that the optimal capacity associated to street users is reached for a higher BS density compared to the optimal capacity of crossroad users. This difference is due to the presence of BSs

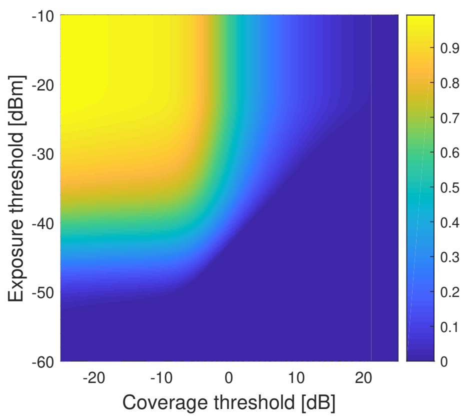

(a) Lower bound on joint metric $J(\theta_c, \theta_e)$ for an arbitrary UE.

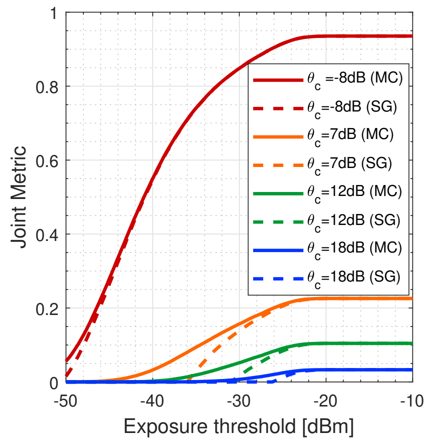

(b) Assesment of the SG lower bound for fixed values of θ_c.

Fig. 5.4 Analysis of $J(\theta_c, \theta_e)$. The parameters are $h_U = 1.5m$, $h_B = 6m$, $\lambda_S = 5km^{-1}$, $\lambda_B = 5km^{-1}$, $P_B = 1W$, $f = 3.6GHz$, $\alpha_L = 1.7$, $\alpha_N = 2.5$, $\alpha_D = 3.5$, $\kappa_L = \kappa_N = \kappa_D = (4\pi f/c)^2$, $\eta_c = 0.1$, $\beta = 0.0004$ and $K = 6$.

which is in average doubled for crossroad users (due to the two streets forming the intersection). In Fig. 5.5b, isocurves of the joint SIR-exposure metric are analysed. Each curve represents the set of thresholds (θ_c, θ_e) satisfied with probability $p \in \{0.1, 0.5, 0.85\}$, for a street or a crossroad user. One can here observe that the achievable performance of the street user is higher than the crossroad user. One justification of this difference comes from the exposure of the crossroad user, which is in average doubled compared to the street user. At a given coverage requirement, the probability for the crossroad user to satisfy an exposure threshold is therefore reduced compared to the street user.

Optimal UE capacity

Fig. 5.6a quantifies the variation of the BS density maximizing the mean capacity as a function of variables β and P_B. This optimal density increases with the blockage probability factor β. Such an increase enables to compensate for the impact of β on the probability of obtaining a NLOS serving

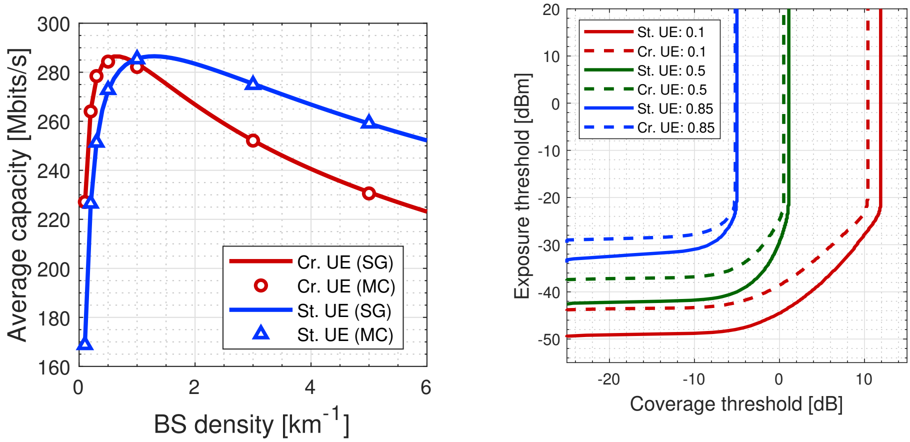

(a) Average UE capacity for $\alpha_L = 2$, $\alpha_N = 2.25$ and $W = -93dBm$.

(b) Isocurves of the joint distribution for $F(\theta_c, \theta_e) \in \{0.1, 0.5, 0.85\}$, $\alpha_L = 2.5$, $\alpha_N = 2.7$ and $W = 0W$.

Fig. 5.5 Analysis of the differences between street (st.) UE and crossroad (cr.) UE. The selected parameters are $h_U = 1.5m$, $h_B = 4.5m$, $\lambda_S = 5km^{-1}$, $\lambda_B = 5km^{-1}$ (for Fig. (b)), $f = 3.6GHz$, $\alpha_D = 3.5$, $\kappa_L = \kappa_N = \kappa_D = (4\pi f/c)^2$, $\eta_c = 0.1$, $\beta = 0.004$, $B = 100MHz$ and $K = 1$.

BS. Regarding the transmit power, the SNR values are by definition proportional to P_B and therefore decrease when its value is reduced. To compensate for this effect, the optimal BS density therefore increases to lower the PL affecting the serving BS. The corresponding maximal capacities are shown in Fig. 5.6b. One can note that even if the BS density is optimized for each pair (P_B, β), the cases of low blockage probability and high transmit power lead to the highest optimal capacity values.

5.1.2 Cox-like environments

We now consider more irregular environments. To model a structured street system, we use a NHPCLP to generate a street network. In many cities, street orientation follows certain trends as streets were constructed gradually around the city center. Although various orientations exist within the city, certain orientations are thus more commonly observed. Therefore,

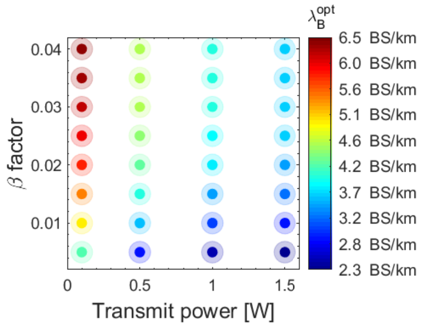

(a) Optimal BS density λ_B^{opt}.

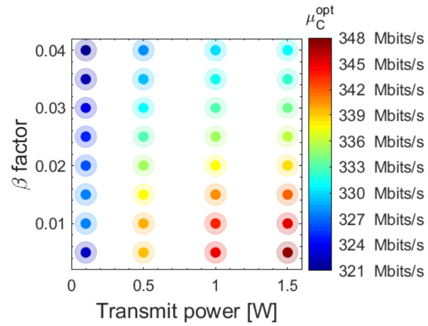

(b) Associated maximal average capacity μ_C^{opt}.

Fig. 5.6 Analysis of the UE capacity as function of β and P_B. The parameters selected are $h_U = 1.5m$, $h_B = 4.5m$, $\lambda_S = 5km^{-1}$, $\lambda_B = 5km^{-1}$, $f = 3.6GHz$, $\alpha_L = 2.5$, $\alpha_N = 2.75$, $\alpha_D = 3.5$, $\eta_c = 0.1$, $\beta = 0.004$, $\kappa_L = \kappa_N = \kappa_D = (4\pi f/c)^2$, $B = 100MHz$, $W = -93dBm$ and $K = 1$.

the thinning function utilized to create the NHPCLP should allow us to accurately model this characteristic. To that extent, we assume a NHPCLP with maximum density $\lambda_s = 0.01[(mrad)^{-1}]$ generated using a thinning function given as follows:

$$p(r,\theta) = \left[\frac{1}{6} + \sum_{\mu_i \in \mathbf{m}} \frac{5}{6} \exp\left(-\left(\frac{\theta - \mu_i}{0.3}\right)^2\right)\right] \exp\left(-\frac{r}{4000}\right)$$

where $\mathbf{m} = \{\pi/4, 3\pi/4, 5\pi/4, 7\pi/4\}$ and $0 \leq \theta \leq 2\pi$.

The above-mentioned thinning function is depicted in Fig. 5.7a. While there is a non-zero probability of generating a street in any direction, the likelihood of generating a street in the directions indicated by vector $\mathbf{m}$ is significantly higher. Moreover, it illustrates that generating streets farther away is less probable, which is often the case in cities where the street pattern tends to be denser in the city center. An example of a corresponding street pattern is shown on Fig. 5.7b. The increased organization is easily observed.

In the following analysis, we will consider two different street tiers and a single roof tier. The tiers' parameters are fixed according to the calibration approach proposed in Section 3.4. These are summarized in Tab. 5.1. In

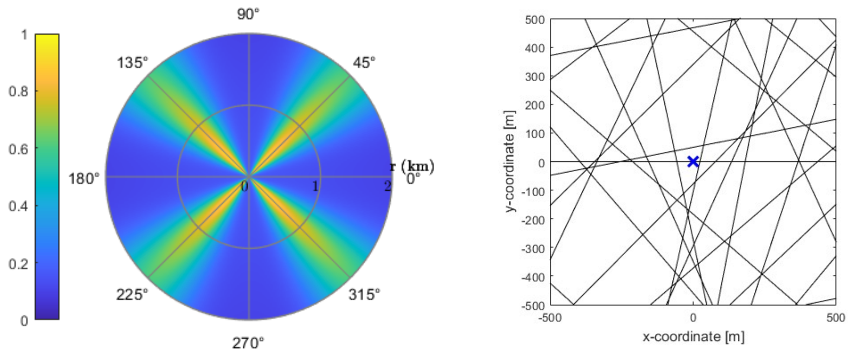

(a) Thinning probability function

(b) Corresponding type of street pattern

Fig. 5.7 Generating a city street pattern with increased organization.

addition, a loss coefficient of $K_{in} = 0.83$ that accounts for wall attenuation is here considered. The operating frequency of both types of tiers is fixed at $f = 3.6GHz$. A standard deviation of $\sigma = 50/3$ is considered to ensure that non-uniform UEs are located within a 50-meter radius of the hotspot BS with a 95% probability (cfr. Section 3.3.7). A street width of $w_s = 35m$ is assumed. Unlike in the previous section, we now implement the strongest average received power association rule along with beamforming.

Impact of the tiers densities

Our initial step in optimizing network deployment starts with the identification of the optimal densities for the street and roof tiers. To accomplish this, we multiply the initial densities by increasing multiplication factors, denoted as η_S for the street tiers and η_B for the roof tiers. In that case, the updated densities are calculated as $\eta_S \lambda_k$ and $\eta_B \lambda_{b,k}$. Figs. 5.8 and 5.9 display the results obtained for uniform UEs and non-uniform UEs, respectively. To ease the comparison, the yellow planes on Fig. 5.9 illustrate the optimal performance achieved for a uniform UE at the studied densities.

We start by observing that for a uniform UE and a low roof tier density, the coverage probability increases progressively as the densities of street tiers increase but saturates some point. On the contrary, for higher roof tier densities, increasing the street densities is directly detrimental to the global coverage probability as the service offered by roof BSs is generally

		Street tiers		Roof tier
		k=1	k=2	k=1
PL exponent (LOS)	$\alpha_{k,L}$	2.27	2.22	2.6
PL intercept ((N)LOS)	κ_L/κ_N	$10^{2.7} f_{GHz}^2$		$10^{2.5} f_{GHz}^2$
PL exponent (NLOS)	$\alpha_{k,N}$	2.4	2.35	2.8
PL exponent (Diff.)	$\alpha_{k,d}$	2.37	2.32	3.1
PL intercept (Diff.)	κ_d	$10^{3.07} f_{GHz}^{0.57}$		1
PL exponent (Build. Pen.)	$\alpha_{k,\tilde{t}}$	2.27	2.22	/
PL intercept (Build. Pen.)	$\kappa_{\tilde{t}}$	$10^{6.7} f_{GHz}^2$		/
Emit power [W]	$P_k/P_{b,k}$	2	2	20
Height [m]	$H_k/H_{b,k}$	6	10	5 (+25)
Density $[km^{-1}]/[km^{-2}]$	$\lambda_k/\lambda_{b,k}$	2	1	3
LOS prob. β-factor	$\beta_{S,k}/\beta_{B,k}$	0.009	0.008	0.005
Beamforming gain [dBi]	G_1/G_2	18/5		6/-7

Table 5.1 Summary of the tiers parameters used in the simulations.

self-sufficient and only additional interference is created.

Moreover, a densification of roof BSs results in a quick then gradual increase in coverage probability. One can observe that a strong interfering BS typically meets three conditions: (1) it has a geometric LOS condition, meaning there are no buildings obstructing the LOS link, (2) there are no obstacles in the UE street that block the LOS link, and (3) the power contributions under the considered beamforming scheme are non-negligible in the UE direction. These BSs are generally located along the UE street, as shown in Fig. 3.4. In our framework, roof BSs are located close to building rooftops and have narrower beams, resulting in a low probability of having such a strong interfering BS. By densifying roof BSs, the probability of having a serving LOS roof BS for which the beam is automatically directed towards the UE increases, with limited risk that a strong interfering roof BS actually exists. This explains the gradual increase in coverage probability. However, beyond a certain densification point, the performance is still expected to deteriorate. Note that this only occurs at unrealistic densities for the considered MBs height. This point will thus be illustrated in the following section for higher MBs heights.

Additionally, we can observe that the global coverage probability achieved at low street tier densities by progressively increasing the density of roof base stations (BS) cannot be reached by densifying street tiers. These observations lead us to believe that adding small cells to the existing cellular network may worsen the global coverage probability. These findings are consistent with the results presented in [60]. Note that this does not necessarily imply that the use of small cells should be completely avoided. It simply means that their usage may have a negative impact on the average coverage probability across all possible UEs and network topologies. For some UEs and for some topologies, the use of small cells can still be beneficial. In addition, at the considered densities, it is still possible to provide all UEs with a minimum QoS (i.e. correspondig to a minimum SINR of -6.5dB) with a probability that is sufficiently high.

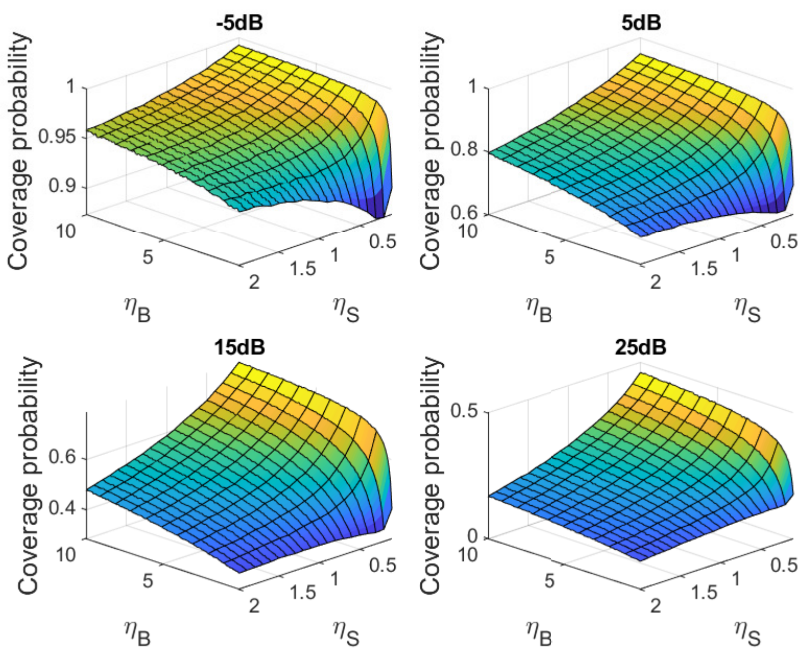

Fig. 5.8 Impact of tier densities on the coverage probability $P_c(\theta_c)$ for a uniform UE at various SINR thresholds

Furthermore, as depicted in Fig. 5.9, a sparse but strategic deployment of small cells can provide non-uniform UEs with a higher probability of achieving higher SINR values. A complementary densification of roof BSs can then be utilized to further improve the coverage of uniform UEs in the network and ensure a minimum QoS for all UEs, while minimizing any negative impact on the high SINR values of non-uniform UEs. On the contrary, further densification of the street tiers can lead to significant degradation of the performance of non-uniform UEs while offering little to no improvement for uniform UEs. Beyond a certain density of roof BSs, the coverage of uniform UEs may even worsen if street tiers are densified.

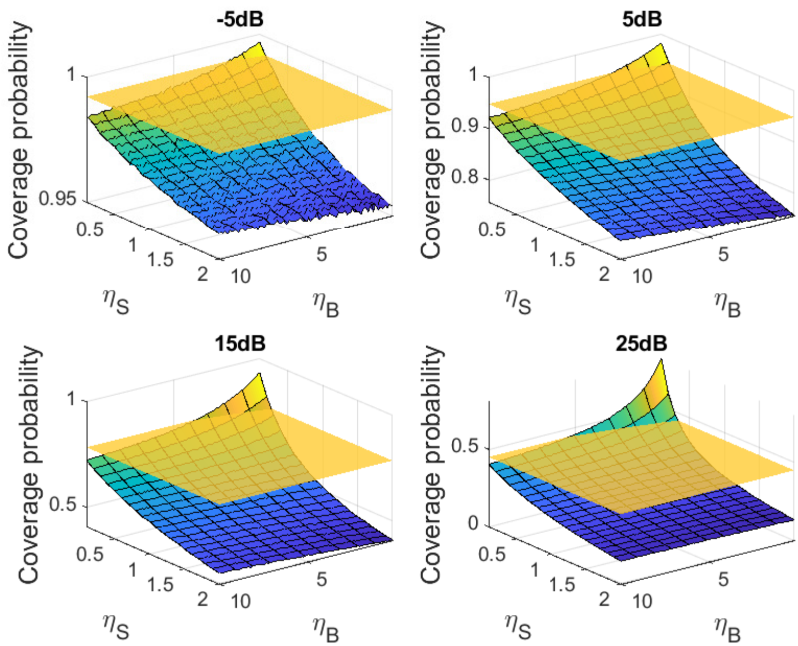

Fig. 5.9 Impact of tier densities on the coverage probability $P_c(\theta_c)$ for a non uniform UE at various SINR thresholds.

Impact of the roof base station height

We will now examine the influence of the MBs height on the network performance. Specifically, we will analyze the effects of a MBS height of $H_{b,k} = 45m$ (+25m) in this section. As per the calibration approach, the PL exponent associated with diffraction is changed to $\alpha_{k,D} = 2.98$. Fig. 5.10 illustrates the impact of raising the MBs height from 30m to 70m on the overall coverage probability for various SINR thresholds at low street tiers

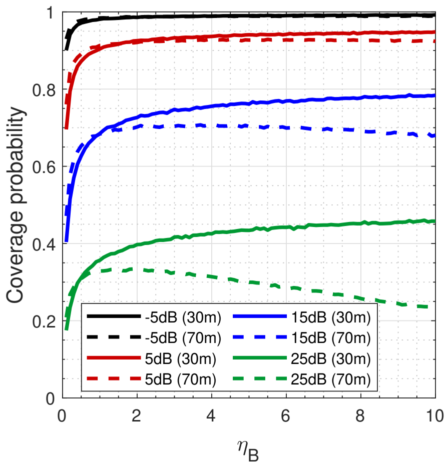

Fig. 5.10 Impact of the roof base station height on the coverage probability $P_c(\theta_c)$ for a uniform UE at low street tiers densities ($\eta_S = 0.1$).

densities. Two key observations can be made from the figure. First, as the height increases, the optimal coverage probability is consistently lower due to several factors such as the increased probability of having LOS interfering BSs, the greater distance to the serving BS, and the amplified diffracted contributions. Secondly, within the range of densities studied, an optimal density can now be identified. Unlike when the MBs height is fixed at 30m, the interference from non-serving roof base stations (BSs) becomes more severe, leading to an earlier drop in the coverage probability during the densification process. This drop is particularly critical for high SINR values.

Performance evaluation for fixed densities

Based on the tendencies observed in the previous sections, we will now definitely fix the densities to $\lambda_1 = 0.6km^{-1}$, $\lambda_2 = 0.3km^{-1}$ and $\lambda_{b,1} = 4.2km^{-2}$. Fig. 5.11 exhibits the achieved performance for both uniform and non-uniform UEs. Non-uniform UEs are shown to attain higher SINR values, and consequently higher throughputs, with higher likelihoods, at the cost of increased exposure due to proximity to the serving BS. These exposure levels however remain below the legal threshold imposed in Brussels.

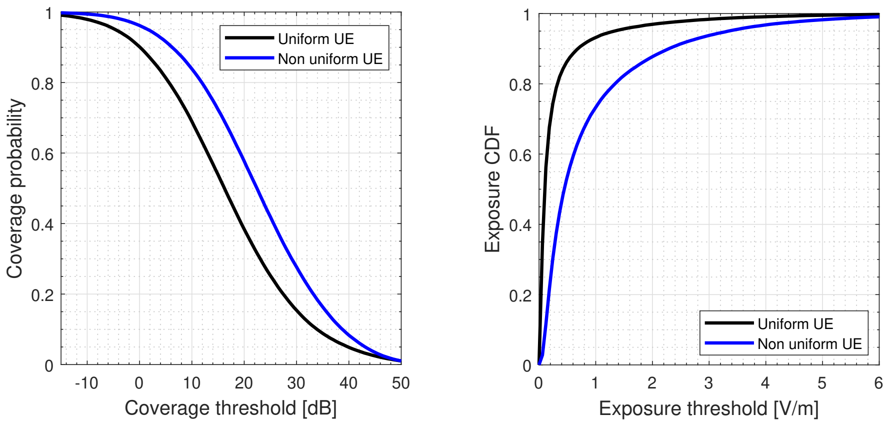

(a) Coverage probability $P_c(\theta_c)$.

(b) Exposure CDF $P_e(\theta_e)$.

Fig. 5.11 Performance analysis of both types of UEs. The densities are $\lambda_1 = 0.6km^{-1}$, $\lambda_2 = 0.3km^{-1}$ and $\lambda_{b,1} = 4.2km^{-2}$.

Using the lookup table proposed in Tab. 4.2, we can determine the probabilities that different modulation schemes can be used with negligible errors. It is demonstrated that a minimum QoS can be provided to the UE with respective probabilities of 96% and 99% for uniform and non-uniform UEs.

Impact of beamforming

We will demonstrate the impact of the beamforming scheme on the network performance. Initially, we considered using antennas with half-beam widths of $\gamma_S = 43°$ for street BSs and $\gamma_B = 2.7°$ for roof BSs. Now, we will examine the effects of using isotropic antennas, antennas with broader beams, and antennas with narrower beams. The respective gains on the main lobe of these antennas are (G_S,G_B)=(0dBi,0dBi), (G_S,G_B)=(15dBi,3.3dBi), and (G_S,G_B)=(19.3dBi,7.3dBi) for street and roof tiers. The antennas with broader and narrower beams are respectively characterized by half-beam widths (γ_S,γ_B) = (80°,5°) and (γ_S,γ_B) = (31°,2°). Fig. 5.12 shows the performance differences in terms of coverage probability and exposure CDF.

Narrower beams have been demonstrated to greatly improve the over-

Modulation	Coding Rate	Throughput [Mbps]	Probability un. UE	Probability non un. UE
out of range			0.04	0.01
QPSK	0.0762	22	0.96	0.99
QPSK	0.1172	33	0.95	0.98
QPSK	0.1885	52	0.93	0.97
QPSK	0.3008	81	0.90	0.96
QPSK	0.4385	113	0.86	0.94
QPSK	0.5879	147	0.83	0.92
16QAM	0.3691	179	0.79	0.90
16QAM	0.4785	226	0.74	0.87
16QAM	0.6016	277	0.68	0.83
64QAM	0.4551	311	0.64	0.80
64QAM	0.5537	370	0.57	0.75
64QAM	0.6504	425	0.50	0.69
64QAM	0.7539	486	0.42	0.62
64QAM	0.8525	545	0.35	0.55
64QAM	0.9258	589	0.31	0.49

Table 5.2 Probabilities to offer the typical UE a given throughput for an available bandwidth of $100MHz$.

all coverage probability. This is due to two factors: a higher power concentration towards the UE and a limited interference resulting from the simultaneous use of beamforming by interfering BS. As shown in Fig. 5.12b, a stronger useful signal is the primary contributing factor. In fact, the exposure level measurement is largely determined by the power received from the useful BS which is higher when a narrower beam is used. At the considered densities, the useful received power thus predominates the SINR value, as the interference level remains relatively low regardless of the beamforming scheme used.

Impact of fading

In this section, we will inspect the impact of fading on the useful link. Specifically, we will analyze Rician fading with a K-factor ranging from 0 to 5. A higher value of the K-factor indicates that the stronger path predominates over the other paths, resulting in a reduced potential for destructive interference on the useful link. Consequently, we expect the final received power to be closer to the power on the strongest path. This phenomenon is illustrated in Fig. 5.13, where we observe that, at a constant

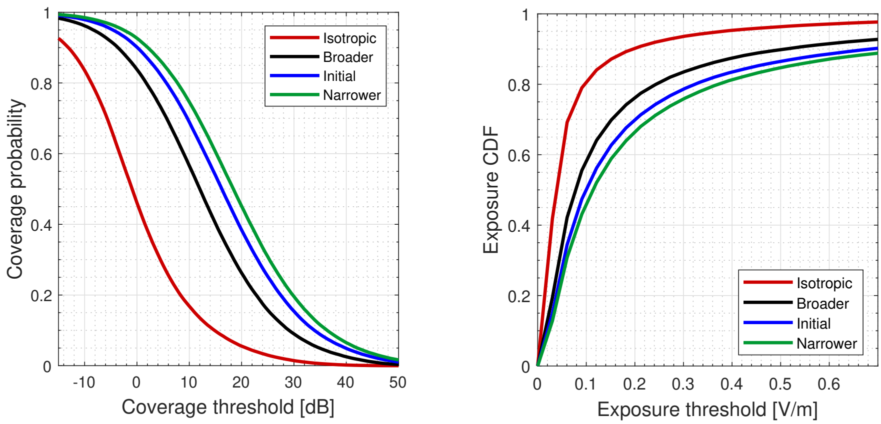

(a) Coverage probability $P_c(\theta_c)$ **(b)** Exposure CDF $P_e(\theta_e)$

Fig. 5.12 Network performance under different beamforming schemes.

SINR threshold, the coverage probability increases with a higher K-factor.

Impact of the UE non-centrality

As previously explained, when analyzing the network using the NHPCLP, the results observed at a typical central UE may not represent the entire network accurately as we have lost the motion-invariance property of PPs. To determine the impact of the UE's non-centrality, we studied a UE located at increasing distances from the city center, where the street density is assumed to be the highest. We chose UEs located at distances of 1096m, 2228m, 3371m, and 4514m. Since street density decreases as we move away from the city center, the interference caused by intersecting streets is lower at greater distances. As the UE performance is primarily affected by its serving BS for the considered densities, the performance difference is most noticeable at high SINR values. Although the performance of a UE located in the city center is shown to be lower than that of a UE in the suburbs, the actual difference is not significant as depicted in Fig. 5.14.

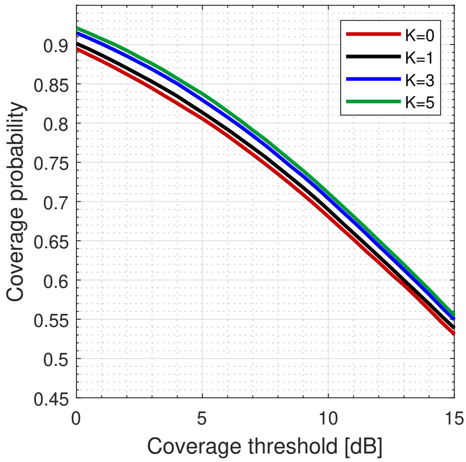

Fig. 5.13 Impact of fading on the coverage probability $P_c(\theta_c)$.

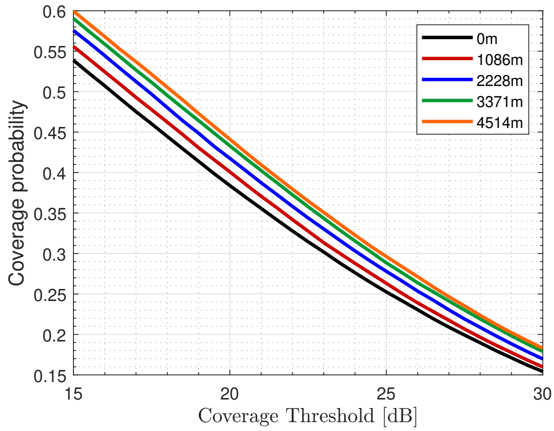

Fig. 5.14 Coverage probability $P_c(\theta_c)$ for a UE located at an increasing distance from the city center.

5.2 Sparse urban environments and rural environments

We will now evaluate areas with lower building density. As previously mentioned, BSs located significantly below the rooftop level and on different streets do not exclusively interact with the UE via building corner diffraction in sparser environments. Rather, they may interact with the UE in LOS with non-zero probability. Similarly, the probability of LOS for roof-mounted BSs is generally higher at the same distance due to a reduced concentration of buildings, and hence may not be limited exclusively to BSs installed on buildings located along street where the UE is located. As explained in Section 3.3.9, modeling such environments requires several modifications. The tiers parameters are modified as shown in Tab. 5.3. Note that $\alpha_{k,\tilde{t},N}$ is the PL exponent for NLOS contributions coming from non typical streets and $\kappa_{\tilde{t},N}$ is the associated PL intercept.

	Street Tiers (suburban)		Roof Tier (suburban)	Street Tiers (rural)		Roof Tier (rural)
	k=1	k=2	k=1	k=1	k=2	k=1
$\alpha_{k,L}$	2.02	1.97	2.38	1.8	1.75	2.15
κ_L	$10^{2.92} f_{GHz}^{2}$		$10^{2.72} f_{GHz}^{2}$	$10^{3.22} f_{GHz}^{2}$		$10^{3.02} f_{GHz}^{2}$
$\alpha_{k,N}$	2.17	2.12	2.8	1.95	1.9	2.5
κ_N	$10^{2.92} f_{GHz}^{2}$		$10^{2.4} f_{GHz}^{2.3}$	$10^{3.22} f_{GHz}^{2}$		$10^{4.07} f_{GHz}^{2.13}$
$\alpha_{k,\tilde{t},N}$	3.53	3.48	/	2.5	2.45	/
$\kappa_{\tilde{t},N}$	$10^{1.94} f_{GHz}^{2.13}$		/	$10^{3.61} f_{GHz}^{1.96}$		/
$\beta_{S,k}$	0.012	0.011	/	0.004	0.003	/

Table 5.3 Modification of the tiers parameters for suburban and rural environments.

We then applied the same densification process used for urban environments and analyzed the resulting coverage probability, which is illustrated in Fig. 5.15. The performance for a uniform UE in suburban and rural areas are respectively depicted in Fig. 5.15a and 5.15b. We specifically focused on the performance of the SINR threshold (-6.5dB) that enables us to provide the UE with a minimum QoS. Our findings suggest that even very low street tier densities can pose challenges, as the probability of being out of range quickly exceeds the 5% threshold usually targeted by operators. While small cells deployments may still be acceptable in suburban environments, they should not be recommended in rural areas. Though, macrocell BSs are shown to provide sufficient coverage even at low roof tier densities, which is consistent with current rural deployments.

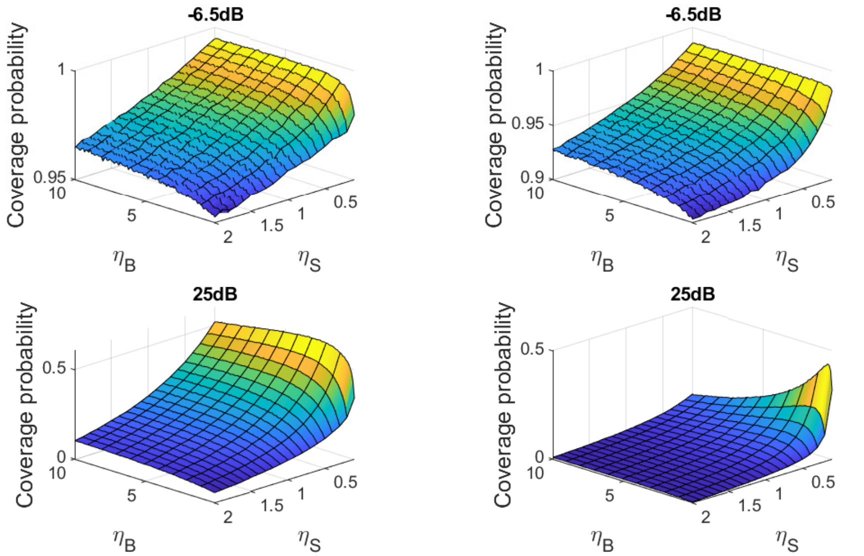

(a) Coverage probability $P_c(\theta_c)$ in suburban environments.

(b) Coverage probability $P_c(\theta_c)$ in rural environments.

Fig. 5.15 Impact of tier densities on the coverage probability $P_c(\theta_c)$ for a uniform UE at various SINR thresholds

As the environment becomes sparser, the coverage probability for the same SINR threshold and tier densities decreases due to the increased interference caused by a more open space. Indeed, the increase in interference cannot be compensated by a smaller PL on the useful link. This effect is particularly noticeable at high SINR values. In rural environments, this effect is especially pronounced, as a SINR of 25dB is almost never reached.

Tab. 5.4 summarizes the association probabilities to the different tiers in the network. As expected, in sparser environments, the probability that a UE will associate itself with non-typical street and roof tiers is higher, while the probability of associating with a BS on the same street is lower. It is noteworthy that the probability of a UE associating itself with a urban small cell BS located in another street is close to zero due to severe building penetration losses. For mathematical tractability, remember that only the contribution received through building penetration can be accounted for in our association rule. As such, the real probability may be slightly higher.

	Association probabilities		
	Urban	Suburban	Rural
Typical street tiers	0.4811	0.2984	0.2096
Non typical street tiers	0.0001	0.1715	0.2237
Roof tier	0.5188	0.5301	0.5667

Table 5.4 Association probabilities in the different environments for the same densities.

5.3 A few words on the numerical complexity

One of the main reasons for developing SG-models is their ability to quickly provide insights on how macro parameters affect the overall performance of a network. This is particularly true for models that exclusively use PPPs. However, this work proposes increased flexibility which leads to a significant increase in numerical complexity. Some of the integrals in the model cannot be solved using standard mathematical methods and must be computed numerically. These integrals may also be nested within other integrals, causing the model's complexity to significantly increase.

As an example, we compare the computational times required to evaluate the coverage probability (cfr. Eq. (4.33)) using MC simulations and stochastic geometry. All computations are performed with MATLAB R2022a on a computer equipped with the processor Intel(R) Core(TM) i7-7700K CPU @ 4.20GHz. The integrals involved are computed using the MATLAB *integral.m* built-in function. This function uses the global adaptive quadrature method that subdivide the integration regions based on largest error until the global error is sufficiently small. It attempts to satisfy $|q - Q| \leq \max(AbsTol, RelTol * |q|)$ where q is the computed value of the integral, Q is the (unknown) exact value and AbsTol and RelTol are respectively the

	a=1	a=5	a=10	a=20
Number of evaluation points	150	510	810	1770

Table 5.5 Evolution of the number of function evaluations for the computation of $\int_0^{10} \exp\left(\cos\left(ax\right)\right)dx$ using the global adaptive quadrature method.

absolute and relative tolerances. For fixed tolerances, the number of required function evaluations depends on the oscillatory characteristics of the integrated function. The more it oscillates, the higher the number of evaluation points is as shown for the integration of $\exp\left(\cos\left(ax\right)\right)$ between 0 and 10 on Tab. 5.5. In most of the studied metrics, the use of the Gil-Pelaez theorem generally includes the computation of oscillatory integrals which therefore increases the overall complexity.

In our comparison, the selected parameters are $h_U = 1.5m$, $h_B = 6m$, $\lambda_S = 12.5km^{-1}$, $\lambda_B = 3km^{-1}$, $P_B = 1W$, $f = 2GHz$, $\alpha_L = 1.7$, $\alpha_N = 2.5$, $\alpha_D = 2.5$, $\kappa_L = \kappa_N = \kappa_D = (4\pi f/c)^2$, $\beta = 0.04$ and $K = 6$. The considered doubly stochastic process has an intensity measure $\Lambda_\Phi(drd\theta) = \lambda_S(0.5\delta_0 + 0.5\delta_{\pi/2})drd\theta$. No beamforming is assumed and the closest BS association rule is considered. The number of MC iterations is fixed to obtain the desired accuracy. The error tolerances are fixed similarly for the SG approach. The time required to run 10^5 MC iterations is 535 seconds. Depending on the considered coverage threshold, the time required using SG lies between 118 and 177 seconds. Note that the times indicated for SG are given for a single coverage threshold evaluation. By contrast, MC simulation enable the computation of the entire SINR CDF with a single run. This illustrates how the runtime gap between MC ang SG starts to decrease with respect to pioneering works where the SG expressions were more tractable. Adding more integrals (e.g. by studying more complex scenarios) further reinforces this last observation.

If we stick to the current framework, either simplifications must be made or the modeler then loses one of the main advantages of SG-based models. Alternatively, future works could be dedicated to the exploration of advanced techniques to enable faster evaluation of such categories of integral.

6

Full validation of stochastic geometry-based models

In recent years, numerous models based on stochastic geometry have been developed. In most cases, these models are validated using Monte Carlo (MC) simulations. Such simulations help to ensure the mathematical accuracy of the expressions developed. However, it remains uncertain whether these models are accurate in the first place. In fact, MC simulations do not enable us to check whether the model itself yields results similar to what would be observed with an actual deployment. In this chapter, we will therefore attempt to further support the results obtained using stochastic geometry and highlight their limitations when necessary. We will pursue two main directions. Firstly, we will run MC simulations that use a deterministic channel model, namely ray tracing, as the propagation model. This will enable us to verify whether the use of simpler propagation models in our stochastic geometry models may endanger the relevance of our conclusions. Then, we will validate the use of doubly stochastic models to model dense urban deployments by comparing them to real cities whose topologies have been extracted from open-access databases.

6.1 Related works

Many works focus on the analysis of emerging networks using pure SG approaches. However, a very limited number of publications propose validations of these SG models using other methods (comparison to datasets, measurements, or softwares capturing additional electromagnetic mechanisms such as diffraction or scattering, etc). In [90], the PPP assumption for the deployment of BSs is assessed using experimental data. By comparison to real deployments of two mobile operators in United Kingdom, this abstraction is shown to be sufficiently accurate in terms of coverage probability. More recently, [91] validated a radar detection analysis using a hybrid of MC and full wave electromagnetic solver based simulations. The simulations were performed using FDTD techniques. [86] conducted a study where they calibrated and compared a SG-based model for the evaluation of the exposure CDF. The researchers used experimental data gathered from two municipalities located in Brussels to perform this analysis. [51] demonstrates that the MPLP is a reliable method for characterizing the ergodic rate in Manhattan networks. This finding was based on a comparison with both the fixed grid model and actual street deployment data from Chicago extracted using the QGIS software. No validation of SG models using other tools (e.g. RT) can be found in the literature.

6.2 Comparison to deterministic channel models

The network topology described in Section 5.1.1 is now equally studied using ray tracing. Only the LOS probability is modified as $p_L(r) = e^{-\beta r^{\gamma}}$.

6.2.1 Ray tracing network topology

In the framework of the RT simulations, the studied environments are identical to the SG model, up to the following modifications:

- Streets are given a non-zero width w_S.
- BSs are located on sidewalks. In a given street, the sidewalk on which each BS is located is randomly chosen. For the sake of practical RT

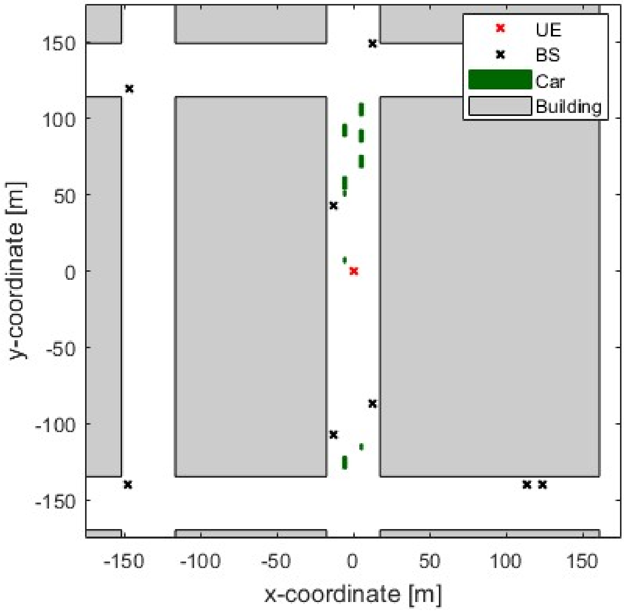

Fig. 6.1 Illustration of an environment generated for ray tracing analysis.

implementation, those are placed at a slight distance $d_{B,BU}$ from the buildings walls.

- In order to model obstacles, parallelepipeds (representing cars and trucks) are generated with density λ_O in the typical street(s). The dimensions of cars is fixed to $L \times l \times H = 3.5m \times 1.5m \times 2m$ for cars and to $L \times l \times H = 8m \times 2.5m \times 3m$ for trucks. While the blockage model of the SG framework considers independent blockage probabilities, these obstacles here induce spatial correlations in the blockages experienced by adjacent BSs.

These modifications are illustrated on Fig. 6.1.

6.2.2 Ray tracing power computation

While many propagation mechanisms exist, only two types are taken into account by the UCLouvain tool: reflection and diffraction (i.e. scattering and other more complex mechanisms are here disregarded). In addition,

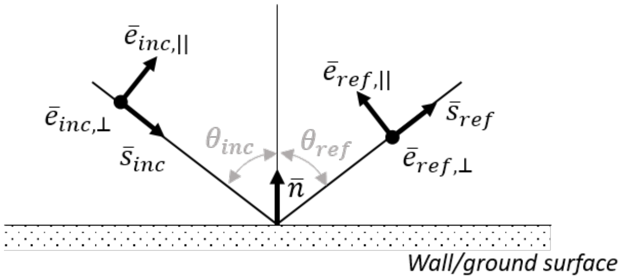

Fig. 6.2 Conventions used for reflection (reproduced from [92])

only outdoor to outdoor scenarios are considered which means both the UE and the BS are exclusively located outside the buildings and so are the paths we identify between these. To keep the computational time in a reasonable range, at most two interactions are considered. Diffraction is only acknowledged on the last interaction. These hypotheses seem not to be too restrictive as an electromagnetic wave which undergone more than two interactions or more than one diffraction is strongly attenuated. Below, you will find how the electrical fields $\in \mathbb{R}^3$ are computed when undergoing the different propagation mechanisms. One will denote the distance between positions X and Y by d_{XY}.

Line of sight contributions

Let $\bar{e}_0$ be the unit vector aligned with the transmitted electric field. The LOS field received from a BS located in B at an observation point P is given by:

$$\bar{e}_{LOS}\left(P\right) = \bar{e}_0 \frac{e^{-jkd_{BP}}}{d_{BP}} \tag{6.1}$$

where k is the wave number.

Reflection

The conventions used for reflection are depicted in Fig. 6.2. Let Q be a reflection point. Using Fresnel dyadic coefficients $\overline{\overline{R}}$, the reflected field $\bar{e}_{ref}\left(P\right)$ at observation point P is given by:

$$\bar{e}_{ref}\left(P\right) = \overline{\overline{R}} \cdot \bar{e}_{LOS}\left(Q\right) \frac{d_{BQ}}{d_{BQ} + d_{QP}} e^{-jkd_{QP}} \tag{6.2}$$

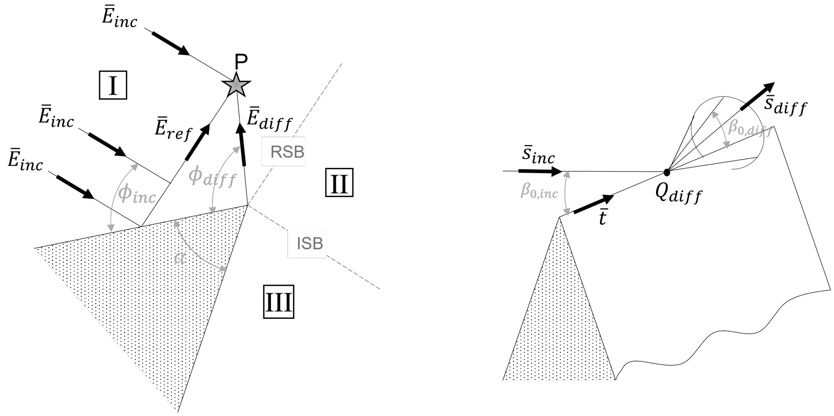

Geometry for diffraction from a wedge *Cone of diffracted rays*

Fig. 6.3 Conventions used for diffraction (reproduced from[92])

where $\overline{\overline{R}}$ are the Fresnel dyadic coefficients computed as follows [92]:

$$\overline{\overline{R}} = R_{\parallel}\bar{e}_{inc,\parallel}\bar{e}_{ref,\parallel} + R_{\perp}\bar{e}_{inc,\perp}\bar{e}_{ref,\perp} \tag{6.3}$$

with

$$R_{\parallel} = \frac{\epsilon_{r,eff}\cos\left(\theta_{inc}\right) - \sqrt{\epsilon_{r,eff} - \sin^2\left(\theta_{inc}\right)}}{\epsilon_{r,eff}\cos\left(\theta_{inc}\right) + \sqrt{\epsilon_{r,eff} - \sin^2\left(\theta_{inc}\right)}} \tag{6.4}$$

$$R_{\perp} = \frac{\cos\left(\theta_{inc}\right) - \sqrt{\epsilon_{r,eff} - \sin^2\left(\theta_{inc}\right)}}{\cos\left(\theta_{inc}\right) + \sqrt{\epsilon_{r,eff} - \sin^2\left(\theta_{inc}\right)}} \tag{6.5}$$

where θ_{inc} is the incidence angle with respect to the plane normal as shown on Fig. 6.2 and $\epsilon_{r,eff}$ is the relative electrical permittivity.

Diffraction

The conventions used for diffraction are depicted in Fig. 6.3. Let S be a diffraction point. Using uniform theory of diffraction (UTD), the diffracted field $\bar{e}_{diff}\left(P\right)$ at observation point P is given by

$$\bar{e}_{diff}\left(P\right) = \overline{\overline{D}} \cdot \bar{e}_{LOS}\left(S\right)\sqrt{\frac{d_{BS}}{d_{SP}\left(d_{BS} + d_{SP}\right)}}e^{-jkd_{SP}} \tag{6.6}$$

where $\overline{\overline{D}}$ are the UTD dyadic coefficient computed as follows [92]:

$$\overline{\overline{D}} = -D_s \overline{\beta}_{0,inc} \overline{\beta}_{0,diff} - D_h \overline{\phi}_{inc} \overline{\phi}_{diff} \tag{6.7}$$

$$\overline{\phi}_{inc} = \frac{\overline{s}_{inc} \times \overline{t}}{\left|\overline{s}_{inc} \times \overline{t}\right|} \tag{6.8}$$

$$\overline{\phi}_{inc} = \frac{\overline{t} \times \overline{s}_{diff}}{\left|\overline{t} \times \overline{s}_{diff}\right|} \tag{6.9}$$

$$\overline{\beta}_{0,inc} = \overline{\phi}_{inc} \times \overline{s}_{inc} \tag{6.10}$$

$$\overline{\beta}_{0,diff} = \overline{\phi}_{diff} \times \overline{s}_{diff} \tag{6.11}$$

where $\overline{t}$ is a unitary vector tangent to the edge, $\overline{s}_{inc}$ is the unit incident direction vector, $\overline{s}_{diff}$ is the unit diffracted direction vector. Initially, the coefficients D_s and D_h should be computed as in [92]. However, to ensure reciprocity by changing the face assignment ("o-" or "n-faces") depending on the region from which the incident ray is coming, we use Guevara's coefficients instead. The angles used to compute Fresnel reflection coefficients are then also slightly adapted as explained in [93]. Their mathematical expressions are omitted in this document

Final received power

Finally, since $\overline{e}_0$ is normalized at the emission, the received power at a typical user location i^* from a given BS j is given by

$$P^{(RT)}_{i^*j} = P_B \left(\frac{4\pi f}{c}\right)^{-2} ||\overline{e}_{tot} \cdot \overline{e}^H_{tot}|| \tag{6.12}$$
$$\text{with} \quad \overline{e}_{tot} = \sum_{n=1}^{N_{paths}} \overline{e}_{n,j}$$

where

- N_{paths} is the number of paths coming from this BS and arriving at the typical user under the considered hypotheses.
- P_B is the transmit effective isotropic radiated power.
- c is the speed of light.
- $\overline{e}_{n,j}$ are the electric fields at i^* computed by means of Eqs. (6.1), (6.2) and (6.6).

6.2.3 Methodology to fix the parameters

In order to compare the SG and RT approaches, the parameters of the two frameworks should be coherently selected. Tab. 6.1 summarizes these macroparameters.

Parameters common to the RT and SG frameworks
R, h_U, h_B, λ_S, λ_B, P_B, B and f
Parameters specific to the RT framework
w_S, $d_{B,BU}$ and λ_O. Ground permittivity: $15 - 1.50j$ (cfr. p. 66-67 of [92]) Building permittivity: $5.3 - 0.42j$ (cfr. p. 66-67 [92])
Parameters specific to the SG framework
β, γ, α_L, α_N, α_D, κ_L, κ_N, κ_D, η_c fading models

Table 6.1 Parameters employed in the SG and RT frameworks.

In the considered case study, the parameters of the first and second line of Tab. 6.1 were set to $R = 2km$, $h_U = 1.5m$, $h_B = 6m$, $\lambda_S = 5km^{-1}$, $\lambda_B = 5km^{-1}$, $P_B = 1W$, $B = 100MHz$, $f = 3.6GHz$, $w_S = 35m$, $d_{B,BU} = 5m$ and $\lambda_O = 20km^{-1}$. We also set $\kappa_L = \kappa_N = \kappa_D = (4\pi f/c)^2$ and $\alpha_D = 3.5$.

From a sufficient amount of RT simulations, we are then able to estimate the other SG parameters based on the statistics of the RT results. The methodology consists of the following steps:

Step 1. RT simulations are performed for a large number of realizations of the MPLP. At each iteration, the received powers $P_{i^*j}^{(RT)}$ at the typical UE are computed using Eq. (6.12). The propagation condition (LOS or NLOS) of each link is also assessed.

Step 2. Based on the statistics of these received powers, the parameters β, γ, α_L and α_N are computed using a RMSE method. The contributions in the typical street(s) are sorted by increasing distance and the PL coefficients that minimize the RMSE observed with the function $P_B\kappa_L r^{-\alpha_L}$ for LOS links and $P_B\kappa_N r^{-\alpha_N}$ for NLOS links are computed. The approach is then used for β and γ by minimizing the RMSE between the observed LOS probability and the function $p_L(r)$.

Step 3. The corresponding fading distribution $f_G(g)$ is then deduced from the PL free received powers computed as $(P_{i^*j}^{(RT)})/(P_B\kappa_L r^{-\alpha_L})$ for

LOS links and $(P_{i^*j}^{(RT)})/(P_B\kappa_N r^{-\alpha_N})$ for NLOS links. An analytical fading model is selected to approximate this empirical distribution.

Step 4. The parameter η_c is independently determined by computing the percentage of users located at crossroads in the RT simulations.

The fitted values obtained in step 1 are $\beta = 0.004$, $\gamma = 0.85$, $\alpha_L = 1.66$, $\alpha_N = 1.93$. The comparison with RT observations for the LOS probability and the PL analysis for LOS links are respectively depicted in Figs. 6.4a and 6.4b.

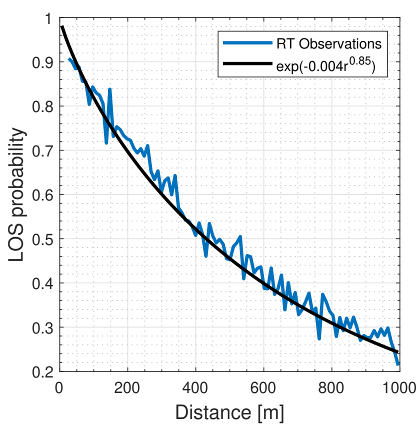

(a) LOS probability: RT vs SG

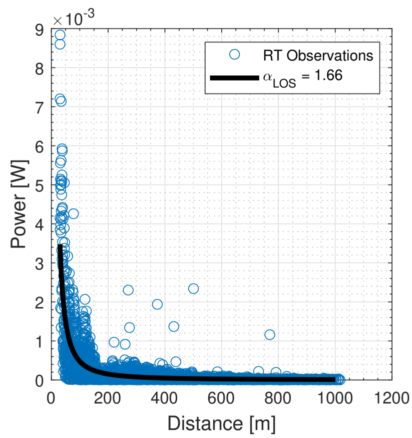

(b) PL model for LOS links: RT vs SG

Fig. 6.4 Selection of the PL parameters (step 2): RT vs SG.

The squared fading gains (i.e. fading powers) of the LOS and NLOS links are then approximated with exponential distributions of rate parameters 1.66 and 0.33 respectively. The comparison with RT observations for the fading model on LOS links is illustrated on Fig. 6.5. The crossroad probability is finally given by $\eta_c = 0.02$.

6.2.4 Numerical results and discussion

Both frameworks were compared for the parameters obtained in the previous section. Figs. 6.6a and 6.6b illustrate the coverage and exposure distributions. The slight differences between the RT and SG curves can be

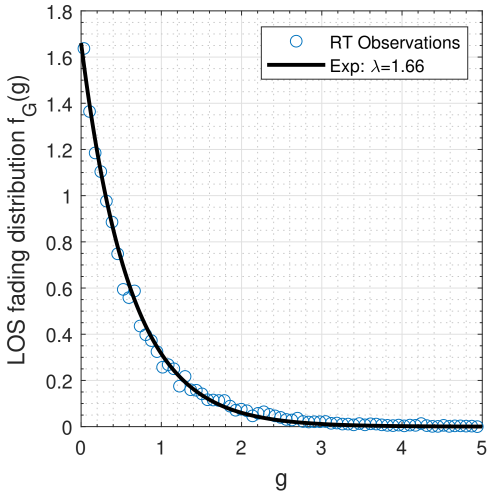

Fig. 6.5 Selection of the fading model of LOS links (step 3): RT vs SG.

explained by means of Fig. 6.6c. This figure shows the CDFs of the useful and interfering powers: $P\left(S > \theta_p\right)$ and $P\left(I_L + I_N + I_D > \theta_p\right)$ where I_L, I_N and I_D are the interference levels coming from LOS and NLOS BSs in the typical street and from diffraction. One can observe that the contribution of the serving BS in SG is slightly overestimated compared to the RT values. This results in coverage and exposure probabilities which are overestimated as well. Figs. 6.6a and 6.6b also illustrate the results obtained when SG fading parameters are not optimized with respect to the RT tool. In that case, only the path loss parameters are optimized and the SG fading distribution is taken as normalized Rayleigh (i.e. with squared channel gains modelled via an exponential distribution of unit rate). One will note the loss of accuracy obtained when both path loss and fading aspects are not optimized.

Fig. 6.7 illustrates the sensitivity of the SG model to potential errors in the estimated path loss exponents. Estimation errors of 5 and 10 percents are introduced. The impact on the distributions of the useful power and of the interference is shown in 6.7a and 6.7b. One can observe that these errors can lead to significant deviations, which highlights the importance of accurately extracting the parameters if SG is to be used.

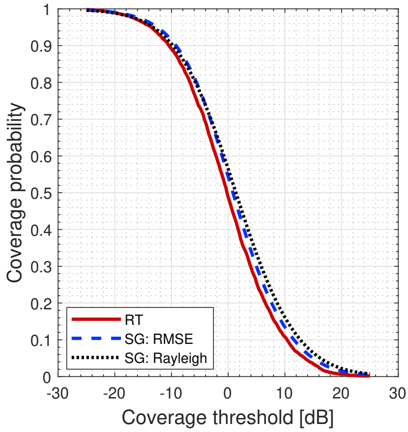

(a) Coverage probability $P_c\,(\theta_c)$.

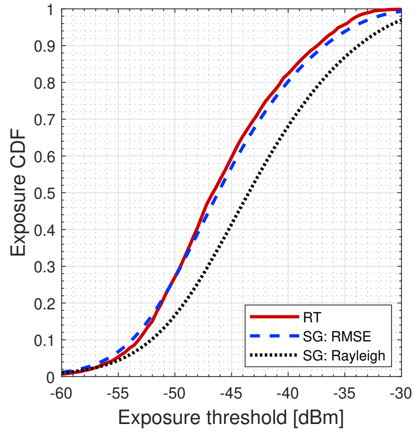

(b) Exposure CDF $P_e\,(\theta_e)$.

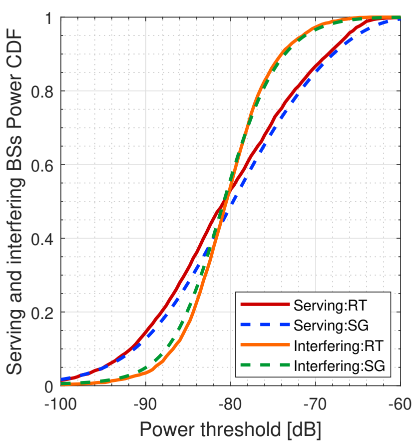

(c) Received and interfering powers (RMSE only)

Fig. 6.6 Comparison of SG and RT approaches.

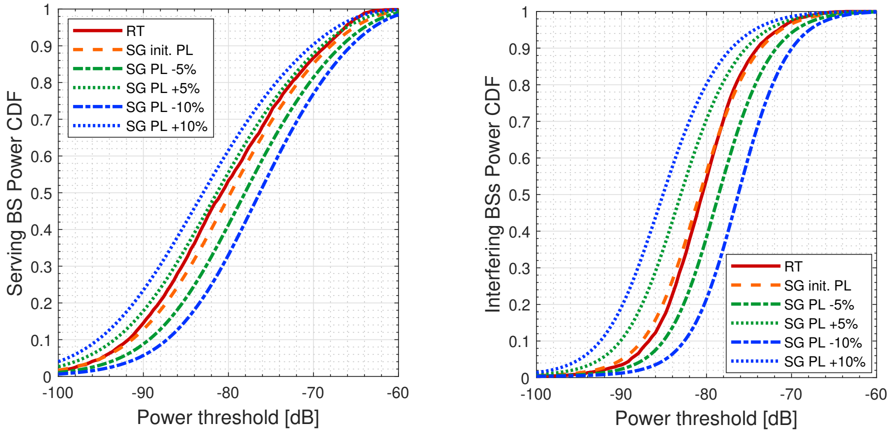

(a) Impact of PL exponents estimation errors on the CDF of the useful received power

(b) Impact of PL estimation errors on the CDF of the aggregate interference

Fig. 6.7 Sensitivity analysis of the estimated PL exponents based on the CDFs of the useful received power $P\left(S > \theta_p\right)$ and of the aggregate interference $P\left(I_L + I_N + I_D > \theta_p\right)$.

6.3 Comparison to real city deployments

To assess the suitability of using doubly stochastic models for real-world city deployments, 3D topologies of several existing cities are now extracted. Our focus will be on Brussels and Barcelona, which respectively represent a Cox-like environment and a Manhattan-like environment. Both cities have openly available three-dimensional models through the Urbis database [94] and the Geoportal de Cartografía database [95], for Brussels and Barcelona respectively. These models provide us with the actual footprints of buildings, their heights, and the street patterns of each city. However, since the height of all buildings is referenced to sea level, the local terrain elevation is subtracted from these heights using available digital terrain models (DTM). This allows us to consider a flat ground. Fig. 6.8 shows these statis-

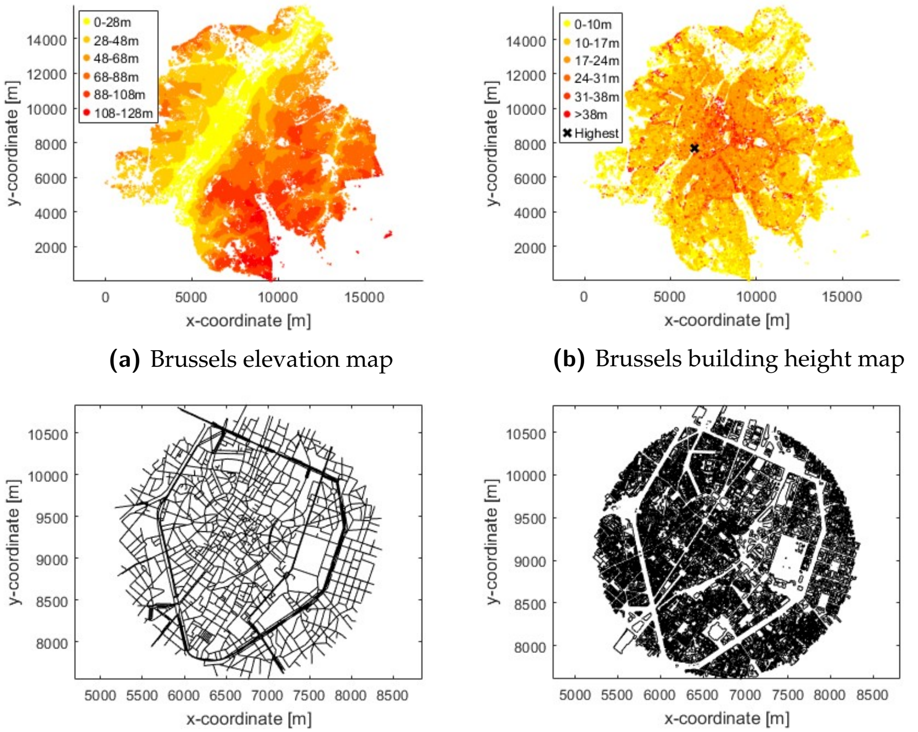

(a) Brussels elevation map

(b) Brussels building height map

(c) Brussels historical center: street pattern

(d) Brussels historical center: building footprints

Fig. 6.8 Topological statistics for the city of Brussels.

tics for the city of Brussels. We additionally consider a rural environment (Walhain) for which only the street pattern and the building footprints are available. The building heights are stochastically generated using the height distribution defined in Section 3.3.9.

As part of our study, square areas that are 0.75km by 0.75km in size are studied. The typical UE is located in a street that passes through the center of this area. Four different types of environments are considered: a Manhattan-style urban environment (i.e. an appropriate neighbourhood of Barcelona), a Cox-style urban environment (i.e. Brussels' historical center), a suburban environment (i.e. Orange neighbourhood in Brussels), and a rural environment (Walhain). A satellite view of these specific environments are shown on Fig. 6.9.

(a) Snapshot of Barcelona (Latitude: 41.388°N-41.399°N, Longitude: 2.158°E-2.176°E).

(b) Snapshot of Brussels' city center (Latitude: 50.841°N-50.853°N, Longitude: 4.336°E-4.358°E).

(c) Snapshot of Orange neighbourhood (Latitude: 50.772°N-50.789°N, Longitude: 4.365°E-4.388°E).

(d) Snapshot of Walhain (Latitude: 50.609°N-50.623°N, Longitude: 4.683 °E -4.704°E).

Fig. 6.9 Studied environments of size 0.75km×0.75km. Top left: Manhattan-like urban environment. Top right: Cox-like urban environment. Top right: Suburban environment. Bottom: Rural environment.

6.3.1 Methodology to extract the parameters

As depicted in Fig. 6.10, the street patterns of each of the considered neighbourhoods undergo the following transformations:

Step 1. **(both)** The original street pattern is approximated by lines as no curved streets can be modeled by the considered models.

Step 2. **(NHPCLP)** Streets that visually appear to be collinear are grouped. In Fig. 6.10, each street in the database is differently colored. It can be observed that many streets with different colors are actually collinear. Therefore, it is necessary to group them together as a single street. Short streets located sufficiently far from the UE are deleted.

Step 2. **(NHPSP)** Only connected collinear streets are grouped.

Step 3. **(NHPCLP)** The Cox equivalent is drawn from the remaining streets.

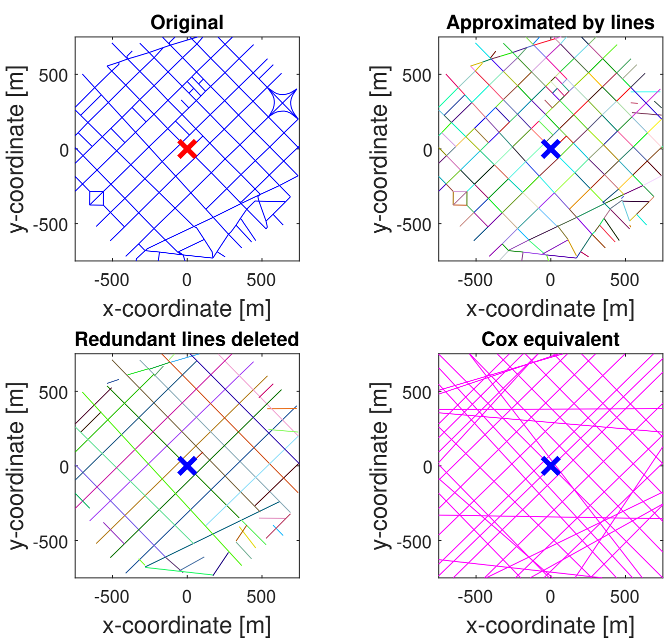

Fig. 6.10 Approach for approximating a neighbourhood by means of a NHPCLP: Barcelona.

From the obtained street pattern, the following statistics are extracted:

- $f_{NHPCLP,\Theta}(\theta)$ the distribution of the street angular orientation θ for the NHPCLP model (cfr. Section 2.1.5).
- $f_{NHPSP,\Theta}(\theta)$ the distribution of the street angular orientation θ for the NHPSP model (cfr. Section 2.1.6).
- $f_{NHPSP,\Phi}(\phi)$ the distribution of the angle ϕ for the NHPSP model (cfr. Section 2.1.6). This angle is the azimuth angle to the middle of all street segments computed with respect to the typical UE.
- $f_L(l)$ the distribution of the street length modeled by a lognormal distribution $\text{Log} - \mathcal{N}(\mu, \sigma)$.
- λ_{eff} the effective density of streets in the considered area. For the NHPCLP, if two street segments can be assumed to be colinear (with some tolerance), then they are considered as a single street.

Unless for the λ_{eff}, these statistics are derived from a larger area that shares the same center to obtain a distribution with enough detail. In order to maintain an analytical framework, all angular distributions are then approximated by a Gaussian mixture. This enables us to incorporate the analytical expression directly into the SG-based model with no need for any numerical evaluation. This approximation is given as follows:

$$f_\theta(\theta) = \sum_{\mu_i \in \boldsymbol{\mu}} C_i \exp\left(- \left(\frac{\theta - \mu_i}{0.6006 w_i} \right)^2 \right) \tag{6.13}$$

where $\boldsymbol{\mu}$, $\mathbf{w}$ and $\mathbf{C}$ are vectors that respectively group the means, widths and maximum values of all gaussians involved in the mixture. The factor $0.6006 = \sqrt{2}/2.355$ is related to the full width at half maximum (FWHM) of the peak.

Figs. 6.11a and 6.11b respectively illustrate the observed distributions $f_{NHPCLP,\Theta}(\theta)$ and their corresponding fitted gaussian mixtures for Brussels and Barcelona. The figures reveal that certain angular values are more frequently observed, highlighting the need for inhomogeneous doubly stochastic models. Specifically, in the case of Barcelona, four distinct peaks can be observed, which is a common characteristic of Manhattan-like environments where all streets are perpendicular. In such cases, the MPLP can serve as a good model candidate. All gaussian mixtures parameters, all

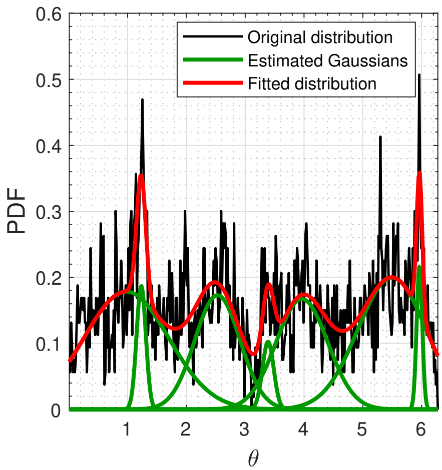

(a) Angular distibution $f_\Theta(\theta)$ of Brussels' city center: NHPCLP.

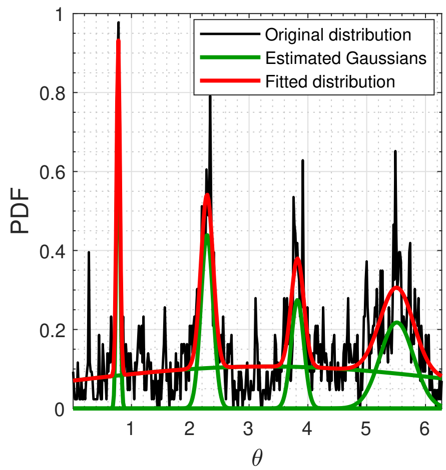

(b) Angular distribution $f_\Theta(\theta)$ of Barcelona: NHPCLP.

Fig. 6.11 Approximating the street angular distribution of the studied environments.

street length distributions parameters and all effective densities are summarized in Tab. 6.2.

6.3.2 Methodology to compare the approaches

In this section, a single roof tier and a single street tier are considered. The parameters discussed in Chapter 5 are equivalently used. In particular, Tabs. 5.1 and 5.3 summarize the parameters for urban and sparser environments. Only the tiers densities are modified to $\lambda_1 = 1km^{-1}$ and $\lambda_{b,1} = 8km^{-2}$. Since a single street tier is studied, note that the parameters listed for the first street tier in these tables are used. The strongest average received power association rule and beamforming are both considered in any case. As it was done in the previous chapter, the coverage probability is computed from our model using the extracted distributions. When necessary, a thinning function that reflects the distributions is used. The initial street density λ_s is fixed in order for the thinned process to have the ob-

	Angular dist.	Street Length dist.	Effective Density [rad$^{-1}m^{-1}$]
Brussels center			
NHPCLP	$\mu = [0.97; 1.23; 2.52; 3.39; 3.96; 5.49; 5.96]$ $\theta : \mathbf{w} = [1.70; 0.19; 0.91; 0.23; 1.04; 1.37; 0.11]$ $\mathbf{C} = [0.18; 0.19; 0.17; 0.10; 0.17; 0.20; 0.22]$	/	0.034
NHPSP	$\mu = [0.37; 0.92; 1.23; 2.26; 2.83]$ $\theta : \mathbf{w} = [0.65; 0.51; 0.16; 1.58; 0.11]$ $\mathbf{C} = [0.27; 0.31; 0.35; 0.37; 0.34]$ $\mu = [0.16; 0.88; 2.11; 4.42; 4.50; 5.43; 6.99]$ $\phi : \mathbf{w} = [0.58; 0.73; 0.77; 8.34; 0.29; 0.70; 0.82]$ $\mathbf{C} = [0.17; 0.12; 0.15; 0.11; 0.11; 0.13; 0.48]$	$\mu = 4.14$ $\sigma = 1.09$	0.26
Barcelona Center			
NHPCLP	$\mu = [0.78; 2.28; 3.30; 3.82; 5.51]$ $\theta : \mathbf{w} = [0.07; 0.24; 8.56; 0.25; 0.67]$ $\mathbf{C} = [0.85; 0.44; 0.11; 0.27; 0.22]$	/	0.007
NHPSP	$\mu = [0.75; 0.77; 2.29; 2.34]$ $\theta : \mathbf{w} = [0.80; 0.04; 0.87; 0.05]$ $\mathbf{C} = [0.43; 2.17; 0.50; 1.55]$ $\mu = [0.89; 2.49; 5.02; 5.61]$ $\phi : \mathbf{w} = [1.90; 1.37; 2.03; 0.20]$ $\mathbf{C} = [0.14; 0.20; 0.19; 0.34]$	$\mu = 4.27$ $\sigma = 0.85$	0.25
Brussels Orange Neighbourhood			
NHPCLP	$\mu = [0.72; 1.93; 2.61; 3.67; 4.43]$ $\theta : \mathbf{w} = [1.98; 0.57; 0.94; 0.32; 2.59]$ $\mathbf{C} = [0.24; 0.28; 0.11; 0.20; 0.09]$	/	0.007
NHPSP	$\mu = [0.20; 0.51; 1.28; 1.79; 2.03]$ $\theta : \mathbf{w} = [0.22; 0.19; 0.34; 2.51; 0.34]$ $\mathbf{C} = [0.48; 0.53; 0.15; 0.27; 1.60]$ $\mu = [1.96; 2.02; 3.40; 5.77]$ $\phi : \mathbf{w} = [2.73; 0.30; 0.54; 1.95]$ $\mathbf{C} = [0.23; 0.50; 0.15; 0.07]$	$\mu = 4.82$ $\sigma = 1.25$	0.024
Walhain			
NHPCLP	$\mu = [0.78; 2.33; 3.66; 5.8]$ $\theta : \mathbf{w} = [0.59; 1.22; 1.02; 1.28]$ $\mathbf{C} = [0.51; 0.14; 0.21; 0.23]$	/	0.004
NHPSP	$\mu = [0.59; 2.02; 2.54]$ $\theta : \mathbf{w} = [0.72; 1.36; 0.39]$ $\mathbf{C} = [0.61; 0.28; 0.38]$ $\mu = [0.70; 2.06; 4.29; 12.24]$ $\phi : \mathbf{w} = [1.2; 0.49; 0.24; 8.81]$ $\mathbf{C} = [0.27; 0.42; 0.20; 0.74]$	$\mu = 6.23$ $\sigma = 1.12$	0.004

Table 6.2 Statistical parameters for all studied environments.

served effective density. To compute the coverage probability in real cities, a sufficient amount of MC simulations are used. The approach is the same as for usual MC simulations up to the following modifications:

1. Street BSs are drawn on the real street pattern with the same density.

Roof BS are drawn on existing buildings with the same density. A constant roof antenna height is considered unless for BSs that should be installed on a BS whose height H_i exceeds this constant antenna height. In that case, the BS height is increased to $H_i + 5$. Except for rural areas, only BSs that actually lie on a rooftop are allowed. Roof BSs initially drawn outside a built area are regenerated. This may lead to a PP slightly different from the PPP. The draw is different for every MC simulation.

2. The LOS condition of all roof BSs is computed according to the real building heights as depicted in Fig. 6.12.

3. A "diffraction region", which is defined as the area visible from the typical street from which first-order diffraction can come, is computed. Only BSs located within this region are considered to interact with the UE through corner diffraction. In contrast, all BSs located on a line or segment that intersects the typical street are assumed to contribute by diffraction in our models. This region as well as an example of BSs draw are shown on Fig. 6.13 for the city of Brussels.

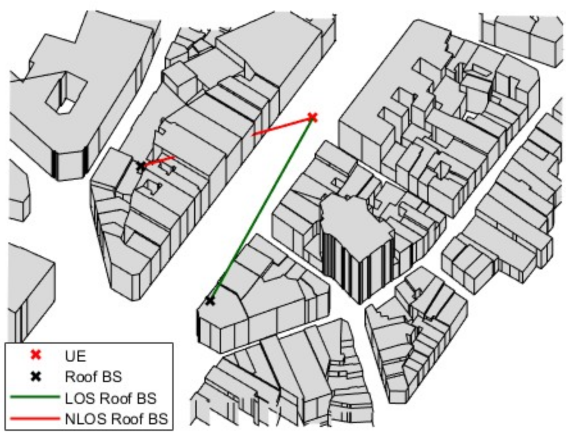

Fig. 6.12 Assessing the LOS conditions of roof BSs in real cities.

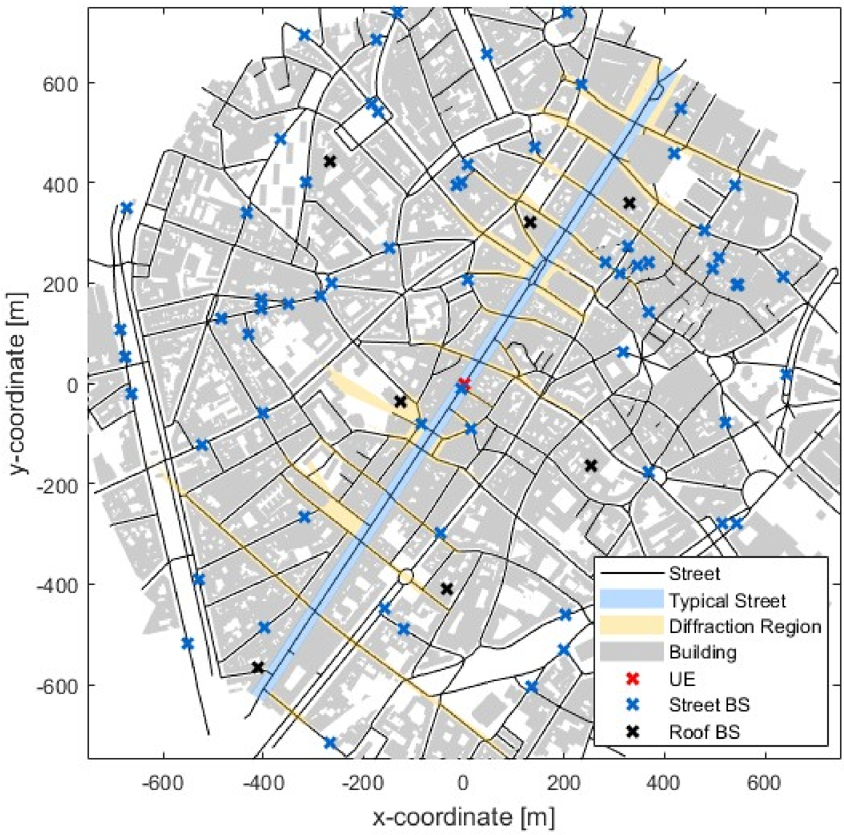

Fig. 6.13 MATLAB reproduction of Brussels' city center: λ_1=1/km and $\lambda_{b,1}$=8/km²

6.3.3 Numerical results and discussion

Fig. 6.15 displays the coverage probability results obtained from 250000 Monte Carlo simulations performed on each city topology. Throughout these simulations , the UE was located at several positions within the selected typical street. This typical street and its length for the different environment are summarized in Tab. 6.3.

We calculated the same metric for each neighborhood using our model,

Environment	Street	Length
Brussels	Boulevard Anspach	750m
Barcelona	Carrer de Pau Claris	750m
Orange Neighbourhood	Avenue du Prince d'Orange	300m
Walhain	Rue du Centre	75m

Table 6.3 Typical streets considered for comparison with our model.

which was implemented with the three different doubly stochastic processes: NHPCLP, NHPLM, and NHPSP. These processes were generated based on the extracted distributions. In addition, a corrected version of the NHPCLP was considered. It is associated with a smaller effective street density resulting from the deletion of far small streets during the parameter extraction. Based on this analysis, we can make two main observations.

First, the infinite length assumption of the NHPCLP is generally shown to lead to an overestimation of the non typical street contributions. In fact, if we observe Fig. 6.13, we can see that in Brussels, street portions that can result in first-order diffraction generally have a finite length. Therefore, the NHPLM may be a better option, as shown on the example of a NHPLM reproduction of Brussels depicted in Fig. 6.14. On the other hand, for Barcelona, the corrected version of the NHPCLP still produces accurate results. This is because the environment mainly consists of streets that cover the entire studied area from which any BS can generally interact through diffraction. Furthermore, the perpendicular streets contribute less to diffraction, which also explains why the infinite street length assumption is not as drastic in Barcelona. Under the considered densities, the peformance is shown to be mostly determined by typical street BSs and roof BSs.

Second, in real cities, it is rare to find two overlapping streets as they are usually separated by buildings or green areas. However, the considered doubly stochastic processes cannot model this repulsion between streets. This is especially problematic for the studied rural and suburban environments where streets are particularly spaced. Not modeling street repulsion is even more critical in such environments because BS located on non-typical streets can interact with UEs in LOS conditions due to the sparser surroundings. The higher probability of LOS and path loss coefficient in rural environments explains a greater impact on the accuracy of the coverage probability obtained for these environments.

Note that in sparser environments, the length of typical streets is quite restricted, which also means that there is a lower probability of having an interfering BS on the typical street at the considered densities. This together with the repulsion between streets explains very high performance in the considered neighbourhoods.

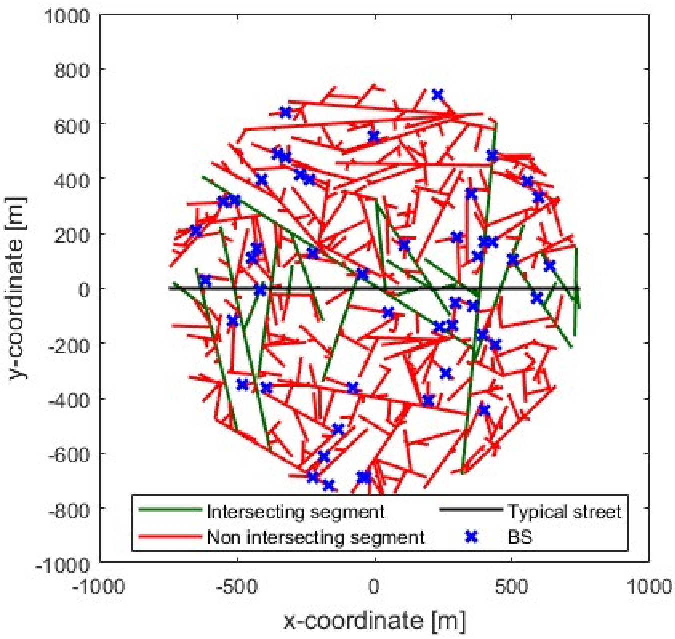

Fig. 6.14 Example of a NHPLM reproduction of Brussels based on the extracted statistics.

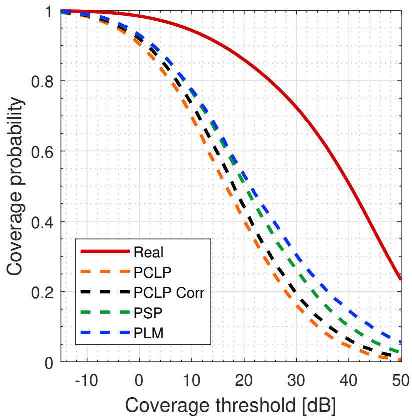

(a) Walhain.

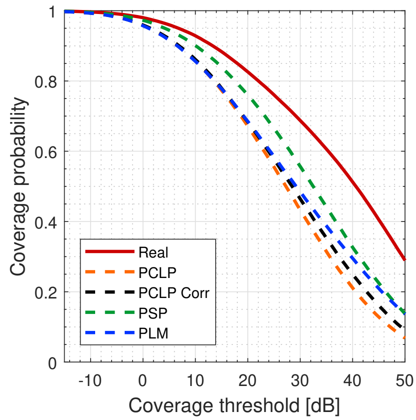

(b) Orange Neighbourhood.

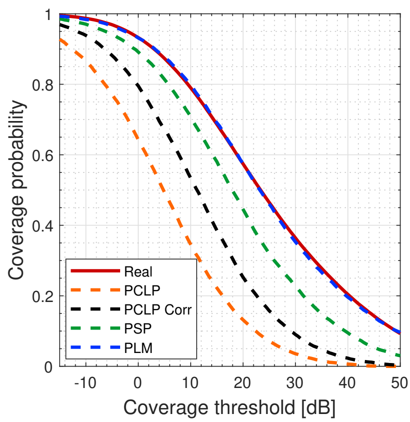

(c) Brussels city center.

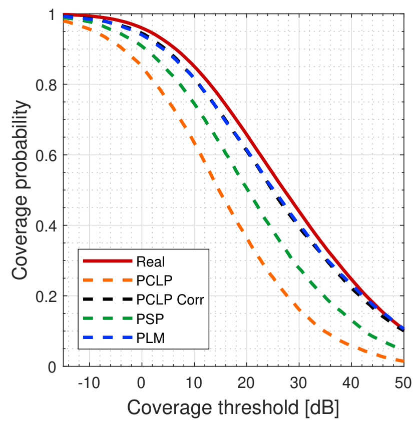

(d) Barcelona.

Fig. 6.15 Comparison for the coverage probability obtained from our model vs. real topologies.

7 Optimization of small cell deployment

So far, our focus has been on studying macro tendencies using SG-based system-level models. Our observations have led us to some recommendations regarding the selection of deployment parameters. However, no actual deployment has been implemented yet. Our next step is to figure out how to deploy BSs among a group of potential locations based on what has been learned from previous chapters. By means of propagation maps, a real deployment is thus optimized in a specific environment using the steepest ascent algorithm. Propagation maps computed with different channel models are shown to lead to different optimal deployments. One of our main objectives in this optimization process is to identify potential trends in these optimal deployments. In particular, we want to know whether an optimization based on simpler propagation-based models or on ray-tracing will lead to similar optimal deployments. If these deployments are not similar, one would like to quantify the losses we can expect if the deployment is performed based on simple propagation models.

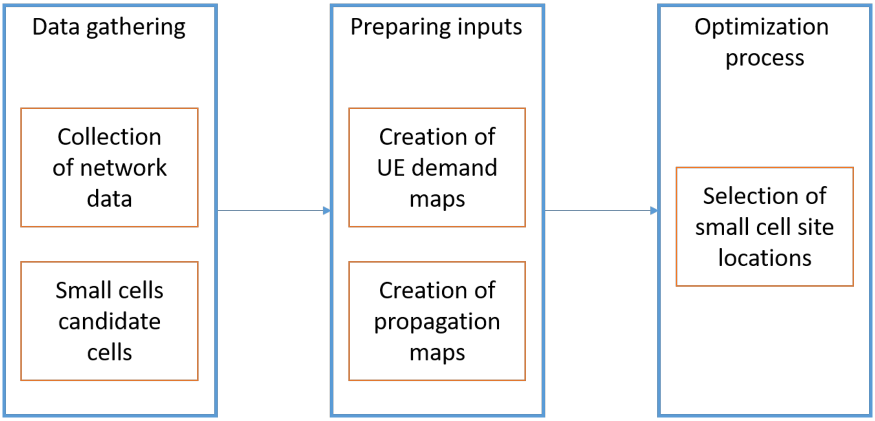

Fig. 7.1 Different steps involved in the optimization approach.

7.1 Preparing the optimization process

In the upcoming sections, the optimization methodology will be outlined. Its goal is to determine the best placement for M^* street BSs to serve the different UEs located within the studied environment. These BSs are selected from a predetermined set of M_C BSs, referred to as candidates. The number of deployable BSs is fixed in order for the linear density to be equal to λ_B, the optimal street tier density. A diagram summarizing the approach is presented in Fig. 7.1. The proposed approach is based on the works presented in [6]. Each step will be explained in detail below.

A square area $\mathcal{A}$ is assumed inside Barcelona. A second square area $\mathcal{A}_{opt} \subset \mathcal{A}$ is drawn at the center of the first bigger area. This second square can be viewed as a new neighborhood where the BSs deployment still needs to be done. It is called the optimization area. The area of $\mathcal{A}_{opt}$ is set to one-fourth of the area of $\mathcal{A}$ to ensure that a UE located at the edge of $\mathcal{A}_{opt}$ experiences a similar level of interference as a UE located at the center of $\mathcal{A}_{opt}$. The power computation nodes and candidates are exclusively located within $\mathcal{A}_{opt}$. It is assumed that all network components positioned outside of $\mathcal{A}_{opt}$ but within $\mathcal{A}$ have already been deployed with the same linear density λ_B. A random road side is assigned to each of them.

7.1.1 Network data

According to what can be observed in Barcelona's Manhattan-like neighbourhoods, building blocks have a square shape of dimensions $100m \times 100m$. The street width is fixed to $w_s = 25m$. All building blocks are here assumed to have the same height $H_b = 40m$. Cars with fixed dimensions $L \times l \times H = 3.5m \times 1.5m \times 2m$ are generated with density λ_O in all streets.

7.1.2 Candidates

As previously mentioned, M_C candidates are considered in $\mathcal{A}_{opt}$ as if they were deployed on lamposts. The set of candidates Ψ_C is fixed. They are placed at a distance $d_{B,w}$ from the different walls and at a height $H_B \ll H_b$. The distance between two consecutive candidates is given by d_B. It is assumed that candidates and BSs deployed outside $\mathcal{A}_{opt}$ sum up to M BSs. All considered candidates and already deployed BSs are assumed to be active at the studied frequency and are supposed to operate at the same power P_B. No power control is performed.

7.1.3 UE demand maps

Obtaining accurate UE demand maps can be a challenging task, and multiple sources may need to be combined to achieve this. It is normally crucial to have precise demand maps because they can influence the deployment of BSs. UEs tend to be unevenly distributed, particularly in urban areas, where they tend to cluster around traffic hotspots. Deploying BSs without considering this uneven distribution may lead to suboptimal deployment in a particular neighborhood, with some BSs being deployed where there is no actual need. As we do not have access to such maps, our optimal deployment will be done for evenly and unevenly distributed UEs that are stochastically generated.

In our study, N computation nodes, representing potential UE locations, are placed on a regular lattice inside the streets of $\mathcal{A}_{opt}$. Each node is placed at a height H_u and located at a distance d_u from its neighbours. Depending on the UEs distribution, each computation node i is associated with a weighting factor w_i. These weighting factors are set to $1/N$ for evenly distributed UEs. Fig. 7.2 illustrates all above-mentioned elements.

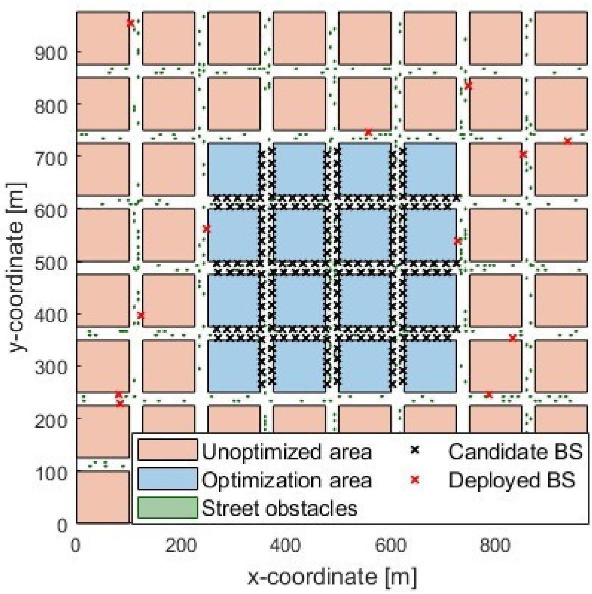

(a) Network Topology.

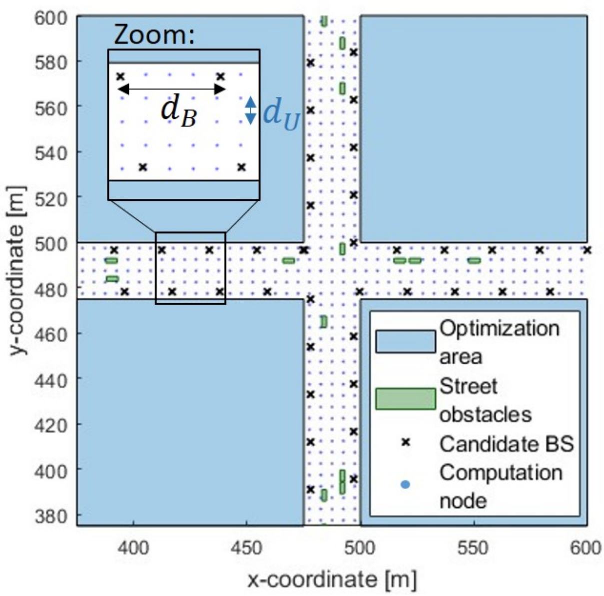

(b) Zoom on the optimization area.

Fig. 7.2 Illustration of the environment subject to optimization.

7.1.4 Propagation maps

The propagations maps P_{RT} and P_{MC} are $N \times M$ power matrices where element P^{ij}_{model} corresponds to the power received at the i-th computation node from the j-th BS using a given propagation model.

Each matrix element P^{ij}_{RT} is computed by means of Eq. (6.12). Additionally, the 3-17 DS sector antenna from RF Elements is considered at the BS. This antenna is said to be optimized for high performance in 3.4-3.8GHz (LTE bands 42, 43) [96]. Each ray in the RT algorithm is thus affected by an antenna gain that depends on its angle of departure. The complete reconstructed 3D radiation pattern is depicted in Fig. 7.3b. Dynamic beam steering is here assumed. For each computation node, the serving BS directs its main lobe towards the strongest path. The main lobe direction (θ,ϕ) of interfering BSs is randomly selected in the set $[0\ 2\pi]\times[-\pi\ 0]$.

Each matrix element P^{ij}_{MC} is computed by means of one of the PL models described in Eqs. (3.12) and (3.14). The choice of the PL model depends on whether the BS and the computation node are located on the same street or not. If they are in the same street, Eq. (3.12) is used and the LOS condition of the considered BS is randomly drawn using the blockage model for street tiers described in Section 3.3.2. Otherwise, Eq. (3.14) is used. The same obstacle density as in Section 6.2.3 is considered. As a consequence, all PL models parameters are fixed according to the same methodology. As a reminder, the parameters were set to $h_U = 1.5m$, $h_B = 6m$, $P_B = 1W$, $f = 3.6GHz$, $d_{B,w} = 5m$, $\lambda_O = 20km^{-1}$, $\kappa_L = \kappa_N = \kappa_D = (4\pi f/c)^2$, $\beta = 0.004$, $\gamma = 0.85$, $\alpha_L = 1.66$, $\alpha_N = 1.93$ and $\alpha_D = 2.1$. The squared fading gains (i.e. fading powers) of the LOS and NLOS links were approximated with exponential distributions of rate parameters 1.66 and 0.33 respectively. The horizontal antenna pattern of Fig. 7.3b is considered to weight the different contributions at the emission. The serving BS directs its main lobe towards the computation node.

An example of power maps for the same BS is depicted in Figs. 7.4a and 7.4b for both models. When no power is received at a given computation node, the corresponding location is whitened. It is noticeable that when a BS is located near a crossroad, the received power levels on the nearest perpendicular street are higher for BSs near the crossroad when the RT algorithm is used. This is because the RT algorithm takes into account

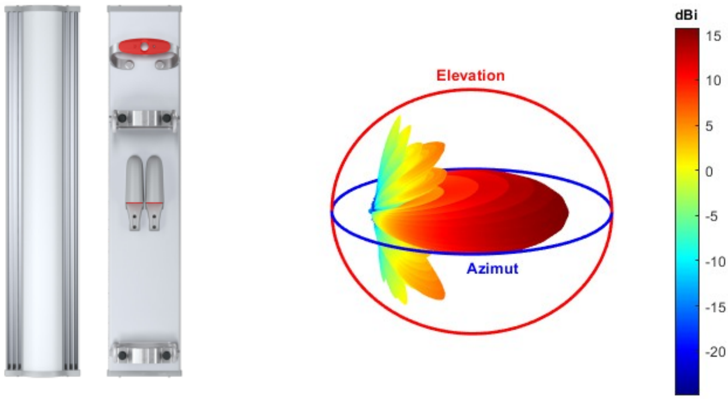

(a) Antenna model.

(b) Associated 3D radiation pattern.

Fig. 7.3 RF elements 3-17 DS sector antenna and its radiation pattern.

strong reflections and/or LOS paths for these BSs. Furthermore, the RT algorithm factors in the location of obstacles to compute power levels. As a result, power levels behind obstacles are naturally lower.

7.2 Optimization strategy

7.2.1 Optimization metric

The goal of the optimization algorithm is to output the optimal subset of candidates that optimizes (here maximizes) a so-called fitness function. This optimal deployment is denoted by BS^*_{model} and its associated optimal fitness value is here given by $P^*_{c,model}$. As the power maps are different for RT and MC, BS^*_{model} usually differs from one model to another. The fitness function is here the weighted coverage probability for a fixed coverage threshold θ_c given by:

$$\sum_{i=1}^{N} w_i \mathbb{1}\left[\frac{P^{ij^*}_{model}}{W + \sum\limits_{\substack{j\in BS_{\mathrm{depl}}\\ j\neq j*}} \mathbf{P}^{ij}_{model} + \sum\limits_{\substack{j\in[M_c+1,\ldots,M]\\ j\neq j*}} \mathbf{P}^{ij}_{model}} > \theta_c\right] \tag{7.1}$$

where BS_{depl} is a considered subset of M^* BSs chosen among the can-

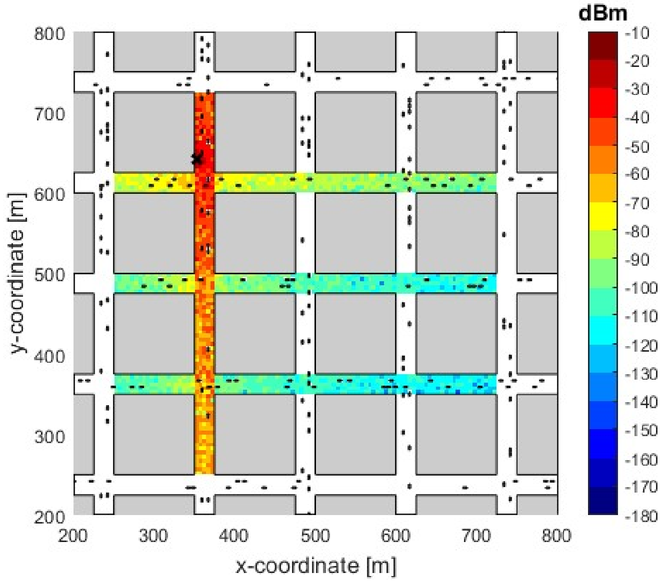

(a) Stochastic geometry power map.

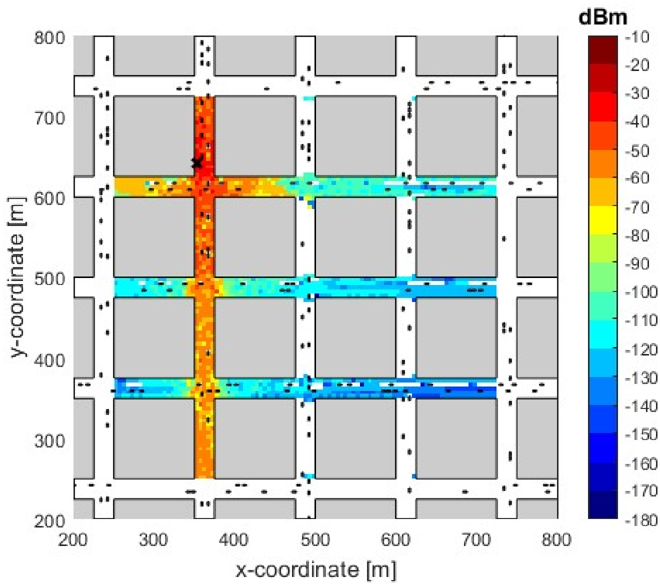

(b) Ray tracing power map.

Fig. 7.4 Illustration of the difference between power maps using two different models for a given BS (black cross).

didates $[1, ..., M_c] \in \Psi_C$ and j^* is the index of the serving BS according to the association rule.

7.2.2 Optimization process

In the framework of the optimization process, a candidate vector $\mathbf{S}$ of size $1 \times M_C$ is assumed where $\mathbf{S}_j$ is equal to 1 if the corresponding j-th candidate is activated and 0 otherwise.

Example 7.1. The vector **S**=[1 0 0 0 1 1 0 1 0 1] means that candidates 1, 5, 6, 8 and 10 are considered to be deployed among 10 candidates.

The steepest ascent (SA) algorithm is then used to optimize this candidate vector. It works as follows:

1. A vector $\mathbf{S}$ with M^* ones and $M_C - M^*$ zeros is randomly generated. The fitness function for the corresponding deployment is computed.
2. The current state of each candidate is successively inverted (i.e. a one/zero becomes a zero/one in the candidate vector). The impact of each inversion on the fitness value observed in step 1 is evaluated. Before studying the next candidate, the state of the current candidate is switched back to its initial value.
3. The candidate activation and deactivation that give us the best improvement with respect to the fitness value observed in step 1 are identified. The candidates associated to the best activation and to the best deactivation are respectively activated and deactivated. This ensures that the new deployment vector still contains M^* ones and $M_C - M^*$ zeros. The fitness value is then recomputed.
4. The process of steps 2 and 3 is repeated until there is no observable improvement in the fitness function.

The SA algorithm is run for a total of 200 times with a different random starting candidate vector at step 1. Repeating the algorithm multiple times in this manner helps to avoid getting stuck in local optima.

7.3 Numerical results

Fig. 7.5 displays the optimal weighted coverage probabilities for different coverage thresholds and for uniformly distributed UEs. Figs. 7.5a and

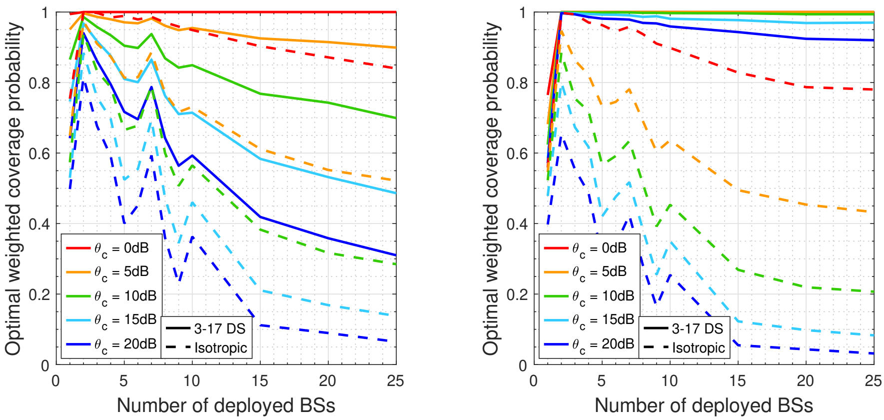

(a) $P^*_{c,MC}$ for a stochastic propagation model

(b) $P^*_{c,RT}$ for ray tracing

Fig. 7.5 Optimal weighted coverage probability as a function of the number of deployed BSs for different coverage thresholds.

7.5b respectively show the optimal values when using the stochastic propagation model and the ray tracing model. Results are presented for both the 3-17 DS antenna and an isotropic antenna. Regardless of the coverage threshold and propagation model used in the optimization, maximum performance is achieved when two BSs are deployed in the considered environment. Deploying only one BS is shown to be suboptimal, and a denser deployment progressively worsens the optimal coverage probability. If the network is congested with only two BSs and cannot accommodate all active UEs, it is still feasible to provide a minimum quality of service (SINR = 0dB) with a 95% probability by deploying up to 7 BSs, even with isotropic antennas. The additional peaks observed in all curves indicate the influence of BSs generated outside the optimization area. Since the locations of these BSs are not optimized, they can have a detrimental effect on the overall coverage probability. To mitigate this impact, one approach could be to average the global probability over multiple realizations of these BSs, which should help to smoothen the effect.

As it can be observed, the use of isotropic antennas reduces the optimal probability due to a weaker useful signal and higher interference level. This is particularly critical in case the RT tool is used. In fact, when the beam direction of the 3D pattern for interfering BSs is randomly selected, the useful signal typically fights only the AWGN. This explains the higher values observed for RT with beamforming. However, this assumption of random beam direction selection for interfering BSs is a strong hypothesis. Using a more realistic beam direction selection and considering a higher number of reflections in the RT tool may lead to lower and more realistic values. On the contrary, the horizontal radiation pattern was used in the framework of the stochastic propagation model. The interfering contributions may, in that sense, be slightly overestimated.

Tab. 7.1 summarizes the average exposure statistics for both models as a function of the number of deployed BSs. The 50th percentile E_{50} of observed exposure values, the 95th percentile E_{95} of observed exposure values and the maximum observed value E_{max} are introduced. The latter value is generally observed just below the antenna. If two BSs are deployed, it is shown that most of the observed values generally fall below the legal threshold set in Brussels (4.34V/m) . The maximum observed value however exceeds this threshold. For this reason, the considered EIRP will be discussed in the next section.

Model	M^*	E_{50}	E_{95}	E_{max}	Model	M^*	E_{50}	E_{95}	E_{max}
MC	1	0.03	1.69	13.92	MC	8	0.65	4.52	20.70
RT		0.06	1.06	6.50	RT		0.55	2.58	11.31
MC	2	0.33	2.60	14.69	MC	9	0.95	4.80	20.68
RT		0.27	1.53	9.93	RT		0.62	2.71	12.11
MC	3	0.34	2.82	16.49	MC	10	1.01	5.09	20.60
RT		0.29	1.67	10.62	RT		0.69	2.79	8.89
MC	4	0.42	3.29	16.73	MC	15	1.52	6.14	24.36
RT		0.36	1.95	11.38	RT		0.97	3.25	19.88
MC	5	0.45	3.45	20.09	MC	20	1.92	6.88	24.69
RT		0.39	2.03	9.68	RT		1.12	3.86	15.66
MC	6	0.60	4.02	21.53	MC	25	2.06	7.54	23.39
RT		0.43	2.24	8.82	RT		1.25	4.30	19.15
MC	7	0.59	4.19	19.01					
RT		0.47	2.39	10.49					

Table 7.1 Average exposure statistics in V/m associated with the optimal deployments.

7.3.1 Impact of the effective isotropic radiated power

Given that the maximum observed exposure value exceeded the legal threshold, the EIRP of all active BSs will now be reduced to bring that value down to acceptable levels. The effect of this power reduction on the optimal achievable coverage probability is then measured. The results indicate that, in the studied environment, a high EIRP was not necessary and this power reduction has little effect on the average UE performance. The minimum QoS can still be provided to the UE with an EIRP as low as 34.8dBm.

EIRP [dBm]	Mod.	0dB	5dB	10dB	15dB	20dB	E_{50}	E_{95}	E_{max}
45.6	MC	1	0,99	0,99	0,97	0,94	0.33	2.60	14.69
	RT	1	1	1	1	1	0.27	1.53	9.93
38.2	MC	1	1	0,99	0,97	0,94	0.14	1.11	6.26
	RT	1	1	1	1	1	0.11	0.65	4.23
34.8	MC	1	1	0,98	0,97	0,93	0.09	0.75	4.24
	RT	1	1	1	1	0,99	0.08	0.44	2.87

Table 7.2 Optimal weighted coverage probability for $M^* = 2$ under varying EIRPs.

7.3.2 Interchanging optimals

Since computing the power contributions from all BSs at all computation nodes is a computationally-intensive task, it is important to understand the true benefits of an approach fully conducted with the RT tool. To address this, an alternative method involves using the optimal deployments BS^*_{MC} obtained through a MC analysis with the RT power maps to evaluate the associated weighted coverage probabilities. The obtained values can then be compared to the ones obtained with the RT optimal deployments BS^*_{RT} to evaluate the subsequent losses. These coverage losses are depicted in Fig. 7.6.

In the case of a small number of deployed BSs and a low target SINR, numerous deployments offer comparable performance due to a bounded fitness function. The optimal deployment obtained with RT is one of these deployments. Hence, the MC analysis does not select a particular deployment based on strategic locations, but rather based on the random fading

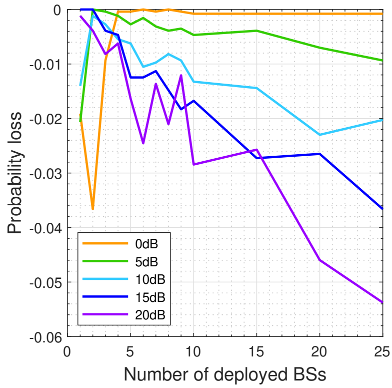

Fig. 7.6 Losses caused by an interchange between optimals.

gains and LOS conditions associated with the selected BSs. These fading gains and LOS conditions, being uncorrelated and random in the way they are generated, may not reflect the actual observed fading gains and LOS conditions. In fact, since the MC approach does not bear in mind the location of obstacles, the selected candidates may not reach all UE locations. Yet, for a low number of deployed BSs, there is little margin for error, and a poor choice may result in lower coverage probabilities. On the contrary, for high SINR values, strategic locations become more important, and the fading gains become less significant.

When a large number of BSs are deployed, their coverage range typically becomes smaller, and the candidate selection is largely influenced by their immediate surroundings. In such scenarios, a deterministic channel model is then more reliable in ensuring an appropriate selection, particularly for high SINR values. This is the reason why the probability losses associated with the optima interchange increase as the network becomes denser.

7.3.3 Impact of an uneven UE distribution

So far, the best way to deploy our resources has been computed assuming that every UE location is equiprobable. However, in urban areas, the

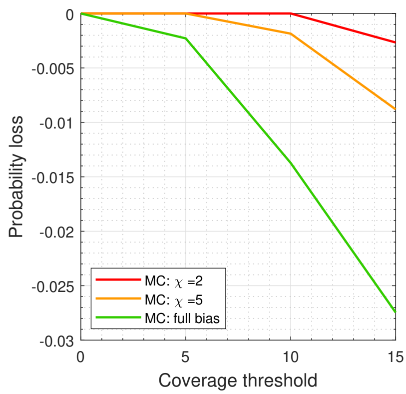

Fig. 7.7 Impact of neglecting uneven UE distribution on optimal deployments: probability losses analysis for a 3-17 DS antenna.

density of active UEs may vary across different parts of the considered environment. The areas with a higher density will be referred to as hotspot in this discussion, and will be assumed to be circular areas with a radius of 100 meters. To account for this uneven distribution, the following weights for the different computation nodes are used:

$$w_i = \begin{cases} \frac{\chi}{\chi N_H + N_{NH}} & \text{if } i \text{ is located in a hotspot region} \\ \frac{1}{\chi N_H + N_{NH}} & \text{otherwise.} \end{cases} \tag{7.2}$$

where N_H/N_{NH} are the number of computation nodes that fall inside/outside the hotspot regions and χ is the bias factor. In case of total bias, the weights for hotspot/non hotspot computation nodes are set to $\frac{1}{N_H}/0$.

Two hotspots centered in [612 270] and [300 488] are considered. Different scenarios to demonstrate the effect of uneven distributions are then studied. We will start by assuming that UEs are uniformly distributed, meaning there is no bias. We will then consider UEs located in the hotspot region with a probability twice as high as any other location ($\chi = 2$), with a probability five times as high as any other location ($\chi = 5$), and finally, exclusively located in the hotspot region (total bias). The obtained results are depicted in Fig. 7.8. As the bias becomes stronger, the optimal candidate locations gradually shift towards the hotspot region for both propagation models. However, the optimal candidates do not necessarily fall in the center of the hotspot regions, as they also need to adapt to the existing BSs and to the street obstacles. Fig. 7.7 characterizes probability losses that arise when we stick to the optimal deployment calculated under the assumption of a uniform distribution. It is logical that these losses increase as the considered coverage threshold becomes larger. Furthermore, as the bias value increases, the losses also become larger, as the actual locations of UEs becomes more and more important.

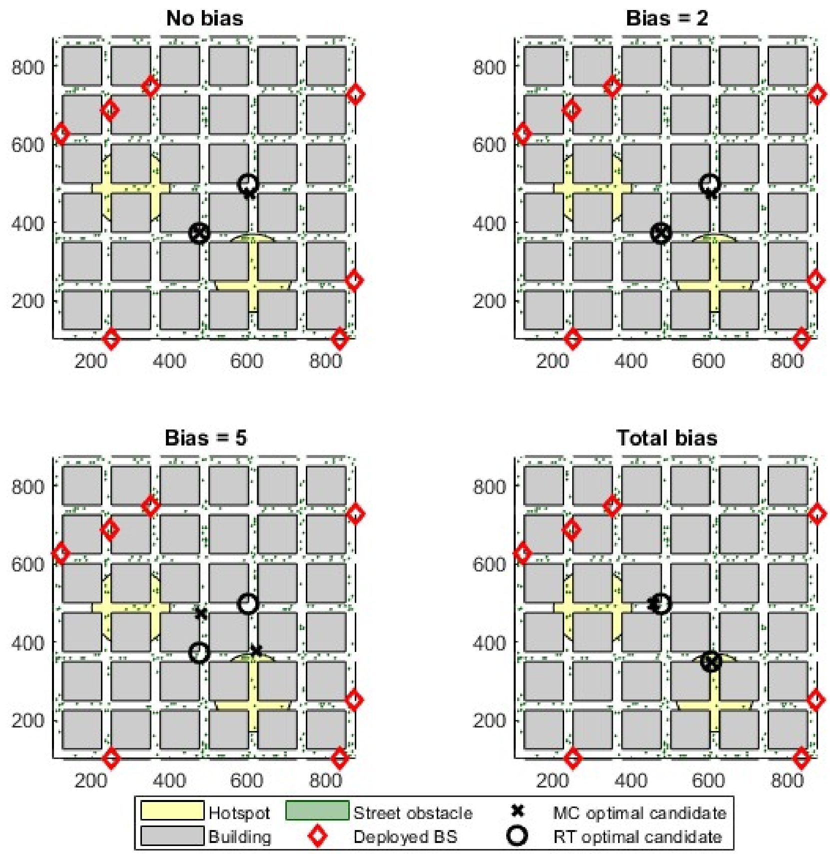

Fig. 7.8 Optimal deployments in case of uneven UE distribution: $M^* = 2$ and $\theta_c = 10dB$.

8 Conclusion

THE aim of this thesis was to investigate the trade-offs between deterministic channel models and simple channel models. With the expected network densification, BSs are expected to be deployed closer to the UE, which implies that site-specific simulations will become more and more relevant. As shorter link distances limit the actual propagation environment, ray tracing has become a suitable candidate for channel modeling. The model becomes even more compelling with the use of higher frequencies in future networks, as they reduce the severity of the ray-optics approximation.

As mentioned earlier, network densification may cause additional interference, which could worsen the coverage currently provided by macro base stations. Moreover, the health risks associated with exposure to EMFs have not been formally proven, and the increased exposure levels resulting from base stations being located closer to the ground level have raised concerns. To investigate these potential issues, a system-level analysis covering multiple scenarios is generally required. Conducting this analysis should enable us to make informed decisions about the adjustment of the network design parameters to allow the coexistence of macro- and micro-tiers, while ensuring that the exposure levels remain below the legal thresholds.

Regrettably, the major drawback of ray tracing is that its computational complexity quickly explodes as the size of the environment being studied becomes larger. Even if the propagation environment is restricted by shorter BS ranges, a large number of in-site simulations should be performed to gain sufficient insight about the optimal deployment trends. In addition, the use of a deterministic propagation model may not actually be necessary as the propagation environment is expected to dynamically and unpredictably change in future networks. Alternative methods should therefore be explored or, at least, a systematic approach should be proposed to combine ray tracing with simpler tools to accurately replicate the network performance.

In that sense, stochastic geometry has played a major role in the last decades. This branch of applied probabilities provides us with an interesting mathematical framework that eases the study of random phenomena in large-scale systems. It has been extensively used for the modeling of many emerging technologies. Despite the plethora of applications of the SG-based models, only a few works have considered a deployment of small cells BSs along streets. In fact, the PPP is often preferred for its mathematical tractability. However, due to a high built-up ratio in dense urban areas, streets are actually the most common location where these BSs are expected to be deployed. For this reason, the proposed work explored the use of doubly stochastic point processes. These processes are characterized by the fact that both the street pattern and the BS locations are stochastically generated. More importantly, BS locations are restricted to lie along these streets. Besides, observations of existing urban street patterns have revealed a degree of structure, particularly in cities that have developed gradually around the historic center. However, existing doubly stochastic models typically assume a uniform distribution of street locations and orientations. To address this limitation, we have introduced a new process called the non-homogeneous Poisson Cox line process (NH-PCLP). Finally, most existing works concentrate on the contributions from streets that are different from the UE's street in the direct path. However, due to the strong building penetration losses, these contributions are typically very low. Therefore, this study rather focuses on the diffraction from building corners in urban areas.

Following the previous discussion, a general multi-tier urban network model that takes into account all the elements mentioned earlier has been introduced in Chapter 3. The proposed model is capable of covering a wide range of scenarios, and its design parameters can easily be modified to gain a better understanding of how they impact the system's performance. In Chapter 4, semi-closed form expressions for commonly studied SINR-based metrics characterizing the latter model under all possible variations are derived. Given the growing skepticism surrounding exposure levels, both exposure-based metrics and joint distributions are also investigated.

A common approach in SG-based works is to assume that the location of the UE can be generated independently of any external factors. However, in real-world scenarios, complete spatial randomness is not always achieved, especially with recent efforts by operators to deploy BSs where the UEs are actually located. To account for this, our analysis was generalized to include UEs whose positions are coupled with a hotspot BS. Additionally, it is important to consider that there is a possibility that a UE may be situated at a street intersection, such as pedestrians waiting at a traffic light. As the performance of a UE located at a street intersection can vary greatly from that of a UE located within a street, a second generalization is being performed to incorporate crossroad UEs.

In Chapter 4, network performance is evaluated in Manhattan-like urban environments, Cox-like urban environments, and sparser environments. The tier parameters were calibrated based on the Winner 2 channel models. When the network is exclusively served by street BSs, it has been shown that neglecting diffracted contributions may lead to a significant overestimation of the coverage probability, particularly in streets that are poorly equipped with network infrastructure or in areas with high street density. Moreover, the existence of crossroad UEs must not be overlooked. In fact, neglecting the existence of such UEs can mislead the decision regarding the optimal BS density, as crossroad UEs require less aggressive densification to achieve optimal average capacity.

When the micro tier is added to the existing macro tier, it is crucial to carefully select both tiers' densities. It was shown that a sparse but strategic deployment of small cells can help the operators to offer higher throughputs in high-traffic areas. To avoid a strong deterioration of the performance in these areas while offering all UEs a minimum QoS, roof tiers can then be densified. Due to a stronger beamforming ability at macro BSs and to a lower probability for roof BS to interfere in LOS conditions, if they are placed sufficiently close to the rooftop level, the coverage can be safely extended. With the ultimately selected densities, 96% of uniform and 99% of non-uniform UEs can benefit from a minimum QoS while maintaining exposure levels below legal thresholds. However, the use of beamforming is critical to attain such a performance. In sparser environments, using small cells may not be recommended due to the higher probability of LOS contributions from non-typical streets and roof BSs.

MC simulations are commonly used to validate SG-based models, allowing verification of their mathematical correctness. However, they do not confirm whether these models yield accurate results in the first place. To validate these models and identify their limitations, in Chapter 6 we successively conducted comparisons with results obtained using a deterministic channel model (ray tracing) and using real city topologies. Our models have been proven to deliver precise outcomes with respect to RT when the PL coefficients and the fading distributions are carefully chosen. Nonetheless, even a slight deviation from these parameters can result in significant inconsistencies. This emphasizes the crucial role of an accurate parameter extraction. In a second phase, we demonstrated that the doubly stochastic models we considered tend to underestimate the coverage probability in real cities since they cannot account for the repulsion between streets. This underestimation is further amplified by the infinite length assumption of the NHPCLP, particularly in sparser environments where the LOS probability is usually higher. In Brussels, the NHPLM was shown to be a more accurate model at the considered densities.

The latter model, however, comes at the price of additional integrals. Unfortunately, this gradual increase in flexibility of SG-based models also comes with a rise in their computational complexity. This is due to the presence of these multiple nested integrals, which can involve the integration of functions with sharp peaks that require time-consuming numerical computations. As a result, the gap between these models and the associated MC simulations is shown to become narrower, and in some cases, the MC simulations can even outperform the analytical models. This last observation goes against one of the main reasons that initiated SG-based models: the runtime.

Finally, we optimized the deployment of small cell BSs for a reference scenario using power levels calculated from both a simple propagation-based model and RT. Although both models generally resulted in similar performance, they produced different deployment patterns. As the network density increased, the optimal deployments determined by RT demonstrated an improvement in overall performance of up to 6% for high SINR values.

8.1 Future research

In this dissertation, only the downlink communications were considered. The proposed approach could therefore be generalized to the uplink (UL) communication. This, however, raises many challenges. For example, the use of power control (PC) techniques such as the fractional power control [97] is highly required to mitigate the UL interference. PC techniques are particularly important in the UL as the UE's device is battery-powered which limits the maximum transmit power. The restricted beamforming ability of mobile UEs further reinforces the importance of PC. Another reason is that excessive but unnecessary transmit power reduces battery life of mobile devices. In case of PC, UE transmit power levels are thus typically impacted by the distance to their serving BS which needs to be modeled. Furthermore, in orthogonal mutliple access schemes, only one UE communicates on a given ressource block in each cell. This makes the point processes used for BSs not perfectly suitable for mobile UEs, as the interfering UEs locations are correlated with the BSs locations. In fact, having a UE in a subregion of a cell means that no interfering UE is found in the rest of the cell, which contradicts the PPP properties. UL models should address this dependency. While the UL analysis was already conducted for usual PPs [97], there is still room for UL models that use doubly stochastic models.

This study only focused on outdoor scenarios, but the metrics analyzed could also be applied to indoor environments. Winner channel models could be similarly used for calibration. That way, the impact of outdoor infrastructure on indoor UE could be evaluated. Furthermore, the use of femtocells could be considered as an additional measure to improve the connection of indoor UEs and reduce the UL exposure due to the proximity of the femto BS.

Due to the increased flexibility of the presented models, its computational complexity has become overwhelming. Therefore, finding a way to simplify the analytical expressions would be a valuable contribution. In a previous study [98], it was found that the coverage probability of cellular network models typically has a consistent shape and is mainly shifted to the left or right. They proposed a method that uses the mean interference-to-signal ratio and the expected fading-to-interference ratio to approximate the coverage probability of more complex point processes by utilizing the coverage probability expression derived for the more tractable PPP. It would be intriguing to investigate whether this approach is suitable for analyzing the models presented in this thesis. Expanding this approach to other metrics is also an intriguing possibility.

Given the observed street repulsion in real city topologies, it would be valuable to explore the potential of repulsive doubly stochastic processes. Although the Matern Hard Core Point process already exhibits repulsion properties for simple point processes, it would be interesting to extend this concept to Cox Line processes. This could be accomplished by using another point process to generate the initial points in the representation space.

Appendices

A Proof of Lemma 4.4

This proof strongly relies on [38]. Given the initial PLLP Ψ_l, the joint void probability is given by:

$$
\begin{aligned}
&\overline{F}_{J,NT}(\theta_1, ..., \theta_K) \\
&\triangleq \mathbb{P}\Big(\mathcal{R}_1(\mathcal{B}_2(\mathbf{0},\theta_1)) = 0, ..., \mathcal{R}_{K_S}(\mathcal{B}_2(\mathbf{0},\theta_{K_S})) = 0\Big) \\
&\overset{(1)}{=} \mathbb{E}_{\Psi_l}\Big[\prod_{l \in \Psi_l}\prod_{\{k\}}\mathbb{P}\Big(\mathcal{R}_k(l \cap \mathcal{B}_2(\mathbf{0},\theta_k)) = 0 \big| \Psi_l\Big)\Big] \\
&\overset{(2)}{=} \mathbb{E}_{\Psi_l}\Big[\prod_{l \in \Psi_l}\prod_{\{k\}}\exp\Big(-\lambda_k v_k(l \cap \mathcal{B}_2(\mathbf{0},\theta_k))\Big)\Big] \\
&\overset{(3)}{=} \mathbb{E}_{\Phi_l}\Big[\prod_{(\rho,\theta) \in \Phi_l}\prod_{\{k\}}\exp\Big(-\lambda_k v_k(l_{(\rho,\theta)} \cap \mathcal{B}_2(\mathbf{0},\theta_k))\Big)\Big] \\
&\overset{(4)}{=} \exp\Big(-\lambda_s \int_0^{\infty}\int_0^{2\pi}\Big[1 - \prod_{\{k\}}\exp\Big(-2\lambda_k\sqrt{\max(0, \theta_k^2 - \rho^2)}\Big)\Big] p(\rho,\theta) d\rho d\theta\Big).
\end{aligned}
$$

where (1) is obtained assuming $l \cap \mathcal{B}_2(\mathbf{0},\theta_k)$ represents the portion of line $l \in \Psi_l$ that lies inside the 2D ball $\mathcal{B}_2(\mathbf{0},\theta_k)$. (2) results from the void probability of K_S independent 1D HPPPs on each line. $v_k(l \cap \mathcal{B}_2(\mathbf{0},\theta_k))$ is the required distance on that line l that would ensure that the closest node on te line is further than θ_k from the origin. (3) follows from the transition from the euclidian space to the representation space. (4) is obtained by applying the PGFL property of 2D PPPs and by definition of $v_k(l \cap \mathcal{B}_2(\mathbf{0},\theta_k))$.

B Proof of Lemma 4.6

The proof is similar to the proof of Lemma 4.4. The joint void probability is here modified as all tiers on non typical streets are linked by the street realization. Since we integrate on the distance r to the closest node of tier $\Xi_{NT,(k^*)}$, other non typical street tiers will be affected by the value of this integration variable r. In fact, each line potentially generated inside the ball $\mathcal{B}_2(\mathbf{0}, r)$ at a given distance ρ has a probability $\exp\left(-2\lambda_{k^*}\sqrt{r^2-\rho^2}\right)$ to be present in a realization where r is actually the distance to the closest node. This is the probability that no node is generated at a distance smaller than r given the distance to the line is ρ. If the initial homogeneous street density is λ_s, network realizations for which r is the distance to the closest node of tier $\Xi_{NT,(k^*)}$ have thus a non homogeneous street density given by:

$$\lambda_s(\rho) = \begin{cases} \lambda_s \exp\left(-2\lambda_{k^*}\sqrt{r^2-\rho^2}\right) & \text{if } \rho < r \\ \lambda_s & \text{elsewhere} \end{cases}$$

As other non typical street tiers are generated on the same streets, network realizations with these characteristics will thus have to be considered. In addition, if r is the distance to the closest node of tier $\Xi_{NT,(k^*)}$, there has to be a line going through that particular node. Taking into account these two elements, we can easily compute the following modified joint CCDF as :

$$\overline{F}_{m,J,NT}(\theta_1, ..., \theta_K, r) = \int_0^\infty \prod_{\{k\}^*} \exp\left(-2\lambda_k\sqrt{\max(0, \theta_k^2 - y^{*2})}\right) f_{C,R}(y^*|r)dy^*$$

$$\exp\left(-\int_0^\infty\int_0^{2\pi}\left[1-\prod_{\{k\}^*}\exp\left(-2\lambda_k\sqrt{\max(0,\theta_k^2-\rho^2)}\right)\right]\lambda_s(\rho)p(\rho,\theta)d\rho d\theta\right).$$

C Proof of Lemma 4.12

The proof relies on Appendix A in [99]. In the following computations, $k \in \{1 - N_S\}]$, $k' \in \{1 - N_B\}$ and $n \in \{L, N\}$. In addition, let us introduce the notation $(k,n)^*$ as the collection of all combinations (k,n) unless the serving one (k^*, n^*). Assuming $\mathcal{S} = P_{k^*} L_{k^*,n^*}^{-1}(R_{T,k^*,n^*})$, the association probability is then computed as:

$$\mathcal{A}_{T,k^*,n^*} = \mathbb{P}\Bigg[\mathcal{S} > \max\Big[\max_{(k,n)^*}\big(P_k L_{k,n}^{-1}(R_{T,k,n})\big), \max_{(k)}\big(P_k L_{\tilde{t},k}^{-1}(R_{NT,k})\big),$$

$$\max_{(k')}\big(P_{b,k'} L_{d,k'}^{-1}(R_{Bd,k'})\big), \max_{(k',n)}\big(P_{b,k'} L_{k',n}^{-1}(R_{B,k',n})\big)\Big]\Bigg]$$

$$\overset{(1)}{=} \mathbb{E}_{R_{T,k^*,n^*}}\Bigg\{\prod_{(k,n)^*}\mathbb{P}\Big[\mathcal{S} > P_k L_{k,n}^{-1}(R_{T,k,n})\Big| R_{T,k^*,n^*}\Big]$$

$$\prod_{(k')}\mathbb{P}\Big[\mathcal{S} > P_{b,k'} L_{d,k'}^{-1}(R_{Bd,k'})\Big| R_{T,k^*,n^*}\Big]$$

$$\prod_{(k',n)}\mathbb{P}\Big[\mathcal{S} > P_{b,k'} L_{k',n}^{-1}(R_{B,k',n})\Big| R_{T,k^*,n^*}\Big]$$

$$\mathbb{P}\Big[\mathcal{S} > P_k L_{\tilde{t},k}^{-1}(R_{NT,k}), \forall k \in [1 - N_S]\Big| R_{T,k^*,n^*}\Big]\Bigg\}$$

$$= \mathbb{E}_{R_{T,k^*,n^*}}\Bigg\{\prod_{(k,n)^*}\mathbb{P}\Big[R_{T,k,n} > z_{T,(k,n)}^{T,(k^*,n^*)}(R_{T,k^*,n^*})\Big]$$

$$\prod_{(k')}\mathbb{P}\Big[R_{Bd,k'} > z_{Bd,(k')}^{T,(k^*,n^*)}(R_{T,k^*,n^*})\Big]$$

$$\prod_{(k',n)}\mathbb{P}\Big[R_{B,k',n} > z_{B,(k',n)}^{T,(k^*,n^*)}(R_{T,k^*,n^*})\Big]\Bigg\}$$

$$\mathbb{P}\Big[R_{NT,k} > z_{NT,(k)}^{T,(k^*,n^*)}(R_{T,k^*,n^*}), \forall k \in [1 - N_S]\Big]$$

$$\overset{(2)}{=} \int_0^\infty \prod_{(k,n)^*}\overline{F}_{C,R_{T,k,n}}\Big(z_{T,(k,n)}^{T,(k^*,n^*)}(r)\Big)\prod_{(k')}\overline{F}_{C,R_{Bd,k'}}\Big(z_{Bd,(k')}^{T,(k^*,n^*)}(r)\Big)$$

$$\prod_{(k',n)}\overline{F}_{C,R_{B,k',n}}\Big(z_{B,(k',n)}^{T,(k^*,n^*)}(r)\Big)$$

$$\overline{F}_{J,NT}\Big(z_{NT,(1)}^{T,(k^*,n^*)}(r), ..., z_{NT,(N_S)}^{T,(k^*,n^*)}(r)\Big) f_{C,R_{T,k^*,n^*}}(r)dr$$

where (1) comes from the independence of almost all tiers. Remember that non typical street tiers are linked by the street realization hence the fact that they can not be treated as if they were independent. (2) follows from the definition of CCDFs.

D Proof of Lemma 4.16

This proof strongly relies on Lemma 3 in [99]. Using Bayes' theorem, we can compute the CDF of the serving distance for street tier $\Phi_{T,(k^*,n^*)}$ as:

$$F_{S,R_{T,k^*,n^*}}(r) = 1 - \frac{\mathbb{P}\left[R_{T,k^*,n^*} > r,\ \text{Association to } \Phi_{T,(k^*,n^*)}\right]}{\mathbb{P}\left[\text{Association to } \Phi_{T,(k^*,n^*)}\right]}$$

Using the same steps and notations as in Appendix C, the numerator is:

$$\begin{aligned}
&\mathbb{P}\left[R_{T,k^*,n^*} > r,\ \text{Association to } \Phi_{T,(k^*,n^*)}\right] \\
&\quad = \mathbb{P}\Bigg[R_{T,k^*,n^*} > r, \mathcal{S} > \max\Big[\max_{(k,n)^*}\left(P_k L_{k,n}^{-1}(R_{T,k,n})\right), \max_{(k)}\left(P_k L_{\bar{t},k}^{-1}(R_{NT,k})\right), \\
&\qquad\qquad \max_{(k')}\left(P_{b,k'} L_{d,k'}^{-1}(R_{Bd,k'})\right), \max_{(k',n)}\left(P_{b,k'} L_{k',n}^{-1}(R_{B,k',n})\right)\Big]\Bigg].
\end{aligned}$$

Knowing the denominator is the association probability $\mathcal{A}_{T,k^*,n^*}$, we conclude:

$$\begin{aligned}
F_{S,R_{T,k^*,n^*}}(r) = 1 - \frac{1}{\mathcal{A}_{T,k^*,n^*}} \int_r^{\infty} &\prod_{(k,n)^*} \overline{F}_{C,R_{T,k,n}}\left(z_{T,(k,n)}^{T,(k^*,n^*)}(x)\right) \\
&\prod_{(k')} \overline{F}_{C,R_{Bd,k'}}\left(z_{Bd,(k')}^{T,(k^*,n^*)}(x)\right) \prod_{(k',n)} \overline{F}_{C,R_{B,k',n}}\left(z_{B,(k',n)}^{T,(k^*,n^*)}(x)\right) \\
&\overline{F}_{J,NT}\left(z_{NT,(1)}^{T,(k^*,n^*)}(x), \dots, z_{NT,(N_S)}^{T,(k^*,n^*)}(x)\right) f_{C,R_{T,k^*,n^*}}(x)dx
\end{aligned}$$

The PDF is then obtained by taking the derivative with respect to r.

E Proof of Lemma 4.22

Assuming $j \in \Phi_{T,(k,n,m)}$, the CF of the interference $I_{T,k,n,m}$ is given by:

$$\phi_{T,(k,n,m)}^{T,(k^*,n^*)}(t|r) = \mathbb{E}_{\Phi_{T,(k,n,m)}}\left[\prod_j \mathbb{E}_{|h_n|^2}\left[\exp\left(jtP_k G_m |h_n|^2 L_{k,n}^{-1}(r')\right)\right] \middle| k^*, n^*\right]$$

$$\phi_{T,(k,n,m)}^{T,(k^*,n^*)}(t|r) \overset{(1)}{=} \mathbb{E}_{\Phi_{T,(k,n,m)}}\left[\prod_j \phi_F\left(P_k G_m L_{k,n}^{-1}(r')t;K\right) \middle| k^*,n^*\right]$$

$$\overset{(2)}{=} \exp\left[2\int_{z_{T,(k,n)}^{T,(k^*,n^*)}(r)}^{\infty} \left[\phi_F\left(P_k G_m L_{k,n}^{-1}(r')t;K\right)-1\right]\lambda_{T,(k,n,m)}(r')dr'\right]$$

In the above developments, (1) is obtained by definition of the CF of the general fading distribution defined in Section 3.3.4. (2) comes from Theorem 2.7 assuming that all interferers undergo the same fading. Due to the association rule, the integration is then limited to $[z_{T,(k,n)}^{T,(k^*,n^*)}(r), +\infty]$ where $z_{T,(k,n)}^{T,(k^*,n^*)}(r)$ is the preference threshold defined in Section 4.3.

F Proof of Lemma 4.26

The proof of the CF of the diffracted signals strongly relies on the proof of Lemma 5 in [32]. For tier with indexes $\{k,m\}$ and for a street i, BSs are initially generated following a 1D PPP of intensity $\lambda_{ld,(k,m)}(r)$ on the x-axis (each BS has thus a x-position $t_j \in \mathbb{R}$). Each node in the NHPCLP is then rotated by an angle θ_i' and translated by $\vec{v} = (|r_i|sin(\theta_i'), |r_i|cos(\theta_i'))$. The coordinates (x_{ij}, y_{ij}) of the j-th BS in street i are thus given by $X_{i,j} = (r_j'cos(\theta_i') - |r_i|sin(\theta_i'), r_j'sin(\theta_i') + |r_i|cos(\theta_i'))$.

Let us define (1) $d_{1,i}(r_i,\theta_i)$, the distance between BS j and the the street corner, (2) $d_{2,j}(y_{ij},\theta_i)$, the distance from the UE to the street corner and (3) $\theta_i^{(B)}(\theta_i)$, the Berg model angle. In the following expressions, it is also assumed that $f_{d,k}(y_{ij},r_i,\theta_i) = L_{d,k}^{-1}(d_{1,i}(r_i,\theta_i), d_{2,j}(y_{ij},\theta_i), \theta_i^{(B)}(\theta_i))$.

On the basis of these notations, the CF of the interference associated to diffraction is derived as follows:

$$\phi_D(t) = \mathbb{E}\left[\exp\left(jtP_k G_m |h_j|^2 f_{d,k}(y_{ij},r_i,\theta_i)\right)\right]$$

$$\overset{(1)}{=} \mathbb{E}_\Phi\left[\left(1 - jtP_k G_m f_{d,k}(y_{ij},r_i,\theta_i)\right)^{-1}\right]$$

Case	Condition	$d_{2,i}(r_i,\theta_i)$	$d_{1,j}(y_{ij},\theta_i)$	$\theta_i^{(B)}(\theta_i)$
$0 \leq \theta_i' \leq \frac{\pi}{2}$ $\frac{\pi}{2} \leq \theta_i \leq \pi$	$r' \geq \frac{-r_i}{\tan(\theta_i-\frac{\pi}{2})}$;y_{ij}^+	$\frac{r_i}{\sin(\theta_i-\frac{\pi}{2})}$	$\frac{y_{ij}}{\sin(\theta_i-\frac{\pi}{2})}$	$\frac{3\pi}{2}-\theta_i$
	$r' < \frac{-r_i}{\tan(\theta_i-\frac{\pi}{2})}$;y_{ij}^-		$\frac{-y_{ij}}{\sin(\theta_i-\frac{\pi}{2})}$	$\theta_i-\frac{\pi}{2}$
$\frac{\pi}{2} \leq \theta_i' \leq \pi$ $\pi \leq \theta_i \leq \frac{3\pi}{2}$	$r' \geq \frac{r_i}{\tan(\frac{3\pi}{2}-\theta_i)}$;y_{ij}^+	$\frac{r_i}{\sin(\frac{3\pi}{2}-\theta_i)}$	$\frac{y_{ij}}{\sin(\frac{3\pi}{2}-\theta_i)}$	$\frac{3\pi}{2}-\theta_i$
	$r' < \frac{r_i}{\tan(\frac{3\pi}{2}-\theta_i)}$;y_{ij}^-		$\frac{-y_{ij}}{\sin(\frac{3\pi}{2}-\theta_i)}$	$\theta_i-\frac{\pi}{2}$
$\pi \leq \theta_i' \leq \frac{3\pi}{2}$ $\frac{3\pi}{2} \leq \theta_i \leq 2\pi$	$r' \geq \frac{-r_i}{\tan(\theta_i-\frac{3\pi}{2})}$;y_{ij}^-	$\frac{r_i}{\sin(\theta_i-\frac{3\pi}{2})}$	$\frac{-y_{ij}}{\sin(\theta_i-\frac{3\pi}{2})}$	$\frac{5\pi}{2}-\theta_i$
	$r' < \frac{-r_i}{\tan(\theta_i-\frac{3\pi}{2})}$;y_{ij}^+		$\frac{y_{ij}}{\sin(\theta_i-\frac{3\pi}{2})}$	$\theta_i-\frac{3\pi}{2}$
$\frac{3\pi}{2} \leq \theta_i' \leq 2\pi$ $0 \leq \theta_i \leq \frac{\pi}{2}$	$r' \geq \frac{r_i}{\tan(\frac{\pi}{2}-\theta_i)}$;y_{ij}^+	$\frac{r_i}{\sin(\frac{\pi}{2}-\theta_i)}$	$\frac{-y_{ij}}{\sin(\frac{\pi}{2}-\theta_i)}$	$\frac{\pi}{2}-\theta_i$
	$r' < \frac{r_i}{\tan(\frac{\pi}{2}-\theta_i)}$;y_{ij}^-		$\frac{y_{ij}}{\sin(\frac{\pi}{2}-\theta_i)}$	$\frac{\pi}{2}+\theta_i$

Table F.1 Summary of Berg model values depending on the different parameters values.

$$\phi_D(t) = \mathbb{E}_{\Phi_l}\left[\prod_{\substack{i\in\Phi_l\\ l\neq l_0}}\prod_{\{k,m\}}\mathbb{E}_{\Phi_{ld,(k,m)}}\left[\prod_{j\in\Phi_{ld,(k,m)}}\left(1\text{-}jtP_kG_mf_{d,k}(y_{ij},r_i,\theta_i)\right)^{-1}\right]\right]$$

$$\stackrel{(2)}{=} \mathbb{E}_{\Phi_l}\left[\prod_{\substack{l\in\Phi_l\\ l\neq l_0}}\prod_{\{k,m\}}\exp\left[\text{-}\lambda_{ld,(k,m)}\int_{-\infty}^{\infty}1\text{-}\left(1\text{-}jtP_kG_mg_{d,k}(i,r')\right)^{-1}dr'\right]\right]$$

$$\stackrel{(3)}{=} \exp\left[\text{-}\lambda_s\int_0^{\infty}\int_0^{2\pi}1\text{-}\prod_{\{k,m\}}\exp\left[\text{-}\lambda_{ld,(k,m)}\int_{-\infty}^{\infty}1\text{-}\right.\right.$$

$$\left.\left.\left(1\text{-}jtP_kG_mh_{d,k}(r,\theta,r')\right)^{-1}dr'\right]p(r,\theta)d\theta dr\right]$$

In the above development, (1) is obtained by definition of the CF of an exponential random variable. (2) is obtained by applying the PGFL with respect to the point processes $\Phi_{ld,(k,m)}$ in each street assuming $g_{d,k}(i,r') = f_{d,k}(r'\sin(\theta_i') + |r_i|\cos(\theta_i'), r_i, \theta_i))$. Finally, (3) is obtained by applying the PGFL with respect to Φ_l with $h_{d,k}(r,\theta,t) = f_{d,k}(r'\sin(\theta') + r\cos(\theta'), r, \theta)$ $= f_{d,k}(r'\sin(\theta-\frac{\pi}{2}) + r\cos(\theta-\frac{\pi}{2}), r, \theta)$. The different situations depending on the rotation angle θ_i' are shown on Figure F.1. Based on this figure, the Berg model values for all cases are then summarized in Table F.1. The end of the proof is straightforward.

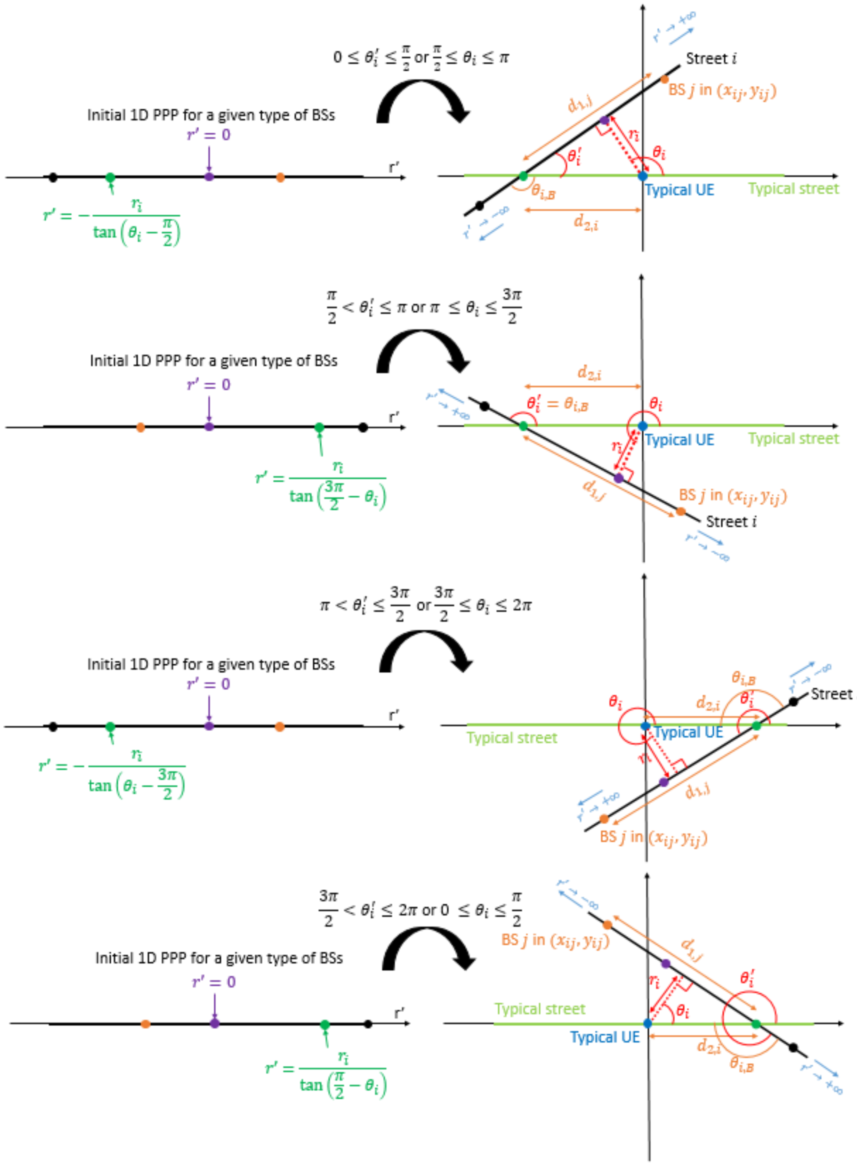

Fig. F.1 Street types with respect to r_i and θ_i values.

G Proof of Lemma 4.34

This proof strongly relies on [100]. The average capacity is given by:

$$\begin{aligned}
\mu_C &\overset{(1)}{=} \mathbb{E}\left[B\log_2\left(1+\frac{S}{I}\right)\right] \\
&\overset{(2)}{=} \frac{B}{\ln(2)}\mathbb{E}\left[\ln\left(1+\frac{S}{I}\right)\right] \\
&\overset{(3)}{=} \frac{B}{\ln(2)}\mathbb{E}\left[\int_0^\infty s^{-1}\left(1-e^{-s\frac{S}{I}}\right)e^{-s}ds\right] \\
&\overset{(4)}{=} \frac{B}{\ln(2)}\mathbb{E}\left[\int_0^\infty \frac{1}{z}\left(e^{-zI}-e^{-z(S+I)}\right)dz\right] \\
&\overset{(5)}{=} \frac{B}{\ln(2)}\int_0^\infty \frac{1}{z}\left(\mathcal{M}_I(z)-\mathcal{M}_{S+I}(z)\right)dz
\end{aligned}$$

where (1) follows from the definition of the average rate, (2) is obtained by change of base and by linearity, (3) results from the following integral $\ln(1+t)=\int_0^\infty s^{-1}\left(1-e^{-st}\right)e^{-s}ds$ for $t\geq 0$ and (4) is obtained by variable change $s=zI$. (5) can then be written by linearity and by interchanging the integral and the expectation thanks to Fubini's theorem as the intergrand is non-negative for $z\geq 0$. In addition, we use the moment generating functions (MGF) defined as $\mathcal{M}_X(t)=\mathbb{E}\left[e^{tX}\right]$. Using the conversion into the corresponding CFs and the properties of CFs, these MGFs computed as:

$$\begin{aligned}
\mathcal{M}_I(z|r) &= \mathbb{E}\left[e^{zI}|r\right] \\
&= \phi_I\left(\frac{-z}{j}\middle|r\right)
\end{aligned}
\qquad
\begin{aligned}
\mathcal{M}_{S+I}(z|r) &= \mathbb{E}\left[e^{z(S+I)}|r\right] \\
&= \phi_S\left(\frac{-z}{j}\middle|r\right)\phi_I\left(\frac{-z}{j}\middle|r\right)
\end{aligned}$$

Assuming the serving tier is tier $\Phi_{T,(k^*,n^*)}$ and averaging over r, we obtain:

$$\begin{aligned}
\mu_C^{T,(k^*,n^*)} = \frac{B}{\ln(2)}\int_0^\infty \frac{1}{z}\phi_D\left(\frac{-z}{j}\right)\int_0^\infty\left(1-\phi_S^{T,(k^*,n^*)}\left(\frac{-z}{j}\middle|r\right)\right) \\
\phi_I\left(\frac{-z}{j}\middle|r\right)f_{S,R_{T,k^*,n^*}}(r)drdz
\end{aligned}$$

where $\phi_I(q|r)$ is defined as in Lemma 4.38.

H Proof of Lemma 4.37

The average is by definition given by

$$\mu_E = \mathbb{E}\Big[S + \sum_{\{j,k,n,m\}} I_{j,k,n,m} + \sum_{\{j,k,m\}} I_{j,d,k,m} + \sum_{\{k,m\}} I_{p,k,m}\Big]$$
$$= \underbrace{\mathbb{E}\Big[\sum_{\{k,m\}} I_{NT,d,k,m}\Big]}_{m_D} + \underbrace{\mathbb{E}\Big[S + \sum_{\{j,k,n,m\}} I_{j,k,n,m} + \sum_{\{k,m\}} I_{Bd,d,k,m} + \sum_{\{k,m\}} I_{p,k,m}\Big]}_{m_O}$$

where m_O represents the mean of the total exposure coming potential serving tiers and m_D the mean exposure associated to corner diffraction for signals coming from non typical streets.

Assuming a serving BS from tier $\Phi_{T,(k^*,n^*)}$ located at a distance r, the second term is computed as:

$$m_{O|r}^{T,(n^*,k^*)} = \mathbb{E}\Big[S + \sum_{\{j,k,n,m\}} I_{j,k,n,m} + \sum_{\{k,m\}} I_{Bd,d,k,m} + \sum_{\{k,m\}} I_{p,k,m} | \{k^*, n^*\}, r\Big]$$
$$= \mathbb{E}_g\left[P_{k^*} G_1 g L^{-1}_{k^*,n^*}(r)\right]$$
$$+ \sum_{\{k,n,m\}} \mathbb{E}_{j\in\Phi_{T,(k,n,m)}}\left[\mathbb{E}_{g_j}\left[P_k G_m g_j L^{-1}_{k,n}(r_j)\right] | r\right]$$
$$+ \sum_{\{k,n,m\}} \mathbb{E}_{j\in\Phi_{B,(k,n,m)}}\left[\mathbb{E}_{g_j}\left[P_{b,k} G_m g_j L^{-1}_{k,n}(r_j)\right] | r\right]$$
$$+ \sum_{\{k,m\}} \mathbb{E}_{j\in\Phi_{Bd,(k,m)}}\left[\mathbb{E}_{g_j}\left[P_{b,k} G_m g_j L^{-1}_{d,k}(r_j)\right] | r\right]$$
$$+ \sum_{\{k,m\}} \mathbb{E}_{j\in\Phi_{NT,(k,m)}}\left[\mathbb{E}_{g_j}\left[P_k G_m g_j L^{-1}_{\bar{t},k}(r_j)\right] | r\right].$$

Each term can be developed using Theorem 2.7 knowing the channel power gain g for all links has a unit mean. The term m_D is similarly computed. By averaging over the distance to the serving BS, one obtains

$$m_O^{T,n^*,k^*} = \int_0^\infty m_{O|r}^{T,(n^*,k^*)} f_{S,R_{T,k^*,n^*}}(r)dr. \tag{1}$$

I Proof of Lemma 4.42

The joint metric can be expressed as

$$
\begin{aligned}
J(\theta_c,\theta_e) \triangleq \mathbb{P}\Big[\frac{S}{I} > \theta_c, S+I<\theta_e\Big] &= \mathbb{P}\Big[I<\frac{S}{\theta_c}, I<\theta_e - S\Big] \\
&= \begin{cases} \mathbb{P}\Big[I<\frac{S}{\theta_c}\Big] & \text{if } \frac{S}{\theta_c} < \theta_e - S \\ \mathbb{P}\Big[I<\theta_e - S\Big] & \text{if } \theta_e - S < \frac{S}{\theta_c} \end{cases} \\
&= \begin{cases} \mathbb{P}\Big[I<\frac{S}{\theta_c}\Big] & \text{if } S < \underbrace{\frac{\theta_c\theta_e}{1+\theta_c}}_{\theta'} \\ \mathbb{P}\Big[I<\theta_e - S\Big] & \text{if } \theta' < S < \theta_e \\ 0 & \text{if } S > \theta_e \end{cases}
\end{aligned}
$$

We then obtain:

$$
J^{T,(k^*,n^*)}(\theta_c,\theta_e|r) = \begin{cases} \mathbb{P}\Big[I<\frac{g\mathcal{S}(r)}{\theta_c}\Big] & \text{if } g<\theta_1(r) = \frac{\theta'}{\mathcal{S}(r)} \\ \mathbb{P}\Big[I<\theta_e - g\mathcal{S}(r)\Big] & \text{if } \theta_1(r) < g < \theta_2(r) = \frac{\theta_e}{\mathcal{S}(r)} \\ 0 & \text{if } g > \theta_2(r) \end{cases}
$$

assuming the user is associated to a BS of tier $\Phi_{T,(k^*,n^*)}$ and defining $\mathcal{S}(r) = P_{k^*}G_m L^{-1}_{k^*,n^*}(r)$.

Let us define $F_I^{T,(k^*,n^*)}(i|r)$ to be the cumulative distribution function of the total interference conditioned on the serving distance r and on the serving tier. Using linearity, the last equality can be rewritten as

$$
\begin{aligned}
J^{T,(k^*,n^*)}\left(\theta,\theta'\right) &= \underbrace{\mathbb{E}_r\left[\int_0^{\theta_1(r)} F_I^{T,(k^*,n^*)}\left(\frac{g\mathcal{S}(r)}{\theta_c}\,\middle|\, r\right) f_G(g)dg\right]}_{T_1} \\
&+ \underbrace{\mathbb{E}_r\left[\int_{\theta_1(r)}^{\theta_2(r)} F_I^{T,(k^*,n^*)}\left(\theta_e - g\mathcal{S}(r)\,\middle|\, r\right) f_G(g)dg\right]}_{T_2}
\end{aligned}
$$

Using Theorem 2.23, the CDF of the total interference can be expressed as:

$$F_I^{T,(k^*,n^*)}(i|r) = \frac{1}{2} - \frac{1}{\pi}\int_0^\infty Im\left[\phi_I(q|r)e^{-jqi}\right]q^{-1}dq.$$

Assuming Rayleigh fading on the useful link, we compute T_1

$$\begin{aligned}
&= \mathbb{E}_r\left[\int_0^{\theta_1(r)}\left(\frac{1}{2} - \frac{1}{\pi}\int_0^\infty Im\left[\phi_I(q|r)e^{-jq\frac{g\mathcal{S}(r)}{\theta_c}}\right]q^{-1}dq\right)e^{-g}dg\right] \\
&\overset{(1)}{=} \mathbb{E}_r\left[\frac{1}{2}F_G(\theta_1(r)) - \frac{1}{\pi}\int_0^\infty\int_0^{\theta_1(r)} Im\left[\phi_I(q|r)e^{-jq\frac{g\mathcal{S}(r)}{\theta_c}}\right]e^{-g}dg\; q^{-1}dq\right] \\
&\overset{(2)}{=} \mathbb{E}_r\left[\frac{1}{2}F_G(\theta_1(r)) - \frac{1}{\pi}\int_0^\infty Im\left[\phi_I(q|r)\int_0^{\theta_1(r)} e^{-jq\frac{g\mathcal{S}(r)}{\theta_c}}e^{-g}dg\right]q^{-1}dq\right] \\
&\overset{(3)}{=} \mathbb{E}_r\left[\frac{1}{2}F_G(\theta_1(r)) - \frac{1}{\pi}\int_0^\infty Im\left[\phi_I(q|r)\frac{1-e^{\theta_1(r)\left(1+j\frac{q\mathcal{S}(r)}{\theta_c}\right)}}{1+j\frac{q\mathcal{S}(r)}{\theta_c}}\right]q^{-1}dq\right]
\end{aligned}$$

where (1) is obtained by linearity and by swapping the integral order. Note that $F_G(g)$ is the CDF of Rayleigh fading power gains. (2) follows from the swap between the integral and the imaginary part. (3) results from $\int_a^b e^{-(1+jc)x}dx = (e^{-a(1+jc)} - e^{-b(1+jc)})/(1+jc)$.

By integrating over r, we obtain

$$\begin{aligned}
T_1 &= \frac{1}{2}\int_0^\infty F_G(\theta_1(r))f_{S,R_{T,k^*,n^*}}(r)dr \\
&\quad - \frac{1}{\pi}\int_0^\infty\int_0^\infty Im\left[\phi_I(q|r)\frac{1-e^{\theta_1(r)\left(1+j\frac{q\mathcal{S}(r)}{\theta_c}\right)}}{1+j\frac{q\mathcal{S}(r)}{\theta_c}}\right]q^{-1}dqf_{S,R_{T,k^*,n^*}}(r)dr.
\end{aligned}$$

Similarly, we have:

$$\begin{aligned}
T_2 = \mathbb{E}_r\Bigg[&\frac{1}{2}F_G(\theta_2(r)) - \frac{1}{2}F_G(\theta_1(r)) \\
&- \frac{1}{\pi}\int_0^\infty Im\left[\phi_I(q|r)e^{-jq\theta_e}\int_{\theta_1(r)}^{\theta_2(r)} e^{jqg\mathcal{S}(r)}e^{-g}dg\right]q^{-1}dq\Bigg]
\end{aligned}$$

$$T_2 \overset{(1)}{=} \mathbb{E}_r\Bigg[\frac{1}{2}F_G(\theta_2(r)) - \frac{1}{2}F_G(\theta_1(r))$$
$$- \frac{1}{\pi}\int_0^\infty Im\left[\phi_I(q|r)e^{-jq\theta_e}\frac{e^{\theta_2(r)\mathcal{S}_2(r)} - e^{\theta_1(r)\mathcal{S}_2(r)}}{\mathcal{S}_2(r)}\right]q^{-1}dq\Bigg]$$
$$\overset{(2)}{=} \frac{1}{2}\int_0^\infty F_G(\theta_2(r))f_{S,R_{T,k^*,n^*}}(r)dr - \frac{1}{2}\int_0^\infty F_G(\theta_1(r))f_{S,R_{T,k^*,n^*}}(r)dr$$
$$- \frac{1}{\pi}\int_0^\infty\int_0^\infty Im\left[\phi_I(q|r)e^{-jq\theta_e}\frac{e^{\theta_2(r)\mathcal{S}_2(r)} - e^{\theta_1(r)\mathcal{S}_2(r)}}{\mathcal{S}_2(r)}\right]q^{-1}dqf_{S,R_{T,k^*,n^*}}(r)dr$$

where (1) results from the following integral computation:

$$\int_a^b e^{(-1+jc)x}dx = \frac{e^{b(-1+jc)} - e^{a(-1+jc)}}{-1+jc}$$

assuming $\mathcal{S}_2(r) = -1 + jq\mathcal{S}(r)$. (2) results from the integration over r.

J Proof of Lemma 4.48

If the serving BS is from tier $\Phi_{T,(k^*,n^*)}$, the CDF of its distance to the UE knowing the condition $\gamma = (k_\gamma, n_\gamma)$ of the hotspot BS is

$$F_{R_{0,\gamma}}^{T,(k^*,n^*)}(r) = 1 - \frac{\mathbb{P}\left[R_{0,\gamma} > r,\ \text{Association to } \Phi_{T,(k^*,n^*)}, \gamma\right]}{\mathbb{P}\left[\text{Association to } \Phi_{T,(k^*,n^*)}, \gamma\right]}.$$

While the denominator is known, the numerator can be computed using the same notations as in Appendix C:

$$\mathbb{P}\left[R_{0,\gamma} > r,\ \text{Association to } \Phi_{T,(k^*,n^*)}, \gamma\right]$$
$$= \mathbb{P}\Bigg[R_{0,\gamma} > r, \mathcal{S} > \max\Big[\max_{(k,n)^*}\left(P_k L_{k,n}^{-1}(R_{T,k,n})\right), \max_{(k)}\left(P_k L_{\tilde{t},k}^{-1}(R_{NT,k})\right),$$
$$\max_{(k')}\left(P_{b,k'}L_{d,k'}^{-1}(R_{Bd,k'})\right), \max_{(k',n)}\left(P_{b,k'}L_{k',n}^{-1}(R_{B,k',n})\right), P_{k_\gamma}L_{k_\gamma,n_\gamma}^{-1}(R_{0,\gamma})\Big]\Bigg]$$

$$
\begin{aligned}
&\mathbb{P}\left[R_{0,\gamma} > r,\ \text{Association to } \Phi_{T,(k^*,n^*)}, \gamma\right] \\
&= \int_0^\infty \prod_{(k',n)} F_{C,R_{B,k',n}}\left(z_{B,(k',n)}^{T,(k^*,n^*)}(x)\right)\mathbb{P}\left[R_{0,\gamma} > r, R_{0,\gamma} > z_{0,(k_\gamma,n_\gamma)}^{T,(k^*,n^*)}(x)\ \right] \\
&\qquad \prod_{(k,n)^*} F_{C,R_{T,k,n}}\left(z_{T,(k,n)}^{T,(k^*,n^*)}(x)\right)\prod_{(k')} F_{C,R_{Bd,k'}}\left(z_{Bd,(k')}^{T,(k^*,n^*)}(x)\right) \\
&\qquad F_{J,NT}\left(z_{NT,(1)}^{T,(k^*,n^*)}(x), ..., z_{NT,(N_S)}^{T,(k^*,n^*)}(x)\right) f_{C,R_{T,k^*,n^*,\gamma}}(x)dx \\
&= \int_0^\infty \prod_{(k',n)} F_{C,R_{B,k',n}}\left(z_{B,(k',n)}^{T,(k^*,n^*)}(x)\right)\Big\{\overline{F}_{C,R_{0,\gamma}}(r)\mathbb{1}\left(r > z_{0,(k_\gamma,n_\gamma)}^{T,(k^*,n^*)}(x)\right) \\
&\qquad + \overline{F}_{C,R_{0,\gamma}}\left(z_{0,(k_\gamma,n_\gamma)}^{T,(k^*,n^*)}(x)\right)\mathbb{1}\left(z_{0,(k_\gamma,n_\gamma)}^{T,(k^*,n^*)}(x) > r\right)\Big\} \\
&\qquad \prod_{(k,n)^*} F_{C,R_{T,k,n}}\left(z_{T,(k,n)}^{T,(k^*,n^*)}(x)\right)\prod_{(k')} F_{C,R_{Bd,k'}}\left(z_{Bd,(k')}^{T,(k^*,n^*)}(x)\right) \\
&\qquad F_{J,NT}\left(z_{NT,(1)}^{T,(k^*,n^*)}(x), ..., z_{NT,(N_S)}^{T,(k^*,n^*)}(x)\right) f_{C,R_{T,k^*,n^*,\gamma}}(x)dx
\end{aligned}
$$

Grouping the elements to obtain $F_{R_{0,\gamma}}^{T,(k^*,n^*)}(r)$ and taking the derivative with respect to r leads to the desired result.

List of publications

Journal papers

- Wiame, C., **Demey, S.**, Vandendorpe, L., De Doncker, P., & Oestges, C. (2023). Joint data rate and EMF exposure analysis in Manhattan environments: stochastic geometry and ray tracing approaches. IEEE Transactions on Vehicular Technology (submitted).
- Quatresooz, F., **Demey, S.**, & Oestges, C. (2021). Tracking of interaction points for improved dynamic ray tracing. IEEE Transactions on Vehicular Technology, 70(7), 6291-6301.

Refereed conference papers

- **Demey, S.**, Wiame, C., Vandendorpe, L., & Oestges, C. (2020). Analysis of wireless device-to-device networks under Rician fading using stochastic geometry. In 2020 IEEE 92nd Vehicular Technology Conference (VTC2020-Fall) (pp. 1-7). IEEE.

COST TDs

- **Demey, S.**, Wiame, C., De Doncker, P., & Oestges, C. (2022). Joint rate and power density analysis in Manhattan environments: (a comparison of) stochastic geometry and ray-tracing approaches. CA20120 TD(22)01063, Bologna Feb. 2022.

- **Demey, S.**, De Doncker, P., & Oestges, C. (2019). A comparison between stochastic geometry and ray-tracing in small cells. CA15104 TD(19)10052, Oulu May 2019.

Bibliography

[1] F. Laricchia, "Number of mobile devices worldwide 2020-2025," 10 2022.

[2] M. K. Weldon, *The future X network: a Bell Labs perspective*. CRC press, 2016.

[3] N. B. Labs, "Future of communications: Nokia bell labs perspective," 2016.

[4] Cisco, "Cisco annual internet report (2018–2023)," tech. rep., Cisco, 2020.

[5] D. López-Pérez, M. Ding, H. Claussen, and A. H. Jafari, "Towards 1 gbps/ue in cellular systems: Understanding ultra-dense small cell deployments," *IEEE Communications Surveys & Tutorials*, vol. 17, no. 4, pp. 2078–2101, 2015.

[6] H. Claussen, D. Lopez-Perez, L. Ho, R. Razavi, and S. Kucera, *Small cell networks: deployment, management, and optimization*. John Wiley & Sons, 2017.

[7] C. Saha, *Advances in Stochastic Geometry for Cellular Networks*. PhD thesis, Virginia Tech, 2020.

[8] P. Fernando, P. Mari, *et al.*, *Modelling the wireless propagation channel: a simulation approach with Matlab*. John Wiley & Sons, 2008.

[9] M. Hata, "Empirical formula for propagation loss in land mobile radio services," *IEEE transactions on Vehicular Technology*, vol. 29, no. 3, pp. 317–325, 1980.

[10] H. Xia, H. L. Bertoni, L. R. Maciel, A. Lindsay-Stewart, and R. Rowe, "Radio propagation characteristics for line-of-sight microcellular and personal communications," *IEEE Transactions on antennas and propagation*, vol. 41, no. 10, pp. 1439–1447, 1993.

[11] J. J. Egli, "Radio propagation above 40 mc over irregular terrain," *Proceedings of the IRE*, vol. 45, no. 10, pp. 1383–1391, 1957.

[12] A. Grami, *Introduction to digital communications*. Academic Press, 2015.

[13] P. Almers, E. Bonek, A. Burr, N. Czink, M. Debbah, V. Degli-Esposti, H. Hofstetter, P. Kyösti, D. Laurenson, G. Matz, *et al.*, "Survey of channel and radio propagation models for wireless mimo systems," *EURASIP Journal on Wireless Communications and Networking*, vol. 2007, pp. 1–19, 2007.

[14] D. He, B. Ai, K. Guan, L. Wang, Z. Zhong, and T. Kürner, "The design and applications of high-performance ray-tracing simulation platform for 5g and beyond wireless communications: A tutorial," *IEEE Communications Surveys & Tutorials*, vol. 21, no. 1, pp. 10–27, 2018.

[15] D. Chizhik, F. Rashid-Farrokhi, J. Ling, and A. Lozano, "Effect of antenna separation on the capacity of blast in correlated channels," *IEEE Communications letters*, vol. 4, no. 11, pp. 337–339, 2000.

[16] W. Weichselberger, M. Herdin, H. Ozcelik, and E. Bonek, "A stochastic mimo channel model with joint correlation of both link ends," *IEEE Transactions on wireless Communications*, vol. 5, no. 1, pp. 90–100, 2006.

[17] A. G. Burr, "Capacity bounds and estimates for the finite scatterers mimo wireless channel," *IEEE Journal on Selected Areas in Communications*, vol. 21, no. 5, pp. 812–818, 2003.

[18] J. Medbo, P. Kyosti, K. Kusume, L. Raschkowski, K. Haneda, T. Jamsa, V. Nurmela, A. Roivainen, and J. Meinila, "Radio propagation modeling for 5g mobile and wireless communications," *IEEE Communications Magazine*, vol. 54, no. 6, pp. 144–151, 2016.

[19] F. Quatresooz and C. Oestges, "Dynamic ray tracing techniques for mobile radio communications," Master's thesis, Université Catholique de Louvain, 2020.

[20] I. A. Hemadeh, K. Satyanarayana, M. El-Hajjar, and L. Hanzo, "Millimeter-wave communications: Physical channel models, design considerations, antenna constructions, and link-budget," *IEEE Communications Surveys & Tutorials*, vol. 20, no. 2, pp. 870–913, 2017.

[21] Z. Yun and M. F. Iskander, "Ray tracing for radio propagation modeling: Principles and applications," *IEEE Access*, vol. 3, pp. 1089–1100, 2015.

[22] F. Fuschini, E. M. Vitucci, M. Barbiroli, G. Falciasecca, and V. Degli-Esposti, "Ray tracing propagation modeling for future small-cell and indoor applications: A review of current techniques," *Radio Science*, vol. 50, no. 6, pp. 469–485, 2015.

[23] T. K. Geok, F. Hossain, M. Kamaruddin, N. Rahman, S. Thiagarajah, A. T. W. Chiat, and C. Liew, "A comprehensive review of efficient ray-tracing techniques for wireless communication," *International Journal on Communications Antenna and Propagation*, vol. 8, no. 2, pp. 123–136, 2018.

[24] F. Quitin, *Channel modeling for polarized MIMO systems*. PhD thesis, Université Catholique de Louvain, Université Libre de Bruxelles, 2011.

[25] B. François and B. Bartłomiej, "Stochastic geometry and wireless networks: Volume i theory," *NoW PublishersBreda*, vol. 55, 2009.

[26] V. H. Mac Donald, "Advanced mobile phone service: The cellular concept," *The bell system technical Journal*, vol. 58, no. 1, pp. 15–41, 1979.

[27] H. M. M. M. Elsawy, *Modeling, analysis, and optimization of random wireless networks: Stochastic geometry approach*. PhD thesis, University of Manitoba, 2014.

[28] K. Ali, *Modeling, Analysis, and Design of 5G Networks using Stochastic Geometry*. PhD thesis, King Abdullah University of Science and Technology, 2018.

[29] S. Zuyev, "Stochastic geometry and telecommunications networks," 2009.

[30] F. Baccelli and X. Zhang, "A correlated shadowing model for urban wireless networks," in *2015 IEEE Conference on Computer Communications (INFOCOM)*, pp. 801–809, IEEE, 2015.

[31] V. V. Chetlur and H. S. Dhillon, "Coverage analysis of a vehicular network modeled as cox process driven by poisson line process," *IEEE Transactions on Wireless Communications*, vol. 17, no. 7, pp. 4401–4416, 2018.

[32] C.-S. Choi and F. Baccelli, "Poisson cox point processes for vehicular networks," *IEEE Transactions on Vehicular Technology*, vol. 67, no. 10, pp. 10160–10165, 2018.

[33] F. Lagum, *Stochastic Geometry-Based Tools for Spatial Modeling and Planning of Future Cellular Networks: Opportunistic Cell Switch-off and Strategic Deployment of Flying Base Stations*. PhD thesis, Carleton University, 2019.

[34] Y. Hmamouche, *Applications of stochastic geometry in the modeling and analysis of wireless networks*. PhD thesis, Ecole nationale supérieure Mines-Télécom Atlantique, 2020.

[35] V. V. Chetlur Ravi, *Stochastic Geometry for Vehicular Networks*. PhD thesis, Virginia Tech, 2020.

[36] M. Haenggi, J. G. Andrews, F. Baccelli, O. Dousse, and M. Franceschetti, "Stochastic geometry and random graphs for the analysis and design of wireless networks," *IEEE journal on selected areas in communications*, vol. 27, no. 7, pp. 1029–1046, 2009.

[37] F. Baccelli, B. Błaszczyszyn, *et al.*, "Stochastic geometry and wireless networks: Volume ii applications," *Foundations and Trends® in Networking*, vol. 4, no. 1–2, pp. 1–312, 2010.

[38] H. S. Dhillon and V. V. Chetlur, "Poisson line cox process: Foundations and applications to vehicular networks," *Synthesis Lectures on Learning, Networks, and Algorithms*, vol. 1, no. 1, pp. 1–149, 2020.

[39] A. Stuart, "Kendall's advanced theory of statistics," *Distribution theory*, vol. 1, 1994.

[40] G. Boeing, "Urban spatial order: Street network orientation, configuration, and entropy," *Applied Network Science*, vol. 4, no. 1, pp. 1–19, 2019.

[41] J. P. Jeyaraj and M. Haenggi, "Cox models for vehicular networks: Sir performance and equivalence," *IEEE Transactions on Wireless Communications*, vol. 20, no. 1, pp. 171–185, 2020.

[42] S. Demey, C. Wiame, L. Vandendorpe, and C. Oestges, "Analysis of wireless device-to-device networks under rician fading using stochastic geometry," in *2020 IEEE 92nd Vehicular Technology Conference (VTC2020-Fall)*, pp. 1–7, IEEE, 2020.

[43] J. Gil-Pelaez, "Note on the inversion theorem," *Biometrika*, vol. 38, no. 3-4, pp. 481–482, 1951.

[44] S. Musa and W. Wasylkiwskyj, "Co-channel interference of spread spectrum systems in a multiple user environment," *IEEE Transactions on Communications*, vol. 26, no. 10, pp. 1405–1413, 1978.

[45] H. ElSawy, A. Sultan-Salem, M.-S. Alouini, and M. Z. Win, "Modeling and analysis of cellular networks using stochastic geometry: A tutorial," *IEEE Communications Surveys & Tutorials*, vol. 19, no. 1, pp. 167–203, 2016.

[46] H. S. Dhillon, R. K. Ganti, F. Baccelli, and J. G. Andrews, "Modeling and analysis of k-tier downlink heterogeneous cellular networks," *IEEE Journal on Selected Areas in Communications*, vol. 30, no. 3, pp. 550–560, 2012.

[47] M. Haenggi, *Stochastic geometry for wireless networks*. Cambridge University Press, 2012.

[48] T. Bai and R. W. Heath, "Coverage and rate analysis for millimeter-wave cellular networks," *IEEE Transactions on Wireless Communications*, vol. 14, no. 2, pp. 1100–1114, 2014.

[49] L. Hardesty, "Nyc allows 5g equipment on streetlamps." `https://www.fiercewireless.com/5g/nyc-allows-5g-equipment-streetlamps`, 04 2020.

[50] G. Mansfield, "Using streetlights to boost 5g deployments in cities." `https://about.att.com/innovationblog/2022/streetlights-to-boost-5g-deployments.html`, 02 2022.

[51] Y. Wang, K. Venugopal, A. F. Molisch, and R. W. Heath, "Mmwave vehicle-to-infrastructure communication: Analysis of urban microcellular networks," *IEEE Transactions on Vehicular Technology*, vol. 67, no. 8, pp. 7086–7100, 2018.

[52] A. I. Akin, I. Stupia, and L. Vandendorpe, "On the effect of blockage objects in dense mimo swipt networks," *IEEE Transactions on Communications*, vol. 67, no. 2, pp. 1059–1069, 2018.

[53] X. Zhang, F. Baccelli, and R. W. Heath, "An indoor correlated shadowing model," in *2015 IEEE Global Communications Conference (GLOBECOM)*, pp. 1–7, IEEE, 2015.

[54] M. K. Müller, M. Taranetz, and M. Rupp, "Analyzing wireless indoor communications by blockage models," *IEEE Access*, vol. 5, pp. 2172–2186, 2016.

[55] Y. Wang, C. Chen, H. Zheng, and X. Chu, "Performance of indoor small-cell networks under interior wall penetration losses," *IEEE Internet of Things Journal*, 2023.

[56] E. Hriba, M. C. Valenti, and R. W. Heath, "Optimization of a millimeter-wave uav-to-ground network in urban deployments," in *MILCOM 2021-2021 IEEE Military Communications Conference (MILCOM)*, pp. 861–867, IEEE, 2021.

[57] B. R. Elbal, M. K. Müller, S. Schwarz, and M. Rupp, "Coverage analysis of relay assisted v2i communication in microcellular urban networks," in *2019 27th European Signal Processing Conference (EUSIPCO)*, pp. 1–5, IEEE, 2019.

[58] V. V. Chetlur and H. S. Dhillon, "On the load distribution of vehicular users modeled by a poisson line cox process," *IEEE Wireless Communications Letters*, vol. 9, no. 12, pp. 2121–2125, 2020.

[59] C.-S. Choi and F. Baccelli, "Modeling and analysis of vehicle safety message broadcast in cellular networks," *IEEE Transactions on Wireless Communications*, vol. 20, no. 7, pp. 4087–4099, 2021.

[60] V. V. Chetlur and H. S. Dhillon, "Coverage and rate analysis of downlink cellular vehicle-to-everything (c-v2x) communication," *IEEE Transactions on Wireless Communications*, vol. 19, no. 3, pp. 1738–1753, 2019.

[61] V. V. Chetlur and H. S. Dhillon, "Success probability and area spectral efficiency of a vanet modeled as a cox process," *IEEE Wireless Communications Letters*, vol. 7, no. 5, pp. 856–859, 2018.

[62] C.-S. Choi and F. Baccelli, "An analytical framework for coverage in cellular networks leveraging vehicles," *IEEE Transactions on Communications*, vol. 66, no. 10, pp. 4950–4964, 2018.

[63] G. Ghatak, A. De Domenico, and M. Coupechoux, "Small cell deployment along roads: Coverage analysis and slice-aware rat selection," *IEEE Transactions on Communications*, vol. 67, no. 8, pp. 5875–5891, 2019.

[64] H.-W. Liu, T.-X. Zheng, Y. Wen, C. Feng, and H.-M. Wang, "Performance analysis of uplink mmwave communications in c-v2x networks," in *GLOBECOM 2020-2020 IEEE Global Communications Conference*, pp. 1–6, IEEE, 2020.

[65] B. Pan and H. Wu, "Success probability analysis of cooperative c-v2x communications," *IEEE Transactions on Intelligent Transportation Systems*, 2021.

[66] J. P. Jeyaraj, M. Haenggi, A. H. Sakr, and H. Lu, "The transdimensional poisson process for vehicular network analysis," *IEEE Transactions on Wireless Communications*, vol. 20, no. 12, pp. 8023–8038, 2021.

[67] M. T. Shah, G. Ghatak, S. Sanyal, and M. Haenggi, "Binomial line cox processes: Statistical characterization and applications in wireless network analysis," *arXiv preprint arXiv:2302.05151*, 2023.

[68] J.-E. Berg, "A recursive method for street microcell path loss calculations," in *Proceedings of 6th International Symposium on Personal, Indoor and Mobile Radio Communications*, vol. 1, pp. 140–143, IEEE, 1995.

[69] J. Järveläinen, S. L. Nguyen, K. Haneda, R. Naderpour, and U. T. Virk, "Evaluation of millimeter-wave line-of-sight probability with point cloud data," *IEEE Wireless Communications Letters*, vol. 5, no. 3, pp. 228–231, 2016.

[70] S. Singh, M. N. Kulkarni, A. Ghosh, and J. G. Andrews, "Tractable model for rate in self-backhauled millimeter wave cellular networks," *IEEE Journal on Selected Areas in Communications*, vol. 33, no. 10, pp. 2196–2211, 2015.

[71] Q. Feng, E. K. Tameh, A. R. Nix, and J. McGeehan, "Wlcp2-06: Modelling the likelihood of line-of-sight for air-to-ground radio propagation in urban environments," in *IEEE Globecom 2006*, pp. 1–5, IEEE, 2006.

[72] F. De Saint Moulin, "Stochastic geometry-based modelling of wireless communication networks : Uav-based networks," Master's thesis, Université Catholique de Louvain, 2020.

[73] T. Hou, Y. Liu, Z. Song, X. Sun, and Y. Chen, "Multiple antenna aided noma in uav networks: A stochastic geometry approach," *IEEE Transactions on Communications*, vol. 67, no. 2, pp. 1031–1044, 2018.

[74] L. Raschkowski, P. Kyösti, K. Kusume, and T. Jämsä, "Channel model," in *ICT-317669-METIS/D1.4*, 2015.

[75] Y. d. J. Bultitude and T. Rautiainen, "Ist-4-027756 winner ii d1. 1.2 v1. 2 winner ii channel models," *EBITG, TUI, UOULU, CU/CRC, NOKIA, Tech. Rep*, 2007.

[76] A. Al-Hourani, S. Kandeepan, and S. Lardner, "Optimal lap altitude for maximum coverage," *IEEE Wireless Communications Letters*, vol. 3, no. 6, pp. 569–572, 2014.

[77] M. Deruyck, *Design of green wireless access networks for outdoor environments: optimization towards power consumption and electromagnetic exposure for human beings*. PhD thesis, Universiteit Gent, 2015.

[78] P. Koivumäki, A. F. Molisch, and K. Haneda, "Line-of-sight probability in cluttered urban microcells: Analyses using poisson point process and point cloud," *IEEE Transactions on Antennas and Propagation*, vol. 70, no. 3, pp. 2161–2173, 2021.

[79] C. E. Shannon, "Communication in the presence of noise," *Proceedings of the IRE*, vol. 37, no. 1, pp. 10–21, 1949.

[80] D. Stoyan, W. S. Kendall, S. N. Chiu, and J. Mecke, *Stochastic geometry and its applications*. John Wiley & Sons, 2013.

[81] J. G. Andrews, F. Baccelli, and R. K. Ganti, "A tractable approach to coverage and rate in cellular networks," *IEEE Transactions on communications*, vol. 59, no. 11, pp. 3122–3134, 2011.

[82] 3GPP, "Radio Frequency (RF) and coexistence aspects (Release 14)," Technical Specification (TS) 38.214, 3rd Generation Partnership Project (3GPP), 10 2018. Version 15.3.0.

[83] S. Pratschner, M. K. Müller, F. Ademaj, A. Nabavi, B. Tahir, S. Schwarz, and M. Rupp, "Verification of the vienna 5g link and system level simulators and their interaction," in *2019 16th IEEE Annual Consumer Communications & Networking Conference (CCNC)*, pp. 1–8, IEEE, 2019.

[84] 3GPP, "Radio Frequency (RF) and coexistence aspects (Release 14)," Technical Report (TR) 38.803, 3rd Generation Partnership Project (3GPP), 03 2022. Version 14.2.2.

[85] N. A. Muhammad, N. Seman, N. I. A. Apandi, C. T. Han, Y. Li, and O. Elijah, "Stochastic geometry analysis of electromagnetic field exposure in coexisting sub-6 ghz and millimeter wave networks," *IEEE Access*, vol. 9, pp. 112780–112791, 2021.

[86] Q. Gontier, L. Petrillo, F. Rottenberg, F. Horlin, J. Wiart, C. Oestges, and P. De Doncker, "A stochastic geometry approach to emf exposure modeling," *IEEE access*, vol. 9, pp. 91777–91787, 2021.

[87] M. Fréchet, "Généralisation du théoreme des probabilités totales," *Fundamenta mathematicae*, vol. 1, no. 25, pp. 379–387, 1935.

[88] C. Wiame, S. Demey, L. Vandendorpe, P. De Doncker, and C. Oestges, "Joint data rate and emf exposure analysis in manhattan environments: stochastic geometry and ray tracing approaches," *arXiv preprint arXiv:2301.11097*, 2023.

[89] J. Feng and Z. Feng, "Optimal base station density of dense network: From the viewpoint of interference and load," *Sensors*, 2017.

[90] W. Lu and M. Di Renzo, "Stochastic geometry modeling of cellular networks: Analysis, simulation and experimental validation," in *Proceedings of the 18th ACM International Conference on Modeling, Analysis and Simulation of Wireless and Mobile Systems*, pp. 179–188, 2015.

[91] S. S. Ram, G. Singh, and G. Ghatak, "Optimization of radar parameters for maximum detection probability under generalized discrete clutter conditions using stochastic geometry," *IEEE Open Journal of Signal Processing*, vol. 2, pp. 571–585, 2021.

[92] C. Oestges, *Propagation Modelling of Low Earth-Orbit Satellite Personal Communication Systems*. PhD dissertation, Université Catholique de Louvain, 2000.

[93] D. Tami, C. G. Rego, D. Guevara, A. Navarro, F. J. Moreira, J. Giménez, and H. G. Triana, "Analysis of heuristic uniform theory of diffraction coefficients for electromagnetic scattering prediction," *International Journal of Antennas and Propagation*, vol. 2018, 2018.

[94] Urbis, "Datastore brussels." `https://datastore.brussels/web/urbis-download`, 03 2023.

[95] A. metropolitana de Barcelona, "Geoportal de cartografia." `https://geoportalcartografia.amb.cat/AppGeoportalCartografia2/index.html?locale=es&Categoria=Cartografia&Producte=1&zoom=5&x=426964.3920988743&y=4578792.012819536#`, 03 2023.

[96] R. Elements, "Array sector 3-17 ds." `https://rfelements.com/assets/Uploads/Datasheet-AS-3-17DS.pdf`, 2021. original document from RF Elements.

[97] W. Xiao, R. Ratasuk, A. Ghosh, R. Love, Y. Sun, and R. Nory, "Uplink power control, interference coordination and resource allocation for 3gpp e-utra," in *IEEE Vehicular Technology Conference*, pp. 1–5, IEEE, 2006.

[98] R. K. Ganti and M. Haenggi, "Asymptotics and approximation of the sir distribution in general cellular networks," *IEEE Transactions on Wireless Communications*, vol. 15, no. 3, pp. 2130–2143, 2015.

[99] H.-S. Jo, Y. J. Sang, P. Xia, and J. G. Andrews, "Heterogeneous cellular networks with flexible cell association: A comprehensive downlink sinr analysis," *IEEE Transactions on Wireless Communications*, vol. 11, no. 10, pp. 3484–3495, 2012.

[100] K. A. Hamdi, "A useful lemma for capacity analysis of fading interference channels," *IEEE Transactions on Communications*, vol. 58, no. 2, pp. 411–416, 2010.